# A First-Principles Framework for Simulating Light and Snow Interactions

by

Petri Matthew Varsa

A thesis
presented to the University of Waterloo
in fulfillment of the
thesis requirement for the degree of
Doctor of Philosophy
in
Computer Science

Waterloo, Ontario, Canada, 2025

**Examining Committee Membership**

The following served on the Examining Committee for this thesis. The decision of the Examining Committee is by majority vote.

| | |
|---|---|
| External Examiner: | Pierre Poulin<br>Professor, Dépt. d'Informatique et de Recherche Opérationnelle,<br>Université de Montréal |
| Supervisor: | Gladimir V. G. Baranoski<br>Professor, Cheriton School of Computer Science,<br>University of Waterloo |
| Internal Member: | Paulo Alencar<br>Adjunct Professor, Cheriton School of Computer Science,<br>University of Waterloo |
| Internal Member: | Jeff Orchard<br>Associate Professor, Cheriton School of Computer Science,<br>University of Waterloo |
| Internal-External Member: | Sander Rhebergen<br>Associate Professor, Dept. of Applied Mathematics,<br>University of Waterloo |

## Author's Declaration

This thesis consists of material all of which I authored or co-authored: see Statement of Contributions included in the thesis. This is a true copy of the thesis, including any required final revisions, as accepted by my examiners.

I understand that my thesis may be made electronically available to the public.

## Statement of Contributions

This dissertation includes co-authored material that has appeared in peer-reviewed journals and conferences. In addition, some material in this work is currently under review. Those original works have been revised and expanded upon, in this thesis.

- "SPLITSnow: A spectral light transport model for snow," published in *Remote Sensing of Environment*, 255:112272:1–20, 2021. All authors contributed to this work. Petri Varsa was the lead author, contributing to writing, software development, conducting experiments, data analysis and correspondence, under the supervision of Gladimir Baranoski. Portions of this publication appear in Chapters 1, 3, 4, 6, 7, and Appendices B and D of this thesis.

- "Rendering the bluish appearance of snow: When light transmission matters," published in *IEEE Computer Graphics and Applications*, 44(1):50–61, 2024. All authors contributed to this work. Petri Varsa was the lead author, contributing to writing, software development, data production, conducting experiments, data analysis and correspondence, under the supervision of Gladimir Baranoski. Portions of this work appear in Chapters 1, 3, 5, 6, 8 and 9 of this thesis.

- "In silico assessment of light penetration into snow: Implications to the prediction of slab failures leading to avalanches," published in K. Schulz, editor, *Proceedings of SPIE*, Volume 11863, pages 1186305:1-10, 2021. All authors contributed to this work. Petri Varsa was the lead author, contributing to writing, conducting experiments, data analysis and correspondence, under the supervision of Gladimir Baranoski. Portions of this work appear in Appendix E.

- "On the sensitivity of snow bidirectional reflectance to variations in grain characteristics," published in C. M. U. Neale and A. Maltese, editors, *Proceedings of SPIE*, Volume 11856, pages 118560G:1–10, 2021. All authors contributed to this work. Petri Varsa was the lead author, contributing to writing, conducting experiments, data analysis and correspondence, under the supervision of Gladimir Baranoski. Portions of this work appear in Appendix F.

- "Environmentally induced snow transmittance variations in the photosynthetic spectral domain: Photobiological implications for subnivean vegetation under climate warming conditions," published in *Remote Sensing*, 16(5):927:1–22, 2024. All authors contributed to this work. Petri Varsa contributed to gathering supporting data, conducting experiments, analyzing their outcomes and editing. Portions of this work appear in Chapter 7 and Appendix D.

- "Black carbon impact on snow and vegetation interactions," currently under review. All authors contributed to this work. Petri Varsa contributed to gathering supporting data, conducting experiments, analyzing their outcomes and editing. Portions of this work appear in Chapter 7, and Appendices C and D.

All other content was expressly written for this dissertation.

**Abstract**

Interactions between light and matter give rise to an abundance of natural phenomena. Common examples include those between light and atmospheric ice crystals producing halos, and between light and liquid water droplets producing rainbows. However, interesting effects may also be observed when light impinges upon more dense materials such as snow. These may be noted as changes to the appearance of the material resulting from variations in the characteristics of the material itself. In some cases, these appearance changes may even manifest themselves as dramatic changes in colour. In this thesis, we study snow as a material and reproduce such phenomena by simulating light interactions with virtual snow samples.

Accordingly, this work presents a first-principles framework for simulating light transport through snow. Data and information that describe the characteristics of snowpacks are obtained from the literature and used to devise a digital representation of them suitable for predicatively modelling light interactions with snow. The employed formulation allows for different virtual snow samples to be investigated. Simulated rays of light are cast into a virtual snow sample, and these rays are reflected and refracted until they exit from the surface of the sample, are transmitted through the sample or are absorbed. The modelling results are recorded as spectral response datasets for evaluation and analysis. These datasets are then compared with measured data and observations reported in the literature in order to assess the simulations' fidelity.

There are a number of study areas where such a framework can make a contribution. In this thesis, we discuss such contributions to two fields of research, namely, computer graphics and remote sensing. From a computer graphics perspective, the outputs of simulating light interactions with snow may be used in natural phenomena visualizations employed for educational and entertainment purposes. From a remote sensing perspective, the simulations may be used to conduct *in silico* experiments that help to shed light on topics that are actively being studied. Furthermore, the simulation outputs may also be used as data products in themselves, to make comparisons against remotely acquired data and support other modelling initiatives.

The proposed framework presented in this thesis encapsulates a body of work that is expected to advance the state of the art of snow appearance modelling using a multi-faceted approach. The foundation of the framework is a novel radiative transfer model of light impingement on snow, whose predictive capabilities are extensively evaluated. Then, data products produced by this framework are used to address open questions in the two fields of interest, *i.e.*, computer graphics and remote sensing. In particular, we describe a method to include the complex, visual phenomena that are predicted by the radiative transfer model introduced here into a traditional rendering pipeline. We also make use of the proposed framework to investigate open problems (*e.g.*, the absorption of solar radiation by snow and the effect that this has on avalanche prediction) with potential interdisciplinary applications.

**Acknowledgements**

I would like to sincerely thank my graduate supervisor, Gladimir Baranoski, for his years of guidance and encouragement, for his excellent advice and for his enduring spirit of collaboration. I would also like to thank my committee members, Prof. Jeff Orchard, Prof. Paulo Alencar for their valuable input throughout this academic journey, as well as Prof. Pierre Poulin and Prof. Sander Rhebergen for their valuable feedback on this work.

I would also like to thank my peers, both past and present, from the Natural Phenomena Simulation Group for all the chats, ideas, good times and memories. Furthermore, I also wish to extend my gratitude to all my fellow graduate students from across the School of Computer Science, the Math Faculty and the greater campus. It is often the people you meet along the journey that colour the steps along the way.

I would like thank Marie Dumont for generously providing access to the datasets which were used in the initial validation of the model presented in this work. I would similarly like to thank Roberto Salzano for providing access to the datasets in the SISpec database, for patiently responding to my inquiries regarding the data and for his help in processing the data files.

Lastly, none of this would have been possible without the love and support of my family. To my two daughters, Lila and Sylvia, thank you for your patience and understanding over these many years when I was often too busy or too tired to be there for you. To my beloved wife, Justyna, thank you most of all for your encouragement to take this journey and for being a supportive partner along the way. I would have never even started down this path without the knowledge that you would be there for me.

## Dedication

Dedicated to my daughters — the two stars that light up my life.

# Table of Contents

# List of Figures

# List of Tables

# Abbreviations

**3D** three dimensional 10, 26, 28, 30, 87, 183–185

**AMD** Advanced Micro Devices Inc. 122

**ASTM** American Society for Testing and Materials 25

**AVIRIS-NG** Airborne Visible-Infrared Imaging Spectrometer — Next Generation 71, 105–107

**BRDF** bidirectional reflectance distribution function 15, 16, 21, 26, 45, 46, 65, 67, 87, 100–105, 131, 132, 181, 182, 184–188

**BSDF** bidirectional scattering distribution function 15, 39, 40, 65

**BSSDF** bidirectional surface-scattering distribution function 6, 15, 40, 57, 65

**BTDF** bidirectional transmittance distribution function 15, 65, 188

**CIE** International Commission on Illumination 72, 73

**CPU** central processing unit 122, 124

**CRC** Originally stood for Chemical Rubber Company 161

**DISORT** DIScrete Ordinate Radiative Transfer 27

**EM** electromagnetic xxviii, 2, 3, 6, 8, 9, 11, 12, 14–16, 28, 47, 48, 66, 80, 81, 84, 88, 91, 130, 131, 158, 172

**FDTD** finite difference time domain 28

**IACS** International Association of Cryospheric Sciences 34

**IHP** International Hydrological Programme 34

**IR** infrared 6, 47, 71, 81, 82, 84, 129, 131, 132

**MAE** Mass Absorption Efficiency xxiii, 49, 92, 94, 95

**PCA** principal component analysis xxiii–xxvii, xxix, 54–56, 58, 72, 108, 110, 114, 116, 117

**PDF** probability density function 19, 21, 163

**RMSE** root mean squared error xxviii, xxix, 72, 78, 79, 81, 82, 85, 86, 89, 114–116, 118

**s.a.c.** specific absorption coefficient 43, 44, 49

**SISpec** Snow & Ice Spectral Library 2.0 69, 81, 83, 168, 169

**SMPTE** Society of Motion Picture and Television Engineers 75

**SNICAR-ADv3** Snow, Ice and Aerosol Radiative model with Adding-Doubling solver, version 3.0 30

**SPLITSnow** *SP*ectral *LI*ght *T*ransport in *Snow* 4–6, 31, 33, 36, 39, 40, 44, 45, 47–49, 54, 57, 63, 64, 68, 70, 71, 75–86, 88–98, 100–102, 105–109, 111–113, 115, 118, 119, 121, 127, 129–133, 161, 166, 168–170, 172, 173, 182, 187

**SSA** specific surface area 29

**SVD** singular-value decomposition 55

**UI** user interface xv, 76, 77

**UNESCO** United Nations Educational, Scientific and Cultural Organization 34

**UV** ultraviolet 6, 9, 48, 81, 82, 85, 92, 129

# List of Symbols

$a^*$ The $a^*$ coordinate in the CIELAB colour space, which spans a green-magenta axis. 73, 115

$A$ Area. Units are $\mathrm{m}^2$ 10

$\mathscr{A}$ The Angstrom exponent used in conjunction with the Mass Absorption Efficiency (MAE) and the reference wavelength, $\lambda_0$, to compute the absorption coefficients, $\alpha_{bc}$ and $\alpha_{brc}$, for carbon-based materials. 49

$b$ The semi-major axis of a prolate spheroid. 40, 41

$b^*$ The $b^*$ coordinate in the CIELAB colour space, which spans the blue-yellow axis. 73, 115

$c$ The semi-minor axis of a prolate spheroid. 41

$C$ The set of "coefficient" values for the basis $V$ determined *via* principal component analysis (PCA). 56

$C'$ The dimensionally reduced set of "coefficient" values for the reduced basis $V'$ determined *via* PCA. 56, 58, 59, 114

$C'_j$ The $j^{\mathrm{th}}$ row of the dimensionally reduced set of "coefficient" values for the reduced basis $V'$ determined *via* PCA. 56

$\mathscr{C}$ The concentration of carbon-based material in a virtual snow sample. The units are $\mathrm{ng\,g^{-1}}$. 49, 50

$d_g$ The distance travelled by light within a snow grain. 43, 48

$d_p$ The distance travelled by light within the pore space (between two grains). 37, 38, 44, 48

$\overline{d}$ The mean distance between snow grains in a simulation. 38, 47, 161–163

$\overline{d}_m$ The mean distance between grains of type $m$ in heterogeneous snow samples. 163

$\mathscr{d}$ The distance a ray traverses through scene geometry while rendering light transmission through snow. 57, 61

$D$ Density of a snow sample in a dry state. More specifically, the density of the snow sample as determined by the volume occupied by the snow grains. Units are expressed as $\mathrm{kg\,m^{-3}}$, although $\mathrm{g\,cm^{-3}}$ is also commonly found in the literature. 37–39, 44, 49, 50, 60, 161, 164–167

$D_{ice}$ The density of solid ice, which varies with temperature. 44, 161, 164–167

$E_i$ Incident irradiance in $\mathrm{W\,m^{-2}}$. 16

$f_r$ The bidirectional reflectance distribution function (BRDF). The units are $\mathrm{sr^{-1}}$. 16, 65

$F$ The facetness parameter used to model crystalline features of snow grains. The parameter is unitless and valid values are in the range of $[0, 1]$, with $0$ representing smooth grains and 1 representing highly faceted grains. 42, 60

$\mathscr{F}_{r_\parallel}$ The Fresnel coefficient (reflectivity) associated with parallel reflection of polarized light. 159

$\mathscr{F}_{r_\perp}$ The Fresnel coefficient (reflectivity) associated with perpendicular reflection of polarized light. 159

$g$ The grain size parameter in the snow model. Units are $\mu\mathrm{m}$. 60

$G(\chi)$ The cross-sectional area of a snow grain with geometry $\chi$ projected onto a plane. 162

$h$ The thickness (or depth) of a sample. Sometimes referred as height, especially when included in a snow profile record. 35, 57, 60

$i$ When used as a subscript, the symbol $i$ indicates incident. 16–18

$I$ Radiant intensity. Units are $\mathrm{W\,sr^{-1}}$. 10

$j$ Index used to refer to rows of a matrix when discussing PCA, to iterate over spectral samples. 56, 59, 72

$k$ The complex part of the index of refraction. Sometimes known as the extinction coefficient. 13, 43, 44, 159

$K$ The geometric attenuation coefficient. 162, 163

$K_1$ The distribution possible snow grain sizes. 162

$K_2$ The distribution of possible snow grain shapes. 162

$K_m$ The cross-sectional area of snow grains per unit volume as seen along a linear distance through a volume of snow for grain type $m$ in a heterogeneous snow sample. 163

$\mathscr{K}$ The absorption index. Used in an alternate form of the complex index of refraction. 159, 160

$l$ The number of columns (wavelengths $\lambda$) in the matrix $M$ used for PCA. 55, 56, 59, 72

$l'$ The dimensionally reduced number of columns (wavelengths $\lambda$) determined using PCA, where $l' \ll l$. 56, 59, 72, 73, 115

$\vec{l}$ A vector that represents the direction to a light source. 20

$\vec{l_n}$ A secondary ray used in a path tracing or other ray tracing algorithms. 21, 57, 58

$L_r$ Reflected radiance. Units are $\mathrm{W\,m^{-2}\,sr^{-1}}$. 10, 16

$L^*$ The lightness coordinate in the CIELAB colour space. 73, 115

$m$ A subscript indicating the $m^{\text{th}}$ grain in a heterogeneous snow sample. 163

$M$ The matrix of spectral transmittance response values used for rendering purposes. 55, 56, 59, 60, 72, 114, 118

$\mathscr{M}$ The mass absorption efficiency of carbon-based material used in conjunction with the reference wavelength ($\lambda_0$) and the Angstrom exponent ($\mathscr{A}$) to compute the absorption coefficients ($\alpha_{bc}$ and $\alpha_{brc}$) for carbon-based materials. 49, 92

$n$ The number of spectral samples. Used in a summation. 72, 74

$n_{r\lambda}$ Number of rays that are reflected from the surface in a simulation in all directions. 66

$n_{t\lambda}$ Number of rays that are transmitted through a material in a simulation in all directions. 66

$n_\lambda$ Number of reflected (or transmitted) rays that escape the surface (subsurface) in a simulation in a particular direction. 65

$\vec{n}$ A vector that represents a normal to a surface. 20, 42

$\vec{n}'$ A vector that represents a normal to a surface which has been perturbed to represent a microfacet. 42

$\mathscr{n}$ The real-valued portion of the complex index of refraction. 13, 14, 159, 160

$\mathscr{n}_i$ The real-valued portion of the complex index of refraction for the material encompassing the incident light. 13, 159, 160

$\mathscr{n}_t$ The real-valued portion of the complex index of refraction for the material encompassing the transmitted light. 13, 159, 160

$N_\lambda$ The total number of rays that are cast in a simulation. 65, 66

$\mathscr{N}(\chi)$ The number density of a snow grain with geometry $\chi$. 162

$p_t$ The probability that a ray will be transmitted through a material or a snow grain. 43, 44, 48

$\mathbb{P}$ The probability of an event occurring, *i.e.*, the $\mathbb{P}(B)$ is the probability that random variable $B$ occurs in a given probability distribution. 18, 19, 162

$\mathscr{p}$ The number of grains in an arbitrary volume of a virtual snow sample. 164–166

$\mathscr{P}$ The porosity is a unitless value that represents the volume fraction of snow that is not occupied by snow grains. 161, 162, 166, 167

$Q$ The radiant energy representing a packet of rays. Units are expressed in J. 10

$r$ When used as a subscript, the symbol $r$ indicates reflected. 16–18, 65

$\vec{r}_n$ A primary ray used in a path tracing or other ray tracing algorithms. 21, 57, 58

$R$ The reflectance factor, which is dimensionless. 17

$R_\parallel$ The square of the Fresnel coefficient (reflectivity) associated with the parallel mode, namely, $F_{r_\parallel}$. 159

$R_\perp$ The square of the Fresnel coefficient (reflectivity) associated with the perpendicular mode, namely, $F_{r_\perp}$. 159

$s$ The number of rows (samples) in the matrix $M$ used for PCA. 55, 56

$S_{bc}$ The sedimentation fraction for black carbon. A unitless number in the range of $[0, 1]$ which determines the fraction of impurities extant in the snow grains (sedimentation) or in the pore space (suspension). 48

$S_{brc}$ The sedimentation fraction for brown carbon. A unitless number in the range of $[0, 1]$ which determines the fraction of impurities extant in the snow grains (sedimentation) or in the pore space (suspension). 48

$\mathscr{S}$ Saturation: The fraction of the pore space that is occupied by water. 44, 50, 164–167

$t$ When used as a subscript, the symbol $t$ indicates transmitted. 18

$U$ Orthonormal matrix that forms a basis for PCA. 55

$\vec{v}$ A vector that represents the direction of the viewer (or eye point). 20

$\overline{v}$ The mean volume of a snow grain in a given virtual snow sample. 164–166

$V$ The set of basis vectors (as column vectors) that are determined for $M$ using PCA. 55, 56

$V'$ The dimensionally reduced set of basis vectors (as column vectors) that are obtained using PCA. 56, 58, 59, 114

$V_g$ The volume fraction occupied by grains within a material is the (unitless) complement to the porosity and equal to $1 - \mathscr{P}$. 162, 163

$V_{g_m}$ The volume fraction of grain type $m$ in heterogeneous snow samples. 163

$\mathscr{V}$ An arbitrary volume of snow in a virtual snow sample. 164–166

$\mathscr{V}_{ice}$ The volume occupied by the grains of ice in an arbitrary volume of snow, $\mathscr{V}$, in a virtual snow sample. 165

$\mathscr{V}_{ps}$ The volume *not* occupied by the grains of ice in an arbitrary volume of snow, $\mathscr{V}$, in a virtual snow sample, *i.e.*, the pore space. This is an actual volume, not a ratio. Namely, not the porosity $\mathscr{P}$. 165

$\mathscr{W}$ Water content: The fraction of the total volume that is occupied by water. 44, 164–166

$x_i$ Intersection point where an incident ray strikes a snow grain. 41, 42

$X_i$ Intersection point where an incident ray strikes a material. 35, 37

$X_r$ Point of exitance where a ray exits a material. 35, 37

$\mathscr{X}$ The volume fraction of a "wet" snow sample occupied by ice grains. 166, 167

$\mathscr{Y}$ The volume fraction of a "wet" snow sample occupied by liquid water. 167

$\alpha$ The absorption coefficient used to compute the probability of absorption *via* the Beer-Lambert law. It has units of $\mathrm{m}^{-1}$. 43, 44, 48

$\alpha_{bc}$ The absorption coefficient for black carbon. 48, 49

$\alpha_{brc}$ The absorption coefficient for brown carbon. 48, 49

$\Delta E^*_{ab}$ The perceptual difference between two coordinates (colours) in the CIELAB colour space. 73

$\eta$ Relative refractive index. *I.e.* $\eta = \eta_1/\eta_2$. 13, 159, 160

$\eta_i$ Refractive index for the material where the illumination is incident. 159

$\eta_t$ Refractive index for the material that light is being transmitted into. 159

$\theta$ Polar angle measured away from the normal to the surface. 10, 16, 20, 42, 57, 60, 61, 66

$\theta_i$ Polar angle of incidence measured away from the normal to the surface. 12, 13, 16–18, 65, 66, 159, 160

$\theta_r$ Polar angle of reflected light measured away from the normal to the surface. 12, 16, 17, 65

$\theta_t$ Polar angle of transmitted light measured away from the direction vector opposite to the normal to the surface. 12, 13, 159, 160

$\lambda$ The wavelength of electromagnetic (EM) radiation (light). 8, 10, 11, 13, 14, 16, 18, 42–44, 48, 49, 55, 65, 66, 92, 158

$\mu$ A value in a uniform distribution. 162

$\mu_{max}$ The maximum value in a uniform distribution. 162

$\mu_{min}$ The minimum value in a uniform distribution. 162

$\xi$ A random variable used in a stochastic process. 38, 39, 42–44, 163

$\overline{\xi}$ The mean value of a probability distribution. 163

$\rho$ Reflectance, which is expressed as a fractional number in the range of $[0, 1]$. 18, 66, 72

$\hat{\rho}$ The spectral reflectance value under test when computing the root mean squared error (RMSE). 72

$\sigma$ The standard deviation of a normal distribution. 42, 162, 163

$\varsigma$ The singular values of $M$ in $\Sigma$ determined using PCA. 56

$\Sigma$ Matrix of singular values of $M$ determined using PCA. 55, 56

$\tau$ Transmittance, which is expressed as a fractional number in the range of $[0, 1]$. 18, 66, 72

$\hat{\tau}$ The spectral transmittance value under test when computing the RMSE. 72

$\phi$ Azimuthal angle measured counter-clockwise away from a point of reference. 16, 42, 66

$\phi_i$ Azimuthal angle of incidence measured counter-clockwise from a point of reference. 16–18, 65, 66

$\phi_r$ Azimuthal angle of reflected light measured counter-clockwise from a point of reference. 16, 17, 65

$\varphi$ The function $\Phi\left(\overline{\xi}, \sigma^2\right)$ is the probability density function for a normally distributed random variable, $\xi$, with mean $\overline{\xi}$. 162, 163

$\Phi$ The radiant power (flux). Units are in $\mathrm{W}$ ($\mathrm{J\,s^{-1}}$). 10, 17, 18

$\Phi_{pd}$ The radiant power (flux) of a perfect, Lambertian reflector. Units are in $\mathrm{W}$ ($\mathrm{J\,s^{-1}}$). 17

$\chi$ A member of the set $\mathrm{X}$, *i.e.*, a member of the set of snow grain geometries. 162

$\mathrm{X}$ The set of all possible snow grain geometries. 162

$\Psi$ Inscribed circle sphericity. 40, 41, 162, 163

$\Psi_{max}$ The maximum inscribed circle sphericity for a normal distribution of sphericities. 162, 163

$\Psi_{min}$ The minimum inscribed circle sphericity for a normal distribution of sphericities. 162, 163

$\overline{\Psi}$ The mean sphericity in a normally distributed set of inscribed circle sphericities. 162, 163

$\omega$ Solid angle with units $\mathrm{sr}$ (steradian). 10, 17

$\Omega$ The projected solid angle on a surface. 65

$\aleph(\Psi)$ The surface area to volume ratio of a prolate spheroid with sphericity $\Psi$. 162, 163

# Chapter 1

# Introduction

The study of material appearance is an important area of scientific research. Such an endeavour fosters better understanding of the interactions between light and the material under investigation. These light-material interactions affect the incoming light from the source so as to change the reflected (or transmitted) light. It may change in colour (spectral distribution), or in direction (spatial distribution) or both. Research conducted into these changes (called responses) has a broad variety of applications in several fields including computer graphics and the environmental sciences. This thesis presents a study of light interactions with snow and attempts to quantify the elicited responses governing the material's appearance.

Snow is a granular material composed of ice crystals. These crystals, which are also referred to as snow grains, are typically millimeter or submillimeter in size. They can be smooth and round, faceted and crystalline, or may possess dendritic (branching) features [60]. The volume fraction of space between the grains is known as the pore space. This space can be composed of air and, to a lesser extent, liquid water. In addition, impurities may exist in a snow sample.

From a computer graphics perspective, the rendering of the material appearance changes brought about by natural phenomena remains an active area of research. The capability of accounting for the changes is important since they provide visual cues that significantly increase the perception of realism of the computer renderings and animations [58, 116]. Furthermore, by determining these features algorithmically rather than specifying them manually, the artists' time may be dedicated to other aspects that cannot yet be determined automatically.

Outside of computer graphics, the study of light transport through snowpacks can be a complex, yet important, problem. The high reflectance and insular properties of snow make it a fundamental component of the climate system for the cryosphere [22]. Snow is also an

important part of the hydrological cycle delivering potable water in snowmelt-dominated regions [21]. Global surface temperature changes alter the seasonality of meltwater run off, thus affecting the temporal availability of fresh water [21, 88, 136]. In addition to environmental factors, modelling the electromagnetic (EM) (*i.e.*, light) interactions with snow has pragmatic applications such as determining snow's effect on sensitive equipment [226]. A detailed understanding of the light interactions with a snowpack is required in order to gain valuable insights into these areas.

In this work, we employ an *in silico* (computational) approach to compute the appearance characteristics of snow. We aim to simulate the interactions between the impinging light with snow so that the resulting responses may be used in a *predictive* manner. The assessment of the predictiveness is rooted in *fidelity* [76]. Although there may be a difference of opinion about the exact definition of fidelity, the basic connotation is clear. In essence, fidelity is "the degree to which a model or simulation reproduces the state and behaviour of a real world object or the perception of a real world object" [78]. Therefore, we evaluate the predictiveness of our model against *real world* data obtained from the literature.

Although commonly thought of as being simply white, the reflective properties of snow undergo a myriad changes that depend upon the properties of the snowpack. For example, even a small amount of impurities may have a dramatic effect on the light that is reflected [232]. In addition to the reflected light, the material properties of snow also affect the quality of the light that has permeated through a mass of the material. In particular, the bluish appearance that can be observed when light is transmitted through snow is arguably among the most fascinating of such changes. In concise terms, it results from the wavelength-dependent attenuation[1] of the transmitted light by the ice crystals that form this granular material [19, 27, 28]. Despite the existing knowledge about its eliciting processes, however, its predictive depiction in computer generated images remains elusive.

The predictive reproduction of this distinctive display of natural phenomena requires careful simulations of the underlying light attenuation processes. These simulations, in turn, rely on the use of detailed light transport algorithms controlled by the wavelength-dependent optical properties of snow. We note that academically and commercially available image synthesis pipelines often adopt simplifying assumptions about these properties, notably with respect to fundamental materials like water and ice. These simplifications include, for instance, using a constant value for the index of refraction across all wavelengths in the visible portion of the EM spectrum, and ignoring absorption effects in this spectral domain. Although these simplifications can reduce rendering costs, they hinder the predictive rendering of material appearance changes with a markedly noticeable wavelength dependency.

[1] Attenuation is the combined effect of absorption and scattering of light [171].

As we shall discuss later in this work, employing a full light transport model may be unsuitable for use on-the-fly during rendering applications demanding high interactivity rates. To overcome these constraints, we will present a practical method for the predictive rendering of the appearance of snow that is based on the effective use of snow reflectance and transmittance data. It takes into account variations not only in light incidence, but also in the physical and morphological characteristics of snow since these factors can significantly affect the material's appearance, particularly within the visible spectral domain [184].

With respect to the environmental sciences, *in situ* measurements of light interactions with snow are costly and not without issues [117]. Furthermore, inaccessible or inhospitable regions may require regular measurements *via* remote sensing techniques, whereby aircraft or satellite imagery is used to monitor snow quantities. A detailed knowledge of how light interacts with snow grains is essential to facilitate the interpretation of the resulting remotely acquired data. Furthermore, although material appearance attributes may be measured in field and laboratory studies, the simulation of light interaction with materials can compliment these empirical studies. Consequently, it may serve to advance the state of the art more rapidly [32], *e.g.*, by elucidating the effect of sample characterization [217].

To this end, the effects of the various characteristics of deposited snow on its spectral responses can be effectively studied using an *in silico* investigation approach [4, 111, 172, 239]. Such an approach may aid the analysis of the interactions between EM radiation and water-ice grains. It can also accelerate the understanding of the relationships between the various snow properties and the response values since each parameter that represents a characterization trait can be varied individually. By comparison, *in situ* (field) experiments may be subject to multiple simultaneous parameter changes due to environmental factors. Similarly, manufacturing artificial snow grains is time consuming and costly, and precise traits are still subject to temporal metamorphism [41, 43]. *In silico* experiments can also be employed to provide a complementary data source for testing analytic models by providing data with adequate angular sampling that may not otherwise be readily available [49].

In this thesis, we present a new first-principles simulation framework that may be effectively employed for those purposes. First-principles approaches have been extensively used in different scientific fields [51]. In the context of our research, we are particularly interested in their use in material appearance modelling. Accordingly, we consider the term *first-principles* as referring to simulating the appearance of a material by explicitly accounting for how its fundamental components interact with light rather than relying on aggregated representations of such interactions.

The light transport model for snow, the core component of the proposed framework, is extensively evaluated both quantitatively by making direct comparisons to measured data ob-

tained from the literature, and qualitatively by comparing predictions made by the model against trends that have been documented [5, 28, 53, 54, 74, 95, 144, 157, 184, 228]. We endeavour to show the value of such an effort by applying it to both computer graphics and interdisciplinary studies.

## 1.1 Overview of Contributions

In this thesis, we present a novel framework for simulating light interactions with snow. One of the contributions of this thesis is the development of a non-deterministic model which we call SPLITSnow (*SP*ectral *LI*ght *T*ransport in *Snow*). It forms the foundation of this conceptual framework [219]. Data inputs to this light interaction model are based on snow characterization data as provided in the literature [29, 60]. These data are used to guide the specification of the set of modelled virtual snow samples. A specific virtual snow sample is specified by selecting a set of characterization values within the physically valid ranges for natural snow. For such a virtual snow sample, geometric optics (light rays) are intersected with the material and response data are collected.

A first-principles approach is taken in the design of the model. Given the material characterization inputs, the model applies fundamental optical theory to compute the path that a light ray takes through a snowpack. Repeated trials are employed to determine the spectral and/or spatial distributions, *i.e.*, the spectral and/or spatial responses. These repeated trials are the expression of a Monte Carlo integration [87].

As stated above, the input characterization data were selected based on reported snow characteristics found in the literature. These include commonly reported data such as grain size[2] and snow depth, but also account for other snowpack features such as water content and grain shape. Water content is also accounted for in the pore space that exists between the snow grains. However, many natural snow samples recorded in the field contain a mixture of snow grain types, *i.e.*, they are heterogeneous in nature. Consequently, a mixture of grain types may be specified as inputs to the model. Furthermore, snowpacks tend to accumulate over a number of snowfall events. Therefore, multiple layers may be specified as inputs to SPLITSnow. Lastly, impurities affecting the light transport may also be added to the snow sample.

The outputs of the SPLITSnow model are appearance attribute data. These data may be used to make meaningful contributions to the field of computer graphics. More specifically, one of

[2]Note that we use both the terms "grain" and "particle" to refer to snow grains. When discussing snow characterization we prefer to use the term *grain* to be consistent with the snow science literature. However, we sometimes use the more general term *particle* when discussing background topics in Chapter 2 and other materials.

the focal points of computer graphics research has been the predictive modelling of material appearance. Although snow is an ubiquitous material, relatively little attention has been directed toward predictively rendering its appearance by the computer graphics community. This may be due to the challenging nature of the associated light attenuation phenomena and the common assumption that snowpacks are achromatic. As another contribution of this thesis, we show that snow exhibits characteristic colour variations under common lighting configurations and provide examples of how these variations may be predictively reproduced in a traditional computer graphics rendering pipeline [218].

The outputted datasets generated by SPLITSnow may also be valuable in fields other than computer graphics. For instance, they may act as a complementary data source to be used for testing analytic models by providing data that is otherwise costly to obtain or unavailable as in the case of Ding *et al.* [49]. Furthermore, the SPLITSnow model may be used to conduct *in silico* experiments for situations where results from field studies have proven to be elusive [18]. As a further contribution, we provide example scientific applications [216, 217] which are discussed in Appendices E and F. For such applications, the outputs of the SPLITSnow model may be treated as the computed results determined by mathematical experimentation [87].

In addition to the modelling of light transport through snow that is discussed in this thesis, related investigations involving other types of particulate material such as sand [7, 9, 11, 10, 12] and Martian regolith [8, 13], were also conducted. As the contributions of these investigations are ancillary to the topic of this thesis, they will not be discussed further and the reader is referred to the publications cited in this paragraph for more details.

In this section, we have provided a brief summary of the contributions of this thesis. Primarily, we present a novel framework for simulating light interactions with snow along with a method to integrate the outputs of simulation into a traditional rendering pipeline for computationally generating images. We also present example applications whereby such a model may be employed to solve problems in the natural sciences. We now conclude this section with a brief comment about what the proposed model is *not*. SPLITSnow is a *local illumination model* [198]. As such, macroscopic features are not modelled. As it will be discussed in Chapter 4, individual grains are modelled for the purpose of computing appearance attributes (which are discussed in Section 2.2). These grains are only ephemeral and are not an output of the system, nor stored explicitly. Thus, large features such as the shapes formed by wind-blown snow, known as sastrugi [95], are not represented. SPLITSnow is not a snow deposition model. In other words, it does not model the placement of snow in a scene, nor does it modify or affect scene geometry, whether it represents snow or not. As we will discuss in Chapter 5, it can be used to compute the colour of snow, given the environmental conditions modelled by other means, when it is associated with existing geometric objects in a computer rendering.

## 1.2 Document Organization

The following chapters present the proposed framework for conducting *in silico* experiments, *i.e.* experiments conducted *via* computer simulation, of light interactions with snow. The supporting tiers of the framework provide data inputs and parameter specifications that are used to guide the development and implementation of the proposed model. More specifically, the model employs geometric optics (sometimes called ray optics) across a band of the EM spectrum that includes not only the visible light spectrum, but also wavelengths in the ultraviolet (UV) and the infrared (IR) domains. This framework also describes the data sources and methodologies employed to evaluate the model's predictions which may also influence the design. The outputs of simulation are data products, themselves, that the framework employs for a variety of purposes.

Chapter 2 provides an overview of the relevant background material. Chapter 3 presents a summary of works related to this thesis. Chapter 4 describes the formulation of the SPLITSnow model in detail. Chapter 5 describes how to integrate the datasets produced by SPLITSnow into a traditional rendering pipeline. In Chapter 6, we discuss the various methodologies used to evaluate the predictions of the model and assess the fidelity of colours produced when used in computer renderings. Chapters 7–9 present the results of the evaluation and provide a discussion of these results. More specifically, Chapter 7 focuses on spectral and spatial distribution results quantified in radiometric terms (*e.g.*, reflectance, transmittance and bidirectional surface-scattering distribution function (BSSDF) [154]), while Chapter 8 presents the results of our data analysis and Chapter 9 showcases the use of the proposed framework in realistic image synthesis. Finally, in Chapter 10, we provide an outline of future work along with concluding remarks.

Six appendices are provided at the end of the thesis. Appendix A provides the geometric optics formulation employed in this work. Appendix B discusses some of the technical details related to a computation pertinent to Chapter 4. Appendix C provides a concise description of how water content is represented within a snow sample, and discusses how to convert from one method of water content specification to another. In addition, Appendix C also discusses "wet" vs. "dry" densities, and provides a procedure to convert from one to the other. Appendix D presents a brief explanation of how measured snow characterization data are interpreted as input to the proposed model. Appendix E outlines an example application whereby data outputted from the SPLITSnow model were employed to analyze snow conditions that could lead to slab avalanche events. The last appendix, Appendix F, discusses a property of snowpacks that pertains to reflectance measurements used to estimate water content contained within the snowpack.

# Chapter 2

# Physical Background

In this chapter, we provide a concise overview of the fundamental concepts that are relevant for this thesis. In Section 2.1, we briefly describe the physical nature of light. We also provide a few details regarding the interaction of light with materials and the source of colour. In Section 2.2, we describe how appearance is measured as well as the various aspects affecting its measurement. In Section 2.3, we briefly discuss Monte Carlo methods [87], and how numerical integration may be accomplished stochastically. Finally, in Section 2.4, we provide an overview of computer graphics rendering concepts used in image synthesis. Many different approaches of image synthesis are extant in the field of computer graphics. To this end, Section 2.4 will only focus on the techniques employed in this work, and will not cover other rendering paradigms such as real-time rendering which is discussed elsewhere [113, 196].

## 2.1 Electromagnetic Radiation and Material Interactions

In this section, we concisely introduce the various processes that have an effect on light transport simulations and image synthesis. Much of the material can be found in texts on optics such as that of Pedrotti and Pedrotti [167] and Born and Wolf [31].

### 2.1.1 The Wave-Particle Duality of Light

At times throughout scientific history, light has been considered to be either a wave or a particle. However, in the previous century it became apparent that light has properties of both waves and particles. This has come to be known as the *wave-particle duality* [167]. The discovery

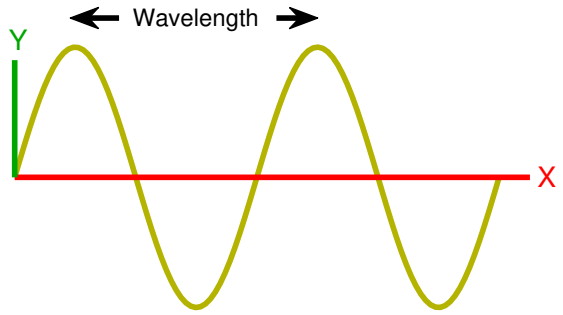


Figure 2.1: A mechanical wave propagates through matter. The direction of energy flow is along the $x$-axis, and the displacement of material is along the $y$-axis.

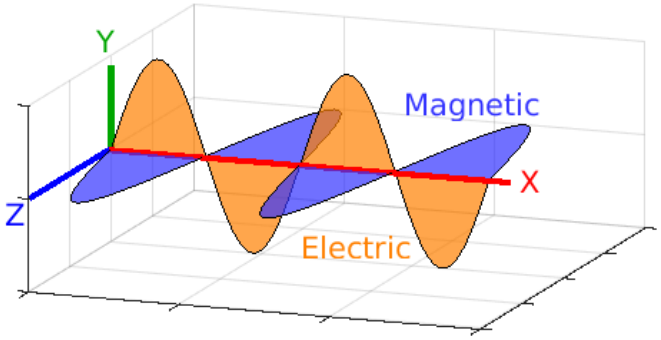


Figure 2.2: An electromagnetic (EM) wave propagates through the EM field. The direction of energy flow is along the $x$-axis and the oscillations of the electric and magnetic fields are along the $y$- and $z$-axes respectively. Based on the diagram provided by Pedrotti and Pedrotti [167].

and mathematical theory that came to describe light is now known as *quantum electrodynamics* [59]. The theory also incorporated magnetism, yielding our modern understanding of light as electromagnetic (EM) radiation [167].

A mechanical wave radiates energy through matter. The wavelength of such a wave is the distance between two consecutive peaks, which is depicted in Figure 2.1. In this figure, the $x$-axis represents the direction travelled by the wave and the $y$-axis represents the displacement of the matter. Correspondingly, Figure 2.2 depicts an EM wave. In this figure, the $x$-axis still represents the direction of radiant energy flow. However, the $y$-axis represents oscillations of an electric field and the $z$-axis represents oscillations of the magnetic field. Different wavelengths, $\lambda$, of EM radiation represent different quantities of energy.

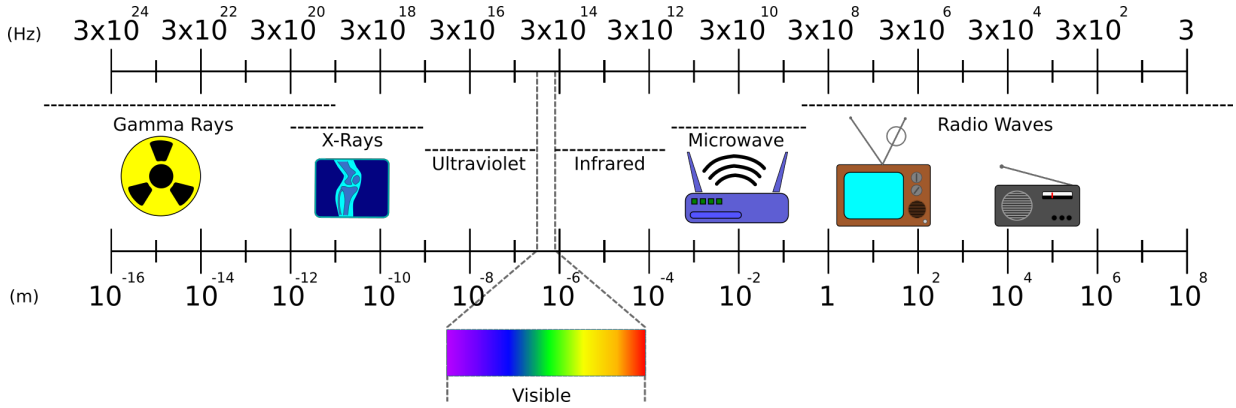


Figure 2.3: The EM spectrum. Short wavelengths (m) are depicted on the left, while long wavelengths are presented on the right. Frequency (Hz) is inversely proportional to wavelength, with high frequencies on the left and low frequencies on the right. Based on the diagram provided by Pedrotti and Pedrotti [167].

The complete EM spectrum (Figure 2.3) is quite large and includes bands such as X-rays and radio waves. However, only a small fraction of the spectrum is visible to the human eye, which only responds to EM stimulus whose wavelengths are in the range of 380 nm ($3.8 \times 10^{-7}$ m) through 780 nm ($7.8 \times 10^{-7}$m) [72]. However, it is most sensitive in the range of 400–700 nm with negligible response to stimuli outside of these values [171]. Surrounding the visible portion of the EM spectrum are other bands. The bands containing the shortest wavelengths are associated with high-energy. These include gamma rays and X-rays. For comparison, X-rays have a wavelength roughly equivalent in size to a water molecule. Bands of EM radiation containing wavelengths that are longer than those in the visible spectrum include microwaves, which can be the size of a small ball, through radio waves which can have wavelengths as long as a football field.

It is interesting to note that not all species of life experience the same spectral responses to light as humans do. For example, some species of butterfly reflect light in the ultraviolet (UV) range very brightly, and have eyes that are sensitive to this part of the EM spectrum [69]. Furthermore, UV light also plays a role in pollination by bees and hummingbirds [48].

### 2.1.2 Radiometric Terms

In this section, we introduce the radiometric terms used to describe the interaction between EM radiation and materials. These terms describe both the measurement of light integrated over a

set of wavelengths and those measurements evaluated at a particular wavelength, $\lambda$ [72]. For brevity, we will not write these terms as a function of $\lambda$. Furthermore, we omit the adjective "spectral" from the definitions.

Radiant energy, $Q$, is a fundamental quantity representing the energy in a collection of rays and has units in joules (J). However, the focus of this work involves quantities of energy flow, since we are concerned with the amount of light striking a surface over a period of time. More specifically, it is assumed that a steady rate of energy flow is hitting the surface of a material. This energy per unit time is *radiant power* (flux) and it is denoted by $\Phi$, which is measured in watts (W or $\mathrm{J\,s^{-1}}$) [198].

In practice, an illumination source has a finite area. Thus, at the point of illumination, the incident light has a radiant power that impinges from a particular direction with its area of illumination defined by a solid angle.[1] The radiant power per unit solid angle for a given direction is called the *radiant intensity* and denoted by $I$ and has units of $\mathrm{W\,sr^{-1}}$. Expressed in terms of radiant power and solid angle, the radiant intensity is given by $I = \mathrm{d}\Phi/\,\mathrm{d}\omega$, where $\omega$ is the solid angle [198].

The last radiometric term to define in this section is *radiance*. Radiance is the reflected quantity that more closely approximates the colour of the surface [198]. It is independent of surface area, the size of the object being inspected and the distance to the observer, and it provides an indication of surface brightness. Radiance may be defined equivalently in terms of the radiant power as:

$$L_r = \frac{\mathrm{d}^2\Phi}{\mathrm{d}\omega\,\mathrm{d}A\cos\theta}, \tag{2.1}$$

where $\mathrm{d}\omega$ is the differential solid angle of the observation, $\mathrm{d}A$ is the differential area surrounding the point of reflection on the surface material and $\theta$ is the angle between the normal to the surface the direction of the observer. Equivalently, radiance may be defined in terms of radiant intensity as:

$$L_r = \frac{\mathrm{d}I}{\mathrm{d}A\cos\theta}. \tag{2.2}$$

### 2.1.3 The Scattering of Light by Materials

This thesis discusses the interaction of light with materials — in particular the interaction of light with snow. Snow is generally considered to be white in appearance, although other colours

[1] A solid angle is the three dimensional (3D) analog to radians. Whereas radians are represented by the arc length of a unit circle, steradians are represented by an area of the unit sphere. The units are expressed in steradians (sr).

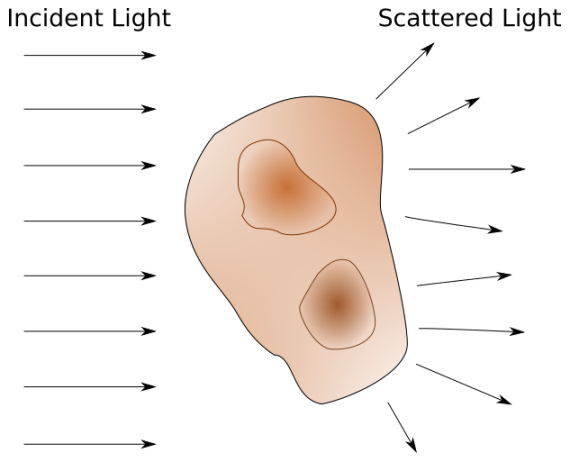


Figure 2.4: Single scattering of light by a particle. Incident light interacts with a single particle and it is subsequently scattered. Based on the diagram provided by Bohren and Huffman [30].

can be manifested [27]. However, when examined with magnification, each crystal (or *grain*) of snow is generally transparent. What then, is the source of the white colour? The simple answer to this question is the random scattering of the incident light by a multitude of snow grains, which are commonly referred to as *particles* in a more general sense. Moreover, the scattering of light may be governed by different processes, which give rise to a variety of phenomena.

For instance, when a material's constituent particles are small compared to the wavelength of EM radiation, the scattering is proportional to $\lambda^{-4}$. This type of scattering is known as *Rayleigh scattering* [167]. It is responsible for the blue colour of the daytime sky. However, when the size of the particles are larger, *i.e.*, their sizes are approaching the wavelength of the incident radiation, Rayleigh scattering no longer effectively models the light-particle interactions. For such cases *Mie scattering* can be used to model the interactions [31]. Although the theory behind Mie scattering is based on spherical particles, it also correctly describes many small particle effects for nonspherical particles [167]. An example of a commonly observed Mie scattering effect is the white colour associated with clouds [31]. This thesis focuses on the scattering exhibited by still larger particles. Namely, those that are significantly larger than the wavelengths used to illuminate the sample. An example of a phenomenon that is produced by the scattering of light through relatively large particles is the scattering of light by atmospheric water droplets that produces a rainbow [138].

Many studies of the scattering of relatively large particles choose to focus their efforts on the scattering of light by a single particle as depicted in Figure 2.4. In this figure, incident light passes through an homogeneous medium, then strikes and interacts with a particle and it is

subsequently scattered. For a beam of light interacting with the particle, one can expect that some (possibly zero) fraction of the light will be reflected off the surface of the particle, while another fraction will be refracted into the particle. Similarly, in the case where light is transmitted into the particle, it may reflect back into the particle at the particle-medium boundary after being transmitted through the particle, or refract back out of the particle. In addition, some fraction of the light may be absorbed. Studies of so called *single scattering* often focus on materials whose particles have regular shape and combine the results of single scattering with analytical theory (*e.g.*, [79, 243]). The resulting angular distribution of light scattered from a single particle is commonly quantified as its *phase function*.[2] The phase function is typically normalized so that the sum total of all contributions in all directions in a sphere surrounding the particle is one [30].

Studying light interactions with a material often requires considering not just a single particle, but a collection of particles [30]. As light traverses the medium (or media), it interacts with several particles before ultimately being reflected by the material, transmitted through the material or absorbed. This is known as *multiple scattering*. This thesis takes a multiple scattering approach to studying light interactions with snow.

### 2.1.4 Geometric Optics and the Complex Index of Refraction

The wave nature of light allows for phenomena that depend upon interference patterns that arise from the crests and troughs of the interacting waves. Such phenomena are known as *interference phenomena* [31]. The wave nature of light is also responsible for *diffraction*,[3] where a beam of light is spread out after passing through a narrow aperture [167]. However, there is a wide range of phenomena that are not suitably handled by wave optics. For such phenomena, visible light and other parts of the EM spectrum can be treated as rays, *i.e.*, geometric optics can be employed in their description and prediction.

As an example, consider Figure 2.5. The incident light direction is measured away from the normal to the surface and is given by $\theta_i$, while $\theta_r$ represents the angle at which light is reflected from the surface. For a perfectly reflecting mirror surface, $\theta_i$ equals $\theta_r$, and the direction of the reflected light can be determined geometrically, while the quantity of reflected light equals the quantity of incident light.

Most objects are not perfect reflectors and some of the light is transmitted through the surface and into the material. The angle of the transmitted light is represented by $\theta_t$, and it can

[2] We remark that phase functions are sometimes used to represent the combined effects of multiple scattering. For more information about this topic, the interested reader is referred to a related work [15].

[3] Diffraction effects are due to the bending of light waves around the edges of obstructions [167].

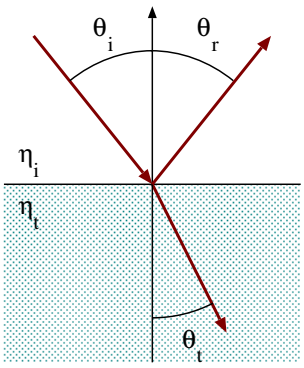


Figure 2.5: Geometrically reflected and transmitted rays of light. Based on the diagram provided by Pedrotti and Pedrotti [167].

be obtained through Snell's law [167]:

$$\frac{\sin\theta_i}{\sin\theta_t} = \frac{n_t}{n_i}, \tag{2.3}$$

where $n_i$ and $n_t$ are usually given as constant, real-valued indices of refraction. The *index of refraction* of a material is the ratio of the speed of light in a vacuum to the speed of light through the material.

For many applications, employing constant, real-valued numbers for $n_i$ and $n_t$ and Equation 2.3 is sufficient. However, for many applications, it is necessary to utilize an index of refraction that varies with the wavelength of illumination. Furthermore, the index of refraction may also specify a complex component, which is also a function of wavelength. Various forms of the complex index of refraction have been used in the literature. In this thesis, we choose to adopt the following form:

$$\eta = n + ik, \tag{2.4}$$

where the index of refraction is given by $\eta$, $n$ is the real part of the index of refraction and $k$ is the complex part of the index of refraction. Both $n$ and $k$ are functions of the wavelength of light, *i.e.*, $n(\lambda)$ and $k(\lambda)$. Again, for brevity, we will not explicitly write each symbol as a function of $\lambda$. Various names have been given to $k$ in the literature. We will refer to $k$ as the complex part of the index of refraction. For consistency with the related literature, we sometimes use the term *extinction coefficient* to refer to $k$. We note that this quantity is associated with the amount of light that may be absorbed by a given material [167].

We note that the wavelength dependency of this quantity is often overlooked either due to the absence of data or for simplification purposes. As stated above, specifying $n$ as a real-valued constant is a simplification that is useful for many purposes, but it is not suitable to

predictively simulate phenomena such as rainbows. In order for a water droplet to split light from an incident light source into its constituent colours, an optical phenomena commonly referred to as dispersion [31], the wavelength dependency of $n$ must be accounted for.

The version of Snell's law given in Equation 2.3 is often employed for dielectrics (poor conductors of electricity) such as water and ice. The more general form of Equation 2.3 that takes into account the complex index of refraction is given in Appendix A. Furthermore, when light is incident on a refractive surface, some fraction of it will be reflected, while some of it will be transmitted. The Fresnel equations [167] (also discussed in Appendix A) are used to determine this fraction. Note that the Fresnel equations also use the complex index of refraction in their formulation.

## 2.2 The Measurement of Appearance

In this section, we outline the measurement of appearance [97] concepts pertaining to this work. The appearance of a given material is determined by the spectral (wavelength dependent) and spatial distributions of light propagated by it. While the former component is associated with appearance attributes such as colour, the latter is associated with attributes such as glossiness and translucency.

These appearance components are determined by the processes affecting the distributions of the light impinging upon the material. The light, itself, is EM energy that first radiates from a source and then interacts with a material, where some components of the EM radiation emerge and continue to radiate. The wavelength, $\lambda$, of this radiative energy is the value that distinguishes one type of radiation from another. In particular, the parameter $\lambda$ provides the spectral distribution, or spectrum, of EM radiation.

Whereas the spectral distribution concerns the distribution of the wavelengths, the spatial distribution is a quantification of the geometric distribution of the response. Figure 2.6 demonstrates the spatial attributes associated with reflection. In Figure 2.6(a), the majority of the light is reflected in the forward direction. Materials with this type of spatial response for reflection tend to look shiny, like a polished apple. In Figure 2.6(b), light is evenly reflected in all directions. This type of spatial reflection has a matte finish, and it is often referred to as diffuse or Lambertian reflection [97]. It is important to note here that the spatial distribution of reflected light may also vary with wavelength. Thus, an object may appear shiny when it propagates light at a certain wavelength, but diffuse when it propagates light at another wavelength.

In an *in situ* study concerning directionally or spatially varying reflectances, the results are

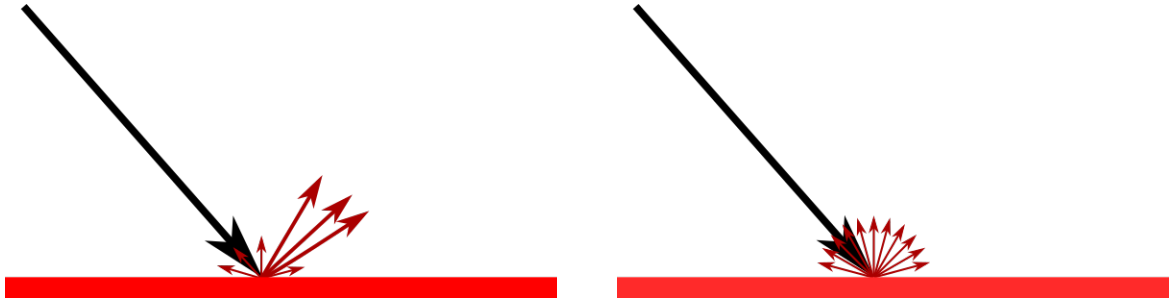

(a) (b)

Figure 2.6: Two examples demonstrating spatially different reflective behaviours. In (a), there is a strong forward component, giving the material a glossy look. In (b), the reflected light is equally distributed in all directions, giving the surface a dull finish.

often described as being goniometric[4] in nature. The tool used to measure these directional (angular) variations is a type of *goniometer* [124]. For experiments involving EM radiation of particular wavelengths of illumination the apparatus is known as a spectro-goniophotometer.

### 2.2.1 Modes of Illumination and Directional Measurement

In this section, we discuss the different types or *modes* of illumination along with the corresponding modes of measurement. In addition, we present additional radiometric terms employed in this thesis. It has been noted that there has been a lack of consistency in radiometric terminology in the literature [192]. For this reason, this thesis will follow the standardization set out previously by other researchers, namely Nicodemus *et al.* [154] and Schaepman-Strub *et al.* [192].

In the most general sense, the bidirectional surface-scattering distribution function (BSSDF) encapsulates the reflectance (and transmittance) of a material. For each wavelength of illumination, the proportion of reflected (or transmitted) radiance to incident flux (power) is specified for each incoming and outgoing direction and position of exitance of the material. If the positional dependency is assumed to be negligible, one can employ the bidirectional scattering distribution function (BSDF) [23]. If only the reflected portion of the BSDF is of concern, it can be expressed in terms of the bidirectional reflectance distribution function (BRDF). Similarly the transmitted portion of the BSDF can be expressed in terms of the bidirectional transmittance distribution function (BTDF). The BRDF is thus defined as the ratio of reflected radiance

[4]Goniometry is the measure of angles or data associated with angles [124].

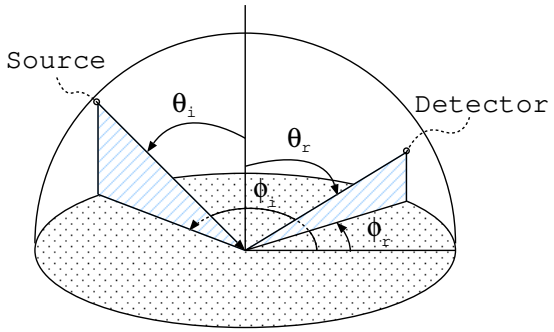


Figure 2.7: Definition of angular measure for incident, $i$, and reflected, $r$, directions. The polar angle, $\theta$, increases away from the normal to the surface, while the relative azimuth angle, $\phi$, increases counter-clockwise in the plane of the sample.

to the incident irradiance and has units of $\mathrm{sr}^{-1}$ (*i.e.*, per steradian or per unit solid angle). Since transmittance is usually handled in a similar manner to reflectance, in the following definitions we concentrate on reflectance and implicitly include transmittance by analogy.

Figure 2.7 provides a reference diagram for light incidence and collection geometry taken into account the definitions provided in this section. The polar angle is measured away from the normal to the surface and it is denoted by $\theta$. The symbol $\phi$ is used to represent the azimuthal angle, which increases counter-clockwise in the plane of the sample. The subscripts $i$ and $r$ indicate the incident and reflected directions, respectively.

There are three modes of EM radiation to consider when measuring the reflectance of a material that have previously been defined [154]. They are *directional*, *conical* and *hemispherical*. Each mode must be considered for both incoming and reflected components, yielding nine combinations. (See Figure 2.8, where four of the nine combinations are depicted.) For instance, the function relating the incident light from one direction of its contribution to the reflected light in another direction is directional-directional, or more concisely called bidirectional. This function is, in fact, the BRDF. The BRDF is defined as the ratio of reflected radiance, $L_r(\theta_i, \phi_i; \theta_r, \phi_r; \lambda)$, to the incident irradiance, $E_i(\theta_i, \phi_i; \lambda)$ for each incident and exitant direction. As a function it is typically expressed as:

$$f_r(\theta_i, \phi_i; \theta_r, \phi_r; \lambda) = \frac{\mathrm{d}L_r(\theta_i, \phi_i; \theta_r, \phi_r; \lambda)}{\mathrm{d}E_i(\theta_i, \phi_i; \lambda)}, \tag{2.5}$$

where $(\theta, \phi)$ pairs represent the directions in spherical coordinates.

As noted in the literature [154], the BRDF is not directly measurable in the field or laboratory since light emitters and detectors utilized in experimental apparatus have a finite area and thus,

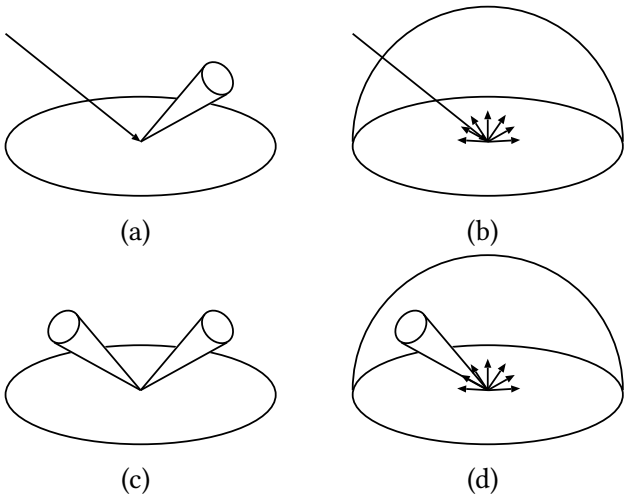


Figure 2.8: Diagrams illustrating four types of reflectance [154]: (a) directional-conical; (b) directional-hemispherical; (c) biconical; and (d) conical-hemispherical.

are conical by design. (See Figure 2.8(c).) More specifically, a source of illumination has a finite area by construction, which is directed at the sample to be measured, yielding a cone as observed from a point on the surface. Similarly, a detector has a surface area. Thus, a laboratory device used to measure reflectance is biconical. Experimental methodologies may employ small sensors to minimize the impact of a biconical setup [35, 54] or account for it by normalizing the measured values using the solid angle of the detector.

This method of measurement usually results in reflectance factor data [192]. For each geometric configuration, this is a ratio of radiant flux reflected by a sample to that reflected by an ideal, diffuse (Lambertian), standard surface. The biconical reflectance factor is given by:

$$R(\theta_i, \phi_i, \omega_i; \theta_r, \phi_r) = \frac{\Phi_r(\theta_i, \phi_i, \omega_i; \theta_r, \phi_r)}{\Phi_{pd}(\theta_i, \phi_i, \omega_i; \theta_r, \phi_r)} \tag{2.6}$$

where $\Phi_r$ represents the amount of light reflected from the material, and $\Phi_{pd}$ represents the amount of light reflected by a perfectly diffuse reflector [97].

Simulations, however, do not have all the same limitations of physical apparatus. With a simulation, it is possible to have directional incidence since the irradiance (the incident radiant flux (power) per unit area [154]) is specified using only two values: the point on the sample and the direction from the source of illumination. Hence, simulations are not restricted to light sources with a finite area. This is depicted in Figure 2.8(a). Thus, an *in silico* experimental methodology may employ a directional-conical mode [124]. For such cases, a similar

normalization (*i.e.*, normalization by the solid angle of the detector) allows for making a direct comparison with measured data.

Directional-hemispherical reflectance is a special case of the conical reflectance where the entire upper hemisphere is used as a single detector. (See Figure 2.8(b).) For this case, the sum total contribution in all directions above the surface gives total hemispherical reflectance. For a simulation the directional-hemispherical reflectance is computed as:

$$\rho(\theta_i, \phi_i; \lambda) = \frac{\Phi_r(\theta_i, \phi_i; \lambda)}{\Phi_i(\theta_i, \phi_i; \lambda)}, \tag{2.7}$$

where $\Phi_i$ represents the incident radiant power (flux) on the surface, and $\Phi_r$ represents the reflected radiant power. An equation similar to Equation 2.7 may be used to compute transmittance, $\tau$, in the lower hemisphere:

$$\tau(\theta_i, \phi_i; \lambda) = \frac{\Phi_t(\theta_i, \phi_i; \lambda)}{\Phi_i(\theta_i, \phi_i; \lambda)}, \tag{2.8}$$

where $\Phi_t$ represents the transmitted radiant power.

Based on the works of Judd [110] and Nicodemus [153, 154], the directional-hemispherical reflectance and the hemispherical-directional reflectance (radiance) factor quantities are considered numerically equivalent for a given direction as a direct consequence of Kirchhoff's law [152] and the Helmholtz reciprocity principle [110]. Hence, for practical purposes, in studies involving the radiometric responses of materials characterized by a near-Lambertian behaviour, such as snow irradiated from an angle of incidence of $0^\circ$ [54, 190], directional-hemispherical reflectance and hemispherical-directional reflectance factor can be used interchangeably [18, 134].

## 2.3 Probability Terminology and Monte Carlo Concepts

In this section, we briefly introduce the terminology that will be used later in this thesis. We begin by providing the definitions for probability terms. We then provide a concise overview of Monte Carlo concepts. For more details, the interested reader is referred to the statistics texts by Wasserman [233] or Ross [185], and to the text on Monte Carlo methods, by Hammersley and Handscomb [87].

Consider a complete set of outcomes, $\mathbb{B}$. For every event, $B \in \mathbb{B}$, a real value is assigned to $B$, namely, $\mathbb{P}(B)$, that is called the probability of $B$. The function $\mathbb{P}$ is called the probability

distribution. Note that $\mathbb{P}(B) \geq 0$ for all $B$ and $\mathbb{P}(\mathbb{B}) = 1$, *i.e.*, the sum of the probabilities of all events is one [233].

A random variable is a mapping, $Y : \mathbb{B} \to \mathbb{R}$, that assigns a real number $Y(a)$ to each outcome $a$. This concept serves as a connection between the data and the sample space, *i.e.*, the values of the probability distribution.

A random variable is continuous if there exists a function $f_Y$ such that $f_Y(y) \geq 0$ for all $x$, the sum of all the values of $f_Y(x)$ is one (*i.e.*, $\int_{-\infty}^{\infty} f_Y(y)\,\mathrm{d}y = 1$), and for each $a \leq b$:

$$\mathbb{P}(a < Y < b) = \int_a^b f_Y(y)\,\mathrm{d}y. \tag{2.9}$$

The function $f_Y$ is called the probability density function (PDF).

We now turn our attention to Monte Carlo methods for the remainder of this section. Monte Carlo methods are a branch of experimental mathematics where one infers conclusions from observations [87, 220]. More specifically in this thesis, we use Monte Carlo integration to evaluate an integral using random sampling. For example, we use random sampling to compute the value of $J$ in the following expression:

$$J = \int f(x)\,\mathrm{d}x. \tag{2.10}$$

This is accomplished by independently sampling $N$ points, $X_1, X_2, \ldots, X_N$ according to a PDF, $p$, and then computing the estimate:

$$F_N = \frac{1}{N} \sum_{i=1}^{N} \frac{f(X_i)}{p(X_i)}. \tag{2.11}$$

Note that we use the symbol $F_N$ for the estimation rather than $J$ to indicate that the estimation is a random variable, and that its value depends upon how many sample points are chosen.

## 2.4 Image Synthesis Background

In this section, we provide a brief overview of the image synthesis concepts employed in this work. In Chapter 5, we present a method to incorporate data produced from the proposed model (which is introduced in Chapter 4) into a traditional image synthesis pipeline. Although we selected to focus on a traditional path tracer [112], the results of this work may be applied to other rendering paradigms.

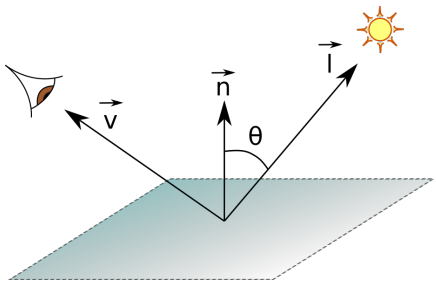


Figure 2.9: Diagram depicting the basic set of data required for a local illumination model. The vector $\vec{n}$ is the normal to the surface, $\vec{l}$ is a vector pointing to a the light source, the vector $\vec{v}$ points to the viewer or eye point, and $\theta$ is the angle between the normal and the source of illumination.

Generally speaking, two types of illumination mechanisms are considered in computer graphics applications: local and global [63, 198]. In the following sections, we concisely examine these mechanisms.

### 2.4.1 Local Illumination Models

Local illumination models are precisely what the name implies, *i.e.*, only local attributes of the object being rendered and direct sources of illumination are required to compute the colour at the point of interest. A simple example is depicted in Figure 2.9.

In Figure 2.9 the vector $\vec{v}$ points to the location of the camera (or the viewer) in the scene, $\vec{n}$ is the normal to the surface, $\vec{l}$ is a vector pointing to the light source, and $\theta$ is the angle between the normal and the light source. A local illumination model is able to compute the colour at the surface of the object given these data and (usually) access to the light source.

We remark that local illumination models can be more complex than described here. Furthermore, local illumination models are typically combined with more sophisticated rendering techniques such as the one discussed in the next section.

### 2.4.2 Global Illumination and Path Tracing

Global illumination in computer graphics is the concept of accounting for lighting effects across the whole scene to be rendered. Rendering techniques that attempt to account for global illumination try to reproduce phenomena such as darkening in the corners of rooms and colours that

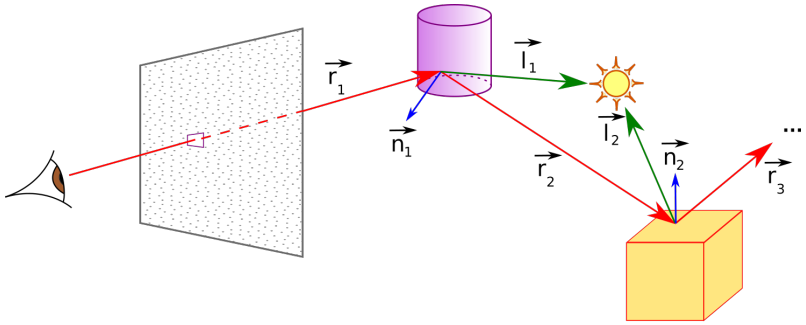


Figure 2.10: Diagram depicting the basic path tracing algorithm.

*bleed* from one surface to another. One of the early global illumination techniques proposed by the computer graphics community is *path tracing* [112]. Figure 2.10 depicts the basic path tracing algorithm.

The path tracing algorithm is both iterative and recursive in nature. In a typical path tracer, rays[5] are iteratively cast for each pixel in the outputted image, *i.e.*, in the rendering. Each ray starts at the camera (or the eye point) of the observer, and it is cast through the current pixel of an image. If an object is struck in the scene, its colour contribution is computed. This is often done with a local illumination model as described in Section 2.4.1. A new direction is then stochastically chosen for the ray and recursively cast into the scene. The direction may be obtained using a PDF or derived from a phase function or a BRDF associated with the object that was struck [198]. The recursion continues until a ray strikes a light source, or is terminated algorithmically. The contribution of each recursively cast ray is typically scaled so that objects closer to the camera (along the path of the ray) express a greater contribution.

Referring to Figure 2.10, ray $\vec{r}_1$ is the primary ray cast through a pixel and $\vec{l}_1$ is the secondary ray used by the local reflection model at the intersection point. Ray $\vec{r}_2$ is cast recursively. The secondary ray $\vec{l}_2$ is used to compute the contribution at the second point of intersection. The recursion continues with primary ray $\vec{r}_3$, *etc.*.

We remark that many, but not all, implementations of the path tracing algorithm make assumptions about the materials being rendered in the scene. First of all, as discussed in Section 2.1.4, some path tracing implementations naively assume that the index of refraction is constant across all visible wavelengths of light. This allows for a single ray to be used for multiple wavelengths of illumination. This assumption, however, hinders the reproduction of

[5]The formulation of a ray includes both a point of origin and a direction. They are symbolically represented here as vector quantities, to indicate their directional component.

spectrally dependent phenomena.

Another assumption implicitly made by the path tracing algorithm is that materials exhibit the Helmholtz reciprocity [110]. Simply put, in reality light is emitted from the source and traces a path toward the viewer or the camera. However, in path tracing, the opposite direction is traced by the rays, *i.e.*, from the viewer to the light. The Helmholtz reciprocity is the assumption that the reflective properties of the materials are the same in both directions, which is not the case for all materials.

# Chapter 3

# Related Work

In this chapter, we present a brief summary of prior works that model snow deposition and light interactions with snow. The intent is not to be exhaustive, but to provide an overview of the various simulation methods relating to snow appearance.

## 3.1 Computer Graphics

Visually depicting snow has long been a topic of interest for the computer graphics community. Initial work tended to focus on modelling the precipitation and placement of snowpack upon objects in the scene, while later works progressively added more enhancements to modelling the aspect of snow accumulation. Other works delved into animating wind-swept snow, either for the purpose of improving the deposition process or for rendering animations. In contrast, there have been relatively few works that attempt to describe the appearance of fallen snow itself. To our knowledge, no attempt to simulate the spectral appearance attributes of snow has been presented in the computer graphics literature to date.

### 3.1.1 Snow Accumulation Models

Early attempts to model the accumulation of particulates focused on dust [94]. Later, related methods were applied to falling snow. For example, Fearing [57] proposed an accumulation model whereby "launch sites" were specified to emit particles upward in order to determine occlusion and to compute the snow mass on geometric surfaces. Later, Muraoka and Chiba [142] added air currents and temperature to their own snow accumulation model. Including another

level of realism to the dynamics of the falling snow. Moeslund *et al.* [141] applied fluid dynamics principles to simulate a wind field and introduced weather parameters such as temperature and snow precipitation rate. Attempts to add even more realism to snow accumulation simulations included efforts to introduce heat transfer for the purpose of simulating freeze/thaw cycles [132] and to incorporate features such as snow bridging [215]. Other efforts attempted to accumulate snow for large alpine scenes [62, 177].

Not all works intended to directly follow the path of adding more physical processes. A model by v. Festenberg and Gumhold [214] instead implemented a statistical method for accumulating snow based on observations, while Hinks and Museth [91] implemented a physically plausible method based on level sets [162].

As computing power increased and 3D rendering chipsets improved, some works focused on rendering snow accumulation in real-time. Haglund *et al.* [82] presented an early work that made use of particle systems [180] to represent falling snow. Their work represented accumulation using a height field which stored the height of the snowpack. Later, Tokoi [212] determined snow occlusion using a shadow buffer technique, which dynamically accumulated snow onto a static scene. This shadow mapping approach was later extended by Reynolds *et al.* [181] to support dynamic scenes. An early effort by Wang *et al.* [227] employed the Boltzmann equation [39] to simulate the dynamic behaviour of the falling snow. Upon deposition, their work used fallen snow flakes to update a height field that represented the total accumulation.

### 3.1.2 Animation

The animation of snow related processes (*e.g.*, precipitation, deformation due to interactions with rigid bodies and self-interactions) is another area where the computer graphics community has focused its attention. Early on, Sims [199] recognized that particle systems would facilitate the animation of falling snow. Later, Langer *et al.* [128] addressed the limitations of particle systems with a hybrid method that adds dynamic texturing. With this hybrid method, dynamic outdoor scenes could be rendered in real-time.

In addition to animating falling snow, other efforts have gone into animating snow that has already been accumulated. For example, Sumner *et al.* [207] implemented a method to deform and animate snow as a result of an impact with a rigid body. Their method allowed for the compression of a height field by footprints *etc.*, and for the material to be displaced to other locations of the height field. Later, Stomakhin *et al.* [205] introduced a material point method that allowed for snow self-interactions such as snow balls gaining mass while rolling down a hill. This work also allowed for rigid body interactions to deform accumulated snow. The method of Stomakhin *et al.* was the first to simulate the behaviour of sticky, wet snow. Subsequently,

a hybrid structure and a texture-mapped shell rendering method was developed by Wong and Fu [237]. Their work further enabled the replication of the basic behaviours of snow at near real-time rendering speeds. Continuing the pursuit of modelling snow at interactive rates, Dagenais *et al.* [47] introduced a level set [162] method that partitioned the problem of simulating snow interactions with rigid bodies into three components. A level set is affected by constructive solid geometry [186] forming the imprints, while a granular simulation deposited the snow that has been displaced by the solid body. The third component of the work by Dagenais *et al.* added a fluid simulation to model the motion of flying snow.

Continuing in the vein of animating snow, Jubert [109] introduced a physical model to compute the transport of snow that is affected by wind and scene geometry. A precomputation is used to estimate the wind and precipitation in the scene. Employing this precomputation, the model advects a particle system of snow through time in order to animate the snow transport. Lastly, Jubert introduces a technique for rendering that employs graphics hardware.

On a grander scale, some works have attempted to model snow that is on descending sloped surfaces in the form of an avalanche. For example, the work of Güçer and Özgüç [80] used molecular dynamics to simulate cascading snow. More recently, Liu *et al.* [129] introduced their own method based on geodynamics to model avalanches.

The works outlined so far, all deal with modelling snow deposition in the form of an accumulation model or the animation of snow as it falls or interacts with rigid bodies. We remark that few works have addressed the actual appearance of snow itself.

### 3.1.3 Snow Appearance

Interestingly, one of the earliest papers to include a discussion of snow in the computer graphics literature gave primary focus to the macroscopic appearance of the material. The work by Krueger [125] presented a "natural" process for producing textures that resembled the aesthetic of sparkles (or glints).[1] Although their work focused on the generation of textures, the study of snow sparkles remains an active area of research using microfacets [44, 225] and other methods of normal distribution [246].

An early effort to compute the appearance of snow was introduced by Nishita *et al.* [155]. This early work addressed the effect that multiple scattering has on the appearance of snow.

[1] The terms "sparkle" and "glint" are not clearly differentiated in the literature. The American Society for Testing and Materials (ASTM) defines sparkle as "the aspect of the appearance of a material that seems to emit or reveal tiny bright points of light that are strikingly brighter than their immediate surround and are made more apparent when a minimum of one of the contributors (observer, specimen, light source) is moved." [1]. We elected to use the term sparkle and implicitly include glints by analogy [56].

They assumed that snow exhibits a white colour and they integrated over a grid of voxels[2] that contained the snow material. They also accounted for the colour contribution due to skylight in the integration process. Later, Yanyun *et al.* [244] were able to render large scenes using a multi-mapping technique. They proposed that displacement maps be used to render nearby snowy features, whereas volumetric textures be utilized for distant features. Although subsurface scattering within snow is not discussed in the work of Yanyun *et al.*, sampling through the volumetric texture allows for realistic images to be generated at a larger scale with many snow-covered features, such as trees, contributing to the final rendering. To address the rendering of snow for real-time applications, Ohlsson and Seipel [158] implemented a shading technique to compute a snow colour function for this purpose. In addition to computing a plausible shading for snow, their work attempted to capture macroscopic features, such as the texture of snow.

More recently, Frisvad *et al.* [64] implemented an analytic model to compute the scattering properties of various materials. These include ice with briny water and air inclusions that act in suspension of a pure ice host material. Their adaptation of Lorenz–Mie theory [73] represents nonspherical particles with the quantity of equivalent spheres[3] that preserves the volume-to-area ratio of the nonspherical particles, and employs a constant for the real part of the index of refraction. However, they incorporate the complex part of the index of refraction for water and ice into their calculations allowing for them to reproduce some effects that are dependant upon absorption. They parameterize their solution by using brine and air fractions and suggest that algae and minerals could also be included. Similarly, Jarabo *et al.* [102] made use of the optical properties discussed by Frisvad *et al.* in their own work. In addition to these two works, Meng *et al.* [135] implemented a multiscale level of detail technique to render granular materials. Among other materials, they also render images of snow at various scales.

The works discussed above focus on either modelling the accumulation of snow on geometric surfaces, animating the action of falling snow, snow deposition, the displacement of snow or they attempt to account for macroscopic features of its appearance. To our knowledge, there are no works in the computer graphics literature that attempt to directly compute the the appearance attributes of snow, notably its colour. This is of particular importance when impurities are present or to address the appearance changes due to morphologically active snow [41, 43]. It is also relevant when light is transmitted though a snowpack into a space such as a snow cave or a dwelling made of snow such as an igloo, or to correctly render the bluish hues observed in depressions made in a snowpack.

[2]The 3D (volume) analogy of a 2D pixel.

[3]Equivalent spheres replace nonspherical objects with a quantity of spheres whose total volume to surface area ratio is the same as the nonspherical object they intend to represent. Although suitable for investigations where hemispherical contributions are averaged, this approximation has been shown to be inadequate when used for investigations that require finer aspects of scattering such as those involving BRDF computations [105].

Due to the scarcity of works addressing the appearance of snow by the computer graphics community, we investigated works presented in other research communities that are interdisciplinary in nature. In the next section, we provide a concise review of models of light and snow interactions presented in the remote sensing literature. These modelling efforts are an important part of elucidating the effects of snow grain characteristics on equivalent water content estimates from remotely acquired observations that are recorded *via* instruments aboard aircraft or *via* satellites.

## 3.2 Snow Reflectance Models Aimed at *In Silico* Studies

This section provides an overview of selected works on the modelling of light and snow interactions using stochastic ray tracing methods, rather than deterministic methods employed to numerically solve related differential equations such as the DIScrete Ordinate Radiative Transfer (DISORT) model [202]. The development of snow reflectance models is described in a manner that highlights the evolution of the various efforts over the previous few decades. The focus of this overview is on models primarily suitable for simulations of light interactions with snow in the visible and infrared domains. The reader interested in modelling efforts in the microwave domain is referred to the comprehensive work in this area by Picard *et al.* [173].

We begin by identifying initial attempts to model snow reflectance using single scattering of spheres combined with analytical theory. Next, a selection of single scattering models that made use of nonspherical shapes are presented before continuing with multiple scattering models. These are subdivided into two categories: those based on a volume of modelled snow grains and those that are based on tomographic scans of snow.

### 3.2.1 Single Scattering

Computational time and memory limitations led many initial works to focus on single scattering and use the computed results as a phase function to supplement a more complex, theoretical analysis. This archetypal method was demonstrated early by Bohren and Barkstrom [28]. Assuming a monodirectional source beam of radiation, they computed the single scattering phenomenological coefficients required for an application of the Mie theory [30] using a single transparent sphere. Later, this was extended to account for snowpack depth to demonstrate a preferential absorption of longer wavelengths in the visible region [27].

A transformative step in the paradigm was to consider nonspherical crystal shapes. Yang and Liou [243] computed the phase function of hexagonal crystals using ray tracing, and com-

pared their results to those obtained by using the finite difference time domain (FDTD) method [66] on a similar crystal shape. The geometric ray tracing method was used for the near field[4] and then transformed to the far field using a novel intensity mapping algorithm. This allowed them to extend their hybrid method to efficiently compute single scattering albedo for small 3D ice crystals that were close to the FDTD results. Grundy *et al.* [79] performed a single scattering simulation for arbitrary polygonal meshes. They focused on computing the single scattering albedo, phase function, polarization[5] and radiative transfer near the grain. They were also able to find an analytical approximation to the single scattering phase function using particle size, aspect ratio, and roughness as parameters. Recognizing the limitations of using "equivalent spheres" [77], Jin *et al.* [105] investigated a variety of shapes and the effect that their different scattering phase function had on bidirectional reflectance. They compared spheres, plates, column crystals and aggregates of columns. The results of these single scattering simulations were input into a radiative transfer model and compared with EM radiation data measured at a wavelength of 870 $\mathrm{nm}$. This wavelength was chosen to avoid the influence of soot and liquid water content. A good agreement was obtained between the measured snow sample and the simulated snow structure, thus demonstrating the degree of fidelity [78] that can be achieved by *in silico* investigations.

### 3.2.2 Multiple Scattering

Although multiple scattering models are more complex, they are able to capture angular effects of reflection [53]. Barkstrom [20] was an early advocate for multiple scattering models. His work used sphere-shaped snow grains to provide a quantitative argument to consider multiple scattering effects. Wiscombe and Warren [235] provided an analytic model, based on Mie theory [73], that used the delta-Eddington approximation [108] to account for multiple scattering. Their model also used spherical snow grains.

A number of attempts have since been made to simulate the 3D structure of snow grains in order to reproduce multiple scattering effects. These efforts focused on modelling the 3D structure of snow samples and then applying ray tracing to compute the scattering profiles. Kaempfer *et al.* [111] tested two different snow representations. Their first attempt consisted of filling a volume with hemispherically-capped cylinders. This allowed for the testing of parameters such as grain size and pore space. Their second attempt recreated the microstructure of snow using an X-ray micro-tomography scan. This did not allow for parameter tuning. Instead,

[4]Near field computations involve those relatively close to the object influencing the EM radiation as opposed to computations involving relatively distant, or far field, interactions [66].

[5]Polarized light consists of rays that have been selectively oriented so that the transverse waves, which are perpendicular to the direction of travel, are all oriented in the same direction [167].

it provided a reconstructed representation of a particular snow sample. Bänninger *et al.* [4] also used tomograph data to investigate biconical reflectance of snow with similar results, and found good agreement between measured and simulated reflectance, while Haussener *et al.* [89] used tomograph data to develop a method for determining snow optical properties. Interestingly, their study [89] provided evidence that employing a simplified morphology in a radiative transfer model will introduce significant errors in the visible and near infrared.

Later, Picard *et al.* [172] returned to the filled volume strategy. Their SnowRat model used a variety of different grain shapes such as spheres, hexahedra, cylinders and hyperboloids. These shapes, and aggregations of these shapes, were tested for their reflectance properties. In particular, the effect of snow grain shape on the specific surface area (SSA)[6] to albedo relationship was investigated at a wavelength of 1310 $\mathrm{nm}$. They demonstrated that, for example, cubic grains reflected approximately 40$\%$ more than spherical grains with the same SSA. Addressing the lack of readily available tomography data for snow, Xiong and Shi [239] generated a Gaussian random field with a qualitatively similar structure to a tomograph [239, 240, 242]. This structure was divided into ice and air by selecting a threshold value. Xiong and Shi later developed an algorithm to successfully determine snow SSA using their model [241].

In addition to the above, a multi-layer model that investigated inhomogeneity of snowpack was implemented by Zhou *et al.* [245]. They determined that in the near infrared, a thickness of 5 $\mathrm{cm}$ is enough to be treated as semi-infinite. However, in the visible, a much larger depth is required.

The models discussed thus far have addressed the reflectance of dry snow. This impacts the results of the models since the optical properties of water differ from those of pure ice forming snow. In particular, the locations and magnitude of the extrema in the imaginary part of the complex index of refraction (see Section 2.1.4) can vary between the two. (The data used in this thesis is discussed later in Chapter 6. See Figure 6.2 for plots of the indices of refraction for water and ice.) The overall reflectance is affected because snow may contain some water content, either as a vapour or in liquid form [41, 43].

Given this discrepancy, Green *et al.* [74] used Mie theory [73] in an attempt to determine the effect that water has on the reflectance on snow. In particular, they focused on the local extrema in the extinction coefficient for ice and water which occur at 1030 $\mathrm{nm}$ and 980 $\mathrm{nm}$, respectively. They demonstrated a shift of the absorption features centred at 1030 $\mathrm{nm}$ toward shorter wavelengths by representing snow grains as water-coated spheres.

It is worth noting that the importance of research initiatives for properly accounting for multiple scattering within snow deposits transcends spectral domains. For instance, Picard

[6]The specific surface area (SSA) is a measure of the surface area per unit of mass [187].

*et al.* [173] have recently remarked that accurate simulations of microwave interactions with snow on the ground would require more advanced scattering models, which, in turn, would demand full 3D representations of snowpack microstructure.

Although this section concentrated on prior works that have employed stochastic methods to model light interactions with snow, one relatively recent deterministic method is concisely addressed here for completeness. Namely, the Snow, Ice and Aerosol Radiative model with Adding-Doubling solver, version 3.0 (SNICAR-ADv3) that was described by Flanner *et al.* [61]. The origins of this model date back to the initial work of Wiscombe and Warren [232, 235] in 1980. However, the latest version of the SNICAR-ADv3 model incorporates research findings from a variety of project sources. This latest revision is of note because it attempts not only to account for atmospheric aerosols as its forbear does [232], but also to account for algae, mineral dust, volcanic ash and brown carbon, although more effort is required in some of these areas.

In this chapter, we have provided a concise summary of works that introduce snow-related models in the literature. Since the main purpose of the framework proposed in this thesis is to study light interactions with snow aiming at generating appearance data for this material, the snow accumulation and animation models summarized in Sections 3.1.1 and 3.1.2 are not suitable for that purpose. Furthermore, although the models discussed in Section 3.1.3 focus on appearance, most do not attempt to directly compute the spectral appearance attributes of snow. Instead, they focus on macroscopic features [125, 225, 244, 246], prioritize optimization [158] or fail to include a number of important snow characterization traits [64, 102]. The appearance models introduced in Section 3.2 are primarily designed to study light interactions with snow. However, many of them focus on single scattering [28, 79, 105, 243], only account for spherical grains [20, 202, 235], do not account for a comprehensive set of snow sample properties [4, 61, 74, 89, 111, 172, 239, 240, 241, 242, 245], or target spectral domains outside of the ranges employed in this thesis [173].

For these reasons, in this work, we selected to employ an abstraction paradigm [115] that enabled us to fully account for the particulate nature of snow while incorporating the specific characteristics that make it markedly distinct from other granular materials like sand. This choice, in turn, allowed us to develop a novel model of light and snow interactions capable of providing high-fidelity spectral and goniometric outputs that can be seamlessly incorporated into rendering systems. The inner workings of this model and its predictive capabilities are addressed in the next chapter.

# Chapter 4

# Modelling Light and Snow Interactions

This chapter provides an overview of the proposed framework's central component, namely a novel light transport model for snow, henceforth referred to as SPLITSnow (*SP*ectral *LI*ght *T*ransport in *Snow*). It builds upon a proven first-principles approach previously used to simulate the light interactions with sand-textured soils [115]. This approach accounts for a wide variety of physical phenomena exhibited by granular materials *via* the stochastic generation of grains on-the-fly throughout the simulation process. While other multiple scattering models that employ ray tracing geometric optics are constrained by the computer memory and the computational complexity of managing a large dataset of grains, this stochastic approach makes use of a single grain at a time. Thus, even semi-infinite samples are within reasonable computational limits without requiring expensive hardware resources. Furthermore, the stochastic generation of surface properties allows for detailed modelling of complex geometries without the requirement to store these primitive shapes. The proposed model can predictively simulate the spectral and spatial distributions of light interactions with snow. The spectral radiometric responses are quantified in terms of spectral reflectance and transmittance, whereas the spatial radiometric responses are quantified in terms of scattering distribution functions.

We begin with a high-level discussion of the architecture and the data considerations that influence the model's design. We then discuss the characterization of snow and the properties that affect light transport through snow. Finally, we discuss the model formulation itself.

Note that for the purpose of clarity, we initially make the assumptions that the snowpack being modelled is pure, homogeneous and comprised of a single layer. More specifically, the sample contains no impurities, variations may exist between grains, but any two separate volumes of snow within the sample have the same set of characterization values, and the snow has consistent properties throughout its depth. We will relax these restrictions in Sections 4.4–4.6.

## 4.1 Data Considerations

Data considerations are an important aspect of model design. These considerations include both data input into the model as well as the data resulting from the output of simulation. Figure 4.1 provides an outline of how data are used in the formulation of the model proposed in this framework.

Starting from the top of Figure 4.1, sample characterization data obtained from the existing literature are used as inputs to the framework. Characterization traits are physical attributes that define the properties of a material. These data directly influence model inputs, design and architecture. In particular, utilizing data as it is commonly presented in the geophysical research [60] and field studies [54, 190] will increase the suitability of the model for performing interdisciplinary *in silico* studies.

As data collected from the literature influences the inputs to a model, so does data collected from the literature that are used in the evaluation of the model. Outputs of the model are tested against these measured values obtained from the literature. In addition to direct measurements, phenomenological trends reported in the literature are also used in the evaluation of a model. More specifically, the model outputs are evaluated to verify whether they reproduce these phenomenological trends. For the purpose of evaluation, in this thesis, we identify changes observed either in the spectral distribution or spatial distribution of light in response to changes in a characterization parameter, as phenomena.

The results of this evaluation process affect the design and implementation of the model, which in turn, may require the collection of more data from the literature. This process is iteratively repeated until the model is able to predictively reproduce the reported phenomenological trends and a suitable agreement with measured data can be produced.

The outputs of the model are material appearance attributes (see Section 2.2) that may be used for a variety of purposes. Accordingly, these attributes may be utilized in image synthesis pipelines or to conduct *in silico* experiments aimed at interdisciplinary investigations and applications.

## 4.2 Snow Characterization

In this section, we give a brief overview of the snow material properties identified in the literature that were selected to be included as characterization parameters for virtual snow samples. In Section 4.3, we provide implementation details for how they were incorporated into the simulations.

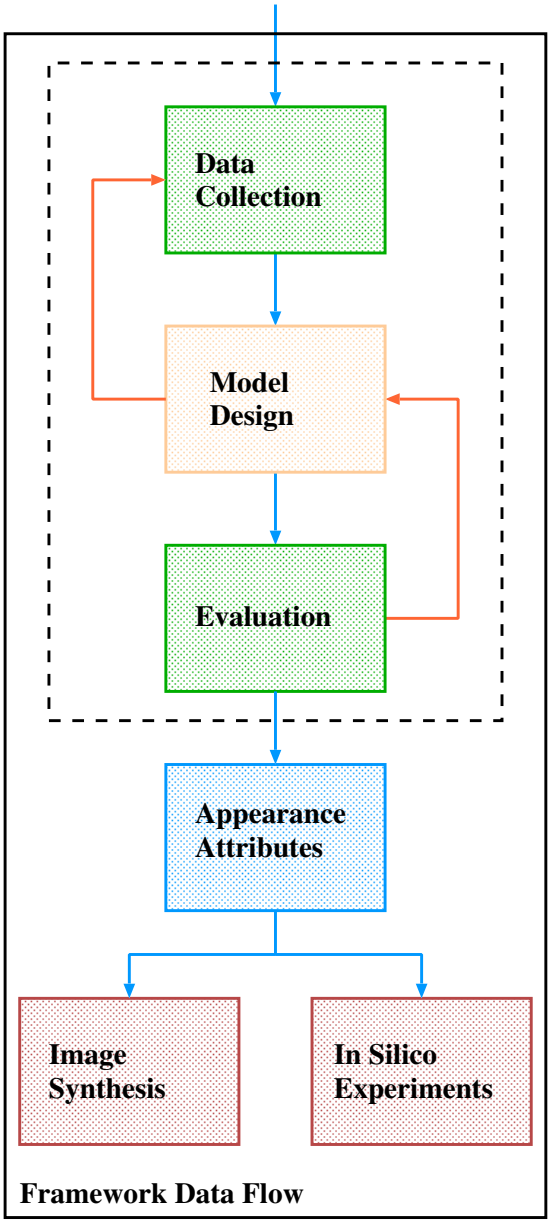


Figure 4.1: Data flow through the SPLITSnow simulation framework. The green *Data Collection* and *Evaluation* modules are framework components that employ data obtained from the literature. The blue *Appearance Attributes* module indicates the framework component that processes and manages the outputs from the modelling framework. Lastly, the red *Image Synthesis* and *In Silico Experiments* modules indicate framework components that synthesize outputted data into products.

| | Parameter | Value Range | Units |
|---|---|---|---|
| ✓ | Particle size | [50, 3000] | $\mu m$ |
| | Temperature | [-40, 0] | $^{\circ}C$ |
| | Sample thickness | [1, 100] | $cm$ |
| | Water saturation (pore space) | [0, 0.5] | unitless |
| | Density | [50, 450] | $kg\,m^{-3}$ |
| ✓ | Facetness | [0, 1] | unitless |
| ✓ | Sphericity | [0, 1] | unitless |

Table 4.1: Snow sample characterization parameters and the range of values modelled in this thesis, which are based on physically valid ranges obtained from the literature [29, 60]. Parameters in the upper section directly employ values obtained from the literature. Values in the lower section are unitless and are used to estimate snow features that are specified qualitatively in the literature. Characterization parameters with a check mark are specified as distributions instead of scalar values.

Effective modelling of a material begins with a study of the characteristics that define a sample. This includes both the enumeration of properties as well as the determination of the physically valid ranges for each of these characteristics. The International Association of Cryospheric Sciences (IACS) in partnership with the United Nations Educational, Scientific and Cultural Organization (UNESCO) International Hydrological Programme (IHP) has published a reference document that provides guidance on the properties used to classify seasonal and machine-made snow [60]. In addition to highlighting various important snow characteristics, typical values for several of the defining traits are provided. Unless otherwise stated, the characterization description and range of physically valid values discussed in this section will come from this IACS reference document [60]. Table 4.1 provides a summary of the characterization attributes, and a depiction of some of these properties is presented in Figure 4.2.

Grain size is one of the most predominantly studied features of snow since it is known to have a significant effect on reflectance [74, 105, 130, 144, 156, 157]. Any model computing the reflectance of light from snowpack samples would be remiss not to include it as a parameter. Water content is another characteristic that has an effect on reflectance. Even though water is the liquid form of ice, it has different optical constants [83, 229]. Water is specified as a fraction of the pore space, which corresponds to the portion of a snow sample's volume that is not occupied by the grains.

Size is not the only characteristic used to describe snow grains. Smoothness and shape are also used to describe them. As it will be discussed in Section 4.3, we represent snow grains as

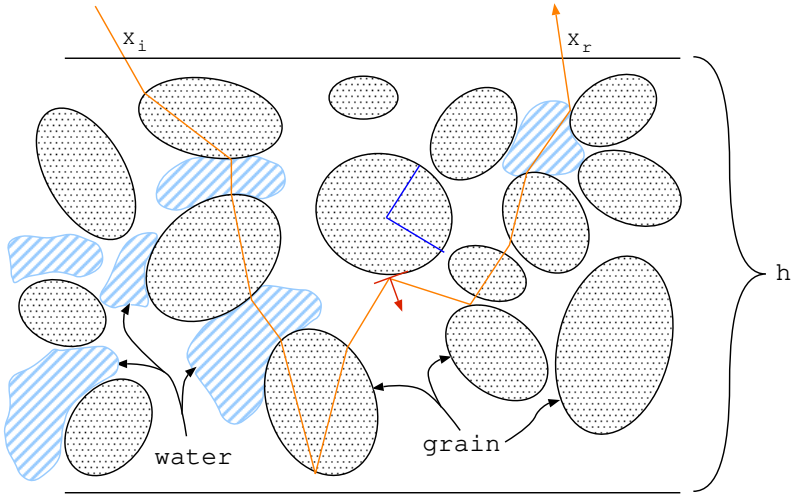


Figure 4.2: Examples of various snow characteristics and their effect on a snow sample. On the left, the snow sample utilizes mostly mid-sized grains, more water and has a lower density. On the right the sample has a greater variety of grain sizes, less water and is more dense. The symbol $X_i$ indicates the location where a light ray enters the material and the symbol $X_r$ indicates the point of exitance after being reflected and refracted through several grains. The thickness of the sample is represented by $h$.

prolate spheroids.[1] These spheroids can be augmented to reflect crystalline features of snow grains by introducing a unitless parameter that controls the distribution of facets on the snow grains, making them have less (low values) or more (high values) crystalline features. (See Section 4.3.2.) We use the term *facetness* to refer to this value. Snow grains also come in various shapes. The sphericity is the parameter used to control the overall shape distribution of the grains. It determines how spherical (high values) or elongated (low values) a snow grain is.

Although the impact of density on snow spectral responses remains to be thoroughly elucidated [18], it is recognized as a key nivological characteristic [60]. Accordingly, it is incorporated into the model formulation as a pertinent parameter. Since the density of ice is a function of temperature [187], the snowpack temperature is also included as a model parameter.

If snow is not optically thick,[2] then light will be transmitted through the volume of the material and less light will be reflected to the surface. Therefore, sample thickness is included

[1] Prolate spheroids have their semi-major axis extended to be greater than their semi-minor (or equatorial) axis such as that of a rugby football. This is in contrast to oblate spheroids whose semi-major axis is less than the semi-minor axis and look squashed [90].

[2] An optically thick volume is one in which light is readily absorbed [29].

as a parameter as it affects both the reflectance and transmittance of snow. We remark that for homogeneous, single layered snow samples, the light transmitted through the bottom of the sample is not reflected back into the sample, *i.e.*, the material beneath the snowpack is assumed to be a perfect absorber at all wavelengths.

## 4.3 Model Formulation

This section describes the basic formulation of the proposed SPLITSnow model. In particular, it focuses on light interactions with a homogeneous sample of pure snow that is consistent throughout its depth. We address aspects associated with layering, heterogeneity and impurities in Sections 4.4, 4.5 and 4.6, respectively. We begin with an overview of the model in Section 4.3.1. Details about the stochastic generation of individual grains are provided in Section 4.3.2. In Section 4.3.3, the simulation of light interactions with individual grains using geometric optics is described. We then discuss light transport through the interstitial medium in Section 4.3.4. Finally, Section 4.3.5 examines two different ways that water content may be specified and provides a mechanism to convert between them.

### 4.3.1 Overview

The proposed model employs a first-principles simulation approach. This approach is implemented using an algorithmic formulation based on the application of Monte Carlo methods [87] and geometric (ray) optics concepts [31] as schematically depicted in Figure 4.3. A light ray (or more concisely, a *ray*) travelling at a specific wavelength is directed toward the sample from the illumination source. The sample is bounded by both upper and lower planes. Within these planes a sequence of grains is instantiated and discarded, keeping only the currently active grain stored in memory. In the diagram depicted in Figure 4.3, the black grain is the current one being examined by the simulation. The faded grains with solid outlines were completed and have been discarded. The faded grains with dashed outlines have yet to be instantiated. All grains are instantiated as needed, and their properties are all determined stochastically. This process is repeated to ensure the convergence of the radiometric quantities being estimated [17, 124].

Figure 4.4 provides a high-level overview of the decision tree that a ray undertakes when interacting with the material. The incident ray is at the top of the flow chart. Given a ray, the first task is the process of grain generation. After grain generation, the ray interacts with the pore space. This may entail the space between two grains, or the space between a grain and the

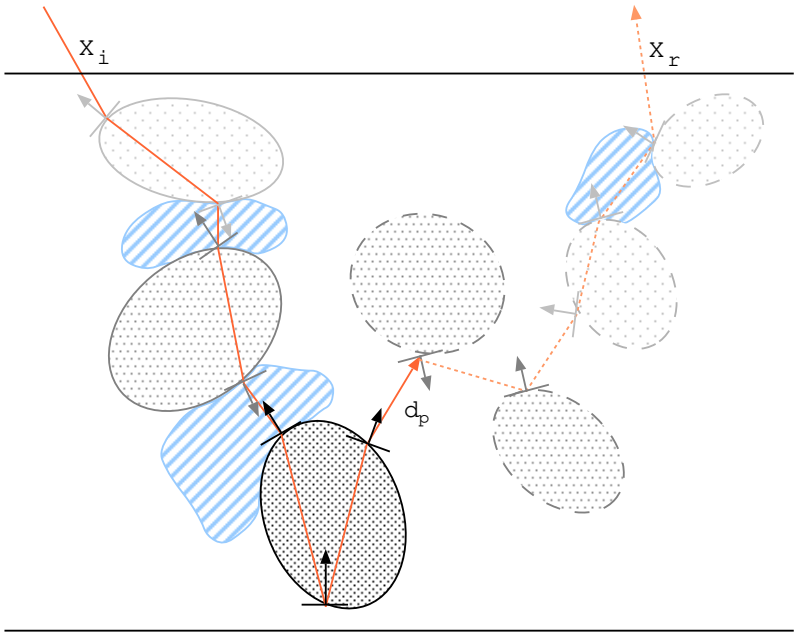


Figure 4.3: Diagram illustrating the traversal of a ray through a given snow sample using the stochastic approach employed by the proposed model. After a ray enters the sample at the point $X_i$, a sequence of grains is generated. Each grain is modelled as a prolate spheroid whose geometric properties are selected stochastically. The distance between grains, $d_p$, is also chosen at random based on the specified sample density, $D$. Grains that have been traversed are shown with a solid outline. Grains that have yet to be instantiated are shown with a dashed outline. Only one grain is required to be stored in memory at a time. This grain is shown with a solid black outline. To simulate the grains' facets, their normal vectors are perturbed using a probability distribution. Air is the default interstitial medium between grains. In this work, water may be used as a second medium. The fraction of pore space that is made up of water is specified as a model parameter. The presence or absence of interstitial water is decided using the water fraction as the probability. The ray's traversal is completed when it exits the sample at the point $X_r$. Alternatively, it can be terminated by an absorption event within the sample.

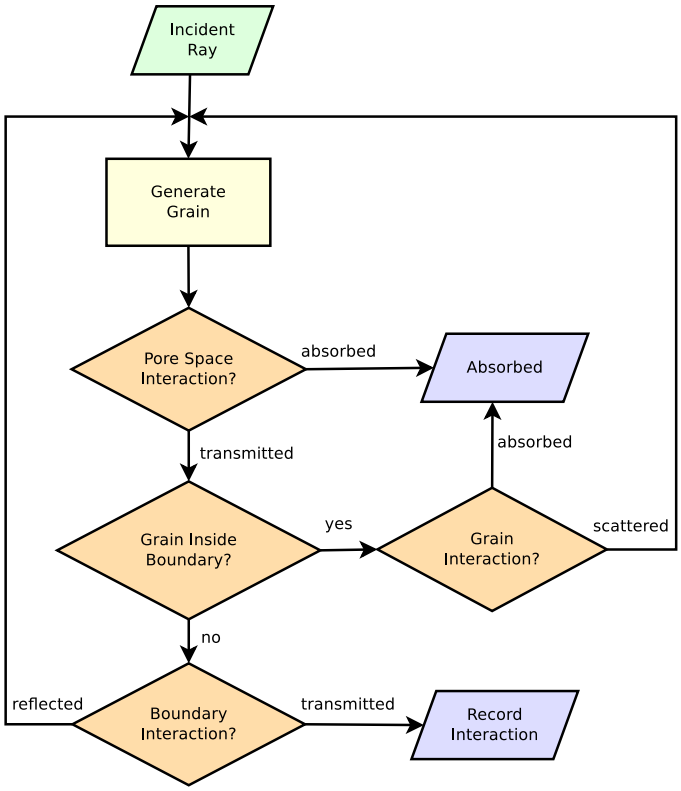


Figure 4.4: Flow chart depicting the high-level decision tree that a ray undertakes when interacting with snow grains. Note the iterative nature of the decision tree, whereby grains are generated on demand until the ray is either absorbed, or exits the material.

material boundary. If a newly generated grain is outside of the material boundary, then the ray interacts with the boundary, rather than the grain. Otherwise, the ray interacts with the grain.

As light first enters the sample, a random distance, $d_p$, to the first grain is computed by using:

$$d_p = -\overline{d} \ln(\xi), \tag{4.1}$$

where $\overline{d}$ is the mean distance between grains, $\ln$ is the natural logarithm, and $\xi$ is a uniformly distributed random variable in the range of $(0, 1)$. The mean distance between the grains is computed from the specified density, $D$, which is a model parameter. Note that $D$ represents the density of the sample in a dry state, *i.e.*, when there is only air in the pore space. Technical details describing the method of computing the mean distance from $D$ are provided in Appendix B. It is worth noting that the density of a sample may be specified in related works [169] with respect to its wet state, *i.e.*, considering the presence of water in the pore space. Accordingly, a

procedure to obtain $D$ from a "wet" density value is outline in Appendix C.

Once a distance is chosen, a grain and its geometric properties are then generated. These properties include the major and minor spheroidal axes, the entry point on the grain and the normal vector at the intersection point. The grain is spatially translated so that the ray strikes the point of intersection precisely. These properties are all determined using specific probability distributions, which are discussed in Section 4.3.2. The ray may then be refracted or reflected using the Fresnel coefficient [167]. (See Appendix A.) The probability of reflection vs. refraction utilizes the Fresnel coefficient as the probability in a Bernoulli trial [233].[3]

If the ray is reflected, then the grain is discarded. At this point, a new distance to the next grain is chosen using Equation 4.1, and another grain is generated with new properties using the same probability distributions. In addition, an interstitial medium is also selected probabilistically. The fraction of pore space that is composed of water is specified as a simulation parameter, and this fraction is used as the probability of success in a Bernoulli trial. In this way, the pore space is represented as being either water or air by the SPLITSnow formulation.

If the light enters the grain, then it is refracted using the grain's complex index of refraction [31]. This (spectrally) wavelength dependent quantity has distinct values for ice and water. The stochastically generated surface normal vector is used with these values to compute the ray's direction within the grain. Once within the grain, the ray may be transmitted or absorbed. To determine whether or not the ray is absorbed by the grain, the length travelled to the exit point and the grain's extinction coefficient are used to compute the probability, which is used in another Bernoulli trial. Should the ray be absorbed, it is discarded along with the grain, and a new ray is cast from the source. Otherwise, the ray reaches the exit point of the grain and the Fresnel coefficient is used once again to determine if the ray is internally reflected or refracted out of the grain and into the medium. A new normal vector is stochastically generated at the potential exit point for this purpose.

Internal reflection may continue until the ray is absorbed or exits the grain. In the former case, the ray is terminated and the grain is discarded. In the latter case, Equation 4.1 is used to compute the distance to the next grain, and an interstitial medium is again probabilistically chosen. It is possible for the interstitial medium to absorb the ray. The distance and the extinction coefficient of the selected interstitial medium are used to probabilistically determine whether this occurs.

Should the ray reach either the upper or the lower bounding plane, then its direction of exitance are used to compute a BSDF value. A set of these values output by the simulations, in turn, can be can be used to obtain a full BSDF profile of a given sample. In this work, no

[3]For some $p \in [0, 1]$ and random variable $\xi \in [0, 1]$, a Bernoulli trial is a success if $\xi \leq p$ [233].

boundaries are imposed on the horizontal dimensions. Consequently, samples are considered infinite in the $x$ and $y$ dimensions, but finite in the $z$-axis (depth). It is worth noting that the BSSDF is well defined since both the position and the direction of exitance are known. However, for most applications, the BSDF will suffice.

There are a number of computational advantages to this approach. First, the amount of in-memory storage is drastically reduced since only one grain is kept at a time. However, eliminating the computational costs of traversing a complex search space provides an even greater benefit. Rather than storing a multitude of grains, which would require the computational cost of searching through the complete set for the nearest grain, the stochastic approach employed by SPLITSnow only requires a small number of calls to a random number generator. It is worth noting that once a ray exits a grain, it will not interact with that specific grain again since the latter has been discarded. Although this aspect may seem restrictive, it is outweighed by the employed approach's intrinsic efficiency. We remark that it aggregates the outcomes of numerous trials for the purpose of Monte Carlo integration. Hence, its algorithms are geared toward maximizing the fidelity-to-cost ratio of the simulations.

### 4.3.2 Grain Generation

The SPLITSnow formulation is not dependent upon any particular grain shape. In this work, prolate spheroids are employed for consistency with the literature on snow deposits subject to morphological changes over time [41, 43], commonly referred to as *faceted particles* [60]. As described below, the SPLITSnow formulation allows crystalline features to be added to the spheroids in the form of microfacets [44, 213]. This representation allows for a variety of morphological ages to be investigated, which are more prevalently the object of geophysical investigations.

The geometric properties of each grain are generated stochastically (see Figure 4.5). These properties include the size, shape, location and the microfacet at the point of intersection. The values assigned to the grains' optical properties, such as the index of refraction and the extinction coefficient for ice, were obtained from datasets available in the literature. The sources of these datasets are provided in Chapter 6.

The grain's semi-major axis, $b$, is a random variable with a uniform probability distribution that allows for a configurable range. Its sphericity, $\Psi$, is also a represented by a random variable based on a probability distribution obtained from the literature [221]. Inscribed circle sphericity [183] relates the overall shape of the grain to a perfect sphere. For a perfect sphere, $\Psi$ is equal to one. Low values of $\Psi$ lead to the generation of shapes that have a high eccentricity. The

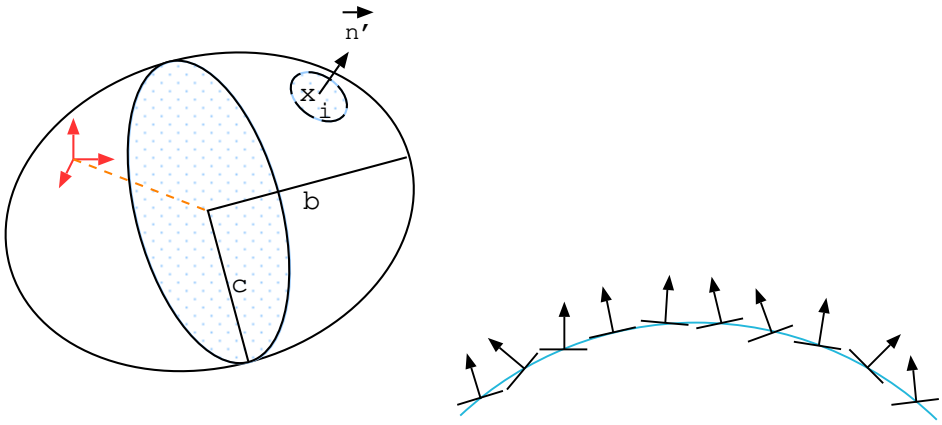


(a) (b)

Figure 4.5: Generated geometric properties of a grain. Diagram (a) depicts its axes and a stochastically selected intersection point on its surface. The semi-major axis, $b$, is chosen at random based on a uniform distribution. The semi-minor axis, $c$, is a function of $b$ and the inscribed circle sphericity, $\Psi$, which is also a random variable (see Equation 4.2). The orientation of the semi-major axis is determined by selecting a uniformly distributed point on a sphere and orienting the axis in the direction of that point. The intersection point on the grain, $x_i$, is uniformly distributed on the spheroid. However, it is restricted to the side facing the incoming ray. The location of the grain is adjusted to ensure that $x_i$ intersects the ray. The local origin of the grain is represented by the red axes, and the orange dashed line represents the particle's translation so that the ray intersects the grain at $x_i$. At $x_i$, the angle of the normal vector away from the orthogonal direction is perturbed using a normally distributed random variable. Diagram (b) illustrates how the surface details are represented as microfacets, which are associated with their specific normal vectors.

semi-major and semi-minor axes are related to $\Psi$ through the following formula:

$$\Psi = \sqrt{\frac{c}{b}}. \tag{4.2}$$

Equation 4.2 can then be used to compute the semi-minor axis, $c$, from $b$ and $\Psi$. Note that the relationship between grain size and sphericity is such that the selected grain size is used for the value of the semi-major axis, $b$.

The orientation of the grain is stochastically chosen by uniformly selecting a point on the unit sphere and orienting the semi-major axis toward this point. The point of intersection with the grain is also distributed uniformly on the surface of the grain. However, it is restricted so

that it must be facing the direction of the incoming ray. The grain is then repositioned (indicated by an orange dashed line in Figure 4.5(a)) so that the incoming ray strikes it at the stochastically selected point. Due to the stochastic nature of this process, it is possible that a grain is partially outside of the material boundaries when close to the upper or lower bounding planes. When this occurs, the grain is rejected and a new one is generated.

### 4.3.3 Light and Grain Interactions

When a propagating ray travelling at a wavelength, $\lambda$, interacts with a grain, it is probabilistically reflected or refracted based on the spectrally-dependent Fresnel coefficient [167]. Therefore, to simulate the faceted features of a morphologically young ice crystal, its normal vector is perturbed at its faceted surface, as depicted in Figure 4.5(a), using a stochastic approach. More specifically, Figure 4.5(a) shows the intersection point, $x_i$, on the surface of the spheroid. For the local area surrounding $x_i$, a new normal vector to the surface is stochastically generated as described below. This keeps the overall grain size consistent while allowing for more faceted forms. The result of this approach is portrayed graphically in Figure 4.5(b).

For a normal vector, $\vec{n}$, of the spheroid at hand, a perturbed normal vector, $\vec{n}'$, is computed using a random variable, $\xi$, that is normally distributed with a mean of zero by the formula:

$$\vec{n} \cdot \vec{n}' = 1 - |\xi|. \tag{4.3}$$

The standard deviation of the normal distribution is defined as:

$$\sigma = \frac{F}{2}, \tag{4.4}$$

where $F$ represents facetness, a tunable model parameter. More precisely, a facetness of zero yields a perfectly smooth spheroid. Since $\vec{n}$ (and by construction $\vec{n}'$) are unit vectors, their inner product results in the cosine of the polar angle $\theta$. The azimuthal angle of the perturbed normal, $\phi$, is selected using a uniform distribution in the range of $[0, 2\pi]$. Using this stochastic method, both faceted and smooth grains are represented efficiently, without the computational overhead of directly accounting for complex details on the grain's surface.

The Fresnel coefficient is then used to determine the probability of reflection. A Bernoulli trial is performed using this probability to determine success. Upon success, the ray is reflected into a stochastically chosen interstitial medium (see Section 4.3.4). Otherwise, the general form of Snell's law that makes use of both the real and imaginary components of the grain's complex index of refraction (See Appendix A) is used to determine the ray's angle of refraction into the grain [31].

Diffraction (wave) effects are not considered since the wavelengths of light used in this investigation are considerably shorter than the separation between the snow grains. The maximum snow density considered in this work is 450 $\mathrm{kg\,m^{-3}}$ [29]. Choosing this density yields the smallest mean distance between snow grains, which computes to roughly $4.3 \times 10^{-4}$ m. (See Appendix B.) The longest wavelength of incident radiation considered in this work is 2500 $\mathrm{nm}$, or $2.5 \times 10^{-6}$ m, which is two orders of magnitude smaller than the smallest mean distance. Furthermore, the grain shapes considered are spheroidal, and thus the apertures between grains generally do not form rectangular patterns with the aperture lengths being significantly greater than their widths — a geometry which is commonly associated with diffraction effects [167].

Within the snow grain, the possibility exists that the ray will be absorbed. The probability of absorption depends upon the length of the path the ray travels through the grain. The (potential) exit point out of the grain is computed geometrically as a ray-object intersection (with the object being represented by the grain's inner surface). The distance travelled within the grain, $d_g$, along that path is thus calculated as the length along the ray between the entry (incidence) point and the exit (exitance) point.[4] The probability of transmission,[5] $p_t$, is a function of this distance, and it is given by the Lambert law [198]:

$$p_t(\lambda) = e^{-\alpha_{ice}(\lambda) d_g}, \tag{4.5}$$

where $\alpha_{ice}(\lambda)$, the specific absorption coefficient (or simply s.a.c.) is computed as:

$$\alpha_{ice}(\lambda) = \frac{4\pi k_{ice}(\lambda)}{\lambda}, \tag{4.6}$$

with $k_{ice}(\lambda)$ representing the extinction coefficient at the wavelength $\lambda$ for ice [230]. Note that $\alpha_{ice}$ has units of $\mathrm{m^{-1}}$. The ray propagation inside a grain is then stochastically terminated if $p_t(\lambda) < \xi$, where $\xi$ corresponds to a random number that is uniformly distributed between 0 and 1.

### 4.3.4 Light Propagation Through the Interstitial Medium

When the ray is propagated through the interstitial medium, either because it has been reflected off a grain, or because it has exited a grain, the optical effects of the interstitial medium must be

[4] In case a given ray bounces multiple times inside a grain, the distance, $d_g$, is recalculated using the previous hit point instead of the ray's incidence point, and the ray propagation (absorption) test is employed again.

[5] Note that there is a typo in our published work [219], namely the word "absorption" was used instead of "transmission" in the introduction of Equation 4.5.

taken into account. The SPLITSnow formulation allows for any number of media to be present in the interstitial (pore) space between grains. However, for the purpose of simulating light interactions with snow, only two media are considered. These are water and air.

The default interstitial medium between the snow grains is air. The fraction of pore space that is made up of water is specified as a model parameter, denoted by $\mathcal{S}$. When the ray enters the pore space, the presence or absence of water is decided using this water saturation parameter ($\mathcal{S}$) as the parameter of success in a Bernoulli trial. If water is chosen ($\xi \leq \mathcal{S}$), then the pore space up to the next grain is assumed to be composed of water. Otherwise, the pore space is assumed to be air.

The distance to the next grain, $d_p$, is stochastically determined using Equation 4.1 as described in Section 4.3.1. Similar to a ray interacting with a grain, a ray traversing the interstitial medium may be absorbed within it, with the probability of transmission being computed using equations analogous to Equations 4.5 and 4.6, except using the constant values for liquid water instead of ice:

$$p_t(\lambda) = e^{-\alpha_{water}(\lambda) d_p}, \tag{4.7}$$

where the s.a.c., $\alpha_{water}(\lambda)$, is computed as:

$$\alpha_{water}(\lambda) = \frac{4\pi k_{water}(\lambda)}{\lambda}, \tag{4.8}$$

with $k_{water}(\lambda)$ representing the extinction coefficient at the wavelength $\lambda$ for water [83, 164, 174]. If the ray is absorbed, then a new ray is cast and the process begins again. Otherwise, a new grain is generated as described in Section 4.3.2. The complex index of refraction for the current medium is used when computing the Fresnel coefficients and employing Snell's law to obtain the direction of propagation of rays interacting with individual grains (Section 4.3.3).

### 4.3.5 A Note on Water Saturation

As discussed in the previous section, the SPLITSnow formulation incorporates water saturation as a fraction of the pore space (denoted by $\mathcal{S}$). However, sometimes (liquid) water is specified as a fraction of the total volume (denoted by $\mathscr{W}$). Equation 4.9 provides a method to convert this quantity to saturation as employed in this work.

$$\mathcal{S} = \frac{D_{ice}\mathscr{W}}{D_{ice} - D}, \tag{4.9}$$

where $D_{ice}$ is the density of ice and $D$ is the density of the sample's snow grains which is specified as an input parameter. For a detailed derivation of Equation 4.9, please see Appendix C.

## 4.4 Multi-layered Samples

So far in this chapter, we presented a formulation of the SPLITSnow model having made the assumption that the entire snow sample was homogeneous throughout its depth. However, such an assumption is not always valid. Indeed, as snow falls in separate weather events, several layers of differing characterizations will form and may be classified differently. In the field, the classification of the layers is represented by a snow profile record which documents the stratigraphic layers of a snowpack. (See Figure 4.6 for an example snow profile record.) This task is usually performed by digging a vertical snow pit and recording observations on a per-layer basis [60].

In order to accommodate layered samples of snow, an iterative approach was employed. Simply put, this feature of the SPLITSnow model allows for layers to be specified from bottom to top, with the basal layer being identified as layer zero. Note that it is not strictly necessary that layer zero be in contact with the underlying surface. However, by default, all light transmitted through this layer will *not* be reflected back into the snowpack, as outlined in Section 4.2. Thus, for a multi-layered snow sample, layer zero is treated in the same manner as a single layer snow sample. However, rather than processing and returning the results of the layer to the user, the results are cached in temporary storage to be utilized by the subsequent, covering layer.

When the implementation instantiates the second layer, *i.e.*, layer one, which is situated above the basal layer, the results obtained from layer zero are specified as a parameter to the forthcoming layer. More specifically, the spectral distribution computed from layer zero is used as an additional parameter to layer one. If a ray is transmitted through layer one into layer zero, rather than assuming a perfect absorber exists, the spectral results of layer zero are sampled. In particular, the reflectance value for the current wavelength of light is used as a test value in a Bernoulli trial. If the random variable is less than the reflectance value, then the ray is *reflected* back into the snow sample; otherwise it is absorbed. This process is repeated for any additional layers above layer one in an iterative process. This accounts for reflection and absorption for all the lower layers since the reflectance of the deeper layers is implicitly accumulated.

For the purpose of computing the reflectance spectra of the subsurface layers of snow, the polar angle of incidence is set to $0^\circ$. This simplifying assumption is rooted in the observation that that for a sample with a significant thickness the mean direction of the rays being transmitted through to the lower layer is in the nadir direction, *i.e.*, straight down from directly above the point of observation. There are two issues with this simplification. First, this simplification may not hold for very thin layers of snow especially when the angle of incidence is significantly greater than zero. Second, as described in Section 7.3, angle of incidence does have a noticeable effect on the BRDF of snow [54, 95, 231, 242]. The significance that this has on the spectral dis-

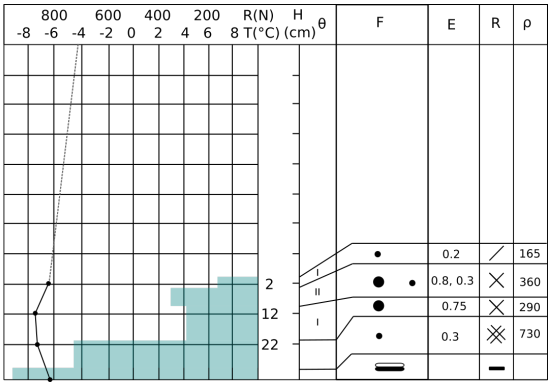


Figure 4.6: An illustrative example of a snow profile diagram [60]. For a brief description of the symbols please refer to Table 4.2.

| Characteristic | Symbol | Unit |
|---|---|---|
| Hardness | R | N |
| Temperature | T | °C |
| Moisture | θ | % |
| Height | H | cm |
| Grain Shape | F | |
| Grain Size | E | mm |
| Density | ρ | $\mathrm{kg\,m^{-3}}$ |

Table 4.2: Symbols employed in snow profile diagrams. See Figure 4.6 for an illustrative example. Vertical bars indicate increasing values for the θ column. H indicates the vertical component irrespective of the slope of the terrain beneath the sample. For additional information, the interested reader is referred to *The International Classification for Seasonal Snow on the Ground* by Fierz *et al.* [60].

tribution for a particular wavelength may depend upon the values selected for the other snow characterization parameters.

Lastly, we note that this iterative approach has only been applied to spectrometric *in silico* studies, and that multi-layer goniometric (BRDF) experiments have been left as future work.

## 4.5 Heterogeneous Samples

For many applications, the distributions discussed in Section 4.3.2 are suitable for describing the grains in a virtual snow sample. However, it is possible that environmental conditions may produce a more heterogeneous snow sample that contains a variety of distributions of snow grains [190]. Typically two or three types of grains may be described in snow profile diagrams. (See Figure 4.6, where layers consisting of multiple types of snow grains are depicted in the second layer form the top.) For such samples, it may be beneficial to specify multiple snow grain types in the virtual snow sample.

The SPLITSnow model supports multiple snow grain types, *i.e.*, *heterogeneous* snow samples. To implement this feature, first the number of different types of snow grains must be specified. For each grain type, enumerated sequentially starting from one, a distinct set of parameter values must be provided. This includes parameter values for the distribution which specifies the grain size, facetness and sphericity. (See Section 4.3.2.) In addition to these values, the fraction of each grain type in the sample must also be specified. Naturally, these fractional values must sum to one.

Note that the addition of grain types to a sample slightly complicates the mean distance computation, namely $\overline{d}$. Section B.2 of Appendix B provides the details. Briefly, the computation of $\overline{d}$ must be performed for each type of grain in the heterogeneous snow sample, and this different value of $\overline{d}$ must be associated with each of the grain types.

## 4.6 Impurities

Thus far, our description of a virtual snow sample has only included pure ice grains and a fractional amount of pure water within the pore space of the sample. However, samples of snow may not be pure. Furthermore, the presence of impurities has an effect on the reflectance (and transmittance) values of snow. In fact, it has been noted in the literature that impurities with quantities as low as one part per million may affect reflectance by 5–15$\%$ [232], and it has been shown experimentally to reduce reflectance in artificially made snow [81] as well as in natural snow [169]. Note that impurities primarily affect the visible wavelengths of EM spectrum [190, 228, 229], whereas the size and shape of the snow grain have a greater affect in the infrared (IR) wavelengths [50]. Thus, quantifying these impurities is an important pursuit, as their presence in surface snow may have an effect not only on the appearance of snow, but also on processes that can alter global climate[6] and sea levels [209]. To this end, the SPLITSnow

[6]Variations in the propagation of photosynthetically active (visible domain) radiation propagated by snow can contribute to vegetation greening, a phenomenon known to be associated with climate change feedback loops [18].

framework allows for the inclusion of trace amounts of carbon-based impurities within the material.

There are two types of carbon-based impurities to consider: black (inorganic) carbon and brown (organic) carbon [160]. Although these two terms have not always been used consistently in the literature, we adopt their use as described by Olson *et al.* [160] in this thesis.

Black (inorganic) carbon is an absorptive material that is produced from combustion. In particular, black carbon is strongly absorptive across all visible wavelengths. Note that sometimes the term *elemental carbon* is used in the literature to refer to black carbon [160, 161]. However, for simplicity, we will avoid the use of this term.

Brown (organic) carbon is also a product of combustion. It is the fraction of the carbon-based material (excluding black carbon) that is more absorptive in the lower wavelengths of the visible spectrum and the UV [160], as opposed to being highly absorptive across all wavelengths. Brown carbon is typically associated with biomass burning [118]. For this reason, it is sometimes referred to as *organic carbon*.

These carbon-based materials affect the absorption of rays traversing a snowpack. To incorporate them into the SPLITSnow formulation, we, therefore, must adapt the method whereby EM radiation is absorbed. This means modifying Equation 4.5. More specifically, we add their contribution to the $\alpha$ term in the exponent of the Beer-Lambert law. Thus, we introduce two new terms, $\alpha_{bc}$ and $\alpha_{brc}$ for black carbon and brown carbon respectively. The contributions of these two terms are linear, and they can be added to the the existing $\alpha$ term as a linear combination.

Recall that Equations 4.5 and 4.7 are used to calculate the probability for transmission of light within the grains of ice and within the interstitial medium, respectively. In order to account for the occurrence of carbon-based impurities in both the ice grains (through a sedimentation process [179]) and in the pore space (through a suspension process [122]), we add a parameter for each type of carbon that allows the fraction of black and brown carbon in sedimentation to be specified as parameters $S_{bc}$ and $S_{brc}$, respectively. These are unitless parameters that take values in the range of $[0, 1]$. As such, either black carbon or brown carbon may be present in the snow grains in the form of sedimentation or in suspension within the pore space. Accounting for carbon-based material in sedimentation and suspension form, leads to more comprehensive versions of Equations 4.5 and 4.7 associated with the Beer-Lambert law, which accounts for the impurities' concentration:

$$p_t(\lambda) = e^{-\left(\alpha_{ice}(\lambda)+S_{bc}\alpha_{bc}(\lambda)+S_{brc}\alpha_{brc}(\lambda)\right)d_g}, \tag{4.10}$$

for computing the probability of a transmission event occurring within the snow grains, and

$$p_t(\lambda) = e^{-\left(\alpha_{water}(\lambda)+(1-S_{bc})\alpha_{bc}(\lambda)+(1-S_{brc})\alpha_{brc}(\lambda)\right)d_p}, \tag{4.11}$$

for computing the probability of a transmission event occurring in the interstitial medium.

As mentioned above, carbon-based impurities are distinguished by their optical properties. We now define these terms more specifically and put them into context for computing the additional spectral absorption they foster. We start with a description of black carbon.

In the SPLITSnow framework, the s.a.c. of black carbon, $\alpha_{bc}$, is computed using the following equation [118, 165, 178]:

$$\alpha_{bc}(\lambda) = \frac{\mathscr{M}_{bc}\lambda_{bc}}{\lambda^{\mathscr{A}_{bc}}} D\mathscr{C}_{bc}, \tag{4.12}$$

where $\mathscr{M}_{bc}$ is the Mass Absorption Efficiency (MAE)[7] (in $\mathrm{m^2\,g^{-1}}$), $\lambda_{bc}$ is the reference wavelength (in $\mathrm{nm}$), $\lambda$ is the wavelength of light currently being examined (also in $\mathrm{nm}$), $\mathscr{A}_{bc}$ is the Angstrom exponent, $D$ is the density[8] of the snow sample (in $\mathrm{kg\,m^{-3}}$) and $\mathscr{C}_{bc}$ is the concentration of the black carbon impurities (in $\mathrm{ng\,g^{-1}}$).

We now turn our attention to brown (inorganic) carbon. Recall from above, that brown carbon is also a product of combustion and that it is more absorptive in lower wavelengths of the visible spectrum. Therefore, its effect on absorption is computed similarly to that of black carbon, albeit, higher values for the Angstrom exponent are often used [118].

In the formulation of the SPLITSnow model, we use a default value of two for the Angstrom exponent for brown carbon and leave the value of the Angstrom exponents with a wide range of possible values as an optional simulation parameter [118, 234]. Thus, for brown carbon, we compute $\alpha_{brc}$ similarly to Equation 4.12. This leads to the following expression:

$$\alpha_{brc} = \frac{\mathscr{M}_{brc}\lambda_{brc}}{\lambda^{\mathscr{A}_{brc}}} D\mathscr{C}_{brc}, \tag{4.13}$$

where $\mathscr{M}_{brc}$ is the MAE (in $\mathrm{m^2\,g^{-1}}$), $\lambda_{brc}$ is the reference wavelength (in $\mathrm{nm}$), $\lambda$ is the wavelength of light currently being examined (also in $\mathrm{nm}$), $\mathscr{A}_{brc}$ is the Angstrom exponent, $D$ is the density of the snow sample (in $\mathrm{kg\,m^{-3}}$) and $\mathscr{C}_{brc}$ is the concentration of the brown carbon impurities (in $\mathrm{ng\,g^{-1}}$).

Sometimes one finds the mass concentration of black (inorganic) carbon or brown (organic) carbon is expressed as $\mathrm{g\,m^{-3}}$ in the literature (*e.g.*, [160]). This is convenient since the units of the equations above expect the concentration to be in these units. However, it is also quite common to see carbon-based impurities specified in $\mathrm{ng\,g^{-1}}$ (*e.g.*, [228]), which is also known as *parts per billion by mass*. When this is the case, we obtain the correct units by multiplying the

[7] The MAE is also regularly referred to as the *mass absorption cross section* (or MAC) in the related literature [195].

[8] A conversion of units is required since the MAE is specified in $\mathrm{m^2\,g^{-1}}$ while the density is specified in $\mathrm{kg\,m^{-3}}$.

concentration by the density of the snow sample, $D$. This ignores the density contribution of the carbon impurities themselves. However, since the quantities are small (measured in parts per billion and ranging in 0.8–32 $\mathrm{ng\,g^{-1}}$ [122]), we found this approximation acceptable.

Lastly, we note that $D$, $\mathscr{C}_{bc}$ and $\mathscr{C}_{brc}$ in Equations 4.12 and 4.13 refer to a snow sample in a dry state. However, if the employed $\mathscr{C}_{bc}$ and $\mathscr{C}_{brc}$ values refer to a sample in a wet state ($\mathcal{S} > 0$), then the $D$ in these equations should be replaced by the $D_{wet}$ (Appendix C), which corresponds to the sample's density calculated considering the presence of liquid water in its pore space.

# Chapter 5

# Snow Appearance Visualization

Realistic reproductions of the outdoor world enhance an observer's experience by setting the scene in a believable surrounding. Accordingly, the rendering of material appearance changes elicited by natural phenomena remains an active area of computer graphics research. However, the intrinsic complexity of these phenomena often poses significant difficulties for their effective incorporation into realistic image synthesis pipelines. As a consequence, non-physical, *ad hoc* approximations are frequently employed. These approximations, however, cannot predictively reproduce the distinctive spectral features of a myriad of these phenomena. The bluish appearance that is observed when light has been transmitted through snow is arguably among the most fascinating, albeit still relatively unexplored, of these spectral features.

The phenomenon is depicted in Figure 5.1. The top photograph was taken inside an igloo, while the bottom photograph is of an illuminated garden lamp that has been covered by snow. Observe that in both cases, the backlit snow has a bluish appearance that is linked to the process of light transmission through the material [19, 27, 28] and the wavelength-dependent absorption exhibited by the ice crystals that form the snowpack. We remark that many modern computer graphics renderers make assumptions about the physical properties of materials in order to simplify the computational cost of generating images. For example, it is commonly assumed that materials fall into one of two categories: conductors and dielectrics, where conductors have the full complex-valued indices of refraction and dielectrics have only the real-valued part. Furthermore, for a given material, it is also commonly assumed that the index of refraction is constant across all wavelengths of light throughout the visible spectrum. We remark that these two simplifications hinder the predictive rendering of many natural phenomena, including well-known optical phenomena such as rainbows [143]. They also hamper the high-fidelity rendering of the bluish appearance that is observed after light is transmitted through snow.

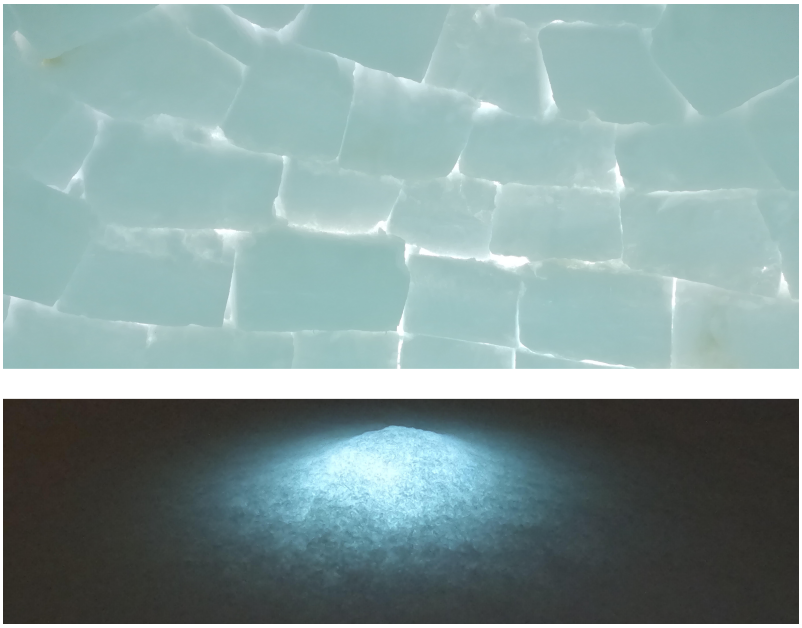

Figure 5.1: Photographs depicting the bluish appearance that is observed when light is transmitted through snow. Top: Daylight transmitted through an igloo wall formed by snow blocks. Bottom: Light transmitted from a garden lamp covered by snow at dusk.[1]

We remark that snow is a common material that is often portrayed in feature films, video games and other media. Many scenes in such media make use of lighting configurations where the light source is obscured by snow. Thus, in addition to computing the spectral reflectance properties of snow, the incorporation of light transmission through snow would enhance the realism of these scenes.

As discussed previously, snow consists of distinct ice grains that are suspended in an air medium. These ice grains are highly transparent. When light is transmitted through snow the material often takes on a bluish appearance [27]. This appearance is elicited by attenuation events within the material [28, 30]. Figure 5.2 provides a simplified illustration of the process for the case of light transmission. In this figure, rays of light reflect and refract through the various grains of ice that form a thickness of snow. As light traverses through the material, the rays are also susceptible to absorption events, even though ice is highly transmissive.

Although snow and ice are frequently treated as perfect dielectrics by the computer graphics community (*i.e.*, only the real-valued component of their index of refraction is considered)

[1]Igloo photograph courtesy of Muntart *via* Getty Images. Garden lamp photograph courtesy of Gabriel E. C. Baranoski.

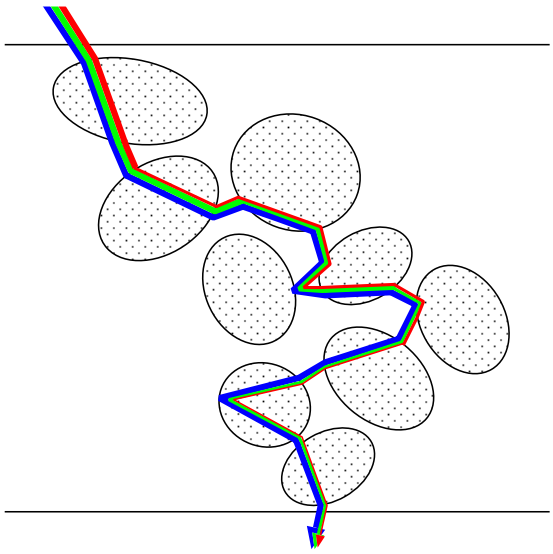

Figure 5.2: Sketch illustrating the selective absorption of light propagating through snow at different wavelengths. Longer wavelengths of light (right), which are at the red end of the visible spectrum, are more likely to be absorbed than shorter wavelengths of light at the blue end of the spectrum (left).

ice does have an extinction coefficient [230], (*i.e.*, the complex portion of the index of refraction) which is required for light absorption calculations. Furthermore, rendering software implementations often make the simplification that the index of refraction is constant across all wavelengths [38]. However, the complex index of refraction of ice is not constant across all wavelengths throughout the visible spectrum. Indeed, ice is more absorptive at red wavelengths [169, 230].

As (light) rays traverse through a snowpack, scattering events (*e.g.*, reflection and refraction) can occur [30]. As a result, the path length of the traversing light may be increased. This phenomenon is known as the *detour effect* [36]. The light-grain interactions along the increased path lengths present several opportunities for absorption events to occur. Since ice is not strongly absorptive, many rays will penetrate to a significant depth within the fallen snow [42, 216]. However, as ice preferentially absorbs (light) rays associated with wavelengths at the red end of the visible spectrum, fewer of these rays will penetrate to greater depths, which is the source of the bluish appearance that is observed [27, 28].

In Figure 5.2, the arrows represent the path taken by a beam of light through a snowpack. Note that for simplicity, only a few grain interactions are included in the figure. The preferential

absorption of light travelling at longer (more red) wavelengths is represented as a thinning of the arrows in the figure. At the exit point of transmission, more photons are transmitted at the blue end of the spectrum versus the red end of the spectrum. When these photons are integrated either by a camera sensor or by the human visual system, a bluish appearance is recorded or perceived.

To predictively reproduce the resulting appearance of snow, in particular, the bluish appearance observed *via* light transmission, we employed the SPLITSnow model to compute the spectral values of the reflected and transmitted light. The methodology employed to assess the predictive capabilities of the SPLITSnow model are discussed in Chapter 6.

Due to its stochastic nature, this model may incur relatively high costs when used on-the-fly in computer graphics applications. To overcome these practical constraints while maintaining a high level of visual fidelity in the rendering of scenes depicting the target phenomenon, we present a framework centred in a methodology based on the availability of snow spectral data.

We note that measured transmittance datasets for snow are scarce in the scientific literature. Furthermore, existing datasets are limited to a small number of snow samples and light incidence geometries. To overcome these data availability constraints, we employed the SPLITSnow model to form a simulated spectral transmittance database, henceforth referred to as the *transmittance database*. We then used principal component analysis (PCA) [176] to reduce the dimensionality of this transmittance database. By employing this technique, a compact representation of this database may be achieved without loss of visual fidelity. Moreover, spectra are efficiently reconstructed using a constant number of floating point operations. For consistency, we also employed the SPLITSnow model to produce a spectral reflectance database for snow. Although the process of transmission and the transmittance database are the focal points of the discussion for the remainder of this chapter, we include reflectance by analogy and only point out differences where appropriate for reflection.

The remainder of this chapter discusses the proposed rendering framework which comprises three stages that are specifically addressed in Sections 5.1–5.3. In Section 5.1 we discuss how to produce the transmittance database of spectral transmittance curves using the first-principles, predictive light transport model proposed in Chapter 4. Section 5.2 discusses how this database is compressed using PCA while ensuring that high-fidelity spectral reconstructions are viable. Finally, in Section 5.3, the specific methods employed to incorporate the spectral reconstructions into a typical image synthesis pipeline, enabling the efficient reproduction of the transmittance-elicited bluish appearance of snow, are discussed.

## 5.1 Spectral Transmittance Database

For the purpose of generating the transmittance database, we selected a variety of snow characterization traits that are known to have an impact on the process of light transmission through snow. We then varied the associated model parameter values through physically valid ranges to generate the database. The parameters we selected were facetness, grain size and density.[2] Each combination of these parameter values constitutes a unique virtual snow sample exemplar.

In addition to these three sample characteristics, light transmission through the material is also affected by other factors, notably the thickness of the snowpack and the angle of incidence to the light source. We, therefore, selected a set of snowpack thicknesses and distinct angles of incidence. For each virtual snow exemplar, we also varied the thickness of the sample and the angle of incident illumination. Hence, these two factors plus the three sample characteristics formed the basis of five dimensions of snow variability.

Lastly, a spectral resolution needed to be selected for the transmittance curves of the transmittance database. The selected spectral resolution was kept consistent for all entries of the database, which was necessary since it was used as the number of columns of a matrix. This matrix was central to the analysis which we discuss in the next section.

## 5.2 Principal Component Analysis

We applied principal component analysis (PCA) [176] to reduce the dimensionality of the transmittance database that contains the spectral light transmittance curves obtained for snow. This database consists of a set of several thousand spectral curves which quantify the relative spectral power distribution of light transmission through snow for various virtual snow samples, thicknesses and angles of incidence (see Section 5.1). For the purpose of this work, it is important to note that the database can be represented as an $s \times l$ matrix $M$, where each row $s$ contains the values of a spectral curve in the database, and each column $l$ is associated with a particular wavelength of light, $\lambda$.

To determine the number of required principal components, we use the method suggested by Pratt [176]. Although several PCA techniques have been developed [107], the singular-value decomposition (SVD) technique has been shown to be numerically stable. SVD factors $M$ into three matrices $M = U\Sigma V^T$, where $U$ is an $s \times s$ orthonormal matrix, $\Sigma$ is an $s \times l$ matrix whose off-diagonal elements are zeros and $V$ is an $l \times l$ orthonormal matrix. For $s \geq l$, observe that

[2] Section 8.1 discusses the rationale for this selection.

the values of $\Sigma$ are the *singular values* of $M$ and they satisfy the condition:

$$\varsigma_1 \geq \varsigma_2 \geq \cdots \geq \varsigma_l \geq 0, \tag{5.1}$$

where each $\varsigma_j$ is the diagonal value for the $j^{\text{th}}$ row of $\Sigma$ [107]. We then compute the $s \times l$ matrix $C = MV$. Using this technique, $V$ contains a new set of basis vectors (as column vectors) and $C$ stores the coefficients of each sample, relative to the new basis, $V$.

To reduce the size of the spectral database, we select $l' \ll l$ columns from the matrices $C$ and $V$. Hence $C'$ is an $s \times l'$ matrix and $V'$ is an $l \times l'$ matrix. To reconstruct the spectrum for a sample at row $j$, a $1 \times l'$ matrix, $C'_j$ is created by selecting the $j^{\text{th}}$ row from $C'$. Multiplying $C'_j$ by ${V'}^T$ yields the reconstructed spectrum. Note that, although there are many implementation strategies for PCA, the implementation of PCA used in this work, aims to minimize the Euclidean norm of the difference between $C$ and $C'$ [107].

## 5.3 Visualization Process

We remark that the visualization process discussed in this section may be applied to any set of snow parameter characterization traits. Furthermore, it may be applied to materials other than snow such as sea ice or translucent fluids. The bluish appearance that is elicited by the process of light transmission through snow is selected to exemplify the method due to its being a more *elusive* phenomenon, and thus allowing for a more in depth assessment of the proposed framework's predictive capabilities. However, as mentioned above, the visualization process described in this section is not limited to transmission, and it is equally applicable to databases containing spectral reflectance curves. For simplicity and conciseness, in the following description of this process, the light reflected by snowy objects was accounted for using a standard local illumination model for diffuse materials. However, where appropriate, considerations specific to reflectance will be discussed.

The spectral curves in the transmittance database are incorporated into a typical rendering pipeline in order to compute the colour exhibited when light is transmitted through snow in winter scenes. To this end, scene geometry that is identified as having a snow material is considered to be translucent in nature. Thus, snowy objects that are hit by a ray are treated as having both a local reflection component and as being emissive, with light having been permeated through the material. The emissive colour is retrieved from the compressed version of the transmittance database, with the specific curve being determined by the characterization of the snow sample and the local geometry of the object in relation to a traditional light source used in a rendering pipeline.

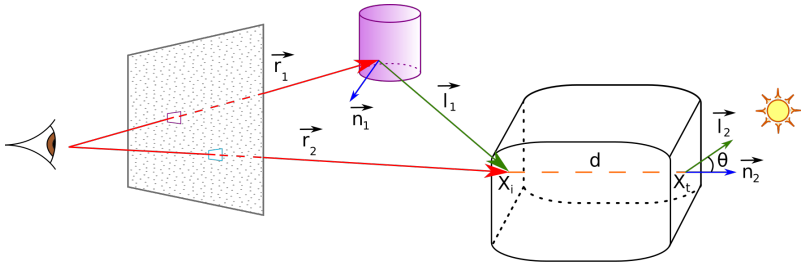


Figure 5.3: Sketch illustrating the key parameters employed in the incorporation of the PCASnow material class into the path tracing algorithm. When a ray hits an object, such as a snow block, associated with the PCASnow material class, the spectral distribution of the light transmitted through this object is obtained from the transmittance database (Figure 5.4) employing the distance $\mathscr{d}$ travelled inside the material (which corresponds to the thickness $h$ of the snow sample) and the angle of incidence $\theta$. Note that $\vec{r}_1$ and $\vec{r}_2$ represent primary rays, while $\vec{l}_1$ and $\vec{l}_2$ represent secondary rays.

For this application, we chose to employ path tracing [112] to render our images, even though the method described here can be incorporated into other image synthesis frameworks. The implementation of the proposed method provides a new material definition class for a typical path tracing renderer [171]. In the remainder of this section, we will refer to this class as *PCASnow*.

When an object associated with the PCASnow material class is hit by a ray, the distance $\mathscr{d}$ travelled inside the material and the angle of incidence $\theta$ with respect to the light source (Figure 5.3) are used in combination with the three snow sample properties (facetness, grain size and density) in order to determine the spectral light distribution that has been transmitted through the snow. To index the compressed database, the three snow sample properties, as well as the sample thickness (represented by the distance $\mathscr{d}$) at the location of interest, and the angle of incidence (represented by $\theta$) must be known.

For a database of spectral *reflectance* curves, the thickness parameter (represented by the distance $\mathscr{d}$) may be omitted if the snow sample is taken to be optically thick. More precisely, for a scene object with a significant thickness, the simplifying assumption may be made to not include thickness as an index variable in the spectral reflectance database.

Again, since our primary goal is to demonstrate the predictive reproduction of the bluish appearance observed when light is transmitted through snow, we concentrate our attention on the spectral distribution of light transmitted through snow samples, and account for its spatial distribution implicitly. It is worth noting that the SPLITSnow model (Chapter 4) is capable

of outputting the BSSDF values [154] since all geometric information, including position and direction of exitance, are known. Nonetheless, we elected to employ an implicit approach based on the precomputed transmittance data so that we could further mitigate computational costs.

Referring to Figure 5.3 to schematically illustrate the aforementioned light and material interactions, a primary ray $\vec{r}_1$ hits an object in the scene. To compute the object's reflectance, secondary ray $\vec{l}_1$ is cast toward a block of snow which indirectly serves as a light source. Similarly, a primary ray $\vec{r}_2$ strikes the snow block directly. For $\vec{r}_2$, both the reflectance and the emissive components contribute to the shading.

To compute the spectral appearance attributes for geometric objects whose colours are affected by light transmitted through snow, there are three aspects of the PCASnow material class implementation to be considered: the snow sample specification, the retrieval of the required spectral curves and the interpolation between the retrieved curves representing the discrete samples. These aspects are implemented as indicated in Algorithms 1–3.

**Algorithm 1** Pseudocode of the algorithm employed to initialize the material used to determine the spectral contribution of light transmitted through snow. In Figure 5.3, this material is applied to the snow block object on the right.

▷ *Initialization of the material (M) using facetness (F), grain size (gs) and density (D)* ◁
$M \leftarrow new\ PCASnow(F, gs, D)$
▷ *Initialization of the scene geometry (G) using material (M)* ◁
$G \leftarrow new\ SceneObject(M)$

To address the first aspect, the *Initialization of the Material*, the model parameter values associated with the desired snow sample must be specified when initializing an instance of the PCASnow material class. More precisely, the facetness, grain size and density must be provided as parameters to the PCASnow material class instantiation. An example is provided in Algorithm 1.

As for the second implementation aspect, *Indexing of the Transmittance Database*, it requires correct indexing into the matrix containing the spectral curves (see Figure 5.4). Recall from Section 5.2 that the PCA approach produces two matrices, the first of which, $C'$, contains numerous rows, that specify the coefficients to the column basis values stored in the matrix $V'$. Algorithm 2 provides details of our implementation, which computed the row index using

an elementary array indexing technique. Since there are five dimensions to consider, index retrieval is akin to a five-dimensional array index computation. The parameters can be indexed in any order, so long as the indexing order of the matrix $C'$ is consistent with the indexing order used to create the matrix $M$, which holds the complete set of computed spectral transmittance curves. We chose to index first by the grain properties (facetness and grain size), and subsequently by the snow sample's density, then by the geometric properties required for rendering (sample thickness and the angle of incidence). This strategy ensures that all spectral transmittance curves for each of the samples are contiguous in memory, which allows for the set of spectra of an entire sample to be cached. Once an index has been retrieved, the selected $1 \times l'$ row ${C'}_j$ of the matrix $C'$ was multiplied by the $l' \times l$ matrix ${V'}^T$ to reconstruct the spectra for that sample.

As mentioned above, this indexing may be performed in any order, so long as indexing the spectral database is consistent with the indexing order for the matrix $M$. For the spectral reflectance database, the same indexing order may be used. However, in the case of the spectral reflectance database, for scene objects that are sufficiently thick, indexing by thickness may not be necessary, and this index variable may not be included. Still, the angle of incidence may potentially be included. This may be in reference to the light that is the source of illumination on the face of the object where the reflection is being computed.

**Algorithm 2** Pseudocode of the algorithm employed to index the transmittance database.

▷ *Indexing of the Transmittance Database* ◁
▷ *Ray-object intersection point is $X_i$ on scene geometry (G)* ◁
$d \leftarrow computeDistanceThroughObject(X_i, G)$
$X_t \leftarrow determineExitPoint(X_i, d)$
▷ *L is a traditional light source in the scene* ◁
$\theta \leftarrow computeAngleToPrimaryLightSource(L, X_t)$
▷ *Use facetness (F), grain size (gs), density (D), d and $\theta$ as index values* ◁
$spectra \leftarrow M[F, gs, D, d, \theta]$

Next, we address the third implementation aspect, the details of which are provided in Algorithm 3. Namely, the *Interpolation of the Spectral Responses*. To generate the transmittance database (and also the reflectance database), we selected a fixed number of angles of incidence and sample thicknesses. As a consequence, interpolations between angles of incidence and sample thicknesses were required.

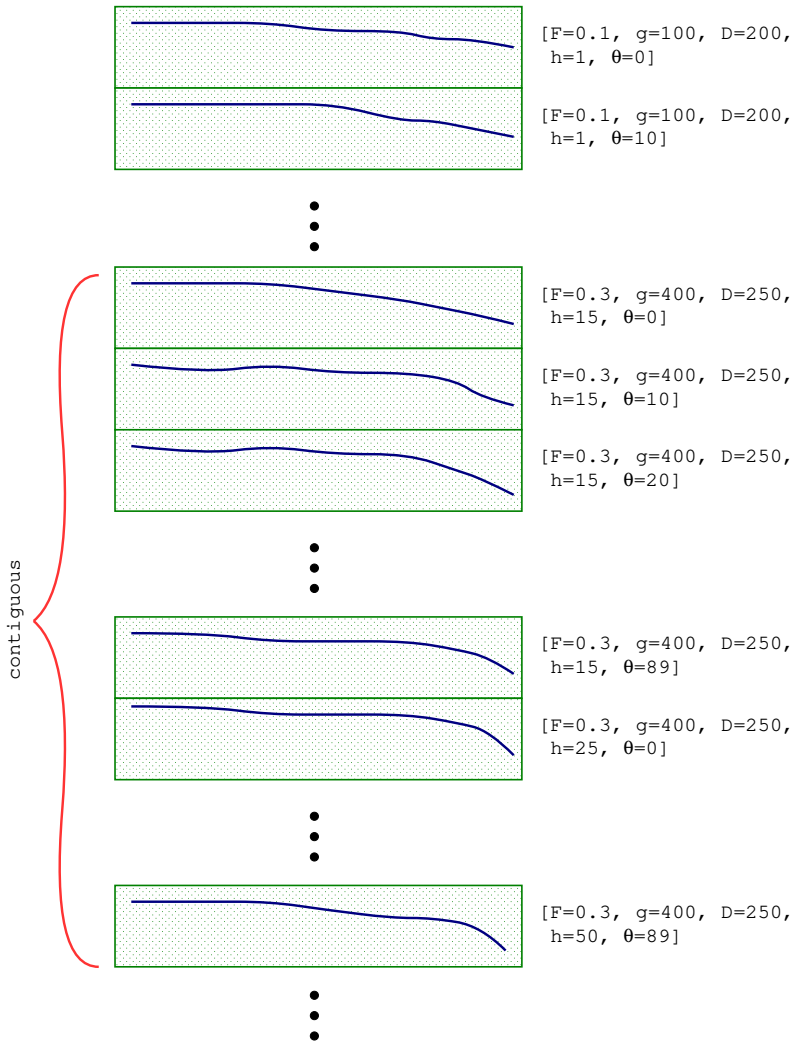


Figure 5.4: Indexing layout of the transmittance database with the curves inside the boxes representing the stored transmittance database entries (rows of matrix $M$, Section 5.2). Indexing is ordered first by facetness ($F$), grain size ($g$) and density ($D$). Indexing is then ordered by sample thickness ($h$) and angle of incidence ($\theta$). This order of indexing ensures that a particular virtual snow sample is laid out contiguously in memory as indicated by the red bracket. Each element of this five-dimensional array contains the spectral transmittance values of the curve for the respective index.

**Algorithm 3** Pseudocode of the algorithm employed to interpolate the retrieved spectral responses. In Figure 5.3, the results of this interpolation may be used by the primary ray $\mathbf{r}_2$ or the secondary ray $\mathbf{l}_1$.

▷ *Interpolation of the Spectral Responses* ◁
▷ *Use facetness (F), grain size (gs) density (D), the sample thickness (d) and angle of incidence ($\theta$) as index values* ◁
▷ *$\lfloor floor \rfloor and \lceil ceiling \rceil$ functions denote lower and upper index values* ◁
▷ *M represents the PCASnow material class instance* ◁
$spectra_{ll} \leftarrow M[F, gs, D, \lfloor d \rfloor, \lfloor \theta \rfloor]$
$spectra_{hl} \leftarrow M[F, gs, D, \lceil d \rceil, \lfloor \theta \rfloor]$
$spectra_{l} \leftarrow cubicSpline(spectra_{ll}, spectra_{hl})$
$spectra_{lh} \leftarrow M[F, gs, D, \lfloor d \rfloor, \lceil \theta \rceil]$
$spectra_{hh} \leftarrow M[F, gs, D, \lceil d \rceil, \lceil \theta \rceil]$
$spectra_{h} \leftarrow cubicSpline(spectra_{lh}, spectra_{hh})$
$spectra \leftarrow linear(spectra_{l}, spectra_{h})$
**return** $spectra$

We chose to use cubic spline interpolation to obtain intermediate values between two given thickness values. These values correspond to the distances travelled, $\mathscr{d}$, by light through the snow block. Note that the cubic interpolation of distance must be performed between the two distances for both the low and the high values of $\theta$. We then interpolate linearly between these two curves, *i.e.*, those that represent the low and high angles of incidence for the cubically interpolated thicknesses. It is also worth mentioning that the cubic interpolation scheme was selected due to the reported nonlinear attenuation of light traversing snow samples [184]. Note that the interpolated spectra are convolved with the relative spectral power distribution of the traditional rendering light source before it is used in local reflectance calculations or added as an emissive contribution.

The boundaries adopted for the minimum and maximum angles of incidence, $\theta$, were $0^\circ$ and $89^\circ$. The transmittance spectra associated with any angle of incidence outside these bounds were assumed to not exhibit any colour. Note that the upper limit of the angle of incidence was set to $89^\circ$ to avoid numeric computation issues with incident light that is parallel to a surface. Similarly, the boundaries for the snow thicknesses were chosen to be 0 $\mathrm{cm}$ and 100 $\mathrm{cm}$. Transmittance spectra through a 0 $\mathrm{cm}$ snow thickness were assumed to have the maximum magnitude and eliciting the colour white. On the other hand, transmittance spectra through

snow thicknesses beyond 100 $\mathrm{cm}$ were assumed to be negligible, and thus, resulting in the colour black.

The spectral reconstructions and visual results of the proposed methods discussed in this chapter are provided in Chapters 8 and 9. The results of the data analysis and colour swatches generated using the spectral reconstructions, which serve to highlight specific chromatic aspects, are included in Chapter 8. Full colour renderings are presented in Chapter 9.

# Chapter 6

# Evaluation Methodology

In this chapter, we discuss the evaluation methodology used to assess the predictability of the SPLITSnow model proposed in Chapter 4. We also discuss the methodology used to assess the fidelity of the reconstructed spectral transmittance curves produced for the purpose of rendering images which was introduced in Chapter 5.

To address the first aspect, *i.e.*, the predictability, we start with a discussion regarding the datasets that are employed in the formulation of the SPLITSnow model and provide information regarding how the datasets are used. We then provide a description of the virtual measurement procedures we employed. This is followed by a discussion of the parameters we examined using these measurement procedures. In addition to this, we provide an example of how the predictability of the SPLITSnow model may be used in the analysis of remotely acquired data.

To address the second aspect, *i.e.*, image synthesis, we begin with a discussion regarding the methods employed for image synthesis verification. We then consider the spectral resolution employed for rendering.

Finally, we elaborate on the reproducibility and dissemination of radiometric predictions provided by the proposed framework.

## 6.1 Datasets and Data Flow Pertinent for Evaluation

We remark that it is not unusual to compare predictions provided by new models being introduced in the literature with simulated readings obtained using existing models, particularly when reliable ground truth data is not available. However, reliable measured radiometric data

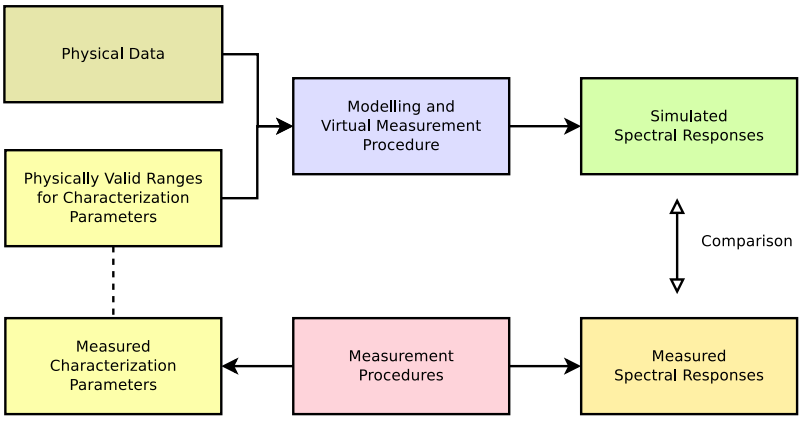


Figure 6.1: Datasets and data flow utilized for the evaluation of the SPLITSnow model. Physical data (*e.g.*, index of refraction) and sample characterization data (*e.g.*, density and thickness) are fed into the model where the virtual measurement procedure produces data for comparison purposes. Similarly, *in situ* measurements of a sample that also include detailed measurements of the sample characterization allow for more direct comparisons to be made when evaluating the simulation results.

for snow is available in the literature, albeit from a moderate number of sources (*e.g.*, [54, 169, 190]). Moreover, comparisons of results provided by different models may be more susceptible to biases associated with the assumptions considered in the design of those models. For these reasons, we believe that, as in any effort in physical sciences, the ground truth to be used in the evaluation of a novel light transport model should be actual measured data. Accordingly, we have elected to evaluate the predictions made by the SPLITSnow model through quantitative and qualitative comparisons with measured data and experimental observations reported in the literature.

Figure 6.1 provides an overview of the datasets and data flow affecting evaluation. Physical data, such as the complex index of refraction, as well as snow sample characterization data are inputs to the model. The characterization values are constrained to physically valid ranges as reported in the literature. The model simulates the light interactions with a virtual snow sample defined by the characterization data, and the virtual measurement procedures (discussed in Section 6.2 below) produce spectral responses that are used for comparison purposes.

Measured response data obtained from field studies are compared to simulation results. Similar to the generation of simulated results, having measured characterization traits allows for better comparisons to be made. Ideally, the measured characterization traits will be used to guide the input characterization parameters employed for simulation. Furthermore, descriptive

details regarding the measurement procedure may also impact the comparisons made between simulated and measured data.

There are two types of comparisons to be made between simulated and measured datasets. First, quantitative comparisons may be made between the simulated and measured responses, and evaluation metrics are used to assess the closeness of the two outputs. These provide the most direct method of comparison. Second, the effects of varying parameter values may also be reported in the literature. For instance, an increase in the density of a snow sample can affect its spectral reflectance. We describe such effects as phenomenological trends that are reported in the literature. Qualitative comparisons are made to evaluate whether the modelling procedure is capable of predicting the same trends.

## 6.2 Virtual Measurement Procedures

As discussed in Chapter 4, an *in silico* experiment is executed by casting rays into a digital representation of the selected snow sample. Once the ray has escaped from the sample, the exitance details are recorded using a virtual goniophotometer [124]. With this procedure, the hemispherical radiometric responses resulting from light interactions with the snow grains are quantifiable in terms of BSSDF since all geometric values, including positions, of the incidence and exitance points are known. We note that to enable comparisons with BRDF data reported in the literature, the separation between incidence and exitance points can be assumed to be negligible so that the model predictions can also be expressed in terms of BSDF [154].

Considering the directional outputs of the simulation, the upper collection hemisphere of this virtual goniophotometer is divided into regions of equal solid angle associated with light sensors (detectors). Since the incident ray is directional, a directional-conical reflectance experiment is undertaken with this type of virtual device. (See Section 2.2.1.) At each detector location, the ratio of impinging rays to the total number of rays cast by the device is divided by the projected solid angle, yielding the BRDF (and the BTDF by analogy, *i.e.*, considering the lower collection hemisphere). By decreasing the solid angle of the virtual collectors, a better approximation to the true BRDF is achieved at the expense of additional computational cost. Thus for each wavelength, $\lambda$, the BRDF is numerically computed as follows:

$$f_r(\theta_i, \phi_i; \theta_r, \phi_r; \lambda) = \frac{n_\lambda\left(\theta_r, \phi_r\right)}{N_\lambda \Omega_r\left(\theta_r, \phi_r\right)}, \qquad [\mathrm{sr}^{-1}] \quad (6.1)$$

where $n_\lambda\left(\theta_r, \phi_r\right)$ is the number of rays striking the collector in the reflected direction on the virtual goniophotometer, $\Omega_r\left(\theta_r, \phi_r\right)$ is the projected solid angle of a given sensor located in

the same direction, $N_\lambda$ is the total number of rays cast, and $(\theta, \phi)$ represent the locations in spherical coordinates [154].

Directional-hemispherical reflectance is a variation of the directional-conical reflectance where the entire upper hemisphere is used as a single detector. Thus, the sum of the contributions of each detector is equal to the sum for the total upper hemisphere. Hence, the directional-hemispherical reflectance can be numerically computed as:

$$\rho(\theta_i, \phi_i; \lambda) = \frac{n_{r\lambda}}{N_\lambda}, \tag{6.2}$$

where $n_{r\lambda}$ is the total number of reflected rays in all directions of the upper hemisphere. Similarly, the directional-hemispherical transmittance can be numerically computed as:

$$\tau(\theta_i, \phi_i; \lambda) = \frac{n_{t\lambda}}{N_\lambda}, \tag{6.3}$$

where $n_{t\lambda}$ is the total number of transmitted rays through the material.

When conducting experiments of light transmission through snow, it is worth mentioning that light penetration measurements conducted *in situ* often rely on the insertion of a sensor probe or measurement device at different depths within a snowpack [184, 189]. Considering the diffuse (Lambertian) nature of light propagation through snow [24], such a setup may allow for light that is backscattered from a greater depth to be detected by a sensor placed at a shallower depth. This can result in a flux reading larger than that of the actual flux transmitted from the sample's top boundary to the sensor's depth. Since we are interested in the EM radiation reaching to a particular depth, and not the reflected radiation, we employ a different setup. More specifically, we compute the transmittance values at the indicated thickness (equivalent to the depth of the samples' bottom boundary). In other words, once a (light) ray exits a snow sample at the specified thickness (bottom depth), it is considered permanently propagated by the snow sample, *i.e.*, it no longer contributes to the sample's transmittance reading at that depth.

Our *in silico* setup for the computation of transmittance as outlined above is consistent with other setups employed in field measurement campaigns [18]. In some of those setups, the transmittance values were measured using a tunnel to place the measurement device at the bottom depth of the snowpack [114, 182]. The values for different thicknesses (depths) were recorded as snow accumulates on a window (port) placed in the top of the tunnel located at snow-soil interface. In an alternative setup [24], the measurement device was positioned underneath a snow slab extracted from a snow bank and placed on a metal table especially configured for that purpose. These setups, albeit more logistically complex, allowed for the measurements to be performed without disturbing the accumulated snow [24, 114, 182], which, we remark, is

more likely to happen when sensors are inserted into a snowpack [184, 189]. Lastly, another arrangement placed a probe on a base before the snowfall season. After a sufficient accumulation of snow, repeated measurements were performed after removing material at regular intervals [169]. Although the sample may be disturbed, this arrangement prevented backscattered light rays from making a contribution to sensors at shallower depths, which is also achieved by our *in silico* experimental setup.

## 6.3 Data Considerations for Radiometric Comparisons

Recall that, characterization data that are provided along side measurement data are used to guide our quantitative comparisons. However, complete descriptions of the samples being measured are uncommon. Therefore, the exploration of the model's characterization parameter space is warranted to some extent.

Grain size is one of the most predominantly observed snow grain characteristics found in the literature since it has a significant effect on reflectance [28, 74, 105, 130, 144, 156, 157]. However, additional snow grain characteristics are utilized to achieve a better fit with the measured reflectance data of snow samples. In view of this, we attempted to determine the set of snow model parameter values that reproduce the spectral reflectance results that were reported in the literature by Dumont *et al.* [54], Perovich [169] and Salvatori *et al.* [190]. The obtained parameter values are determined by iteratively exploring the model parameter space being sure to employ values that are within physically valid ranges [29, 60]. Furthermore, all sample characterization data measurements that were recorded as part of the *in situ* measurement processes were analyzed and used to limit the scope of the search space of the model's input parameter space.

We remark that our quantitative comparisons were complemented by comparisons between model predictions and trends that have been reported in the literature. The latter include both reflectance and transmittance changes. For evaluation purposes, several model parameters that describe the virtual snow sample are subjected to variation. These include grain size, facetness and density. More specifically, *in silico* experiments are conducted by varying the individual parameters, which are assessed against the expected effects on reflectance and transmittance (*i.e.*, the phenomenological trends) as reported in the literature. In addition to snow grain attributes, we also investigate the effects of water content, as it has an application in determining near-surface water saturation of snowpack for remote sensing [53, 74]. Geometric aspects, including snowpack thickness and the angles of incidence, are also considered.

We then investigate the effect of model parameters on BRDF trends. We qualitatively compare predictions made by changes in grain size and facetness with trends that have been re-

ported in the literature. Moreover, we test the effect of varying the angle of incidence and the wavelength of the illumination source. The predictions made by these experiments are also qualitatively compared to the reported trends.

Note that for spectral studies of reflectance and transmittance, we use the angle of incidence of $0^\circ$. We remark that controlled studies of spectral reflectance and transmittance trends of particulate materials often use this angle of incidence. (For example, see Bänninger and Flühler[5], Ciani *et al.* [40], Dumont *et al.* [54], and Nakamura *et al.* [144].) However, when investigating directional trends, it is more common to find studies in the literature where the angle of incidence is varied. We follow this strategy of varying the angle of incidence when making comparisons to trends observed with a directional component.

While *in situ* and laboratory experiments that quantify directional reflectance data are fundamentally important, sometimes there are geometric limits on the incidence and reflectance angles to be measured depending upon the apparatus design. With an *in silico* experiment, there are no such limitations. Furthermore, the effectiveness-to-cost ratio of investigations can be improved by pairing traditional and *in silico* experiments since the latter enables a precise control of the parameters under study. However, while distinct polar angles of incidence are considered in this investigation, we fix the azimuthal angle at $0^\circ$. We remark that SPLITSnow is a local light interaction model. Accordingly, macroscopic features like sastrugi [95] and wind effects [137], that can lead to an azimuthal asymmetry of light propagated by snowpacks covering relatively large areas, are outside our current scope of simulations.

We also remark that the spectral indices of refraction and extinction coefficients of water and ice are incorporated in the formulation of the SPLITSnow model (see Chapter 4). Thus, in our simulations, we employ spectral curves (Figure 6.2) obtained from the literature on these optical properties of water [83, 164, 174, 223] and ice [230].

As briefly mentioned earlier, we quantitatively compare spectral reflectance values obtained using the SPLITSnow model with spectral reflectance values measured by Dumont *et al.* [54]. It is worth noting that they chose to perform the bulk of their analyses on their Sample 3 which, according to them, provided results consistent with those obtained for their other samples. Therefore, we evaluate SPLITSnow simulated results through comparisons with measurements obtained from this sample. We will refer to the virtual snow sample with parameter values used to reproduce the reflectance curve of this measured dataset as the *representative sample* in the remainder of this work, and we consider these characterization parameter values to be suitable for use as *baseline* parameter values in our experiments.

For their analyses of reflectance, Dumont *et al.* [54] employed a sample container that was cylindrical with a 15 $\mathrm{cm}$ radius and 12 $\mathrm{cm}$ depth. However, they used a cuboid sample holder that was 16.5 $\mathrm{cm}$ deep to determine their radiometric bottom losses, which were found to be

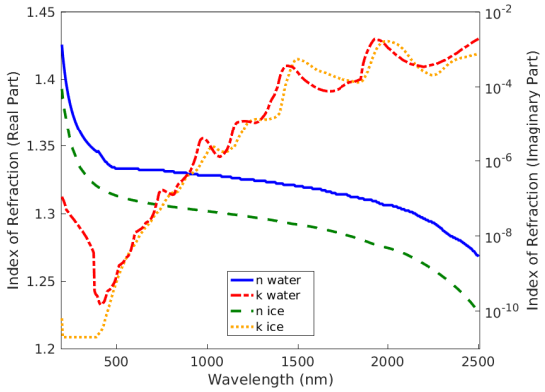


Figure 6.2: Complex index of refraction curves for both water [83, 164, 174, 223] and ice [230] used in this work. The real part of the index of refraction for water and ice are denoted by blue solid and green dashed lines respectively. The imaginary part of the index of refraction (*i.e.*, the extinction coefficient) for water and ice are denoted by red dash-dotted and orange dotted lines respectively. The vertical scale for the real part of the index of refraction is linear, while the vertical scale for the imaginary part of the index of refraction is logarithmic.

less than $1\%$. Since transmittance is also an output of the SPLITSnow model, we were able to verify that its bottom losses are similar to those reported by Dumont *et al.* [54]. For these direct comparisons, we consider a spectral resolution of $10\ \mathrm{nm}$ in our simulations, which is sufficient to describe spectral features present in the actual measured data of the representative sample that was captured using the same or a coarser resolution [54].

In addition, we provide quantitative comparisons to datasets provided by Salvatori *et al.* [190]. We remark that whereas Dumont *et al.* [54] provided goniometric data of the measured samples, Salvatori *et al.* [190] provided only spectral reflectance factor data. Although the characterizations of the measured samples in the Snow & Ice Spectral Library 2.0 (SISpec) database [190] are often more complete than the characterization data provided by Dumont *et al.* [54].

These two datasets [54, 190] only provide reflectance data. Undoubtedly, experimental studies of transmittance of light through snow are scarce in the snow literature [24, 68, 169]. This scarcity may be explained by the intrinsic limitations of *in situ* measurements, which are difficult to conduct [70]. For instance, while attempting to place sensors within a snow layer, one may inadvertently disturb the structure of the snowpack [184, 189], which may affect the measurements' reliability [55], or because back scattering and the detour effect allow for light transmitted beneath the sensor to affect the measurement. (See Section 6.2.) To our knowledge, the transmittance studies available in the literature were all performed in the field and were

affected by impurities [169], morphological changes [68] or variations in solar radiation [24]. In light of these considerations, we elected to make a comparison with transmittance data provided by Perovich [169]. More specifically, a comparison is made to his "January 18" sample, which we abbreviate as *P18*.

As outlined above, to further assess the predictability of the proposed model, we qualitatively evaluate it by examining the impact that various snow grain sizes have on simulated results, as well as other snow characterization parameter values. For example, experimental evidence suggests that reflectance decreases as grain size increases [28, 144]. *In silico* experiments pertaining to other characterization parameters such as facetness, water content and density, are also conducted. We also investigate similar spectrometric trends regarding transmittance and qualitatively compare our findings with observations reported in the literature. Lastly, we conduct directional-hemispherical reflectance experiments to assess the predictive capabilities of the SPLITSnow model with respect to radiometric responses of multi-layered samples (Section 4.4), heterogeneous samples (Section 4.5) and samples containing black carbon and brown carbon impurities (Section 4.6).

Such systematic investigations usually require specific variations in selected snowpack characteristics while the others are kept fixed. This control is difficult to be achieved under field conditions in which the changes are elicited by environmental factors that may affect multiple of those characteristics of the snowpack simultaneously [41]. While such controlled experiments can be attempted under laboratory conditions, usually artificially prepared snow samples lack the morphological diversity (*e.g.*, different grain sizes and shapes) found in natural samples [190], which limits the scope of the observations that can be derived from their outcomes. Moreover, experiments involving light transmission on scattering materials conducted under field or laboratory conditions have to face another challenging aspect, namely the control of incident illumination [24].

As noted by Bänninger and Flühler [5], there are optical similarities between snow and other granular materials. As such, the effects of varying particular snow grain parameter values on transmittance for snow can be assessed by examining the transmittance profiles of other granular materials (*e.g.*, sand) from a qualitative perspective. For example, as the thickness (depth) of the deposits of these materials increases, the transmittance decreases [5, 40]; as grain size increases, the transmittance increases [5, 40, 208]; and as porosity increases (*i.e.*, density decreases), the transmittance increases [159, 238]. Accordingly, we perform transmittance experiments in which we assess the proposed model's predictive capabilities with respect to these aspects.

The incorporation of facets in the formulation of the proposed model allows it to efficiently represent complex grain features which are relevant [53] when considering the angular details

of snow reflectance for remote sensing [104]. We perform *in silico* goniometric reflectance experiments, which we qualitatively compare with field observations reported in the literature, to illustrate this aspect. For example, a decrease near nadir and an increase in forward direction (with respect to the scattering limb) are observed in the simulated results. Both effects are described in the literature [54, 95, 119]. An increased polar angle of incidence is associated with a stronger forward peak [54, 95, 137]. Finally, smaller grains exhibit a stronger forward peak when compared to larger grains [54].

In this work, we primarily consider the snow temperature to be -1°C since the temperature of snow is typically near its melting point [60]. Furthermore, simulations in which we varied only the ice temperature in the range of -40–0°C showed little difference in reflectance.

## 6.4 Analysis of Remotely Acquired Data

In this section, we outline the evaluation of the predictive capabilities of the proposed framework with respect to remotely acquired data. It consists in comparing simulated reflectance curves with reflectance data obtained by the Airborne Visible-Infrared Imaging Spectrometer — Next Generation (AVIRIS-NG) instrument [75, 86]. This instrument is a spectrometer that takes readings in the visible and IR domains from 380–2510 nm with a 5 nm spectral resolution. The instrument is fixed to an aircraft. For each "flight" a 600 pixel wide image is captured across the length of the flightpath. Each pixel contains a complete spectral reading of solar illumination reflected from the surface below. The data are freely available on the AVIRIS-NG website.[1] In addition to the spectrometric data, each pixel also contains geographic information.

The simulated values are obtained using the SPLITSnow model (Chapter 4) and compared against values obtained from selected pixels from flight line *ang20160217t074158*, which was captured over the mountainous state of Himachal Pradesh, India. This flight line was chosen due to the abundance of snow and since cloud conditions were listed as clear. The solar altitude at the time of the flight was 27.7°, or 62.3° away from the vertical.

Selecting a mountainous region introduces a challenge to the study of reflectance since the slope of the terrain affects the angle incidence of the light from the sun. To compensate for this, we use the estimated elevation data provided in the dataset to compute the gradient (which quantifies the rate of change of elevation) for each pixel. These gradients are then used to find a $5 \times 5$ pixel area exhibiting little horizontal and vertical change in elevation.

[1] https://avirisng.jpl.nasa.gov/

## 6.5 Reconstructed Data Verification

In Chapter 5, we describe the process employed to generate images depicting snow appearance attributes, notably those associated with the bluish colour that is observed when light is transmitted through snow. Recall from Section 5.2 that principal component analysis (PCA) compresses the transmittance database by selecting a value for $l' \ll l$ to reduce the dimensionality of the database. To evaluate the choice of $l'$, we compare the reconstructed spectral curves against the original database of transmittance spectral curves, $M$.

We use two metrics to evaluate the quality of the spectral reconstructions. First, we calculate the root mean squared error (RMSE) between spectral curves in the transmittance database and the reconstructed curves. Second, we determine the coordinates for the original transmittance curves and their respective reconstructions in the CIELAB colour space[2] in order to quantify the perceptual differences between the two representations [204].

We test various quantities of principal components (*i.e.*, values of $l'$), reconstruct the complete set of spectra using the reduced number of components, and compare the reconstructions with the transmittance database. First, we compare the RMSE between each transmittance curve and the associated reconstructed curve. The RMSE is computed using the formula:

$$RMSE = \sqrt{\frac{1}{n}\sum_{j=1}^{n}\left(\tau_j - \hat{\tau}_j\right)^2}, \tag{6.4}$$

where $\tau_j$ is the transmittance value for $j^{\text{th}}$ wavelength, $\hat{\tau}_j$ is the reconstructed transmittance value for the same wavelength and $n$ is the number of spectral samples. (Note that the RMSE can also be computed for spectral reflectance responses by replacing $\tau_j$ and $\hat{\tau}_j$ with $\rho_j$ and $\hat{\rho}_j$, respectively.)

Although computing the error between two spectral curves provides insight into their relative difference, it does not provide a measure of the visual similarity for human observers. To achieve that, the second metric we employ involves the computation of the perceptual differences using device-independent International Commission on Illumination (CIE)-based distances. More specifically, we compute the Euclidean distances in the CIELAB colour space, which provides a quantifiable measure of visual difference for an average human observer [204].

To obtain the CIELAB differences, we first compute the CIEXYZ tristimulus values[3] by performing a multiplication of the spectral curve with the illuminant's relative spectral power

[2]CIELAB is a colour space that represents colours so that the relative distances between colour coordinates quantifies the relative difference between the two colours for an average human observer [204].

[3]CIEXYZ is a colour space that represents colours using three tristimulus coordinates, $X$, $Y$ and $Z$, that are based on the stimuli experienced by a standard human observer [204].

distribution and the spectral response of the human photoreceptors [85, 93]. We chose to employ the standard CIE D65 illuminant (average daylight) for this purpose [96]. We then convert the XYZ tristimulus values into the CIELAB colour space using standard techniques [33]. Further details regarding the process of determining the trichromatic colour values for a spectral distribution can be found in a standard text such as that by Stone [206].

The conversion to CIELAB coordinates is performed for both the reconstructed and the original transmittance spectral curves. Once the CIELAB representations for the curves are obtained, the CIELAB differences are computed using the formula:

$$\Delta E^*_{ab} = \sqrt{(\Delta L^*)^2 + (\Delta a^*)^2 + (\Delta b^*)^2}, \tag{6.5}$$

where $\Delta L^*$, $\Delta a^*$ and $\Delta b^*$ are the differences between the respective $L^*$, $a^*$ and $b^*$ coordinates.

In this work, we select the smallest number of principal components (*i.e.*, the smallest value for $l'$) whose reconstructions yield a maximum perceptual difference below 2.3, which correspond to the experimentally determined perceptibility threshold for an average human observer [131, 204].

Finally, we provide a visual representation of this perceptual difference result. Namely, we generate colour swatches for the samples with the two greatest perceptual differences. More precisely, we use the same aforementioned multiplication process to compute the CIELAB coordinates, except that the final transformation is into the sRGB colour space [33, 93, 206]. For consistency, we employ the CIE D65 standard illuminant as indicated before [96]. For illustrative purposes, we modulate the swatches with an achromatic texture that approximates the macroscopic features of the snow samples as observed after light has been transmitted through a thickness of the material.

## 6.6 Spectral Resolution for Rendering

We note that the spectral resolution and the choice of illuminant can have a significant impact on the results of the multiplication process outlined in the previous section. In order to render images, we employ the completely reconstructed spectra (31 spectral samples), rather than tristimulus values (three spectral samples). This choice was based on the importance of spectral information for the rendering of real world materials [106].

To illustrate this aspect, we generated swatches for a given snow sample through the multiplication process of selected illuminants' spectral power distributions (Figure 6.3 (top)), the sample's transmittance curve (Figure 6.3 (middle)) and the broad spectral responses of the human

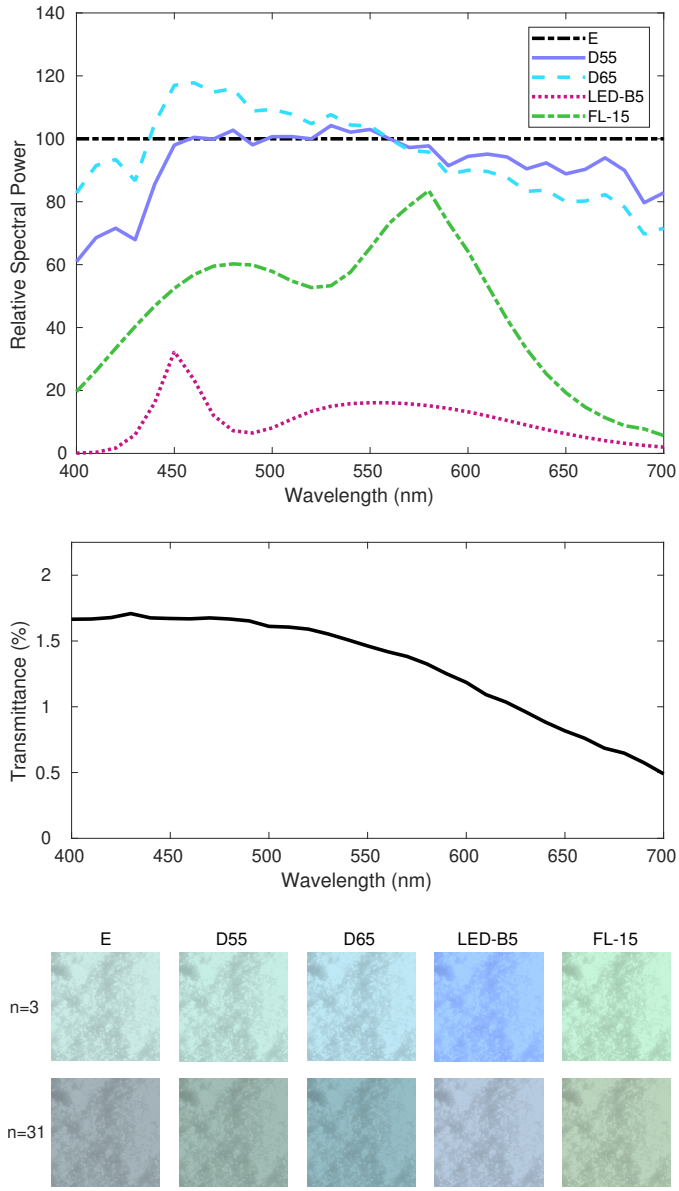


Figure 6.3: Components of the multiplication process employed to generate swatches for a backlit snow sample characterized by a mean grain size, facetness, thickness, and density equal to 400 $\mu$m, 0.3, 15 cm, and 300 $\mathrm{kg\,m^{-3}}$, respectively. Top: plots of the relative spectral power distributions of selected CIE illuminants (E, D55, D65, LED-B5, and FL-15) [37]. Middle: transmittance curve computed for the snow sample considering an angle of incidence of $0°$. Bottom: snow swatches generated using different numbers ($n$) of wavelengths, namely 3 (455, 551, and 608 nm) and 31 (equally spaced in the 400-700 nm interval).

photoreceptors [85, 96]. This last step was performed using a standard CIEXYZ to sRGB colour system conversion procedure [14] and considering the CIE standard illuminants E (equal energy), D55 (5,500 $\mathrm{K}$ daylight), D65 (6,500 $\mathrm{K}$ natural daylight), LED-B5 (phosphor-type LED #5), and FL-15 (fluorescent type 15) [37]. As a final step, we applied an achromatic texture to present the obtained colours on the swatches (Figure 6.3 (bottom)).

The swatches shown in Figure 6.3 (bottom) were generated using the multiplication process outlined in Section 6.5. Those in the top row were obtained using only three sample wavelengths (455, 551 and 608 $\mathrm{nm}$), which correspond to the chromaticity coordinates of standard Society of Motion Picture and Television Engineers (SMPTE) monitors [14]. The swatches in the bottom row depict the same snow samples generated using 31 sample wavelengths. It can be observed that there is a noticeable difference between the swatches obtained using tristimulus values and those obtained using 31 samples taken across the visible spectrum.

By visually inspecting the swatches shown in Figure 6.3 (bottom), it can also be noted that the choice of illuminant can have a significant impact on the depicted colourations. Nonetheless, examining the swatches generated using a flat, equal energy light source (illuminant E), one can verify that the colourations are still largely dependent on the transmittance values.

It is worth noting that, depending on the spectral characteristics of a given illuminant, it may be possible to employ less than 31 equally-spaced spectral samples and still maintain the visual fidelity of the generated swatches. However, in order to determine the ideal number and location of spectral samples for a given illuminant, one may need to employ a perceptually-based approach similar to that proposed by Kravchenko *et al.* [123].

## 6.7 Reproducibility and Dissemination

We have made the SPLITSnow model available for online use (both spectrometric [146] and goniometric [145] versions) to enable the reproduction [168] and extension of the *in silico* experiments described in this thesis. Its deployment was carried out using a model distribution framework [6] designed for this purpose. Both graphical and numerical results are returned *via* email to the user for subsequent analysis. In addition, we have also provided online access to the supporting data (complex indices of refraction, *etc.*) used in our investigation [147].

The default values assigned to the snow parameter values depicted on the model's web page (Figure 6.4) correspond to the representative sample, *i.e.*, the values used to make comparisons with Sample 3 provided by Dumont *et al.* [54]. However, a variety of reasonable values are permitted for the parameters for the assessment of different phenomenological observations.

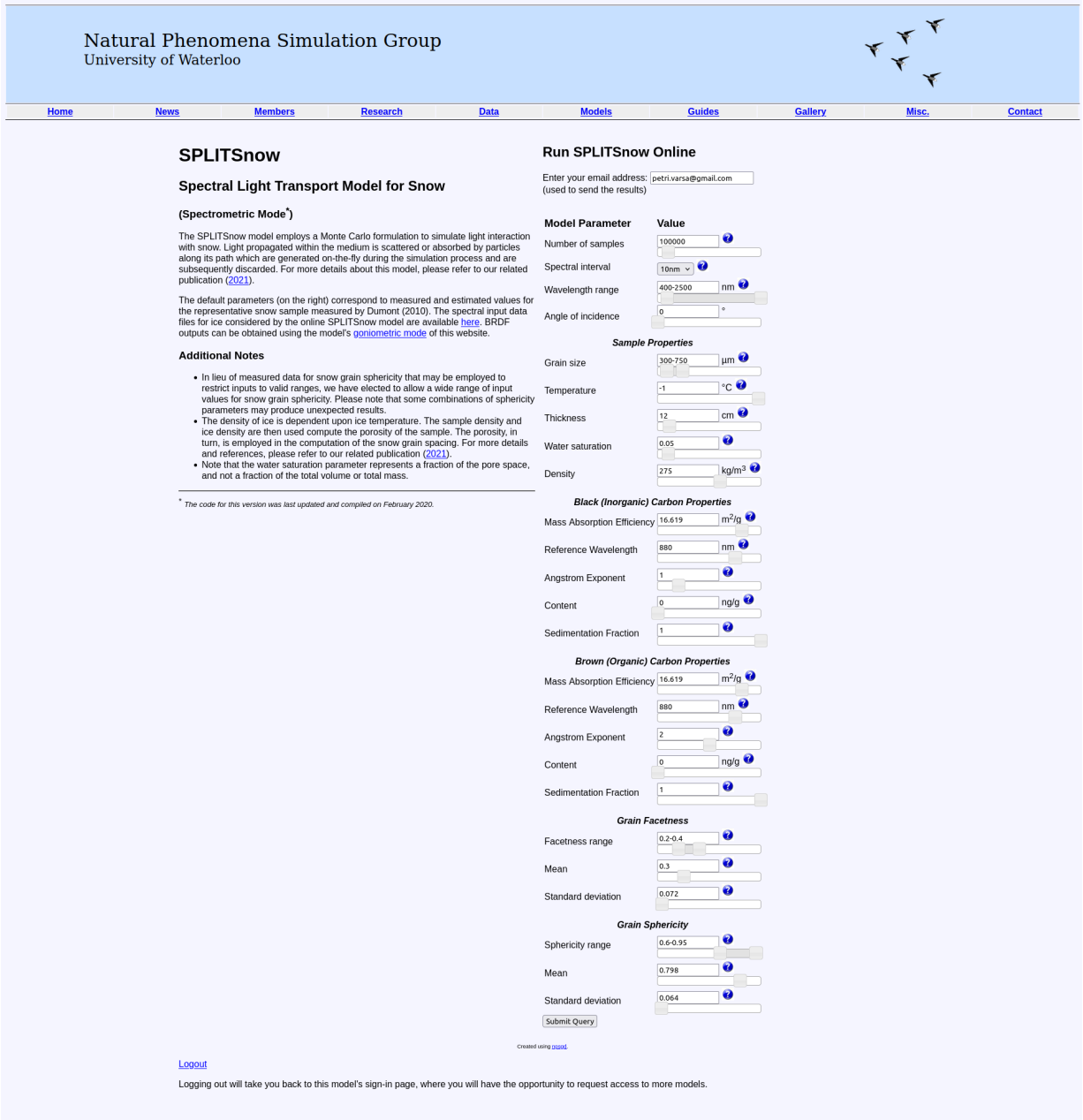


Figure 6.4: Screenshot of a user interface (UI) deployed to enable the use of SPLITSnow model (Chapter 4) in simulations of light interactions with snow samples that may contain impurities.

Note that Figure 6.4 depicts the UI for the spectrometric mode of the SPLITSnow model. The UI for this mode of the model was selected for clarity since the main snow characterization parameters are present. Other modes of the model formulation are also available for online use upon request. These include the spectrometric modes that facilitate both heterogeneous and multi-layer use cases, as well as the goniometric mode. The heterogeneous spectrometric mode [148] allows for up to three grain types to be specified within a snow sample, whereas the multi-layer spectrometric mode [149] allows for snow samples consisting of up to four layers. Finally, the goniometric mode [145] allows for experiments to be conducted with spatially distributed values.

# Chapter 7

# Spectrometric and Goniometric Results

In this chapter, we compare the simulated results generated by the proposed SPLITSnow model with measured data provided by Dumont *et al.* [54], Salvatori *et al.* [190] and Perovich [169]. As outlined in Chapter 6, we also present the results of our *in silico* experiments that make comparisons to spectrometric reflectance and transmittance trends and evaluate these against observed trends that have been previously reported in the literature. We then provide our *in silico* experimental simulation results that make predictions of goniometric trends and compare these against the measured responses reported in the literature. Finally, we present an example use case of the proposed framework where we make comparisons between modelled data and data that has been acquired remotely.

## 7.1 Quantitative Spectrometric Comparisons

Figure 7.1 presents a graph depicting a comparison of model predictions with measured data provided by Dumont *et al.* [54] (for their Sample 3) considering an angle of incidence of 0°. A detailed characterization of the snow grain size for the sample was not provided by Dumont *et al.* [54] along with their measured data. However, in their own comparisons to previous models, they used average grain sizes ranging from 100–1000 $\mu\mathrm{m}$, and stated that their own "grain size measurements are too rough to be suitable as inputs." Furthermore, based on the description of their samples, it has been inferred that the measured sample's grains are within this range.

As it can be observed in Figure 7.1, a close agreement has been achieved for reflectance throughout the entire measured spectrum (400–2500 $\mathrm{nm}$). The computed RMSE between the

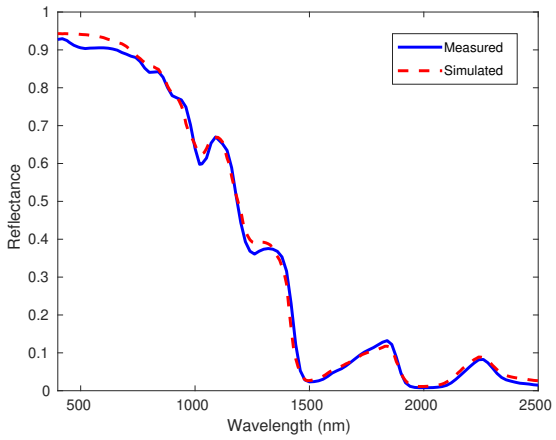


Figure 7.1: Comparison of measured and simulated directional-hemispherical reflectance curves. The measured curve was provided by Dumont *et al.* [54] (for their Sample 3). The simulated curve was obtained using the SPLITSnow model and the parameter data values provided in Table 7.1.

two curves is 0.0177. It has been noted by Jacquemoud *et al.* [98], that RMSE values below 0.03 indicate good spectrum reconstruction, notably for remote sensing applications. In addition, note that prominent maxima are aligned. In particular, alignment is observed at the 1030 $\mathrm{nm}$ maxima. This suggests that the fraction of the pore space occupied by water that was used in the simulation (0.05) is consistent [74] with the residual water in their Sample 3.

The model parameter values employed to obtain these results are presented in Table 7.1. Values in the top portion of the table represent those that were explored experimentally to achieve the closest congruence with measured data. Values in the lower section of the table were directly stated by Dumont *et al.* [54]. A summary of how these values were selected is presented in Appendix D. However, some aspects of the process are provided here for illustrative purposes.

As described in Chapter 4, facetness is a unitless parameter that is used to model the fine details of the grains' rough surface. The description of the sample provided by Dumont *et al.* [54] indicates that it consisted of "rounded grains and mixed forms." Based on this description, the exploration of the parameter space focused on rounded grains. Best results were obtained using a normal probability distribution with a mean facetness of 0.3 and a standard deviation of 0.072. These values produce mostly smooth grains with some facets in the SPLITSnow formulation.

The differences between the measured and simulated curves are more pronounced in the 400–800 $\mathrm{nm}$ region of the spectrum. There is a number of possible explanations for these differences. First, relatively small amounts of impurities, as low 1 part per million, can reduce

| Parameter | Value | Units |
|---|---|---|
| Particle size minimum | 300 | [μm] |
| Particle size maximum | 750 | [μm] |
| Water saturation | 0.05 | |
| Facetness minimum | 0.2 | |
| Facetness maximum | 0.4 | |
| Facetness mean | 0.3 | |
| Facetness standard deviation | 0.072 | |
| Sphericity minimum | 0.6 | |
| Sphericity maximum | 0.95 | |
| Sphericity mean | 0.798 | |
| Sphericity standard deviation | 0.064 | |
| Density | 0.275 | $[\mathrm{g\,cm^{-3}}]$ |
| Temperature | -1 | [°C] |
| Sample thickness | 12 | [cm] |
| Polar incidence angle | 0° | |
| Wavelength range | 400–2500 | [nm] |

Table 7.1: SPLITSnow parameter values employed in the characterization of the representative snow sample considered in the *in silico* experiment to generate the reflectance curves depicted in Figure 7.1. Values used in the upper section were found through parameter exploration. Values in the lower section correspond to the snow sample used in the actual experiments [54].

hemispherical reflectance by 5–15% [232]. Although Dumont *et al.* [54] stated that their sample was taken from a relatively isolated location, they did not rule out the presence of contaminants from nearby sources (*e.g.*, vehicular traffic) or deposited from atmospheric air currents, that could have affected the measurement results. Second, we remark that in the absence of precise information, the values assigned to a number of the sample characterization parameters correspond to average data provided in the literature.

We remark that Dumont *et al.* used a 16.5 $\mathrm{cm}$ thick sample to estimate the bottom losses in the description of their methodology [54], which they found to be less than $1\%$ at the 630 $\mathrm{nm}$ wavelength. However, their experiments were conducted using samples that were only 12 $\mathrm{cm}$ thick. Simulated results obtained using the SPLITSnow model also indicate that approximately $1\%$ of EM radiation is transmitted at the 630 $\mathrm{nm}$ wavelength for a 16.5 $\mathrm{cm}$ thick sample. However, the bottom losses are $2\%$ for the same virtual sample that is only 12 $\mathrm{cm}$ thick.

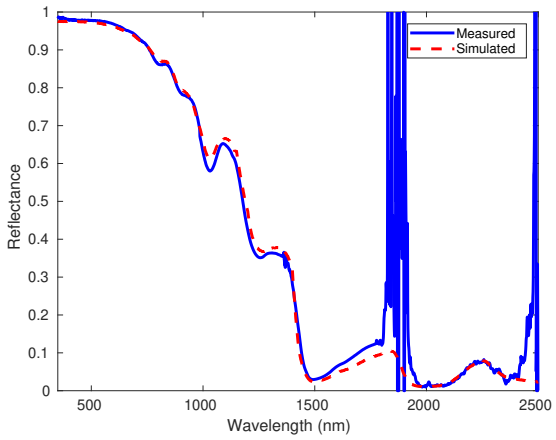


Figure 7.2: Comparison of measured and simulated directional-hemispherical reflectance curves. The measured curve corresponds to SISpec Sample 195 [190]. The simulated curve was obtained using the SPLITSnow model and the parameter data values provided in Table 7.2.

In addition to the experiment involving the representative sample, we also conducted an experiment to match a spectral dataset provided in the SISpec database [190]. Besides providing spectral data in the visible ($\approx$ 400–780 $\mathrm{nm}$) and the IR ($\approx$ 780–2500 $\mathrm{nm}$), this dataset also includes spectral measurements in the UV ($\approx$ 350–400 $\mathrm{nm}$). Figure 7.2 presents the reflectance dataset from the SISpec database [190] (SISpec Sample 195) along with reflectance values produced by simulation. The parameter values used to produce the simulation curve are presented in Table 7.2 and Table 7.3 provides numerical comparison data between the measured values and the values produced by simulation. The RMSE values were computed for the UV-A ($\approx$ 350–400 $\mathrm{nm}$), visible ($\approx$ 400–780 $\mathrm{nm}$) and IR-A ($\approx$ 780–1400 $\mathrm{nm}$). The RMSE error values are below the target value of 0.03 [98] as discussed above. Note that due to the noise in the measured data (possibly from atmospheric water vapour [65, 86]), the total RMSE excludes wavelengths between 1750 $\mathrm{nm}$ and 2000 $\mathrm{nm}$ and wavelengths greater than 2350 $\mathrm{nm}$. Excluding these values the RMSE is 0.016, which indicates a good agreement between the two curves [98].

We remark that the results presented in Figure 7.2 demonstrate an improved agreement in the visible range ($\approx$ 400–780 $\mathrm{nm}$) of the EM spectrum, when compared to Figure 7.1. Whereas the measured dataset presented in Figure 7.1 was collected in continental Europe [54], the SISpec dataset presented in Figure 7.2 was collected at high latitudes in the Arctic on the Svalbard archipelago, where the samples were less susceptible to the presence of impurities.

Although the measured dataset presented in Figure 7.1 was collected by Dumont *et al.* [54] in a relatively remote region of the French Alps (Col de Porte), amenities and roads do sur-

| Parameter | Value | Units |
|---|---|---|
| Particle size minimum | 150 | [μm] |
| Particle size maximum | 800 | [μm] |
| Water saturation | 0 | |
| Facetness minimum | 0.1 | |
| Facetness maximum | 0.4 | |
| Facetness mean | 0.25 | |
| Facetness standard deviation | 0.1 | |
| Sphericity minimum | 0.9 | |
| Sphericity maximum | 0.97 | |
| Sphericity mean | 0.935 | |
| Sphericity standard deviation | 0.05 | |
| Density | 340 | [$\mathrm{kg\,m^{-3}}$] |
| Temperature | -3 | [°C] |
| Sample thickness | 10 | [cm] |

Table 7.2: SPLITSnow parameter values employed in the characterization of the snow sample considered in the *in silico* experiments resulting in the simulated reflectance curve depicted in Figure 7.2. The angle of incidence is 0° and the wavelength range is 350–2500 nm.

| Spectral Domain | Value |
|---|---|
| UV-A | 0.009 |
| Visible | 0.005 |
| IR-A | 0.021 |
| Total | 0.016 |

Table 7.3: RMSE values comparing the measured [190] and simulated curves in Figure 7.2 for various spectral ranges. Namely, the UV-A (≈ 350–400 nm), visible (≈ 400–780 nm), IR-A (≈ 780–1400) and total (350–2500 nm). Note that the RMSE calculation for Sample 195 excludes the noise (possibly from atmospheric water vapour [65, 86]) observed in the measured data, for wavelengths near 1800 nm and 2400 nm.

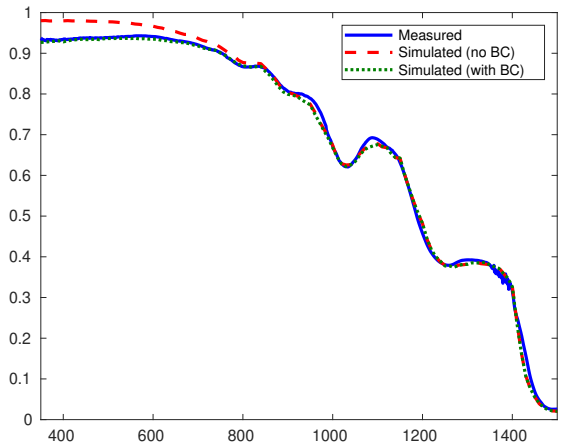


Figure 7.3: Comparison of measured and simulated directional-hemispherical reflectance curves. The blue solid curve represents the measured data (SISpec Sample 197 [190]). The red dashed curve was produced using the SPLITSnow model and did not account for any impurities. The green dotted curve was produced using the SPLITSnow model but *did* account for black carbon impurities. Both simulated curves used the parameter data values provided in Table 7.4.

round the region. Furthermore, no attempt was made to quantify the impurities that may have been present in their sample. As stated previously, even trace amounts of impurities may have a dramatic effect on snow reflectance [232], and the effect is mostly in the visible domain [190, 228, 229].

Pursuant to this, we present experimental results that account for the presence of impurities in snow as described in Section 4.6. This experiment presents a comparison to measured reflectance values provided by Salvatori *et al.* [190]. To begin, we conducted an exploration of the characterization parameter space employed by the SPLITSnow formulation with the intention of finding parameter values that would yield close agreement between the measured reflectance curve associated with SISpec Sample 197 and the resulting modelled curve. (See Appendix D for details regarding the parameter selection process.) These parameter values are presented in Table 7.4, and the results are presented in Figure 7.3. They show that the modelled reflectance values in the visible domain ($\approx$ 400-700 $\mathrm{nm}$) were noticeably higher. We found that the addition of a small quantity of black (inorganic) carbon (6 $\mathrm{ng\,g^{-1}}$) was sufficient to lower the reflectance in this domain and yield a closer agreement.

In Figure 7.3, the blue solid curve represents the measured data provided in the SISpec database for Sample 197 [190]. The red dashed curve was produced using the SPLITSnow model and the characterization parameter values in Table 7.4, except that no impurities were included.

| Parameter | Value | Units |
|---|---|---|
| Particle size minimum | 400 | [μm] |
| Particle size maximum | 1000 | [μm] |
| Water saturation | 0 | |
| Facetness minimum | 0.2 | |
| Facetness maximum | 0.4 | |
| Facetness mean | 0.3 | |
| Facetness standard deviation | 0.1 | |
| Sphericity minimum | 0.6 | |
| Sphericity maximum | 0.95 | |
| Sphericity mean | 0.8 | |
| Sphericity standard deviation | 0.07 | |
| Density | 300 | $[\mathrm{kg\,m^{-3}}]$ |
| Temperature | -1 | $[^{\circ}\mathrm{C}]$ |
| Sample thickness | 19 | [cm] |
| Polar incidence angle | 0° | |
| Wavelength range | 350–1500 | [nm] |
| Mass Absorption Efficiency | 16.619 | $[\mathrm{m^2\,g^{-1}}]$ |
| Reference Wavelength | 880 | [nm] |
| Angstrom Exponent | 1 | |
| Content | 6 | $[\mathrm{ng\,g^{-1}}]$ |
| Sedimentation Fraction | 1.0 | |

Table 7.4: SPLITSnow parameter values employed in the characterization of the snow sample considered in the *in silico* experiment to produce Figure 7.3. Values used in the upper section were determined by examining the profile diagram associated with the measured data, and by conducting a parameter space search, as discussed in Section 7.1. Values in the lower section correspond to those used for black (inorganic) carbon [103, 178, 179].

The green dotted curve was also obtained using the SPLITSnow model and the parameter values in Table 7.4 *with* black carbon impurities included in the virtual snow sample. We remark that the addition of black carbon primarily affects values in the visible domain ($\approx$ 400–700 nm), while the impurities' impact on the spectral response in the IR domain ($\approx$ 700–1500 nm) is significantly lower. These results are consistent with those discussed in Section 4.6. Namely, that impurities primarily affect the visible wavelengths of EM spectrum [190], whereas the size and shape of the snow grain have a greater affect in the IR wavelengths [50].

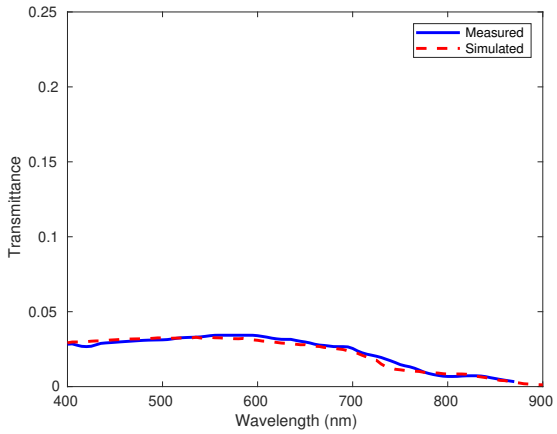


Figure 7.4: Comparison of measured and simulated directional-hemispherical transmittance curves. The measured curve corresponds to transmittance values measured by Perovich [169] for a wet snow sample. The simulated curve was obtained using the SPLITSnow model and the parameter data values are provided in Table 7.5.

In Table 7.4, the parameter values in the upper portion of the table correspond to the SPLITSnow parameters used for pure snow. We note that these parameter values are based on those provided in the description of the measured snow sample [190]. The parameter values in the lower half of the table correspond to those used for black (inorganic) carbon [103, 178, 179]. A quantity of 6 $\mathrm{ng\,g^{-1}}$ (or 6 parts per billion by mass[1]) was sufficient to reduce the reflectance in the UV ($\approx$ 350–400 $\mathrm{nm}$) and visible ($\approx$ 400–700 $\mathrm{nm}$) domains. For this experiment, we made the assumption that the black carbon existed as sedimentation. We computed the RMSE between the two curves representing the measured values for Sample 197 and the simulated results using the parameter values including black carbon. The calculated value, 0.011, indicates a good agreement [98].

To assess the ability of the proposed model to predictively reproduce spectral transmittance values of light permeating through snow, we now present the results of an experiment that makes comparisons to measured data provided by Perovich [169]. More specifically, we compare simulation results against the transmittance data acquired by Perovich in 1996 on January 18$^{\mathrm{th}}$, which we refer to as *P18*. (See their Figure 7(b).) On this date, the snow sample measured by Perovich was 11 $\mathrm{cm}$ thick and consisted of rounded grains measuring 500–1000 $\mu\mathrm{m}$ in diameter. The density varied throughout the sample between 300 $\mathrm{kg\,m^{-3}}$ and 439 $\mathrm{kg\,m^{-3}}$, and the sample was described as being "saturated." Lastly, Sample P18 was measured near Hanover, NH, USA, where there were "probably more contaminants in the snowpack than in the isolated polar re-

[1]We remark that 6 $\mathrm{ng\,g^{-1}}$ is within the reported ranges employed for impurities found in snow [228].

| Parameter | Value | Units |
|---|---|---|
| Particle size minimum | 500 | [μm] |
| Particle size maximum | 1000 | [μm] |
| Water saturation | 0.18 | |
| Facetness minimum | 0.1 | |
| Facetness maximum | 0.3 | |
| Facetness mean | 0.2 | |
| Facetness standard deviation | 0.1 | |
| Sphericity minimum | 0.7 | |
| Sphericity maximum | 0.95 | |
| Sphericity mean | 0.85 | |
| Sphericity standard deviation | 0.1 | |
| Density | 300 | $[\mathrm{kg\,m^{-3}}]$ |
| Temperature | -1 | $[^\circ\mathrm{C}]$ |
| Sample thickness | 11 | [cm] |
| Polar incidence angle | 0° | |
| Wavelength range | 400–900 | [nm] |
| Mass Absorption Efficiency | 16.619 | $[\mathrm{m^2\,g^{-1}}]$ |
| Reference Wavelength | 880 | [nm] |
| Angstrom Exponent | 1 | |
| Content | 5 | $[\mathrm{ng\,g^{-1}}]$ |
| Sedimentation Fraction | 0.5 | |

Table 7.5: SPLITSnow parameter values employed in the characterization of the snow sample considered in the *in silico* experiment to produce Figure 7.4.

gions," and their own findings suggested the "presence of contaminants in the snow" [169]. The results of this experiment are presented in Figure 7.4 and the parameter values used to produce the simulation results are provided in Table 7.5.

In Figure 7.4, the blue solid curve represents the transmittance values measured by Perovich [169] for a wet snow sample. The red dashed curve was produced using the SPLITSnow model. The RMSE between the two curves was computed to be 0.002. To obtain the of parameter values employed to produce the simulated curve, we used the specific values provided by Perovich [169] in his description of the sample, namely grain size and sample thickness. We then conducted a search of the parameter space to obtain a match, employing other sample characterization information provided by Perovich as starting points. More details about the

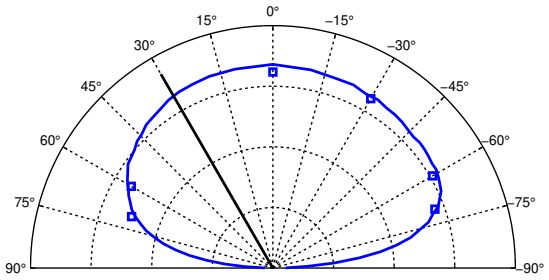


Figure 7.5: Comparison of measured [54] data points and a simulated BRDF curve through the principal plane. A wavelength of 600 $\mathrm{nm}$ and an angle of incidence of 30° were employed to allow for comparisons between the simulated curve (blue solid line) and the data points (blue squares) provided by Dumont *et al.* [54]. The remaining parameter values are provided in Table 7.1. The direction of incidence for both measured and simulated data is indicated as a black solid (straight) line.

selection of parameter values for the sample considered in this experiment can be found in Appendix D.

To conclude this section we make a direct comparison to a dataset that includes spatially varying reflectance values. For this, we return to the dataset provided by Dumont *et al.* [54]. The results are presented in Figure 7.5. This figure presents both a simulated BRDF plot through the principal plane[2] (blue curve) and measured values provided by Dumont *et al.* [54] (blue squares) with respect to their Sample 3, which is the same sample used as a basis of the representative sample. The angle of incidence (30°, black straight line) is the same for both measured and simulated values. Due to the mechanical nature of the apparatus [35] employed to conduct the measurements, the value at 30° could not be measured [54]. However, we remark that the simulated values adhere to the measured values obtained by Dumont *et al.* [54].

## 7.2 Qualitative Spectrometric Comparisons

In this section, we focus on phenomenological trends that have been described in the literature and assess how the model proposed in Chapter 4 can reproduce them when input parameters are varied. First, we examine spectrometric reflectance trends, then spectrometric transmittance trends and finally goniometric (BRDF) trends.

[2]The principal plane is a slice through a 3D dataset that includes the illumination source and the normal to the surface.

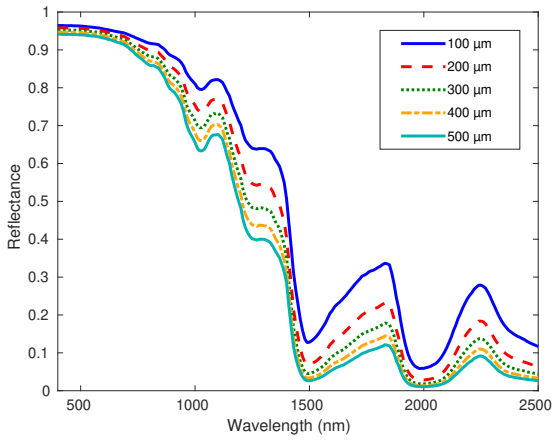


Figure 7.6: Simulated directional-hemispherical reflectance curves computed using the SPLITSnow model considering various sizes of snow grains (100–500 µm) and an angle of incidence of 0°. The remaining sample characterization parameter values are provided in Table 7.1.

### 7.2.1 Reflectance Trends

In this section, we present the results of our *in silico* experiments that examine the spectral distribution of EM radiation that is reflected in the upper hemisphere above the surface of a virtual snow sample. Unless otherwise stated, all parameter values correspond to those depicted in Table 7.1, which correspond to the representative sample, except for the independent variable under test.

The first experiment addressed the effect of grain size on reflectance. Figure 7.6 shows the results. Reflectance was computed for four different mean grain sizes. The reported mean grain sizes are all chosen to be the centre of a uniform distribution within a range of $\pm 50$ µm. As reported in the literature [28, 144], reflectance decreases as grain size increases. This behaviour is observed in the modelled curves presented in Figure 7.6. Sensitivity to grain size is the lowest in the visible domain, and prominent in the 700–1300 nm band as expected [156]. Furthermore, the effect of the absorptance minima of ice [230] at 1800 nm and 2250 nm can also be observed in the modelled curves depicted in Figure 7.6.

The second experiment addressed the effect of facetness on reflectance. We remark that precipitated snow will undergo a morphological process that erodes the facets and leaves smooth grains [41]. In the SPLITSnow formulation, a low facetness represents a grain whose surface has few crystalline features, with a facetness of zero yielding a perfectly smooth grain. A high facetness characterizes a grain whose surface has many fine details. Figure 7.7 demonstrates

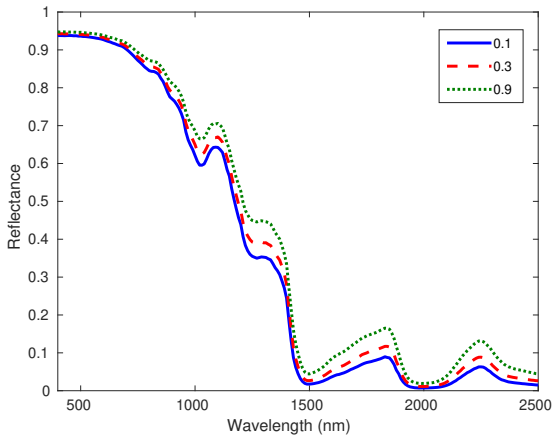


Figure 7.7: Simulated directional-hemispherical reflectance curves computed using the SPLITSnow model considering various degrees of facetness (0.1–0.9) and an angle of incidence of 0°. The remaining parameter values are provided in Table 7.1.

the effect of facetness on reflectance. This experiment shows that an increase in facetness will increase the total reflectance. Note that the 700–1300 $\mathrm{nm}$ band that is affected by grain size [157] is also affected by the microstructure of the grains. The 1800 $\mathrm{nm}$ and 2250 $\mathrm{nm}$ peaks exhibited in the infrared are similarly affected. These trends demonstrate the importance of accounting for grain facets in the formulation of a model for snow reflectance. In particular, any attempt to estimate grain size from reflectance (*e.g.*, [157]) can be improved by also examining the effect of facetness at these peaks.

Our third experiment investigates the effect of density on reflectance. Reflectance is known to be weakly dependent upon snowpack density when the thickness is effectively semi-infinite. Bohren and Beschta [29] observed a reflectance variation of less than 1% after compaction in the 350–2800 $\mathrm{nm}$ range. Our *in silico* spectrometric reflectance experiment reproduces this result. Using the parameters from Table 7.1 with the minimum (300 $\mathrm{kg\,m^{-3}}$) and maximum (450 $\mathrm{kg\,m^{-3}}$) densities reported in their study, the difference between the two reflectance curves are presented in Figure 7.8. The RMSE is less than 0.007 and the mean percent difference is 2.0%, which is similar in magnitude to the experimental results obtained by Bohren and Beschta [29].

As discussed in Section 4.4, the SPLITSnow framework supports snowpacks consisting of multiple layers. It has been documented in the literature that the surface layer of a snowpack heavily influences the spectrometric distribution of light [190]. To this extent, often only the surface layer is reported in the characterization of snow samples [191]. Figure 7.9 demonstrates this trend. The solid blue curve was produced using the SPLITSnow framework and a single layer of snow that is composed of large, smooth, highly spherical snow grains. (See Table 7.6.)

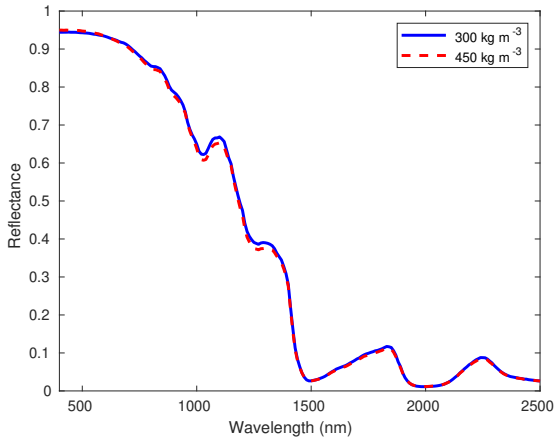


Figure 7.8: Simulated directional-hemispherical reflectance curves computed using the SPLITSnow model considering two different densities (300 and 450 $\mathrm{kg\,m^{-3}}$) and an angle of incidence of 0°. The remaining parameter values are provided in Table 7.1.

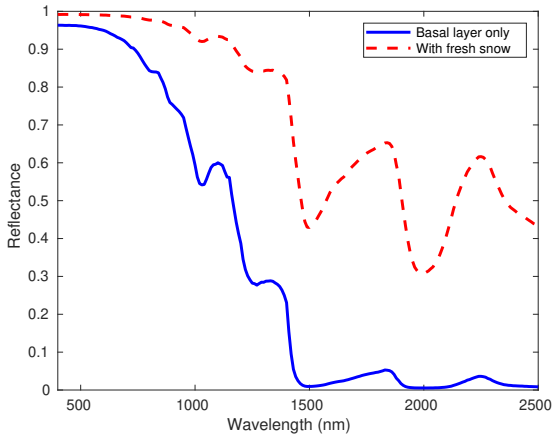


Figure 7.9: Simulated directional-hemispherical reflectance curves computed using the SPLITSnow model for virtual snowpacks formed by one (basal layer only) and two (basal layer covered by a fresh snow layer) snow layers. The blue solid curve corresponds to the single-layered snowpack consisting of large, smooth snow grains with a spherical shape that is 15 $\mathrm{cm}$ thick. The red dashed curve corresponds to the two layered sample with a 1 $\mathrm{cm}$ layer of small, faceted and elongated snow grains placed on top of the same basal layer. Parameter values employed to generate the curves depicted in this figure are presented in Table 7.6.

| Parameter | Basal Layer | Surface Layer | Units |
|---|---|---|---|
| Particle size minimum | 900 | 10 | $[\mu\mathrm{m}]$ |
| Particle size maximum | 1000 | 100 | $[\mu\mathrm{m}]$ |
| Water saturation | 0 | 0 | |
| Facetness minimum | 0.05 | 0.8 | |
| Facetness maximum | 0.15 | 0.99 | |
| Facetness mean | 0.1 | 0.9 | |
| Facetness standard deviation | 0.075 | 0.5 | |
| Sphericity minimum | 0.6 | 0.3 | |
| Sphericity maximum | 0.95 | 0.9 | |
| Sphericity mean | 0.798 | 0.5 | |
| Sphericity standard deviation | 0.072 | 0.15 | |
| Density | 375 | 225 | $[\mathrm{kg\,m^{-3}}]$ |
| Temperature | -5 | -5 | $[^{\circ}\mathrm{C}]$ |
| Layer thickness | 15 | 1 | $[\mathrm{cm}]$ |
| Polar incidence angle | $0^{\circ}$ | $0^{\circ}$ | |
| Wavelength range | 400–2500 | 400–2500 | $[\mathrm{nm}]$ |

Table 7.6: SPLITSnow parameter values employed in the characterization of the snow sample considered in the *in silico* experiment to generate the reflectance curves depicted in Figure 7.9. Values in the basal layer column were used to produce the single layer sample represented by the blue solid curve. Both layers were used to produce the red dashed curve.

This basal layer of snow is 15 $\mathrm{cm}$ thick. The dashed red curve in Figure 7.9 was produced considering the same basal layer of snow covered by a thin, 1 $\mathrm{cm}$ thick layer of snow. This surface layer consists of small, faceted, elongated snow grains.

Observe that although the overall qualitative trends between the two curves in Figure 7.9 are maintained, the magnitude of the reflectance and the relative magnitude of the peaks have been dramatically altered by the addition of the a thin layer of faceted snow crystals. Although the total thickness of the sample has been increased by 1 $\mathrm{cm}$ with the addition of the surface layer, this does not account for the changes in reflectance. As reported by Salvatori *et al.* [190], the grain characteristics of the top layer have a strong influence on the spectral distribution of reflected EM radiation.

Although many snow samples are homogeneous and can be characterized by a single snow grain type throughout the sample, some snow sample characterizations include multiple snow grain types throughout a single layer. (See Figure 4.6 and Section 4.5.) For such cases, it is common practice to characterize snow grains using "effective" properties [77] (*e.g.*, using optically-

equivalent grain size instead of actual grain size [60]). This is especially true with analytical modelling approaches (*e.g.*, see Kokhanovsky and Zege 2004 [121] and Picard *et al.* [173]). However, with disparate grain forms, it may be desirable to represent multiple types of snow grains within a single layer. The SPLITSnow formulation accounts for this aspect.

Figure 7.10 presents the results of simulation using three different snow samples. The characterization parameter values for the two types of snow grains used in these three samples are provided in Table 7.7. For all three snow samples, the density was set to 275 $\mathrm{kg\,m^{-3}}$, the saturation was set to 0.05 and the angle of incidence was $0^{\circ}$. The solid blue curve was produced using a virtual snow sample that employs exclusively large grains whose parameter values are provided in Table 7.7. The dotted green curve was produced using a virtual snow sample that employs exclusively small grains whose parameter values are provided in Table 7.7. Lastly, the dashed red curve was provided using an equal part by quantity of each of the two grain types.

To conclude this section, we present two experiments that account for the presence of impurities in snow as described in Section 4.6. We remark that, for black carbon, the Angstrom exponent is often set to a value of one [118, 160].[3] Furthermore, we note that a value of $16.6 \times 880 \approx 14625$ is commonly used for the computation of the Mass Absorption Efficiency (MAE) for black carbon (*e.g.* [71, 118, 165, 195, 197, 209]).[4] Consequently, we follow suit and use the values 16.619 $\mathrm{m^2\,g^{-1}}$ for the MAE, 880 $\mathrm{nm}$ for the reference wavelength, and 1 for the Angstrom exponent.

Our first experiment involving impurities attempts to reproduce the trend that as black carbon is added to the sample then reflectance decreases. Figure 7.11 demonstrates the results. As can be observed, when black carbon is added to pure snow, the reflectance decreases, primarily in the UV and visible ranges. This trend was reported by Wiscombe and Warren [235]. (See also Warren [228].) Their analytic model demonstrates qualitatively similar results when similar quantities of black carbon are added to a pure snow sample.

Our second experiment investigating impurities in snow examines brown carbon and the impact of variations in the Angstrom exponent. Recall from above, that we employed a value of one for the Angstrom exponent to produce Figures 7.3 and 7.11. Brown carbon, on the other hand, is characterized by having a higher Angstrom exponent [118]. Although Kirchstetter and Novakov [118] found that an Angstrom exponent of two is suitable for brown carbon produced

[3] Experimental results form Kirchstetter and Novakov [118] verify the suitability of this value. However, other values may sometimes be employed [34, 99, 197].

[4] According to the work of Ramachandran *et al.* [178, 179], the MAE for black carbon, $\mathscr{M}_{bc}$, and the reference wavelength, $\lambda_{bc}$, are usually set to 16.6 $\mathrm{m^2\,g^{-1}}$ and 880 $\mathrm{nm}$ when conducting studies involving this impurity. This is due to the fact that these values are used for calibrating the measurement equipment frequently used to conduct these field studies.

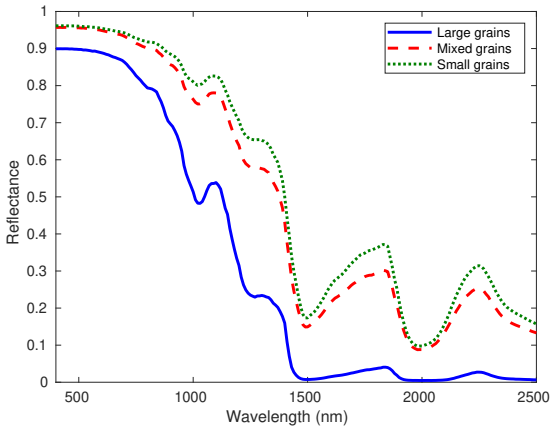


Figure 7.10: Simulated directional-hemispherical reflectance curves computed using the SPLITSnow model considering heterogeneous grain types. The blue solid curve was produced using large grains, the red dashed curve was produced using heterogeneous (mixed) grains and the green dotted curve was produced using small grains.

| Parameter | Large Grains | Small Grains | Units |
|---|---|---|---|
| Particle size minimum | 800 | 200 | [μm] |
| Particle size maximum | 1000 | 400 | [μm] |
| Facetness minimum | 0.01 | 0.7 | |
| Facetness maximum | 0.2 | 0.9 | |
| Facetness mean | 0.1 | 0.8 | |
| Facetness standard deviation | 0.05 | 0.5 | |
| Sphericity minimum | 0.8 | 0.3 | |
| Sphericity maximum | 0.99 | 0.7 | |
| Sphericity mean | 0.9 | 0.5 | |
| Sphericity standard deviation | 0.064 | 0.1 | |

Table 7.7: SPLITSnow parameter values employed in the characterization of the snow sample considered in the *in silico* experiment to generate the reflectance curves depicted in Figure 7.10.

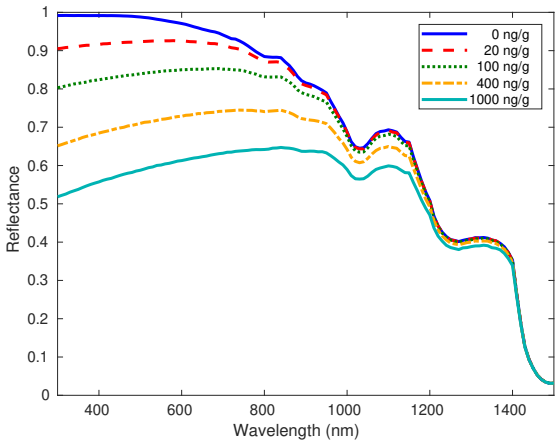


Figure 7.11: Simulated directional-hemispherical reflectance curves computed using the SPLITSnow model considering various quantities of black (inorganic) carbon. The MAE was set to 16.619 $\mathrm{m}^2\,\mathrm{g}^{-1}$, the reference wavelength was set to 880 $\mathrm{nm}$, the Angstrom exponent was set to 1 and the sedimentation fraction was set to 0.5. The incident angle, grain size and sample thickness were set to 60°, $1000 \pm 500$ $\mu\mathrm{m}$ and 50 $\mathrm{cm}$, respectively. The remaining parameter values are provided in Table 7.1.

by biomass burning, other values are also mentioned in the related literature [201]. The results of this experiment are presented in Figure 7.12.

The Angstrom exponent is varied from 1 (the value often associated with black carbon) to 2, (the value commonly used for brown carbon [118, 160]). Recall from Equation 4.13 that the Angstrom exponent is in the denominator of the equation and serves to reduce the effect of brown carbon on absorption. In other words, higher values of the Angstrom exponent are expected to increase the reflectance by reducing the absorption elicited by carbon-based material. All other characterization parameter values were the same as those used in the representative sample that are provided in Table 7.1.

### 7.2.2 Transmittance Trends

The presence of a thin layer of snow covering remote sensing targets can be sufficient to affect the detection and interpretation of their spectral signatures. Moreover, it can alter the photobiology of vegetation, and, thus, the sustainability of ecosystems, notably in high altitude and high latitude regions [18]. Hence, it is important to evaluate the predictive capabilities of the SPLITSnow model with respect to light transmitted through snow layers. This was carried out

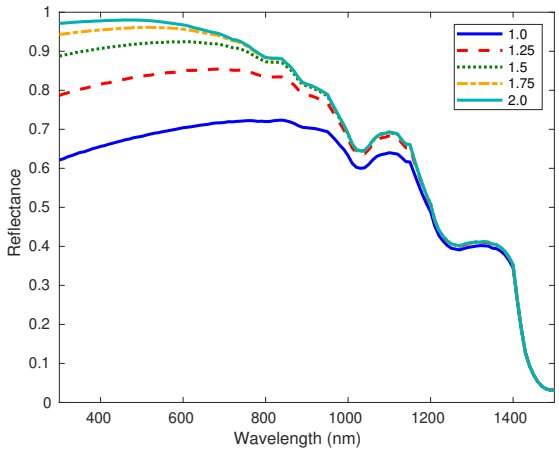


Figure 7.12: Simulated directional-hemispherical reflectance curves computed using the SPLITSnow model considering various values of the Angstrom exponent. 500 $\mathrm{ng\,g^{-1}}$ of brown (organic) carbon were employed to produce each curve. The MAE was set to 16.619, the reference wavelength was set to 880 and the sedimentation fraction was set to 0.5. The remaining parameter values are provided in Table 7.1.

through a series of *in silico* transmittance experiments, whose results we compared with field observations reported in the literature.

Since studies of snow transmittance are scarcer than those performed on reflectance, we performed comparisons of model predictions with qualitative trends reported for other granular materials, such as sand-textured soils, in the literature. There are known phenomenological similarities between sand-textured soils, made up of quartz crystals, and snow, made up of ice crystals, with respect to radiant transfer at wavelengths sufficiently shorter than the size of the grains [5].

Unless otherwise noted, the experiments described in this section employed the parameter values of the representative sample presented in Table 7.1. In all experiments, the sample thickness has been adjusted to 2 $\mathrm{cm}$, except where thickness is used as the independent variable. Note that the experiments in this section are restricted to the 400–1420 $\mathrm{nm}$ band since transmittance values at wavelengths higher than 1420 $\mathrm{nm}$ were all computed to be zero due to the strong absorptance of snow constituent materials, notably, ice and water, in the infrared domain.

In our first transmittance experiment, whose results are presented in Figure 7.13, we addressed the effect of sample thickness (snow depth) on transmittance. As described in the literature [5, 40, 45, 67, 169], when the sample thickness increases the transmittance decreases. Note

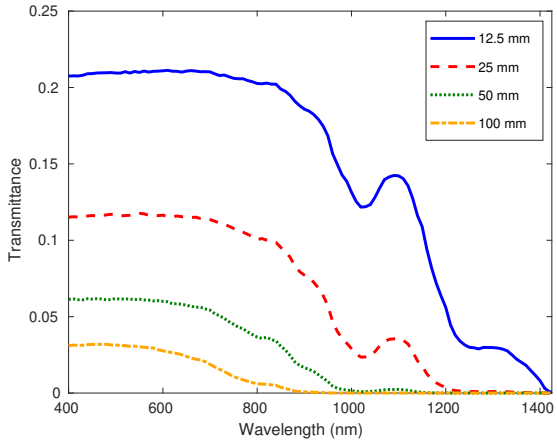


Figure 7.13: Simulated directional-hemispherical transmittance curves computed using the SPLITSnow model considering various sample thicknesses (12.5–100 $\mathrm{mm}$) and an angle of incidence of 0°. The remaining parameter values are provided in Table 7.1.

that the sample thickness is doubled from one experimental instance to the next and the corresponding transmittance curves are approximately halved in the visible range ($\approx$ 400–700 $\mathrm{nm}$). We remark that there is a low amount of absorptance of ice in this band (see Figure 6.2). However, where there are local maximum in absorptance, there is an even greater decrease in transmittance. For example, the absorption maximum at 1030 $\mathrm{nm}$ (Figure 6.2, orange dotted line) corresponds to the minima in the transmittance.

In our second transmittance experiment, whose results are presented in Figure 7.14, we addressed the effect of grain size on transmittance. As reported in the literature [5, 40, 45, 67, 169, 208], transmittance is correlated with grain size, *i.e.*, as the grain size increases the transmittance also increases. Larger grains, while being more absorptive, are also known to decrease the amount of scattering [40, 45, 67, 169]. The resulting effect is that the absorption-to-scattering ratio is increased, which increases the depth to which light penetrates into the material.

In our third transmittance experiment, whose results are presented in Figure 7.15, we addressed the effect of water content. We note that the addition of water to sand-textured soils is known to significantly affect the qualitative trends observed in their measured transmittance spectra [26, 40, 67, 169, 208, 211, 238]. For translucent sand-textured soils, both Woolley and Stoller [238] and Bliss and Smith [26] observed that as water saturation increases, transmittance also increases. However, for dark soils, they measured a decrease in transmittance as water saturation increased. This is explained by the increase in absorption [208]. These trends are both visible in our simulation results presented in Figure 7.15. In the visible spec-

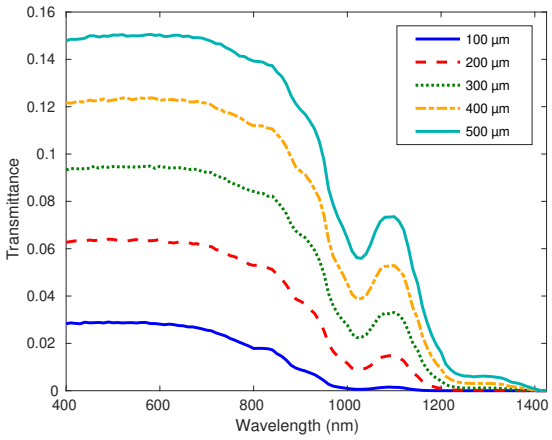


Figure 7.14: Simulated directional-hemispherical transmittance curves computed using the SPLITSnow model considering various sizes of snow grains (100–500 µm), an angle of incidence of 0° and a sample thickness of 2 cm. The remaining parameter values are provided in Table 7.1.

trum (≈ 400–700 nm), ice grains are translucent and transmittance increases as saturation is increased, which corresponds to the trend reported by Woolley and Stoller [238] and Bliss and Smith [26] for translucent materials. However, in the 800–1450 nm band, where there is an increase in absorptance (see Figure 6.2), snow behaves like a "dark" material and the trend is reversed. This also agrees with the experimental observations reported by Woolley and Stoller [238] and Bliss and Smith [26] with respect to light transmission through particulate materials.

Our fourth transmittance experiment investigates the effect of density. For optically thin snowpack, density affects how light is transmitted to the underlying surface, which can affect estimates of snow cover in remote sensing applications [84]. Figure 7.16 depicts the results of the experiment. As the density increases, the transmittance decreases as expected for particulate materials [45, 67, 159, 169, 238]. An increase in density affects the light propagated through a snow deposit as it allows for more absorption and scattering events. The net impact of these effects is a reduction in transmittance.

It is commonly reported in the literature that, for snow, as density increases transmittance also increases (*e.g.*, [45, 182, 184, 189]). However, this is opposite to the trend showcased in Figure 7.16, and reported by Ollerhead [159] and Woolley and Stoller [238] for particulate materials. Incidentally, none of the aforementioned works carried actual controlled experiments on the independent effects of density changes on snowpack's transmittance, and instead cite previous works that describe this trend. To our understanding, the explanation for this apparent discrepancy lies on how the field observations were reported in the seminal work by

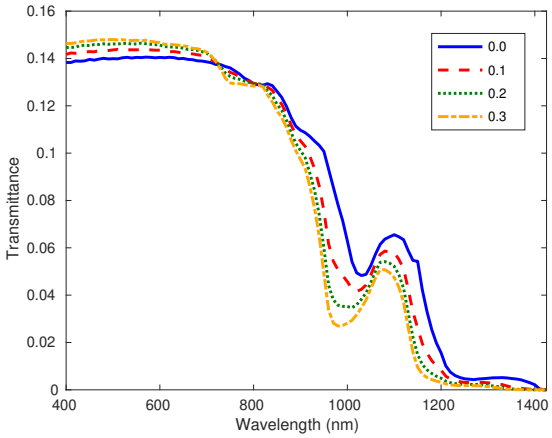


Figure 7.15: Simulated directional-hemispherical transmittance curves computed using the SPLITSnow model considering various values for water saturation (0–0.3), an angle of incidence of 0° and a sample thickness of 2 $\mathrm{cm}$. The remaining parameter values are provided in Table 7.1.

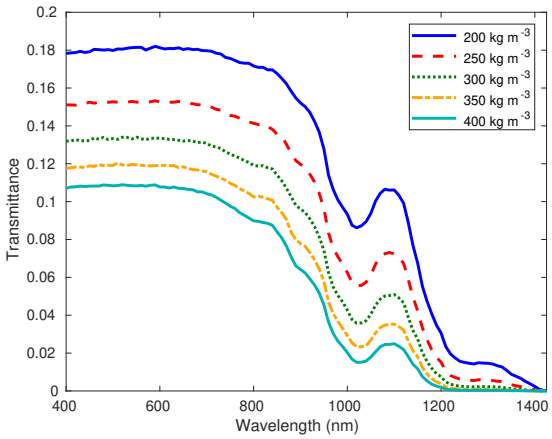


Figure 7.16: Simulated directional-hemispherical transmittance curves computed using the SPLITSnow model considering various densities (200–400 $\mathrm{kg\,m^{-3}}$), an angle of incidence of 0° and a sample thickness of 2 $\mathrm{cm}$. The remaining parameter values are provided in Table 7.1.

Gerdel in 1948 [67]. Since then, Gerdel's results have been interpreted and cited in those later publications.

For instance, as we underscored in a recent publication [18], Robson and Aphalo [184] stated that snow transmittance increases with increased density citing the work by Richardson and Salisbury [182], while Saarinen *et al.* [189] mentioned the same transmittance-density relationship citing the work of Curl *et al.* [45]. Richardson and Salisbury [182], in turn, cited the works by Curl *et al.* [45] and Gerdel [67] when they mention increases in light transmission through a snowpack following an increase in its density, while Curl *et al.* [45] themselves cited the work of Gerdel [67] when they made the same statement.

Upon a closer examination of Gerdel's field observations [67], a few elucidative aspects stand out. First, his measurements did not include spectral distributions. Instead, they corresponded to the total amount of radiance from 250–3000 $\mathrm{nm}$ penetrating the snowpack. Second, indeed Gerdel [67] initially mentioned that the amount of transmitted radiation increases with increased density. However, while describing his experiments in more detail, he also reported that the increase in density was accompanied by a substantial increase in grain size and, in some measurement instances, it was also accompanied by an increase in the percentage of free water (associated with the snowpack's water saturation level). In fact, Gerdel explicitly states that the "increase in density was accompanied by a distinct increase in the size of the snow crystals" [67]. More recently, Perovich [169] suggested that density might have been just a proxy for other snow characteristics, notably grain size, in previous investigations of its relationship with snow optical properties [18].

As discussed earlier, the change in snow grain size also has an effect on the light penetration, and by extension transmission, through snow. More precisely, an increase in grain size is associated with an increase in light transmittance, as illustrated in Figure 7.14. In our fifth transmittance experiment, we show how a concomitant increase in density and grain size can lead to a transmittance increase. The results of this experiment are presented in Figure 7.17, which depicts plots of two virtual snow samples with differing density and grain size values.

The blue solid curve in Figure 7.17 has a low density (200 $\mathrm{kg\,m^{-3}}$) and a low mean grain size (100 $\mu\mathrm{m}$). Whereas the red dashed curve has both higher values for density and grain size (400 $\mathrm{kg\,m^{-3}}$ and 500 $\mu\mathrm{m}$, respectively). All other parameter values are those provided in Table 7.1. As is evident in Figure 7.17, when the density is increased along with grain size (as reported by Gerdel [67]) then the transmittance increases.

Hence, as corroborated by our density related findings, presented in Figures 7.16 and 7.17, the effects of density on the snow transmittance may vary depending of whether or not it is accompanied by changes in the other key characteristics such as grain size. Later (in Chapter 9), we will also provide a visual demonstration of this effect.

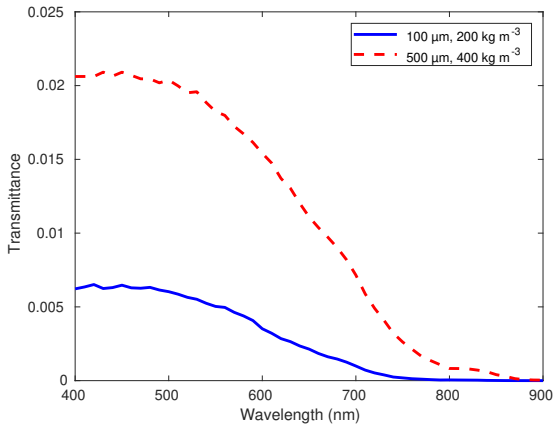


Figure 7.17: Simulated directional-hemispherical transmittance curves computed using the SPLITSnow model demonstrating the combined effect of density and grain size. The blue solid curve employs both a low value for the mean grain size (100 µm) and a low value for density (200 $\mathrm{kg\,m^{-3}}$). The red dashed curve employs both a high value for mean grain size (500 µm) and a high value for density (400 $\mathrm{kg\,m^{-3}}$). The remaining parameter values are provided in Table 7.1.

## 7.3 Goniometric Assessments

In this section, we compare goniometric simulated results with phenomenological traits observed in goniometric measurements reported in the literature. In addition to these comparisons, we also present the results of two *in silico* experiments on the effects of different grain characteristics on directional reflectance.

Figure 7.18 presents simulated BRDF plots obtained for the representative snow sample considering three (polar) angles of incidence. Each plot corresponds to reflectance values taken through the principal planes. In their field study, Hudson *et al.* [95] described two main features which are also reproduced by these simulated results. First, the reflectance values measured for reflection angles close to the zenith[5] were lower than those measured for reflection angles close to the horizon. Second, this phenomenon becomes more noticeable for larger angles of incidence. Both features can be observed in the plots depicted in Figure 7.18.

Figure 7.19 presents a simulated BRDF plot obtained considering a wavelength of 1800 $\mathrm{nm}$ and an angle of incidence of 69.3°. Notice that in addition to the features outlined above, a reduction in the reflectance values (represented by a concave shape) near the zenith can be

[5]The point directly above an observer, perpendicular to the surface.

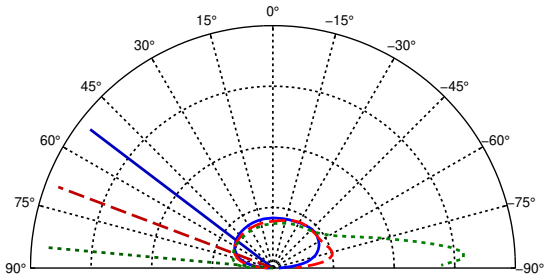


Figure 7.18: BRDF plot (through the principal plane) computed for the representative sample considering various angles of incidence and a wavelength of 600 $\mathrm{nm}$. The three angles of incidence, 52.8° (blue solid curve), 69.3° (red dashed curve) and 84.8° (green dotted curve), were employed to allow predictive comparisons with the results provided by Hudson *et al.* [95]. The snow thickness is set to 25 $\mathrm{cm}$. The remaining parameter values are provided in Table 7.1. The directions of incidence are indicated with matching (straight) lines.

observed. This distinct darkening feature is apparent in the measured data obtained by Hudson *et al.* [95] for the same wavelength and angle of incidence. Dumont *et al.* [54] also observed this feature in their measured data, which they deemed "nadir darkening."

Figure 7.20 presents simulated BRDF plots obtained considering the same angle of incidence (69.3°) and using two wavelengths (600 and 1800 $\mathrm{nm}$) associated with markedly distinct spectrometric reflectance values. The red dashed curve is reproduced from Figure 7.18, and the blue solid curve is reproduced from Figure 7.19. For illustrative purposes, both curves in Figure 7.20 are presented using the same scale. As it can be observed, the amount of directional variation is greater for wavelengths associated with relatively low spectrometric reflectance values as reported by Hudson *et al.* [95]. This trend is also consistent with observations made by Xiong *et al.* [242]. For 1800 $\mathrm{nm}$, they note that grain shape plays an important role in bidirectional reflectance modelling, and that models employing only spherical snow grains tend to overestimate the amount of scattering in the forward direction. For 600 $\mathrm{nm}$, where the total reflectance is greater, the angular dependence is weaker. However, as indicated by Xiong *et al.* [242], models employing nonspherical grains are able to reproduce the bidirectional reflectance pattern with greater fidelity. This effect of grain shape on directional reflectance aids in the characterization of snow surface scattering properties since snow tends to have a high reflectance in the forward direction when the angle of incidence is in the neighbourhood of 70° [49].

Besides the behaviours highlighted above, Dumont *et al.* [54] identified two other qualitative trends related to the polar angle of incidence. These trends can also be reproduced by the

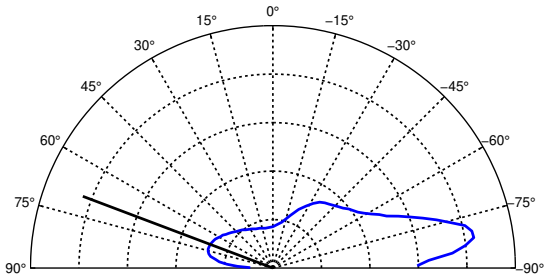


Figure 7.19: BRDF plot (through the principal plane) computed for the representative sample considering an angle of incidence of 69.3° and a wavelength of 1800 nm. These values were employed to allow qualitative comparisons with the data provided by Hudson *et al.* [95]. The snow thickness is set to 25 cm. The remaining parameter values are provided in Table 7.1. The direction of incidence is indicated with a black solid (straight) line.

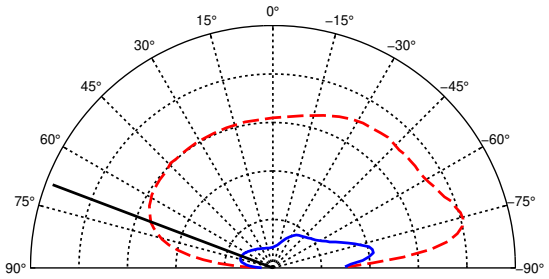


Figure 7.20: BRDF plots (through the principal plane) computed for the representative sample considering an angle of incidence of 69.3° and two wavelengths, namely 600 nm (red dashed curve), and 1800 nm (blue solid curve). These values were employed to allow qualitative comparisons with the data provided by Hudson *et al.* [95]. The snow thickness is set to 25 cm. The remaining parameter values are provided in Table 7.1. The direction of incidence is indicated with a black solid (straight) line.

SPLITSnow model as described next.

The first trend refers to a nearly Lambertian behaviour of snow reflectance for an angle of incidence of 0°. The blue solid curve in Figure 7.21 indicates that the proposed model can capture this behaviour.

The second additional trend noted by Dumont *et al.* [54] is that at an angle of incidence of 30°, the forward scattering peak becomes apparent. Similarly, the SPLITSnow model can also capture this behaviour as indicated by the red dashed curve in Figure 7.21. Dumont *et al.* [54] further remarked that, at an angle of incidence of 60°, the forward scattering peak is even more

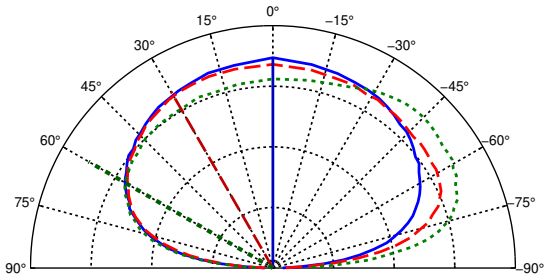


Figure 7.21: BRDF plots (through the principal plane) computed for the representative sample considering three angles of incidence and a wavelength of 600 $\mathrm{nm}$. The three angles of incidence, 0° (blue solid curve), 30° (red dashed curve), and 60° (green dotted curve) were employed to allow qualitative comparisons with the data provided by Dumont *et al.* [54]. The remaining parameter values are provided in Table 7.1. The directions of incidence are indicated with matching (straight) lines.

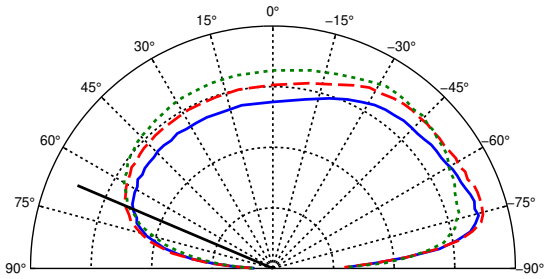


Figure 7.22: BRDF plots (through the principal plane) computed for the representative sample considering a (polar) angle of incidence of 67°, a wavelength of 600 $\mathrm{nm}$ and three grain sizes. The blue solid curve is associated with the presence of coarse-sized grains (1.5–3 $\mathrm{mm}$), the red dashed curve with the presence of middle-sized grains (as specified in Table 7.1), and the green dotted curve with the presence of fine-sized grains (0.03–0.3 $\mathrm{mm}$). The remaining parameter values are provided in Table 7.1. The direction of incidence is indicated with a black solid (straight) line.

pronounced. This is also reproduced by our simulation as demonstrated by the green dotted curve in Figure 7.21.

Apart from the trends outlined above, Dumont *et al.* [54] also noted that grain size has a measurable effect on directional reflectance. They observed that their maximum reflectance factor was higher for the samples that consisted of smaller grains. Warren *et al.* [231], in turn, indicated that this phenomenon is wavelength dependent, *i.e.*, when absorption is high and grain sizes are large, the opposite is to be expected. To determine whether the proposed model

can also account for these behaviours, we conducted *in silico* experiments in which we varied both the wavelength and the average grain size.

Figure 7.22 presents the results of the experiment that reproduces the behaviour reported by Dumont *et al.* [54] earlier above. In this experiment, we considered a wavelength of 600 $\mathrm{nm}$ and an angle of incidence of 67°. At 600 $\mathrm{nm}$ the extinction coefficients for both water and ice are low (see Figure 6.2). Note that the forward scattering peak with the smallest magnitude was elicited by the fine grained snow.

Figure 7.23 presents the results of the experiment involving the wavelength dependency observed by Warren *et al.* [231]. In this experiment, we considered a wavelength of 1450 $\mathrm{nm}$. We note that the extinction coefficient values for water and ice at this wavelength are higher than those at 600 $\mathrm{nm}$ (see Figure 6.2). The angle of incidence and the grain sizes are the same as those used to generate the results presented in Figure 7.22. As it can be verified in these results, the fine grained snow elicited the forward scattering peak with the greatest magnitude. Thus, the SPLITSnow model correctly reproduces the behaviour reported by Warren *et al.* [231].

Finally, we performed an experiment to investigate the effect of facetness on directional reflectance. *In situ* controlled experiments assessing this effect are not readily documented in the literature. However, anecdotal evidence exists to suggest that the quantity of facets should have an impact on directional reflectance [54]. Indeed, the results of our experiment, which are presented in Figure 7.24, indicate that samples whose grains are characterized by low facetness exhibit greater angular variation for their BRDF values than samples whose grains are characterized by high facetness. A more detailed treatment of this phenomenon is provided in Appendix F.

## 7.4 Comparison with Remotely Acquired Data

In this section, we illustrate how the proposed framework may be applied to remotely acquired data. We examined a dataset obtained from the Himalayan mountains as part of the NASA AVIRIS-NG mission [75, 86]. Figure 7.25 presents our comparison results.

In Figure 7.25(a), the selected area of observation is displayed using a portion of the "quick-look" image dataset, which is a version of the dataset that has been processed for viewing. The inset image is a 500% magnification of the region enclosed by the red square. No interpolation was used so that the original pixel values are preserved. The black square within the inset image demarcates the 25 pixels selected for analysis. We selected the pixels in this region due to their limited change in elevation, *i.e.*, the surface is level and the elevation gradient is small. In fact,

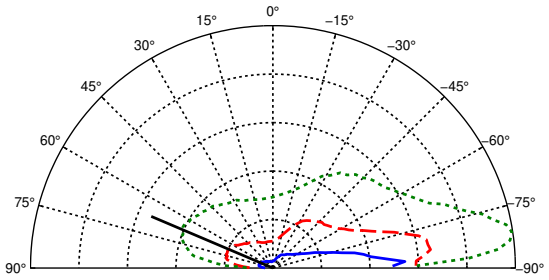


Figure 7.23: BRDF plots (through the principal plane) computed for the representative sample considering a (polar) angle of incidence of 67°, a wavelength of 1450 $\mathrm{nm}$ and three grain sizes. The blue solid curve is associated with the presence of coarse-sized grains (1.5–3$\mathrm{mm}$), the dashed red curve with the presence of middle-sized grains (as specified in Table 7.1), and the green dotted curve with the presence of fine-sized grains (0.03–0.3 $\mathrm{mm}$). The remaining parameter values are provided in Table 7.1. The direction of incidence is indicated with a black solid (straight) line.

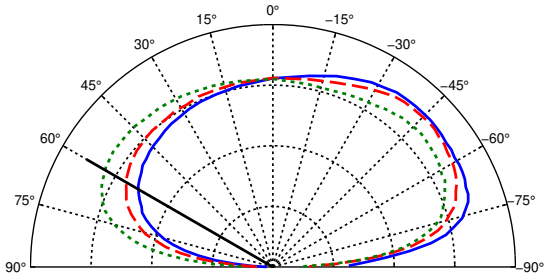


Figure 7.24: BRDF plots (through the principal plane) computed for the representative sample considering a (polar) angle of incidence of 60°, a wavelength of 600 $\mathrm{nm}$ and three different facetness values. The blue solid curve is associated with low facetness (0.0–0.2), the red dashed curve is associated with an intermediate facetness (0.2–0.4), and the green dotted curve is associated with a high facetness (0.8-1.0). The remaining parameter values are provided in Table 7.1. The direction of incidence is indicated with a black solid (straight) line.

the selected pixels are associated with a maximum elevation gradient of 0.165 and a mean elevation gradient of 0.067. Eight of the selected pixels are associated with a gradient smaller than 0.1. The average reflectance was then computed for the 25 selected pixels. In Figure 7.25(b), a comparison between the average measured reflectance values of the selected region (black squares) with values produced using the SPLITSnow model (blue curve) is provided. Bars are used to indicate the minimum and maximum reflectance values for the 25 pixels.

We remark that interpretation of signals detected from instrumentation aboard aircraft is

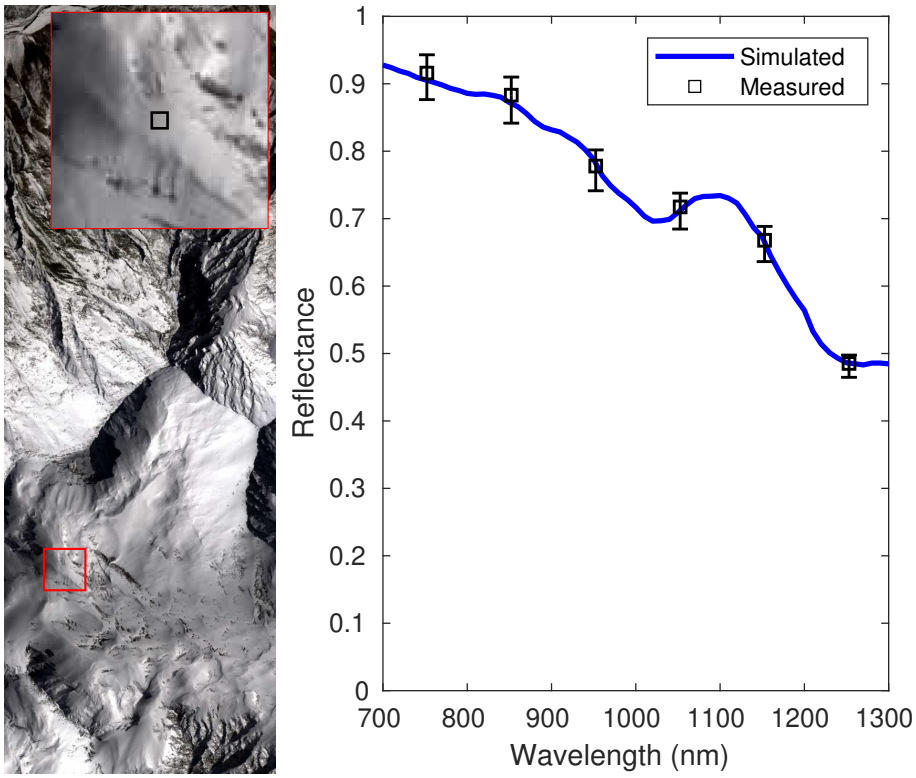


(a) (b)

Figure 7.25: Comparison of measured (obtained by the AVIRIS-NG [86] mission) and simulated data. The simulated directional-hemispherical reflectance curve was obtained using the SPLITSnow model and the sample characterization parameter values provided in Table 7.1, except that the snow depth was set to 25 $\mathrm{cm}$ and the angle of incidence was set to 62.3°. A portion of the "quicklook" image from the *ang20160217t074158* flight line over Himachal Pradesh, India, is presented in (a). The inset image presents an enlargement of the region of study that has not been interpolated. The selected pixels are demarcated by a black square in the inset image. This region is represented by a grid of $5 \times 5$ pixels. In (b), the simulated reflectance curve is depicted by the blue solid line. The black squares indicate the average reflectance values for the 25 selected pixels and the bars indicate the minimum and maximum values for the selected pixels.

| Wavelength (nm) | Simulated | Measured | | |
|---|---|---|---|---|
| | | Minimum | Mean | Maximum |
| 842.25 | 0.878 | 0.848 | 0.890 | 0.916 |
| 1037.76 | 0.692 | 0.669 | 0.701 | 0.721 |
| 1237.93 | 0.495 | 0.464 | 0.484 | 0.496 |

Table 7.8: Comparison of measured (obtained from the AVIRIS-NG dataset) and simulated reflectance values at selected wavelengths. The measured values correspond to the reflectances of the 25 pixels forming the region (inset) shown in Figure 7.25(a), and the simulated values were computed using the SPLITSnow model.

more difficult compared to field studies and laboratory experiments [120], and compensation is required for atmospheric absorption and scattering [65, 210]. Thus, the comparisons detailed in this section were performed against the correction outputs provided by the "Level 2" algorithm [210], which attempts to reduce measurement biases over snow-covered terrain.

Gao and Goetz [65] note that atmospheric water vapour transmittance values are greater than 99% in narrow bands surrounding specific wavelengths, 840 nm, 1040 nm and 1240 nm, whereas other wavelength bands, such as 940 nm and 1140 nm, are sensitive to water vapour absorption. To minimize bias due to atmospheric water vapour, we provide a comparison between simulated and measured reflectance values for the three wavelengths at which high transmission was noted. These data are presented in Table 7.8. The three wavelengths presented in the table were chosen among those employed by the AVIRIS-NG instrument directly since they are the nearest to the high-transmittance bands described by Gao and Goetz [65]. The simulated values were also computed using the same wavelengths for the purpose of direct comparison. The relative errors between average measured pixel values and the simulated values are all below 2.3%. The mean percent difference for the minimum and maximum values is 3.6%. Hence, the results of our comparisons indicate that the predictions provided by the proposed framework can contribute to the reliable interpretation of remote sensing signals from snow-covered landscapes. Furthermore, they may also aid in the determination of aerosol optical thickness where advanced surface reflectance models are needed by elucidating the surface contribution to top-of-atmospheric reflectance [120].

# Chapter 8

# Data Analysis Results

In this chapter, we assess the effectiveness of the method proposed in Chapter 5 for visually reproducing the appearance attributes of snow, notably those associated with light transmission. We begin with a brief examination of the procedure leading to the selection of the parameter values used to generate the spectral transmittance database. Next, we present an analysis of the benefits obtained from applying the principal component analysis (PCA) technique to the database. Finally, we examine the visual fidelity of the spectral reconstructions obtained using PCA and showcase the impact of snow parameter variations on its bluish appearance.

## 8.1 Spectral Transmittance Database

As discussed in Chapter 5, we generated a database of spectral transmittance curves using the SPLITSnow framework. To generate this database, we selected three snow characterization traits, namely, facetness, grain size and density, that are known to have a considerable impact on light transmission through snow [219]. In this work, we considered virtual snow samples with nine different grain sizes, five different degrees of facetness and five densities, yielding 225 unique snow exemplars. These exemplars are illustrated in Figure 8.1, which depicts a reconstructed spectral transmittance curve for each of the 225 virtual snow samples.

We also identified two other traits that have an impact on appearance. Namely, snowpack depth and the angle of incident illumination. To account for these two factors, we also considered eleven different snowpack thicknesses and ten distinct angles of incidence. Accounting for these five factors, we computed the transmittance values for $24750$ spectral curves, which were included in the transmittance database. Lastly, for each transmittance curve, we considered a

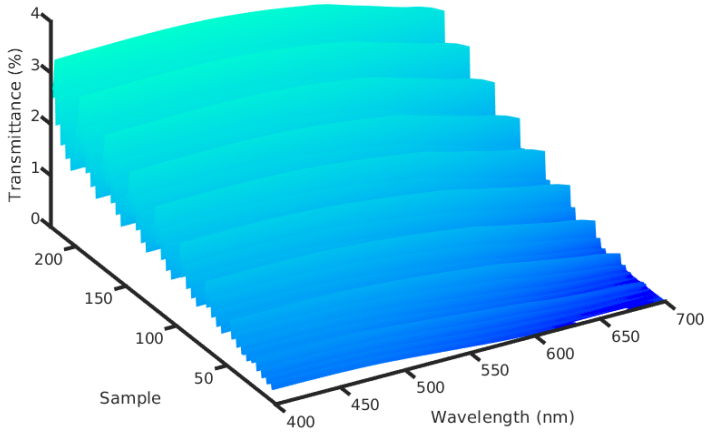


Figure 8.1: Reconstructed spectral transmittance curves for each of the 225 snow exemplars employed in this work. The plotted spectral curves were produced using an angle of incidence of 0°, and the samples are 15 $\mathrm{cm}$ thick. The samples are ordered first by grain size, then decreasing density, and then finally by facetness.

spectral resolution of 10 $\mathrm{nm}$, yielding 31 wavelengths in the visible spectrum (400–700 $\mathrm{nm}$). Table 8.1 lists the specific values considered for each parameter.

Note that the remaining model parameters, namely sphericity, temperature, saturation, black (inorganic) carbon content and brown (organic) carbon content were kept fixed for practical purposes. More specifically, the mean sphericity was set to 0.798 with a standard deviation of 0.064. Also the minimum and maximum sphericities were set to 0.6 and 0.95 respectively. Furthermore, the temperature of all snow exemplars in the transmittance database was set to -1°C. Lastly, the samples were assumed to be in a dry (saturation equal to zero) and pure (no black or brown carbon content) state.

We remark that the spectral transmittance curves forming the database were computed using the SPLITSnow light transport model described in Chapter 4. As discussed in that chapter, this model makes use of geometric (ray) optics to simulate light interactions with snow grains. For the computation of each transmittance curve in the transmittance database, $10^5$ rays (per sample wavelength) were employed in order to attain asymptotically convergent radiometric quantities [17].

| Parameter | Values | Range | Units |
|---|---|---|---|
| Mean Facetness | 0.1, 0.3, 0.5, 0.7, 0.9 | $\pm 0.1$ | |
| Mean grain size | 100, 150, 200, 250, 300, 350, 400, 450, 500 | $\pm 50$ | µm |
| Density | 200, 250, 300, 350, 400 | | $\mathrm{kg\,m^{-3}}$ |
| Snow thickness | 1, 1.5, 2, 3, 5, 7, 10, 15, 25, 35, 50 | | cm |
| Angle of incidence | 0, 10, 20, 30, 40, 50, 60, 70, 80, 89 | | degrees |
| Sphericity | 0.798 (mean) | $[0.6, 0.95]$ | |
| Temperature | -1 | | °C |
| Saturation | 0 | | |
| Inorganic (Black) Carbon | 0 | | $\mathrm{ng\,g^{-1}}$ |
| Organic (Brown) Carbon | 0 | | $\mathrm{ng\,g^{-1}}$ |

Table 8.1: Parameter values used to create the transmittance database of spectral transmittance curves. Model parameters listed in the upper portion of the table were varied through the values listed. Model parameters listed in the lower portion of the table were kept fixed.

The raw simulation output of this computation produced a database that was larger than 200 MB. This database was processed and reformatted so it could be represented by a single matrix for use with PCA (see Section 5.2).

As previously discussed, three snow characterization traits were selected and their associated model parameter values were varied (within the limits observed in nature [29, 60]) to produce 225 virtual snow samples. For each of these traits, which have been documented in the literature [5, 54, 159, 208, 238], we selected a uniform distribution of parameter values to be included in this work. For snow grain size, where there was a greater effect on spectral curves, we included nine different parameter values. For facetness and density, only five values were selected. To highlight the effect that these snow sample traits have on spectral transmittance, we plotted the spectral transmittance values when each of these traits is varied in Figures 8.2–8.7. For the sake of clarity, only a subset of the selected parameter values for snow are depicted in each plot. To produce these plots, default values were selected for the virtual snow samples, and only the parameter value under test was varied. The default values are given in Table 8.2.

Figure 8.2 depicts the trend of increasing grain size. Observe that a greater percentage of light is transmitted for all wavelengths in the visible spectrum as the grain size increases. However, as snow grain facetness increases, less light is transmitted as shown in Figure 8.3. Lastly, Figure 8.4 demonstrates the trend that the transmittance values of visible light tend to decrease as density increases.

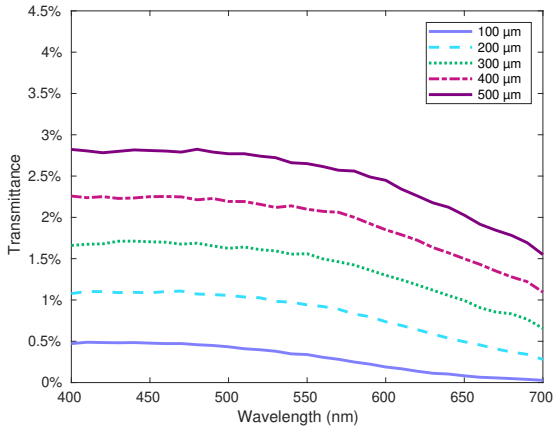


Figure 8.2: Simulated spectral transmittance curves for a typical snow sample computed using the SPLITSnow model and considering variations in grain size. Except for the parameter under test, all other parameter values are set to the default values specified in Table 8.2. Grain size is varied from 100–500 µm.

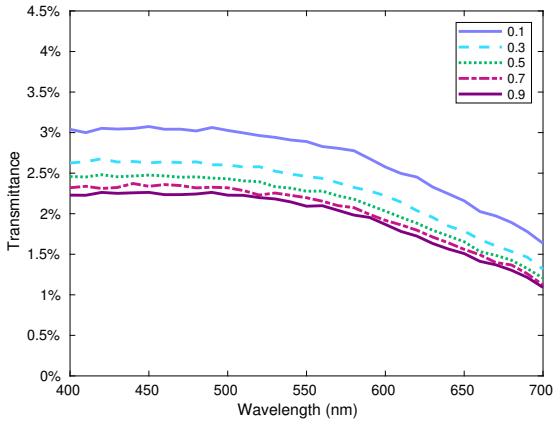


Figure 8.3: Simulated spectral transmittance curves for a typical snow sample computed using the SPLITSnow model and considering variations in facetness. Except for the parameter under test, all other parameter values are set to the default values specified in Table 8.2. Facetness is varied from 0.1 to 0.9 (unitless).

| Parameter | Value |
|---|---|
| Grain size range ($\mu$m) | 300–750 |
| Facetness (unitless) | $0.3 \pm 0.1$ |
| Density ($\mathrm{kg\,m^{-3}}$) | 275 |
| Sample thickness ($\mathrm{cm}$) | 12 |
| Angle of incidence ($^\circ$) | 0 |

Table 8.2: SPLITSnow parameter values employed in the characterization of the snow sample used to obtain the data presented in Figures 8.2–8.7.

The angle of incidence also has an impact on the process of light transmission through snow. Furthermore, this parameter is also important for many rendering applications. As described in Section 2.4, the path tracing algorithm traces paths stochastically from the viewer (or the virtual camera) back to a light source. As such, the angle of incidence of light impingement on objects in the scene can be at any angle in the upper hemisphere. Therefore, due to its importance for rendering applications, we selected ten values for this parameter to include in the transmittance database. The trend observed when the angle of incidence is varied for a selection of angles is depicted in Figure 8.5.

The final dimension to address is snow sample thickness. Light transmission through snow is significantly impacted by the thickness of the sample [5] and the relationship is non-linear [219]. In order to select the set of snow sample thicknesses to include in the transmittance database, we examined several thicknesses (varying from 1 $\mathrm{cm}$ to 100 $\mathrm{cm}$) of a single snow sample and produced spectral transmittance curves for each thickness. We then integrated each spectral curve to compute the total transmittance for all wavelengths of each curve. Figure 8.6 presents a log-log plot of these results. The near linearity of this curve indicates that the quantity of light transmitted roughly obeys a power law relationship with snow sample thickness. Therefore, we chose to include thickness values (see Table 8.1) that roughly follow such a relationship. This computational experiment indicated that less than 0.3$\%$ of light was transmitted below a depth of 100 $\mathrm{cm}$, and less than 0.7$\%$ of light was transmitted below a depth of 50 $\mathrm{cm}$. Accordingly, we opted to include a value of 50 $\mathrm{cm}$ as our thickest sample, and to consider all transmittance values beyond 100 $\mathrm{cm}$ to be negligible. Similarly, for a snow thickness of 0 $\mathrm{cm}$ we assume that light is transmitted completely. Although the transmittance values for snow sample thicknesses of 0 $\mathrm{cm}$ and 100 $\mathrm{cm}$ are not explicitly stored in the transmittance database, they will be used implicitly as part of the visualization process (see Section 5.3). The transmittance values for a subset of the sample thicknesses that are stored in the transmittance database are plotted in Figure 8.7.

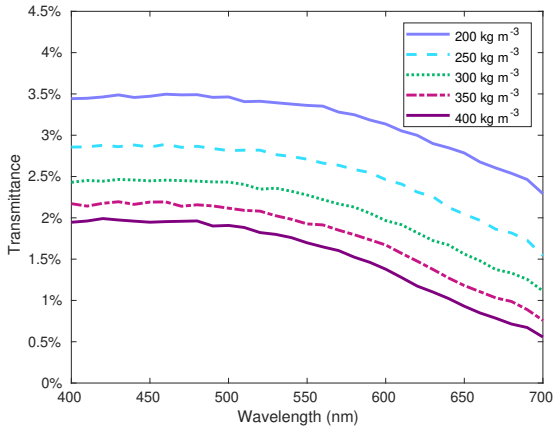


Figure 8.4: Simulated spectral transmittance curves for a typical snow sample computed using the SPLITSnow model and considering variations in density. Except for the parameter under test, all other parameter values are set to the default values specified in Table 8.2. Density is varied from 200–400 $\mathrm{kg\,m^{-3}}$.

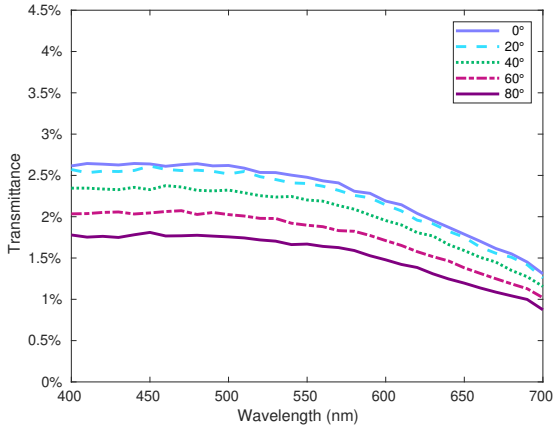


Figure 8.5: Simulated spectral transmittance curves for a typical snow sample computed using the SPLITSnow model and considering distinct angles of incidence. The angle of incidence is varied from 0°–80°. All other parameter values are set to the default values specified in Table 8.2.

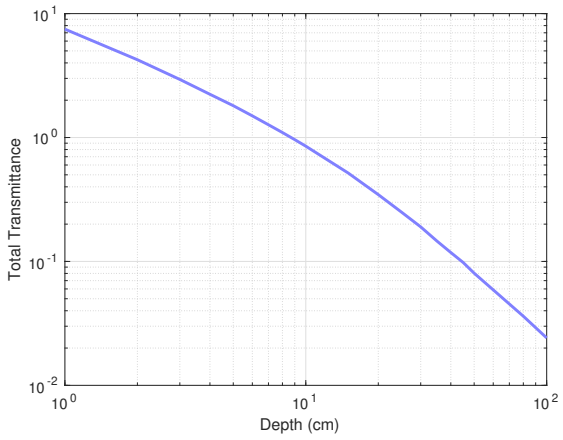


Figure 8.6: Log-log plot of total transmittance vs. snow thickness. Transmittance values are integrated across the visible spectrum to compute the sum total transmittance across all wavelengths. All other parameter values are set to the default values specified in Table 8.2

## 8.2 Transmittance Database Compression

We applied the PCA technique discussed in Section 5.2 to the database of spectral transmittance curves. Our intent was to reduce the dimensionality of the database for the purpose of implementing an efficient technique to reconstruct the stored spectral light transmittance curves. Recall from Section 8.1 that a total of 225 snow exemplars were included in the transmittance database. For each sample, ten angles of incidence and eleven sample thicknesses were chosen for rendering purposes, and the spectral transmittance curves were sampled at 31 wavelengths. Thus, the database is represented by a $24750 \times 31$ matrix $M$, whose 24750 rows correspond to the spectral curves and 31 columns correspond to the sampled wavelengths of light. Therefore, the database contains over 750 thousand numeric values. Our experiments (discussed below) indicated that two principal components were sufficient to reconstruct the spectra without loss of visual fidelity. Using two components for the application of PCA reduced the dimensionality of this database down to the two matrices: a $24750 \times 2$ matrix $C'$ and the $31 \times 2$ matrix $V'$. This yielded a PCA representation requiring only 6.5% of the storage space employed for the original database. Furthermore, it is orders of magnitude smaller than the raw simulation output which exceeded 200 $\mathrm{MB}$ in size.

Recall that we employed two criteria to determine the number of principal components that are sufficient to reproduce the spectral curves. More specifically, we calculated the RMSE values and the perceptual differences as discussed in Section 6.5.

The RMSE values were computed using Equation 6.4. This computation was performed be-

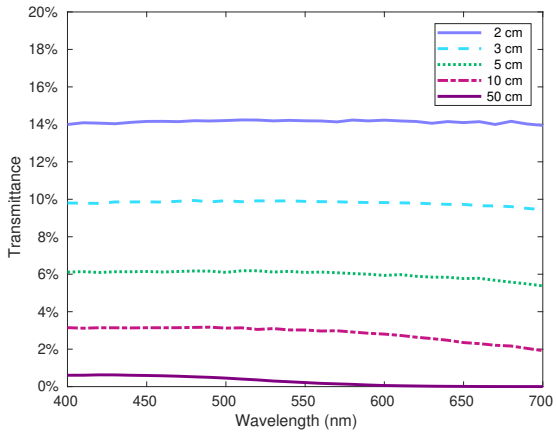


Figure 8.7: Simulated spectral transmittance curves for a typical snow sample computed using the SPLITSnow model and considering distinct thickness values. All other parameter values are set to the default values specified in Table 8.2

tween every curve in the transmittance database and its associated reconstruction using various numbers of principal components. The results of this analysis are presented in Table 8.3, where the minimum, mean and maximum error values are given. As expected, the greatest error was reported for the fewest number of principal components used in the curves' reconstructions.

We remark that the maximum RMSE value for one principal component ($l' = 1$) is markedly different than the maximum RMSE value for the spectral reconstructions produced using two principal components ($l' = 2$). We also note that utilizing three and four principal components does reduce the RMSE error values. However, the reduction in error between the reconstructions using two and three principal components is significantly less than the reduction in error when adding the second principal component. Similarly, adding a fourth component further reduces the error, but the reduction in mean error is even less significant. This indicates that the greatest benefit-to-cost ratio is observed when using two principal components.

Although the RMSE values suggested that employing two principal components provided the greatest benefit-to-cost ratio, we were primarily interested in preserving the visual fidelity of the spectral responses. To numerically assess the fidelity of the spectral reconstructions on the human visual system, we computed the $L^*a^*b^*$ coordinates in the CIELAB colour space for the reconstructed curves and the respective curves in the transmittance database. As discussed in Section 6.5, the CIELAB difference between the two values yields a measure of the perceptual difference observed by the visual system of an average human observer. The results of this analysis are presented in Table 8.4.

We remark that two colours in the CIELAB colour space with a Euclidean distance less

| Components | RMSE | | |
|---|---|---|---|
| | Minimum | Mean | Maximum |
| 1 | 0.00013 | 0.00149 | 0.00470 |
| 2 | 0.00010 | 0.00060 | 0.00192 |
| 3 | 0.00006 | 0.00047 | 0.00191 |
| 4 | 0.00003 | 0.00045 | 0.00183 |

Table 8.3: RMSE values between spectral reconstructions of transmittance values/curves provided in the transmittance database. The reconstructions were conducted using PCA. Minimum, mean and maximum values were computed using various numbers of principal components.

| Components | Perceptual Difference | | |
|---|---|---|---|
| | Minimum | Mean | Maximum |
| 1 | 0.0043 | 0.7612 | 2.8638 |
| 2 | 0.0031 | 0.2720 | 1.3955 |
| 3 | 0.0012 | 0.1074 | 0.5203 |
| 4 | 0.0003 | 0.0519 | 0.2672 |

Table 8.4: Perceptual difference values between spectral reconstructions of transmittance values/curves provided in the transmittance database. The reconstructions were conducted using PCA. Minimum, mean and maximum values were computed using various numbers of principal components.

than 2.3 have been experimentally determined to be indistinguishable for an average human observer [131, 204]. As shown in Table 8.4, when we employed just a single principal component, the maximum difference was 2.8, which is significant enough to be noticeable. However, when we employed two principal components to reconstruct the spectral transmittance values, the resulting max perceptual difference was less than 1.4. When three and four principal components were used to reconstruct the transmittance spectral curves, the perceptual differences were still lower, with the maximum differences being 0.52 and 0.27, respectively. Although these reconstructions exhibit smaller error values and are closer CIELAB matches, the added fidelity is not perceptually significant for an average human observer [131, 204]. Therefore, the reconstructed spectral values used in the renderings presented in this thesis were obtained by employing two principal components.

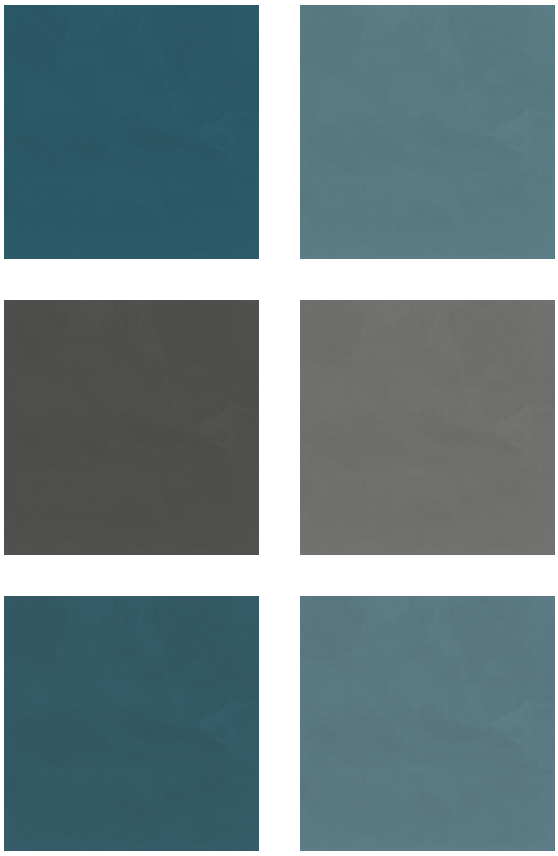

Figure 8.8: Snow swatches generated for two samples, denoted A (left) and B (right), with the greatest perceptual differences between the original and the reconstructed spectral transmittance curves. The snow sample parameter values are provided in Table 8.5. Swatches in the top row were generated using the original values in the transmittance database. Swatches in the middle and bottom rows were generated using one and two principal components, respectively.

## 8.3 Visual Fidelity

To examine the visual fidelity associated with our PCA-based spectral reconstructions, we generated swatches using the transmittance database and transmittance curves reconstructed using both one and two principal components. We then visually compared the results. Two examples of these comparisons are presented in Figure 8.8. The snow samples' parameter values considered in these examples are provided in Table 8.5.

| Parameter | A | B |
|---|---|---|
| Grain size ($\mu$m) | 500 | 500 |
| Density ($\mathrm{kg\,m^{-3}}$) | 350 | 400 |
| Facetness (unitless) | 0.1 | 0.1 |
| Angle of incidence (degrees) | 10 | 0 |
| Thickness ($\mathrm{cm}$) | 25 | 15 |

Table 8.5: SPLITSnow parameter values used in the characterization of virtual snow samples (A and B) employed in the generation of the swatches presented in Figure 8.8.

The swatches in the top row were created using the original transmittance database spectra (*i.e.*, the values stored in the matrix, $M$). The middle row contains swatches generated using a single principal component. Finally, the bottom row was obtained using two principal components.

The snow samples in Figure 8.8 exhibited the two greatest perceptual differences when only a single principal component was used. Observe the visual similarity between swatches generated with reconstructed values employing two principal components and swatches generated with the original transmittance database curves.

The spectral curves used to create the swatches depicted in Figure 8.8 are presented in Figure 8.9. The three curves in Figure 8.9 (top) show the original spectral transmittance curves of the transmittance database for the left column of Figure 8.8, including the reconstructions made using both one and two principal components. Figure 8.9 (bottom) shows the respective curves for the swatches in the right column of Figure 8.8. We remark that the reconstruction using two principal components adheres to the same trends observed in the transmittance database. This is consistent with the RMSE values presented in Table 8.3.

## 8.4 Snow Characterization Variability

To showcase the effects that the various parameters have on the bluish appearance of the snow samples, we generated swatches using the extreme values the three snow characterization parameters, namely grain size, facetness and density. These swatches are presented in Figure 8.10. The minimum and maximum values assigned to these parameters were used in the generation of the swatches in the left and right columns, respectively. In the top row, the minimum (100 $\mu$m) and maximum (500 $\mu$m) grain sizes were used to generate the two swatches. In the middle row, the minimum (0.1) and maximum (0.9) values of facetness were utilized. Finally, in the bottom

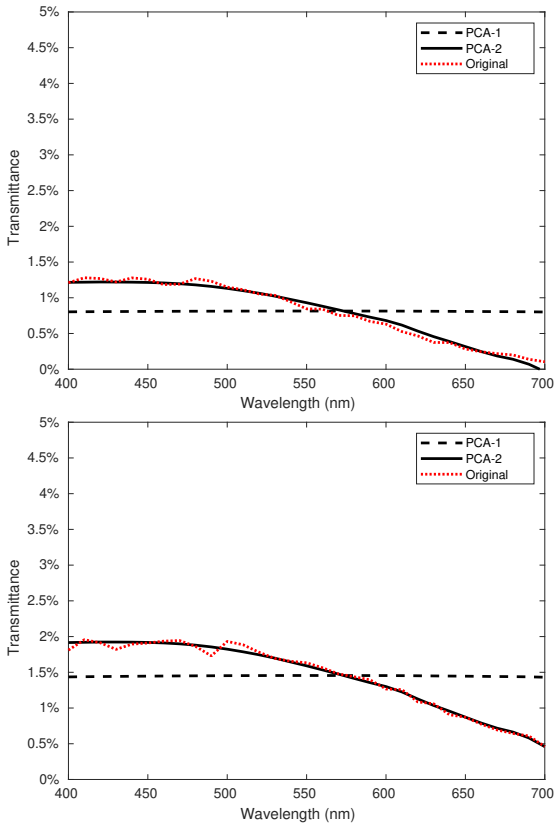


Figure 8.9: Spectral transmittance curves employed to generate the swatches depicted in Figure 8.8. Top: Spectral transmittance values of the transmittance database for sample A, plus the spectral transmittance values recreated using both one and two principal components. Bottom: Spectral transmittance values of the transmittance database for sample B, plus the spectral values recreated using both one and two principal components.

row, the minimum (200 $\mathrm{kg\,m^{-3}}$) and maximum (400 $\mathrm{kg\,m^{-3}}$) values of density were employed. The SPLITSnow parameter values used as default characterization values that are not subject to variation are provided in Table 8.6. For the pair of swatches in each row, the perceptual difference values between the two swatches were calculated using Equation 6.5. The corresponding values from top to bottom are 17.2, 3.4 and 9.3, respectively. We note that these values are consistent with the differences in the magnitude of the spectral transmittance curves (presented in Figures 8.2–8.4) associated with variations in grain size, facetness and density, respectively. In the next chapter, we illustrate the impact of another key snow parameter, its thickness.

Figure 8.10: Snow swatches generated from virtual snow samples considering different values for sample parameters (grain size, facetness and density). The minimum (left) and maximum (right) values of each parameter were used to generate the swatches. Top: Swatches generated employing a grain size of 100 $\mu\mathrm{m}$ and 500 $\mu\mathrm{m}$. Middle: Swatches generated employing a facetness of 0.1 and 0.9. Bottom: Swatches generated employing a density of 200 $\mathrm{kg\,m^{-3}}$ and 400 $\mathrm{kg\,m^{-3}}$. The parameters not subject to variation were set to the values presented in Table 8.6.

| Parameter | Value | Units |
|---|---|---|
| Grain Size | $400 \pm 50$ | µm |
| Density | 300 | $\mathrm{kg\,m^{-3}}$ |
| Facetness | $0.3 \pm 0.1$ | |
| Angle of incidence | 0 | degrees |
| Thickness | 15 | cm |
| Sphericity (mean) | 0.798 | |
| Sphericity (minimum) | 0.6 | |
| Sphericity (maximum) | 0.95 | |
| Sphericity (standard deviation) | 0.064 | |

Table 8.6: SPLITSnow parameter values used as default characterization values of the virtual snow samples employed in the generation of the swatches presented in Figure 8.10. The parameters in the top portion of the table were subject to variation in the creation of Figure 8.10, whereas the parameters in the bottom portion of the table were fixed for the generation of all swatches.

# Chapter 9

# Visual Results

In this chapter, we address potential realistic image synthesis applications of the proposed framework. We begin with the presentation of images that highlight specific appearance changes elicited by reflection and transmission of light through snow. We then provide images to showcase the applicability of the proposed framework to the rendering of scenes depicting more comprehensive appearance changes resulting from light and snow interactions.

## 9.1 Specific Appearance Changes

Figure 9.1 presents images depicting appearance variations produced by light transmission through four blocks of snow of varying thicknesses. The blocks were rendered using the PCASnow material implementation class described in Section 5.3 and employing a standard D65 illuminant [37]. The blocks are backlit by an unseen light source. The thicknesses of the blocks are approximately 5, 10, 15 and 30 $\mathrm{cm}$, starting from the left. In order to focus on the colour change due to volume thickness, no textures were employed. The PCASnow material class was initiated using a snow sample with a mean grain size of 400 $\mu\mathrm{m}$, a density of 300 $\mathrm{kg\,m^{-3}}$ and a moderately low quantity of crystalline features (facetness) of 0.3. We remark that there is an observable change in appearance of the transmitted light as the thickness of the snow increases.

The oblique-angled image in Figure 9.1 (right), *i.e.*, the 30 $\mathrm{cm}$ thick snow block, takes less than one minute to render on an Advanced Micro Devices Inc. (AMD) Ryzen Threadripper 3990X central processing unit (CPU) with 64 computing cores. The rendered image contains $1080 \times 1080$ pixels and was rendered using 100 samples per pixel. To render the image, the

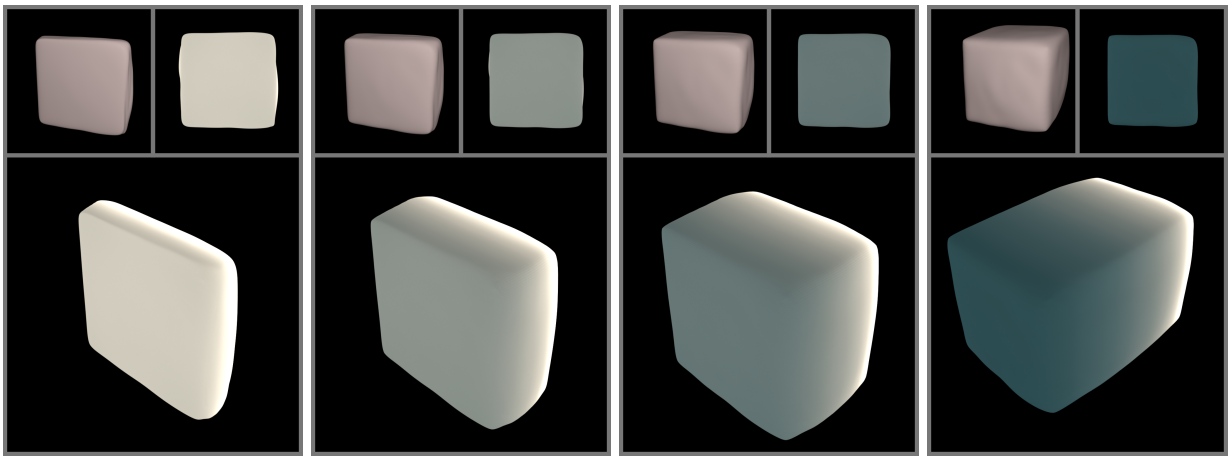

Figure 9.1: Sequence of rendered images depicting light interactions with four different blocks of snow. From left-to-right, the snow blocks are approximately 5, 10, 15, and 30 $\mathrm{cm}$ thick. Each sequence component contains three images. Upper-left image: The geometry is rendered using a standard local illumination model and a point light source situated near the eye-point. Upper-right image: The geometry is rendered using the process described in Section 5.3. The light source is behind the snow block and the viewing direction is perpendicular to the snow block. Bottom image: The same technique is employed as in the upper-right image. However, the viewing direction is oblique to the snow block.

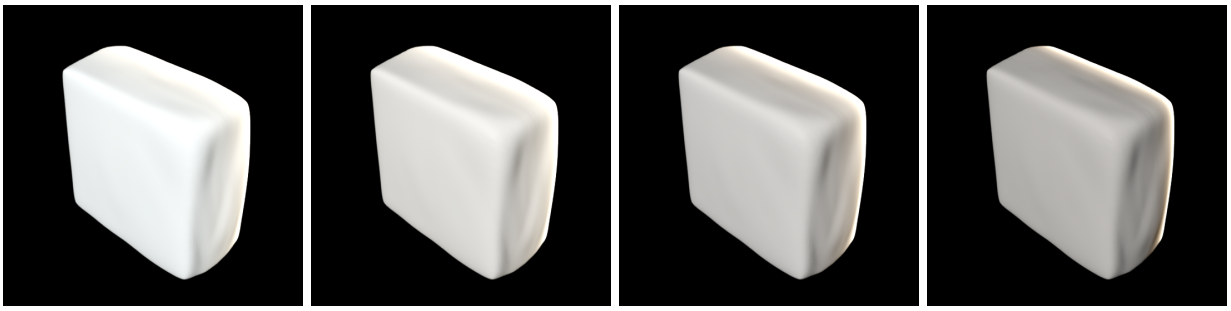

Figure 9.2: Sequence of rendered images depicting light interactions with a block of snow containing four different quantities of impurities. From left-to-right, the quantity of impurities are 0, 20, 100 and 400 $\mathrm{ng\,g^{-1}}$. A point light source is located in front of the snow block to account for the effects of reflection. A second light source is located behind the snow block to account for the effects due to light transmission.

transmittance database was queried approximately 90 million times to obtain the spectral transmittance values. For the purpose of comparison, the time required to conduct a full light transport simulation for a single spectral transmittance curve for a volume of snow that is 30 $\mathrm{cm}$ thick with the same snow characteristics utilizing the same CPU is approximately 7.5 $\mathrm{min}$.

Figure 9.2 depicts the same 10 $\mathrm{cm}$ snow block as the one presented in Figure 9.1, but repeated four times. The same light source is positioned behind the block of snow. However, an additional, point light source is placed in front of the snow block. The snow sample properties are also kept the same as in Figure 9.1, except that black carbon impurities are added to the snow. From left-to-right, the quantities of impurities are 0, 20, 100 and 400 $\mathrm{ng\,g^{-1}}$. To render these images, a reflectance database containing impurities was generated. This reflectance database was incorporated into the renderer using the techniques described in Chapter 5. Observe that even a small quantity of impurities (20 $\mathrm{ng\,g^{-1}}$, second from the left) is sufficient to noticeably darken the snow sample. Also, following a substantial increase in black carbon content (400 $\mathrm{ng\,g^{-1}}$), the snow sample is markedly darkened (rightmost rendering). Note that the impurities in each rendering were specified as being black carbon with an Angstrom exponent value of one and a sedimentation fraction value of one.

## 9.2 Comprehensive Appearance Changes

To further demonstrate the applicability of the proposed framework, we rendered two demonstration scenes that also use the PCASnow material class discussed in Section 5.3. The first scene, presented in Figure 9.3, depicts a rendering of light transmission through snow with the camera positioned on the inside of an igloo and a light source located outside of the igloo. The igloo is formed by snow blocks whose thicknesses are approximately 15 $\mathrm{cm}$. To extend our scope of observations, the image was generated using a directionally uniform D55 (5500K daylight) illuminant [37, 96]. All light rays inside the igloo have been transmitted through the geometry that represents the igloo wall *via* the PCASnow material class to account for indirect illumination effects. In addition to the bluish hue exhibited by the light transmission, we remark that exterior light also *bleeds* through the snow at the seams between the blocks, where the geometry is comparatively thin, thus brightening the surface.

For illustrative purposes, we rendered the same scene using only a standard local illumination model employed for the reflectance calculation (Figure 9.3, inset). Since transmittance through the snow blocks is not considered in the inset image, a point light source was placed inside of the igloo to enable the visualization of the blocks.

The second demonstration scene, presented in Figure 9.4, depicts the Stanford Dragon geometry [46] rendered considering seven different virtual snow samples. The geometry has been

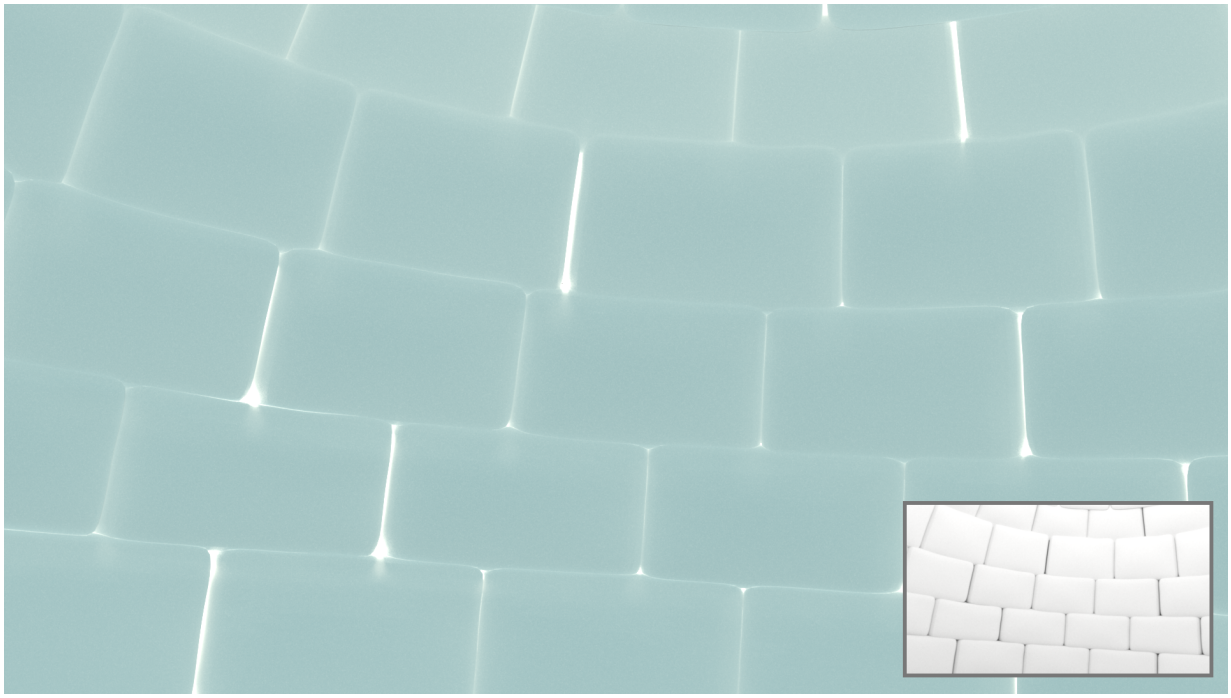

Figure 9.3: Rendered images depicting the inside of an igloo formed by snow blocks. The main image was rendered using reconstructed spectra that were produced by employing the methodology presented in Chapter 5. We remark that more light is transmitted where the snow thins between the snow blocks whose thicknesses are approximately 15 $\mathrm{cm}$. Inset: The same scene rendered to illustrate the blocks' arrangement. For the inset image, a standard, local illumination model was employed in conjunction with an interior light source.

scaled so that the diameter of the body's main section is approximately 30 $\mathrm{cm}$ in diameter, with the thickest part of the geometry (including the front legs) being approximately 80 $\mathrm{cm}$ in thickness. Note that the variations of the thickness of the geometry contribute to the tonal gradations of colour including white, various shades of blue and dark tones. Each rendering is backlit using a point light source of the same intensity and utilizes the D65 standard illuminant [37]. The main (top) image illustrates more diversely the snow appearance changes associated with thickness variations affecting light transmission. The virtual snow sample considered in the rendering of this image is characterized by a facetness of 0.3, grain size of 250 $\mu\mathrm{m}$ and a density of 300 $\mathrm{kg\,m^{-3}}$.

It has been well established in the literature, that grain size has a large effect on the transmission of light through snow [46, 67, 169, 184]. To showcase the effects of concomitant grain

Figure 9.4: Rendered images depicting the Stanford Dragon [46] represented by seven distinct virtual snow sample characterizations. Top: Medium values for grain size and density were employed. Second row: minimum grain size (left) and maximum grain size (right) values were employed. Third row: minimum density (left) and maximum density (right) values were employed. Bottom row: minimum grain size and minimum density (left) and maximum grain size and maximum density (right) were employed. See Table 9.1 for the specific values assigned to the aforementioned parameters.

| Image Location | Grain Size (μm) | Density ($\mathrm{kg\,m^{-3}}$) |
|---|---|---|
| Top | 250 | 300 |
| Row 2, left | 100 | 300 |
| Row 2, right | 500 | 300 |
| Row 3, left | 250 | 200 |
| Row 3, right | 250 | 400 |
| Row 4, left | 100 | 200 |
| Row 4, right | 500 | 400 |

Table 9.1: SPLITSnow parameters values employed in the creation of Figure 9.4. All renderings were created using a facetness value of 0.3.

size and thickness variations, we also rendered the Stanford Dragon scene using low and high values for the samples' grain size, namely 100 $\mu\mathrm{m}$ and 500 $\mu\mathrm{m}$. The remaining parameter values were kept the same as those used to render the main (top) image. The resulting images are presented in the second row of Figure 9.4. Observe that the virtual snow sample with the larger grain size (second row, right) allows more light to be transmitted and exhibits a more vivid blue hue than the main (top) image. This is in contrast to the virtual snow sample with the smaller grain size (second row, left) that displays the opposite effect when compared to the main image (top).

We then rendered the same scene using two different values of snow density, namely 200 $\mathrm{kg\,m^{-3}}$ and 400 $\mathrm{kg\,m^{-3}}$. The remaining parameter values were kept the same as those used to render the main (top) image. The resulting images are presented in the third row of Figure 9.4. We remark that the lower density sample (third row, left) allows for a greater quantity of light to be transmitted through the sample when compared to the main (top) image. Similarly, the snow sample with the higher density value (third row, right) exhibits lower transmittance values when visually compared with the main (top) image. We remark that this trend is consistent with the observations regarding density and snow transmittance presented in Section 7.2.2.

Finally, we rendered the same scene using the same density and grains size values used to produce Figure 7.17. As discussed in 7.2.2, when there are concomitant changes in both sample density and grain size, the transmittance values may increase as can be observed in Figure 9.4, bottom. The bottom left image uses both low values for density and grain size, whereas the bottom right image uses both high values. With such concomitant changes to the characterization parameter values, it is possible for the overall transmittance to increase. This is despite the increase in density which, in isolation, has the effect of decreasing the transmittance

in particulate materials [159, 238].

We remark that the presented demonstration scenes (Figures 9.3 and 9.4) are intended to serve as illustrative examples of potential uses of the proposed method in realistic image synthesis applications. These applications may involve objects with distinct geometrical complexities and be subjected to different illumination conditions. Furthermore, the depicted visual aspects can be regarded as a small subset of the myriad of snow appearance changes that can be predictively prompted by systematically varying the values of the material characterization parameters considered in this section.

# Chapter 10

# Conclusion

Material appearance modelling is an important and challenging area of study within the computer graphics field [51]. In the last decades, much effort has been directed toward the development of predictive models that can contribute not only to the advancement of realistic image synthesis, but also to a broad scope of research initiatives. This is especially true when the fidelity of modelled predictions can be comprehensively assessed.

It is in this context that we have presented the simulation framework discussed in this thesis. Central to this framework is the SPLITSnow model. This is a novel, first-principles, light transport model for snow, whose predictive capabilities have been extensively evaluated through quantitative comparisons to measured data and qualitative comparisons to trends reported in the literature. The results of these comparisons have shown that a high degree of fidelity has been achieved. Accordingly, this has allowed for contributions to be made in a number of application areas, which we summarize in the next section.

## 10.1 Contributions

The work presented in this thesis enabled a myriad of contributions to computer graphics and related fields. Among these contributions, we can emphasize the development of the SPLITSnow model itself [219]. The model supports two modes of execution. The first is the spectrometric mode, whereby spectral reflectance (and transmittance) experiments may be conducted throughout a number of spectral domains. These include not only visible light, but also ultraviolet (UV) and infrared (IR) light as well. The second supported mode allows goniometric experiments to be conducted. Experiments conducted in this mode typically focus on a fixed

set of wavelengths at a time and collect a dataset of directional reflectance (or transmittance) values for each wavelength.

Additionally, the model specifications presented in the original publication describing SPLITSnow [219], which includes support for a number of snow characterization parameters such as grain size, grain shape, facetness, temperature, sample thickness, water saturation and density, a number of extensions to the model have been presented in this thesis. The first of these extensions allows for the inclusion of impurities to the snow sample. Both black carbon and brown carbon impurities may be included. Both types of impurities may be specified as being in suspension or sedimentation. The second extension introduces support for multi-layered snow samples. This allows for a set of snow characterization parameter values to be specified for a basal layer, as well as separate sets of characterization parameter values for additional layers that represent subsequent snow falls. The third extension introduces support for a heterogeneous collection of snow grains to be specified within a virtual snow sample.

The framework described in this thesis also includes components that can be utilized to support specific graphics applications. For instance, we describe a method to incorporate spectrally-varying data into a traditional computer graphics renderer [218]. This method enables the incorporation of spectrally-dependent phenomena into a traditional rendering pipeline. In addition to this, we have also made the spectral transmittance database associated with the description of this method available online [147].

The proposed framework may be employed to address open problems and to clarify misconceptions in the literature. These include, for instance, the issue addressed in Section 7.2.2 where concomitant changes in both grain size and density lead to the repeated, erroneous statement that transmittance increases with density [18].

To further showcase the applicability of the proposed framework to other fields, we have employed it to study a variety of open problems. For example, we used it to examine electromagnetic (EM) radiation penetration depth in order to elucidate the conditions under which dry slab avalanches may form [216]. (See also Appendix E.) Our findings indicated that grain size and density contribute to subsurface weak layer formation, which is consistent with analytic descriptions of crystal growth [42].

We also utilized the proposed framework to investigate the effect of snow grain properties on reflectance [217]. (See also Appendix F.) In this study, we observed that facetness is an important grain property in studies that attempt to estimate water content in a snowpack, and that future studies may be improved by accounting for this property of snow.

More recently, we have employed the SPLITSnow framework to study how changes in snow cover affect biological processes in plants at photosynthetically active wavelengths [18]. In that work, we examined particular ratios of EM radiation that are potentially important to

photobiological processes such as germination, the emergence of plant organs and cold tolerance. Our findings indicated that the net effect of snow melting and settling processes may favour an increase in productivity of vegetation, a phenomenon commonly referred to as greening [188, 224].

Finally, we have made the SPLITSnow model available for online use [145, 146], hence facilitating the reproduction of our results and enabling its use in interdisciplinary investigations carried out by the research community at large. In the words of Roger D. Peng [168], "Replication is the ultimate standard by which scientific claims are judged." It is our sincere hope that future works will utilize the SPLITSnow model and incorporate the generated data into their research projects. Indeed, as discussed in the literature [49, 76, 200], when the acquisition of comprehensive measured datasets is challenging, high-fidelity modelled data may provide a viable alternative.

## 10.2 Future Work

There are three main avenues for future work related to the research described in this thesis. The first is represented by extensions to the proposed framework. The second addresses rendering enhancements. The third is associated with the use of the proposed framework in interdisciplinary research initiatives. In the remainder of this section, we elaborate on these possibilities.

### 10.2.1 Model Extensions

There are a number of model extensions to consider. First, although crystalline features are built into the SPLITSnow formulation in the form of microfacets [44], it may be interesting to add other crystal formations to the framework. Picard *et al.* [172] addressed this aspect to some extent. More specifically, they observed variations in reflectance based on various crystal types. That work, however, was focused on the IR domain.

Another potential benefit to incorporating differently shaped grains into the SPLITSnow formulation would be to consider the alignment of the shaped grains. For instance, the orientation of elongated snow grains or hexagonally-shaped snow crystals may allow for the reproduction of other effects. In particular, it may be that the bidirectional reflectance distribution function (BRDF) varies azimuthally given the orientation of the snow crystals. This would permit *in silico* experiments where the azimuthal component of the view direction is also of importance and for circumstances where the reflectance varies with that component. It would

be a step forward in the modelling of material appearance since most of the works in this area, with a few noteworthy exceptions (*e.g.*, [175, 236]), usually assume the reflective behaviour of natural materials to be isotropic, *i.e.*, azimuthally symmetric [16].

In our *in silico* goniometric (BRDF) experiments, we assumed the snow samples to be homogeneous and single-layer materials. In the future, we intend to relax these assumptions. This is useful for scenarios where the bulk of a snowpack is composed of a blend of ice crystals or old, smooth grains with a thin layer of faceted snow on the surface. There are some technical issues to be overcome for multi-layered BRDF support. For instance, the entirety of the BRDF may need to be cached from lower layers so that it could be sampled. Note that the azimuthal component of the angle of incidence has an effect on bidirectional reflectance as can be observed in the IR spectrum (*e.g.*, Figure F.2 in Appendix F). A potential solution to this issue would be to conduct "nested" simulations, whereby light propagating to lower layers will recursively execute a simulation with the lower-layer's parameter values.

Another avenue for expanding the scope of applications of the proposed framework would be to extend the multi-layered approach (discussed in Section 4.4) to represent diverse materials. For instance, rather than a multi-layered snowpack having snow as the basal layer, the basal layer may be specified as another material such as soil or plant matter. For the remote sensing community, this would aid in the identification of terrains covered by a relatively thin layer of snow. For the field of computer graphics, this would enable the predictive rendering of smooth transitions from a snow cover to a substrate material as the former recedes and becomes progressively thinner.

### 10.2.2 Rendering Enhancements

In the future, we intend to include more samples in the spectral database employed by the proposed visualization process (Chapter 5). We remark that differences in snow characterization values have an effect on the spectral transmittance curves. By increasing the number of characterization parameter values employed, a greater variety of snowpack conditions will be available for use in image synthesis pipelines.

We also intend to include the spectral *reflectance* curves in the database, as snow sample characterization also has an effect on the reflectance [137]. It would also be valuable to include more snow sample parameters, such as liquid water content, to the combined transmittance and reflectance database proposed here. This would allow for an even greater number of virtual snow samples to be included into image synthesis pipelines.

Finally, we remark that the SPLITSnow model is a local illumination model. Consequently, macroscopic geometric features, such as sastrugi [95], are not addressed in its formulation.

In the future, it would be interesting to investigate the incorporation of algorithms to enable the physically-based rendering of these features as well as view-dependent effects such as sparkles [56, 246]. The recent works by Nguyen *et al.* [150, 151] may be used to support initiatives aimed at the predictive visual depiction of these effects.

### 10.2.3 Interdisciplinary Investigations

As highlighted earlier, predictive simulations of light interactions with snow grains are of interest for remote sensing and related fields. An understanding of how various snow grain characteristics affect reflectance and transmittance is necessary to identify and quantify properties of natural snowpacks. Accordingly, the proposed framework can be employed to assess snowpacks with different characterizations so that improved estimates of their morphological features can be obtained.

In addition to this, the extensions discussed in Sections 4.4–4.6 may be utilized to conduct future *in silico* studies. For example, the multi-layer extension that was introduced in Section 4.4, could be employed to study the effect of new-fallen snow on reflectance. This, in turn, could lead to better estimates of water content in a snowpack where such conditions are present. The presence of impurities, which was examined in Section 4.6, can be utilized in climate studies. More specifically, it would be interesting to attempt to quantify the effects of impurities deposited in pristine snow due to forest fires or due to dust storms. Lastly, the SPLITSnow formulation quantifies both reflectance and transmittance response values. It therefore implicitly accounts for absorptance. Future projects that make use of these values could be valuable in studies of increased heat transfer to and from snowpacks due to biomass burning [99].

In order to foster new advances in this area, the scientific community needs to provide continuing support for field studies aimed at the collection of spectral datasets on snow radiometric responses to distinct illumination and environmental conditions. To increase their usefulness, these datasets should include detailed characterizations of the measured snow samples to facilitate accurate reproduction of the spectral responses through *in silico* experiments.

Once the predictive capabilities of a simulation framework are established, it can be used to generate comprehensive *in silico* datasets to support the investigation of open scientific problems for which actual data cannot be obtained in a cost-effective manner due to technical and/or logistical limitations. For example, variations on the light transmission profiles of snowpacks located at the top of mountains during different times of the year. These *in silico* datasets could also be "fed" into artificial intelligence or machine learning algorithms dedicated to climate change studies and predictions [140].

We believe that the pairing of measurement efforts with *in silico* investigations will be instrumental to strengthen the knowledge foundation required for the development of more effective technologies aimed at the remote sensing of snow and snow-covered targets. Viewed in this context, the work described in this thesis also aims to serve as a catalyst for future synergistic research initiatives in these increasingly relevant areas of research.

# References


[1] Standard terminology of appearance. Technical Report E284-17, ATSM International, West Conshohocken, PA, USA, 2017.

[2] T. Aoki, T. Aoki, M. Fukabori, A. Hachikubo, Y. Tachibana, and F. Nishio. Effects of snow physical parameters on spectral albedo and bidirectional reflectance of snow surface. *J. Geoph. Res.-Atmos.*, 105(D8):10219–10236, 2000.

[3] S. Baggi and J. Schweizer. Characteristics of wet-snow avalanche activity: 20 years of observations from a high alpine valley (Dischma, Switzerland). *Nat. Hazards*, 50(1):97–108, 2009.

[4] D. Bänninger, C. S. Bourgeois, M. Matzl, and M. Schneebeli. Reflectance modeling for real snow structures using a beam tracing model. *Sensors*, 8(5):3482–3496, 2008.

[5] D. Bänninger and H. Flühler. Modeling light scattering at soil surfaces. *IEEE T. Geosci. Remote*, 42(7):1462–1471, 2004.

[6] G. V. G. Baranoski, T. Dimson, T. F. Chen, B. W. Kimmel, D. Yim, and E. Miranda. Rapid dissemination of light transport models on the web. *IEEE Comput. Graph.*, 32(3):10–15, 2012.

[7] G. V. G. Baranoski, M. Iwanchyshyn, B. W. Kimmel, P. M. Varsa, and S. R. Van Leeuwen. Evaluating the effects of distinct water saturation states on the light penetration depths of sand-textured soils. In C. M. U. Neale and A. Maltese, editors, *Proc. SPIE 11856*, volume 11856, page 118560U. International Society for Optics and Photonics, SPIE, 2021.

[8] G. V. G. Baranoski, M. Iwanchyshyn, B. W. Kimmel, P. M. Varsa, and S. R. Van Leeuwen. Exploring the transmission of VNIR light through Martian regolith. In *Geoscience and Remote Sensing Symposium (IGARSS)*, pages 6155–6158, 2021.

[9] G. V. G. Baranoski, M. Iwanchyshyn, B. W. Kimmel, P. M. Varsa, and S. R. Van Leeuwen. On the red to far-red ratios of light propagated by sand-textured soils. In *Geoscience and Remote Sensing Symposium (IGARSS)*, pages 6443–6446, 2021.

[10] G. V. G. Baranoski, B. W. Kimmel, and P. M. Varsa. Assessing the impact of porosity variations on the reflectance and transmittance of natural sands. *J. Appl. Remote Sens.*, 13(2):024522, 2019.

[11] G. V. G. Baranoski, B. W. Kimmel, P. M. Varsa, and M. Iwanchyshyn. On the light penetration in natural sands. In *Geoscience and Remote Sensing Symposium (IGARSS)*, pages 6933–6936, 2019.

[12] G. V. G. Baranoski, B. W. Kimmel, P. M. Varsa, and M. Iwanchyshyn. Porosity effects on red to far-red ratios of light transmitted in natural sands: implications for photoblastic seed germination. In C. M. U. Neale and A. Maltese, editors, *Proc. SPIE 11149*, volume 11149, pages 111490O:1–15. International Society for Optics and Photonics, SPIE, 2019.

[13] G. V. G. Baranoski, B. W. Kimmel, P. M. Varsa, and M. Iwanchyshyn. What can terrestrial sand-textured soils reveal about the composition of core materials forming Martian regolith. In *Geoscience and Remote Sensing Symposium (IGARSS)*, pages 6015–6018, 2019.

[14] G. V. G. Baranoski and A. Krishnaswamy. *Light & Skin Interactions: Simulations for Computer Graphics Applications*. Morgan Kaufmann/Elsevier, Burlington, MA, USA, 2010.

[15] G. V. G. Baranoski, A. Krishnaswamy, and B. Kimmel. Increasing the predictability of tissue subsurface scattering simulations. *Visual Comput.*, 21(4):265–278, 2005.

[16] G. V. G. Baranoski and J. Rokne. *Light interaction with plants: A computer graphics perspective*. Horwood Publishing, Chichester, UK, 2004.

[17] G. V. G. Baranoski, J. G. Rokne, and G. Xu. Virtual spectrophotometric measurements for biologically and physically-based rendering. *Visual Comput.*, 17(8):506–518, 2001.

[18] G. V. G. Baranoski and P. M. Varsa. Environmentally induced snow transmittance variations in the photosynthetic spectral domain: Photobiological implications for subnivean vegetation under climate warming conditions. *Remote Sens.*, 16(5):927:1–22, 2024.

[19] H. W. Barker and A. V. Korolev. An update on blue snow holes. *J. Geoph. Res.-Atmos.*, 115(D18):D18211:1–10, 2010.

[20] B. R. Barkstrom. Some effects of multiple scattering on the distribution of solar radiation in snow and ice. *J. Glaciol.*, 11(63):357–368, 1972.

[21] T. P. Barnett, J. C. Adam, and D. P. Lettenmaier. Potential impacts of a warming climate on water availability in snow-dominated regions. *Nature*, 438(7066):303, 2005.

[22] R. G. Barry. The cryosphere and climate change. In Michael C. MacCracken and Frederick M . Luther, editors, *Detecting the Climatic Effects of Increasing Carbon Dioxide*, chapter 6, pages 109–148. US Dept. of Energy Washington, DC, Washington, DC, 1985.

[23] F. O. Bartell, E. L. Dereniak, and W. L. Wolfe. The theory and measurement of bidirectional reflectance distribution function (BRDF) and bidirectional transmittance distribution function (BTDF). In *Radiation Scattering in Optical Systems*, volume 257, pages 154–160. International Society for Optics and Photonics, 1981.

[24] D. Beaglehole, B. Ramanathan, and J. Rumberg. The UV to IR transmittance of Antarctic snow. *J. Geoph. Res.-Atmos.*, 103(D8):8849–8857, 1998.

[25] K. W. Birkeland. Terminology and predominant processes associated with the formation of weak layers of near-surface faceted crystals in the mountain snowpack. *Arctic Alpine Res.*, 30(2):193–199, 1998.

[26] D. Bliss and H. Smith. Penetration of light into soil and its role in the control of seed germination. *Plant Cell Environ.*, 8(7):475–483, 1985.

[27] C. F. Bohren. Colors of snow, frozen waterfalls, and icebergs. *J. Opt. Soc. Am.*, 73(12):1646–1652, 1983.

[28] C. F. Bohren and B. R. Barkstrom. Theory of the optical properties of snow. *J. Geophys. Res.*, 79(30):4527–4535, 1974.

[29] C. F. Bohren and R. L. Beschta. Snowpack albedo and snow density. *Cold Reg. Sci. Technol.*, 1(1):47–50, 1979.

[30] C. F. Bohren and D. R. Huffman. *Absorption and scattering of light by small particles*. John Wiley & Sons, Toronto, Canada, 1983.

[31] M. Born and E. Wolf. *Principles of Optics: Electromagnetic Theory of Propagation, Interference and Diffraction of Light*. Cambridge University Press, Cambridge, UK, 7$^{th}$ edition, 1999.

[32] S. Bottaro and K. Lindorff-Larsen. Biophysical experiments and biomolecular simulations: A perfect match? *Science*, 361(6400):355–360, 2018.

[33] D. H. Brainard. Color appearance and color difference specification. In S. K. Shevell, editor, *The Science of Color*, chapter 5, pages 191–216. Elsevier Ltd., Amsterdam, 2003.

[34] N. L. Briggs and C. M. Long. Critical review of black carbon and elemental carbon source apportionment in Europe and the United States. *Atmos. Environ.*, 144:409–427, 2016.

[35] Olivier Brissaud, Bernard Schmitt, Nicolas Bonnefoy, Sylvain Doute, Patrick Rabou, Will Grundy, and Michel Fily. Spectrogonio radiometer for the study of the bidirectional reflectance and polarization functions of planetary surfaces. 1. design and tests. *Appl. Optics*, 43(9):1926–1937, 2004.

[36] W. L. Butler. Absorption spectroscopy *in vivo*: Theory and application. *Annu. Rev. Plant Phys.*, 15:451–470, 1964.

[37] E. C. Carter, J. D. Schanda, R. Hirschler, S. Jost, M. R. Luo, M. Melgosa, Y. Ohno, M. R. Pointer, D. C. Rich, F. Viénot, L. Whitehead, and J. H. Wold. Colorimetry. Technical Report CIE 015:2018, International Commission on Illumination (CIE), 2018.

[38] V. S. Castillo. Realistic rendering of blue ice. Master's thesis, Bournemouth University, Dorset, UK, 2009.

[39] S. Chen and G. D. Doolen. Lattice Boltzmann method for fluid flows. *Annual Review of Fluid Mechanics*, 30(1):329–364, 1998.

[40] A. Ciani, K. U. Goss, and R. P. Schwarzenbach. Light penetration in soil and particulate materials. *Eur. J. Soil Sci.*, 56:561–574, 2005.

[41] S. C. Colbeck. An overview of seasonal snow metamorphism. *Rev. Geophys.*, 20(1):45–61, 1982.

[42] S. C. Colbeck. Snow-crystal growth with varying surface temperatures and radiation penetration. *J. Glaciol.*, 35(119):23–29, 1989.

[43] S. C. Colbeck. A review of sintering in seasonal snow. Technical Report 97-10, U.S. Army Cold Regions Research and Engineering Lab, Hanover, NH, USA, December 1997.

[44] R. L. Cook and K. E. Torrance. A reflectance model for computer graphics. *ACM T. Graphic.*, 1(1):7–24, 1982.

[45] H. Curl, Jr., J. T. Hardy, and R. Ellermeier. Spectral absorption of solar radiation in alpine snowfields. *Ecology*, 53(6):1189–1194, 1972.

[46] B. Curless and M. Levoy. A volumetric method for building complex models from range images. In *Proceedings of the 23rd Annual Conference on Computer Graphics and Interactive Techniques*, SIGGRAPH '96, page 303–312, New York, NY, USA, 1996. Association for Computing Machinery.

[47] F. Dagenais, J. Gagnon, and E. Paquette. An efficient layered simulation workflow for snow imprints. *Visual Comput.*, 32(6):881–890, 2016.

[48] M. G. G. de Camargo, K. Lunau, M. A. Batalha, S. Brings, V. L. G. de Brito, and L. P. C. Morellato. How flower colour signals allure bees and hummingbirds: A community-level test of the bee avoidance hypothesis. *New Phytologist*, 222(2):1112–1122, 2019.

[49] A. Ding, Z. Jiao, Y. Dong, X. Zhang, J. I Peltoniemi, L. Mei, J. Guo, S. Yin, L. Cui, Y. Chang, and R. Xie. Evaluation of the snow albedo retrieved from the snow kernel improved the Ross-Roujean BRDF model. *Remote Sens.*, 11(13):1611, 2019.

[50] F. Domine, R. Salvatori, L. Legagneux, R. Salzano, M. Fily, and R. Casacchia. Correlation between the specific surface area and the short wave infrared (SWIR) reflectance of snow. *Cold regions science and technology*, 46(1):60–68, 2006.

[51] J. Dorsey, H. E. Rushmeier, and F. X. Sillion. *Digital modeling of material appearance*. Morgan Kaufmann/Elsevier, New York, USA, 2008.

[52] J. Dozier, R. E. Davis, and A. W. Nolin. Reflectance and transmittance of snow at high spectral resolution. In *Geoscience and Remote Sensing Symposium (IGARSS)*, pages 662–664. IEEE, 1989.

[53] J. Dozier and T. H. Painter. Multispectral and hyperspectral remote sensing of alpine snow properties. *Annu. Rev. Earth Pl. Sc.*, 32:465–494, 2004.

[54] M. Dumont, O. Brissaud, G. Picard, B. Schmitt, J.-C. Gallet, and Y. Arnaud. High-accuracy measurements of snow bidirectional reflectance distribution function at visible and NIR wavelengths — Comparison with modelling results. *Atmos. Chem. Phys.*, 10(5):2507–2520, 2010.

[55] R. V. Dunkle and J. T. Bevans. An approximate analysis of the solar reflectance and transmittance of a snow cover. *J. Meteorol.*, 13(2):212–216, 1956.

[56] F. Fan and G. V. G. Baranoski. A study on rendering techniques to visually represent sparkles. Technical Report CS-2024-02, University of Waterloo, Waterloo, Canada, 2024.

[57] P. Fearing. Computer modelling of fallen snow. In *Proceedings of the 27th Annual Conference on Computer Graphics and Interactive Techniques (SIGGRAPH'00)*, pages 37–46. Association for Computing Machinery, 2000.

[58] J. A. Ferwerda. Three varieties of realism in computer graphics. In *Human vision and electronic imaging VIII*, volume 5007, pages 290–297. SPIE, 2003.

[59] R. P. Feynman. *Quantum Electrodynamics*. Advanced Book Classics Series. Addison-Wesley, Reading, MA, USA, 1998.

[60] C. Fierz, R. L. Armstrong, Y. Durand, P. Etchevers, E. Greene, D. M. McClung, K. Nishimura, P. K. Satyawali, and S. Sokratov. The international classification for seasonal snow on the ground. Technical Report 83, UNESCO-IHP, Paris, France, 2009.

[61] M. G. Flanner, J. B. Arnheim, J. M. Cook, C. Dang, C. He, X. Huang, D. Singh, S. M. Skiles, C. A. Whicker, and C. S. Zender. SNICAR-ADv3: A community tool for modeling spectral snow albedo. *Geosci. Model. Dev.*, 14(12):7673–7704, 2021.

[62] D. Foldes and B. Benes. Occlusion-based snow accumulation simulation. In John Dingliana and Fabio Ganovelli, editors, *Workshop in Virtual Reality Interactions and Physical Simulation "VRIPHYS" (2007)*, pages 35–41. The Eurographics Association, 2007.

[63] Alain Fournier. From local to global illumination and back. In *Proceedings of Eurographics Workshop on Rendering*, pages 127–136, Dublin, Ireland, June 1995.

[64] J. R. Frisvad, N. J. Christensen, and H. W. Jensen. Computing the scattering properties of participating media using Lorenz-Mie theory. *ACM T. Graph.*, 26(3):60:1–10, July 2007.

[65] B.-C. Gao and A. F. H. Goetz. Column atmospheric water vapor and vegetation liquid water retrievals from airborne imaging spectrometer data. *J. Geoph. Res.-Atmos.*, 95(D4):3549–3564, 1990.

[66] S. D. Gedney. *Introduction to the Finite-Difference Time-Domain (FDTD) Method for Electromagnetics*, volume 27 of *Synthesis digital library of engineering and computer science*. Morgan & Claypool, San Rafael, CA, USA, 1st edition, 2011.

[67] R. W. Gerdel. Penetration of radiation into the snow pack. *EOS T. Am. Geophys. Union*, 29(3):366–374, 1948.

[68] S. Gerland, G. E. Liston, J.-G. Winther, J. B. Ørbæk, and B. V. Ivanov. Attenuation of solar radiation in Arctic snow: Field observations and modelling. *Ann. Glaciol.*, 31:364–368, 2000.

[69] H. Ghiradella, D. Aneshansley, T. Eisner, R. E. Silberglied, and H. E. Hinton. Ultraviolet reflection of a male butterfly: Interference color caused by thin-layer elaboration of wing scales. *Science*, 178(4066):1214–1217, 1972.

[70] J. C. Giddings and E. LaChapelle. Diffusion theory applied to radiant energy distribution and albedo of snow. *J. Geoph. Res.*, 66(1):181–189, 1961.

[71] S. Gilardoni, E. Vignati, and J. Wilson. Using measurements for evaluation of black carbon modeling. *Atmos. Chem. Phys.*, 11(2):439–455, 2011.

[72] A. S. Glassner. *Principles of Digital Image Synthesis*, volume 1. Morgan Kaufmann Publishers, Inc., San Francisco, USA, 1995.

[73] G. Gouesbet and G. Gréhan. *Generalized Lorenz-Mie Theories*. Springer, Cham, Switzerland, 3rd edition, 2023.

[74] R. O. Green, J. Dozier, D. Roberts, and T. Painter. Spectral snow-reflectance models for grain-size and liquid-water fraction in melting snow for the solar-reflected spectrum. *Ann. Glaciol.*, 34:71–73, 2002.

[75] R. O. Green, M. L. Eastwood, C. M. Sarture, T. G. Chrien, M. Aronsson, B. J. Chippendale, J. A. Faust, B. E. Pavri, C. J. Chovit, M. Solis, M. R. Olah, and O. Williams. Imaging spectroscopy and the airborne visible/infrared imaging spectrometer (AVIRIS). *Remote Sens. Environ.*, 65(3):227–248, 1998.

[76] D.P. Greenberg, K.E. Torrance, P. Shirley, J. Arvo, E. Lafortune, J.A. Ferwerda, B. Walter, B. Trumbore, S. Pattanaik, and S.-C. Foo. A framework for realistic image synthesis. In *Proceedings of the 24th annual conference on computer graphics and interactive techniques*, pages 477–494. Association for Computing Machinery, 1997.

[77] T. C. Grenfell and S. G. Warren. Representation of a nonspherical ice particle by a collection of independent spheres for scattering and absorption of radiation. *J. Geoph. Res.-Atmos.*, 104(D24):31697–31709, 1999.

[78] D. C. Gross. Report from the fidelity implementation study group. In *Spring Simulation Interoperability Workshop*, 1999.

[79] W. M. Grundy, S. Douté, and B. Schmitt. A Monte Carlo ray-tracing model for scattering and polarization by large particles with complex shapes. *J. Geoph. Res.-Planet.*, 105(E12):29291–29314, 2000.

[80] D. Güçer and H. B. Özgüç. Simulation of a flowing snow avalanche using molecular dynamics. *Turk. J. Electr. Eng. Co.*, 22(6):1596–1610, 2014.

[81] O. L. Hadley and T. W. Kirchstetter. Black-carbon reduction of snow albedo. *Nat. Clim. Change*, 2(6):437–440, 2012.

[82] H. Haglund, M. Andersson, and A. Hast. Snow accumulation in real-time. In *The Swedish Chapter of Eurographics (SIGRAD 2002)*, pages 11–15. Linköping University Electronic Press, 2002.

[83] G. M. Hale and M. R. Querry. Optical constants of water in the 200-nm to 200-µm wavelength region. *Appl. Optics*, 12(3):555–563, 1973.

[84] D. K. Hall and G. A. Riggs. Accuracy assessment of the MODIS snow products. *Hydrol. Process.*, 21(12):1534–1547, 2007.

[85] R. Hall. Comparing spectral color computation methods. *IEEE Comput. Graph.*, 19(4):36–45, 1999.

[86] L. Hamlin, R. O. Green, P. Mouroulis, M. Eastwood, D. Wilson, M. Dudik, and C. Paine. Imaging spectrometer science measurements for terrestrial ecology: AVIRIS and new developments. In *Aerosp. Conf. Proc.*, pages 1–7. IEEE, 2011.

[87] J. M. Hammersley and D. C. Handscomb. *Monte Carlo Methods*. Chapman and Hall, London, UK, 1964.

[88] P. Han, D. Long, Z. Han, M. Du, L. Dai, and X. Hao. Improved understanding of snowmelt runoff from the headwaters of China's Yangtze River using remotely sensed snow products and hydrological modeling. *Remote Sens. Environ.*, 224:44–59, 2019.

[89] S. Haussener, M. Gergely, M. Schneebeli, and A. Steinfeld. Determination of the macroscopic optical properties of snow based on exact morphology and direct pore-level heat transfer modeling. *J. Geoph. Res.-Earth*, 117(F3), 2012.

[90] D. Hilbert and S. Cohn-Vossen. *Geometry and the Imagination.* AMS Chelsea Publsihing, Providence, RI, USA, 1999.

[91] T. Hinks and K. Museth. Wind-driven snow buildup using a level set approach. In *Eurographics Ireland Workshop Series*, volume 9, pages 19–26, 2009.

[92] G. Hong. Estimating effective snow grain size using normalized channel ratios of MODIS 0.86 and 1.64 micron bands. In *Geoscience and Remote Sensing Symposium (IGARSS)*, pages 2956–2959. IEEE, 2020.

[93] J. J. Hopfield. Olfaction and color vision: More is simpler. In N. P. Ong and R N. Bhatt, editors, *More is different: Fifty years of condensed matter physics*, chapter 17, pages 269–284. Princeton University Press, Princeton, NJ, USA, 2001.

[94] S.-C. Hsu and T.-T. Wong. Simulating dust accumulation. *IEEE Comput. Graph.*, 15(1):18–22, 1995.

[95] S. R. Hudson, S. G. Warren, R. E. Brandt, T. C. Grenfell, and D. Six. Spectral bidirectional reflectance of Antarctic snow: Measurements and parameterization. *J. Geoph. Res.-Atmos.*, 111(D18), 2006.

[96] R. W. G. Hunt and M. Pointer. *Measuring Colour*. Wiley, Chichester, UK, 4th edition, 2011.

[97] Richard S. Hunter and Richard W. Harold. *The Measurement of Appearance*. John Wiley & Sons, Toronto, Canada, 2nd edition, 1987.

[98] S. Jacquemoud, S. Ustin, J. Verdebout, G. Schmuck, G. Andreoli, and B. Hosgood. Estimating leaf biochemistry using PROSPECT leaf optical properties model. *Remote Sens. Environ.*, 56:194–202, 1996.

[99] C. D. Jain, H. S. Gadhavi, T. Wankhede, K. Kallelapu, S. Sudhesh, L. N. Das, R. U. Pai, and A. Jayaraman. Spectral properties of black carbon produced during biomass burning. *Aerosol Air Qual. Res.*, 18(3):671–679, 2018.

[100] B. Jamieson. A synthesis of geological hazards in Canada. In G. R. Brooks, editor, *Geological Survey of Canada Bulletin: Bulletin 548*, chapter Snow avalanches, pages 75–94. Natural Resources Canada, Ottawa, Canada, 2001.

[101] J. B. Jamieson. *Avalanche Prediction for Persistent Snow Slabs*. PhD thesis, The University of Calgary, Calgary, AB, Canada, November 1995.

[102] A. Jarabo, C. Aliaga, and D. Gutierrez. A radiative transfer framework for spatially-correlated materials. *ACM Trans. Graph.*, 37(4):83:1–13, 2018.

[103] S. G. Jennings and R. G. Pinnick. Relationships between visible extinction, absorption and mass concentration of carbonaceous smokes. *Atmos. Environ.*, 14(10):1123–1129, 1980.

[104] Z. Jiao, A. Ding, A. Kokhanovsky, C. Schaaf, F.-M. Bréon, Y. Dong, Z. Wang, Y. Liu, X. Zhang, S. Yin, L. Cui, L. Mei, and Y. Chang. Development of a snow kernel to better model the anisotropic reflectance of pure snow in a kernel-driven BRDF model framework. *Remote Sens. Environ.*, 221:198–209, 2019.

[105] Z. Jin, T. P. Charlock, P. Yang, Y. Xie, and W. Miller. Snow optical properties for different particle shapes with application to snow grain size retrieval and MODIS/CERES radiance comparison over Antarctica. *Remote Sens. Environ.*, 112(9):3563–3581, 2008.

[106] G. M. Johnson and M. D. Fairchild. Full-spectral color calculations in realistic image synthesis. *IEEE Comput. Graph.*, 19(4):47–53, 1999.

[107] I. T. Jolliffe. *Principal component analysis*. Springer-Verlag, New York, New York, 2nd edition, 2002.

[108] J. H. Joseph, W. J. Wiscombe, and J. A. Weinman. The delta-Eddington approximation for radiative flux transfer. *J. Atmos. Sci.*, 33(12):2452–2459, 1976.

[109] A. Jubert. Simulation du transport de neige. Master's thesis, Université de Montréal, Montreal, QC, Canada, July 2018.

[110] D. B. Judd. Terms, definitions, and symbols in reflectometry. *J. Opt. Soc. Am.*, 57(4):445–452, Apr 1967.

[111] T. U. Kaempfer, M. A. Hopkins, and D. K. Perovich. A three-dimensional microstructure-based photon-tracking model of radiative transfer in snow. *J. Geoph. Res.-Atmos.*, 112(D24), 2007.

[112] J. T. Kajiya. The rendering equation. In *Proceedings of the 13th Annual Conference on Computer Graphics and Interactive Techniques (SIGGRAPH'86)*, pages 143–150, New York, NY, USA, 1986. ACM.

[113] J. Kessenich, G. Sellers, and D. Shreiner. *OpenGL® Programming Guide: The Official Guide to Learning OpenGL®, Version 4.5 with SPIR-V*. Addison-Wesley, Toronto, Canada, 9th edition, 2016.

[114] S. L. Kimball, B. D. Bennett, and F. B. Salisbury. The growth and development of montane species at near-freezing temperatures. *Ecology*, 54(1):168–173, 1973.

[115] B. W. Kimmel and G. V. G. Baranoski. A novel approach for simulating light interaction with particulate materials: Application to the modeling of sand spectral properties. *Opt. Express*, 15(15):9755–9777, 2007.

[116] B. W. Kimmel, G. V. G. Baranoski, T. F. Chen, D. Yim, and E. Miranda. Spectral appearance changes induced by light exposure. *ACM T. Graphic.*, 32(1), February 2013.

[117] N. J. Kinar and J. W. Pomeroy. Measurement of the physical properties of the snowpack. *Rev. Geophys.*, 53(2):481–544, 2015.

[118] T. W. Kirchstetter, T. Novakov, and P. V. Hobbs. Evidence that the spectral dependence of light absorption by aerosols is affected by organic carbon. *J. Geoph. Res.-Atmos.*, 109(D21), 2004.

[119] W. H. Knap and C. H. Reijmer. Anisotropy of the reflected radiation field over melting glacier ice: Measurements in Landsat TM bands 2 and 4. *Remote Sens. Environ.*, 65(1):93–104, 1998.

[120] A. A. Kokhanovsky. *Aerosol Optics: Light Absorption and Scattering by Particles in the Atmosphere.* Springer Science & Business Media, New York, NY, USA, 2008.

[121] A. A. Kokhanovsky and E. P. Zege. Scattering optics of snow. *Appl. Optics*, 43(7):1589–1602, 2004.

[122] L. Kou. *Black carbon: Atmospheric measurements and radiative effect.* PhD thesis, Dalhousie University, 10 1996.

[123] B. Kravchenko, G. V. G. Baranoski, T. F. Chen, E. Miranda, and S. R. Van Leeuwen. High-fidelity iridal light transport simulations at interactive rates. *Comput. Anim. Virtual Worlds*, 28(1755):1–10, 2017.

[124] A. Krishnaswamy, G. V. G. Baranoski, and J. G. Rokne. Improving the reliability/cost ratio of goniophotometric comparisons. *J. Graph. Tools*, 9(3):1–20, 2004.

[125] W. Krueger. Intensity fluctuations and natural texturing. In *Proceedings of the 15th Annual Conference on Computer Graphics and Interactive Techniques (SIGGRAPH'88)*, pages 213–220, New York, NY, USA, 1988. Association for Computing Machinery.

[126] M. Kuhn. Spectroscopic studies at McMurdo, South Pole and Siple stations during the austral summer 1977-78. *Antarct. J. U.S.*, 13:178–179, 1978.

[127] M. Kuhn. Bidirectional reflectance of polar and alpine snow surfaces. *Ann. Glaciol.*, 6:164–167, 1985.

[128] M. S. Langer, L. Zhang, A. W. Klein, A. Bhatia, J. Pereira, and D. Rekhi. A spectral-particle hybrid method for rendering falling snow. In *Proceedings of the Fifteenth Eurographics Conference on Rendering Techniques*, EGSR'04, page 217–226, Goslar, DEU, 2004. Eurographics Association.

[129] X. Liu, Y. Chen, H. Zhang, Y. Zou, Z. Wang, and Q. Peng. Physically based modeling and rendering of avalanches. *Visual Comput.*, 37:2619–2629, 2021.

[130] A. Lyapustin, M. Tedesco, Y. Wang, T. Aoki, M. Hori, and A. Kokhanovsky. Retrieval of snow grain size over Greenland from MODIS. *Remote Sens. Environ.*, 113(9):1976–1987, 2009.

[131] M. Mahy, L. Van Eycken, and A. Oosterlinck. Evaluation of uniform color spaces developed after the adoption of CIELAB and CIELUV. *Color Res. Appl.*, 19(2):105–121, 1994.

[132] N. Maréchal, E. Guérin, E. Galin, S. Mérillou, and N. Mérillou. Heat transfer simulation for modeling realistic winter sceneries. *Comput. Graph. Forum*, 29(2):449–458, 2010.

[133] D. McClung and P. A. Schaerer. *The Avalanche Handbook*. The Mountaineers Press, Seattle, WA, USA, 3rd edition, 2006.

[134] S. Mekhontsev, A. Prokhorov, and L. Hanssen. Experimental characterization of blackbody radiation sources. In Z. M. Zhang, B. K. Tsai, and G. Machin, editors, *Radiometri Temperature Measurements II: Applications*, volume 43 of *Experimental Methods in the Physical Sciences*, chapter 2, pages 57–136. Elsevier, Boston, USA, 2010.

[135] J. Meng, M. Papas, R. Habel, C. Dachsbacher, S. Marschner, M. Gross, and W. Jarosz. Multi-scale modeling and rendering of granular materials. *ACM Trans. Graph.*, 34(4):49:1–13, 2015.

[136] S. Metsämäki, K. Böttcher, J. Pulliainen, K. Luojus, J. Cohen, M. Takala, O.-P. Mattila, G. Schwaizer, C. Derksen, and S. Koponen. The accuracy of snow melt-off day derived from optical and microwave radiometer data–a study for Europe. *Remote Sens. Environ.*, 211:1–12, 2018.

[137] W. E. K. Middleton and A. G. Mungall. The luminous directional reflectance of snow. *J. Opt. Soc. Am.*, 42(8):572–579, 1952.

[138] M. G. J. Minnaert. *Light and Color in the Outdoors*. Springer-Verlag, New York, USA, 1993. Translated and Revised by Len Seymour.

[139] Michael I. Mishchenko, Janna M. Dlugach, Edgard G. Yanovitskij, and Nadia T. Zakharova. Bidirectional reflectance of flat, optically thick particulate layers: An efficient radiative transfer solution and applications to snow and soil surfaces. *J. Quant. Spectrosc. Ra.*, 63(2-6):409–432, 1999.

[140] R. Mitra, S. F. McGough, T. Chakraborti, C. Holmes, R. Copping, N. Hagenbuch, S. Biedermann, J. Noonan, B. Lehmann, A. Shenvi, X. V. Doan, D. Leslie, G. Bianconi, R. Sanchez-Garcia, A. Davies, M. Mackintosh, E.-R. Andrinopoulou, A. Basiri, C. Harbron, and B. D. MacArthur. Learning from data with structured missingness. *Nat. Mach. Intell.*, 5(1):13–23, 2023.

[141] T. B. Moeslund, C. B. Madsen, M. Aagaard, and D. Lerche. Modeling Falling and Accumulating Snow. In Mike Chantler, editor, *Vision, Video, and Graphics (2005)*. The Eurographics Association, 2005.

[142] K. Muraoka and N. Chiba. Visual simulation of snowfall, snow cover and snowmelt. In *Proceedings Seventh International Conference on Parallel and Distributed Systems: Workshops*, pages 187–194. IEEE, 2000.

[143] F. K. Musgrave. Prisms and rainbows: a dispersion model for computer graphics. In *Proceedings of Graphics Interface '89*, pages 227–234, Toronto, Ontario, Canada, 1989. Canadian Man-Computer Communications Society.

[144] T. Nakamura, O. Abe, T. Hasegawa, R. Tamura, and T. Ohta. Spectral reflectance of snow with a known grain-size distribution in successive metamorphism. *Cold Reg. Sci. Technol.*, 32(1):13–26, 2001.

[145] Natural Phenomena Simulation Group. *Run SPLITSnow Online (Goniometric Mode)*. Waterloo, Canada, 2020. http://www.npsg.uwaterloo.ca/models/splitsnow-gonio.php.

[146] Natural Phenomena Simulation Group. *Run SPLITSnow Online (Spectrometric Mode)*. Waterloo, Canada, 2020. http://www.npsg.uwaterloo.ca/models/splitsnow-i.php.

[147] Natural Phenomena Simulation Group. *Snow Data*. Waterloo, Canada, 2020. http://www.npsg.uwaterloo.ca/data/snow.php.

[148] Natural Phenomena Simulation Group. *Run SPLITSnow Online (Heterogeneous Spectrometric Mode)*. Waterloo, Canada, 2024. http://www.npsg.uwaterloo.ca/models/splitsnow-h.php.

[149] Natural Phenomena Simulation Group. *Run SPLITSnow Online (Multi-layer Spectrometric Mode)*. Waterloo, Canada, 2024. http://www.npsg.uwaterloo.ca/models/splitsnow-ml.php.

[150] M. Nguyen, J.-B. Thomas, and I. Farup. Statistical analysis of sparkle in snow images. *J. Imaging Sci. Techn.*, 66(5):050404:1–11, 2022.

[151] M. Nguyen, J.-B. Thomas, and I. Farup. Exploring imaging methods for *in situ* measurements of the visual appearance of snow. *Geosci.*, 14(2):35:1–15, 2024.

[152] F. E. Nicodemus. Directional reflectance and emissivity of an opaque surface. *Appl. Opt.*, 4(7):767–775, Jul 1965.

[153] F. E. Nicodemus. Reflectance nomenclature and directional reflectance and emissivity. *Appl. Opt.*, 9(6):1474–1475, Jun 1970.

[154] F. E. Nicodemus, J. C. Richmond, J. J. Hsia, I. W. Ginsberg, and T. Limperis. *Geometrical considerations and nomenclature for reflectance*. US Department of Commerce, National Bureau of Standards, Washington, D.C., USA, 1977.

[155] T. Nishita, H. Iwasaki, Y. Dobashi, and E. Nakamae. A modeling and rendering method for snow by using metaballs. *Comput. Graph. Forum*, 16(3):C357–C364, 1997.

[156] A. W. Nolin and J. Dozier. Estimating snow grain size using AVIRIS data. *Remote Sens. Environ.*, 44(2-3):231–238, 1993.

[157] A. W. Nolin and J. Dozier. A hyperspectral method for remotely sensing the grain size of snow. *Remote Sens. Environ.*, 74(2):207–216, 2000.

[158] P. Ohlsson and S. Seipel. Real-time rendering of accumulated snow. In *The Swedish Chapter of Eurographics (SIGRAD 2004)*, number 7 in 13, pages 25–31. Linköping University Electronic Press, 2004.

[159] J. Ollerhead. Light transmittance through dry, sieve sand: Some test results. *Ancient TL*, 19(1):13–17, 2001.

[160] M. R. Olson, V. M. Garcia, M. A. Robinson, P. Van Rooy, M. A. Dietenberger, M. Bergin, and J. J. Schauer. Investigation of black and brown carbon multiple-wavelength-dependent light absorption from biomass and fossil fuel combustion source emissions. *J. Geoph. Res.-Atmos.*, 120(13):6682–6697, 2015.

[161] M. R. Olson, W. Yuqin, B. de Foy, Z. Li, M. H. Bergin, Y. Zhang, and J. J. Schauer. Source attribution of black and brown carbon near-UV light absorption in Beijing, China and the impact of regional air-mass transport. *Sci. total env.*, 807(2):150871:1–11, 2022.

[162] S. Osher and J. A. Sethian. Fronts propagating with curvature-dependent speed: Algorithms based on Hamilton-Jacobi formulations. *J. Comput. Phys.*, 79(1):12–49, 1988.

[163] T. H. Painter and J. Dozier. Measurements of the hemispherical-directional reflectance of snow at fine spectral and angular resolution. *J. Geoph. Res.-Atmos.*, 109(D18), 2004.

[164] K. F. Palmer and D. Williams. Optical properties of water in the near infrared. *J. Opt. Soc. Am.*, 64(8):1107–1110, 1974.

[165] K. Park, J. C. Chow, J. G. Watson, D. L. Trimble, P. Doraiswamy, K. Park, W. P. Arnott, K. R. Stroud, K. Bowers, R. Bode, A. Petzold, and A. D. A. Hansen. Comparison of continuous and filter-based carbon measurements at the Fresno supersite. *J. Air Waste Ma.*, 56(4):474–491, 2012.

[166] A. Patil, G. Singh, S. Kumar, S. Mani, D. Bandyopadhyay, B. R. Nela, M. Musthafa, and S. Mohanty. Snow characterization and avalanche detection in the Indian Himalaya. In *Geoscience and Remote Sensing Symposium (IGARSS)*, pages 2005–2008. IEEE, 2020.

[167] F. L. Pedrotti and L. S. Pedrotti. *Introduction to Optics*. Prentice Hall, Upper Saddle River, NJ, USA, 2nd edition, 1993.

[168] R. D. Peng. Reproducible research in computational science. *Science*, 334(6060):1226–1227, 2011.

[169] D. K. Perovich. Light reflection and transmission by a temperate snow cover. *J. Glaciol.*, 53(181):201–210, 2007.

[170] M. P. Petrov, A. Y. Terzhevik, N. I. Palshin, R. E. Zdorovennov, and G. E. Zdorovennova. Absorption of solar radiation by snow-and-ice cover of lakes. *Water Resour.*, 32(5):496–504, 2005.

[171] M. Pharr, W. Jakob, and G. Humphreys. *Physically based rendering: From theory to implementation*. Morgan Kaufmann, Cambridge, MA, USA, 3rd edition, 2016.

[172] G. Picard, L. Arnaud, F. Domine, and M. Fily. Determining snow specific surface area from near-infrared reflectance measurements: Numerical study of the influence of grain shape. *Cold Reg. Sci. Technol.*, 56(1):10–17, 2009.

[173] G. Picard, M. Sandells, and H. Löwe. SMRT: An active–passive microwave radiative transfer model for snow with multiple microstructure and scattering formulations (v1.0). *Geosci. Model. Dev.*, 11(7):2763–2788, 2018.

[174] R. M. Pope and E. S. Fry. Absorption spectrum (380–700 nm) of pure water. II. Integrating cavity measurements. *Appl. Optics*, 36(33):8710–8723, 1997.

[175] P. Poulin and A. Fournier. A model for anisotropic reflection. In *Proceedings of the 17th Annual Conference on Computer Graphics and Interactive Techniques (SIGGRAPH'90)*, SIGGRAPH '90, page 273–282, New York, NY, USA, 1990. Association for Computing Machinery.

[176] W. K. Pratt. *Digital Image Processing*. Wiley, Hoboken, New Jersey, 4th edition, 2007.

[177] S. Premože, W. B. Thompson, and P. Shirley. Geospecific rendering of alpine terrain. In *Eurographics Workshop on Rendering Techniques*, pages 107–118. Springer, 1999.

[178] S. Ramachandran and S. Kedia. Black carbon aerosols over an urban region: Radiative forcing and climate impact. *J. Geoph. Res.-Atmos.*, 115(D10), 2010.

[179] S. Ramachandran and T. A. Rajesh. Black carbon aerosol mass concentrations over Ahmedabad, an urban location in western India: Comparison with urban sites in Asia, Europe, Canada, and the United States. *J. Geoph. Res.-Atmos.*, 112(D6), 2007.

[180] W. T. Reeves. Particle systems — A technique for modeling a class of fuzzy objects. *ACM T. Graphic.*, 2(2):91–108, 1983.

[181] D. T. Reynolds, S. D. Laycock, and A. M. Day. Real-time accumulation of occlusion-based snow. *Visual Comput.*, 31(5):689–700, 2015.

[182] S. G. Richardson and F. B. Salisbury. Plant responese to the light penetrating snow. *Ecology*, 58(5):1152–1158, 1977.

[183] N. A. Riley. Projection sphericity. *J. Sediment. Res.*, 11(2):94–95, 1941.

[184] T. M. Robson and P. J. Aphalo. Transmission of ultraviolet, visible and near-infrared radiation to plants within a seasonal snowpack. *Photochem. Photobiol. Sci.*, 18(1):1963–1971, 2019.

[185] S. M. Ross. *A first course in probability*. Prentice Hall, Upper Saddle River, NJ, USA, 5th edition, 1998.

[186] S. D. Roth. Ray casting for modeling solids. *Computer Graphics and Image Processing*, 18(2):109–144, 1982.

[187] J. R. Rumble, editor. *CRC Handbook of Chemisty and Physics*. CRC Press/Taylor & Francis, Boca Raton, FL, USA, 100$^{\text{th}}$ edition, 2019. (Internet Version).

[188] S. B. Rumpf, M. Gravey, O. Brönnimann, M. Luoto, C. Cianfrani, G. Mariethoz, and A. Guisan. From white to green: Snow cover loss and increased vegetation productivity in the European Alps. *Science*, 376(6597):1119–1122, 2022.

[189] T. Saarinen, S. Rasmus, R. Lundell, O.-K. Kauppinen, and H. Hänninen. Photosynthetic and phenological responses of dwarf shrubs to the depth and properties of snow. *Oikos*, 125(3):364–373, 2016.

[190] R. Salvatori, R. Salzano, M. Valt, R. Cerrato, and S. Ghergo. The collection of hyperspectral measurements on snow and ice covers in polar regions (SISpec 2.0). *Remote Sensing*, 14(9):2213:1–14, 2022.

[191] R. Salzano. Private Communication, March 2023.

[192] G. Schaepman-Strub, M. E. Schaepman, T. H. Painter, S. Dangel, and J. V. Martonchik. Reflectance quantities in optical remote sensing — Definitions and case studies. *Remote Sens. Environ.*, 103(1):27–42, 2006.

[193] J. Schweizer, J. B. Jamieson, and M. Schneebeli. Snow avalanche formation. *Rev. Geophys.*, 41(4), 2003.

[194] J. Schweizer and M. Lütschg. Characteristics of human-triggered avalanches. *Cold Reg. Sci. Technol.*, 33(2-3):147–162, 2001.

[195] S. Segura, V. Estellés, G. Titos, H. Lyamani, M. P. Utrillas, P. Zotter, A. Stephan H. Prévôt, G. Močnik, L. Alados-Arboledas, and J. A. Martínez-Lozano. Determination and analysis of *in situ* spectral aerosol optical properties by a multi-instrumental approach. *Atmos. Meas. Tech.*, 7(8):2373–2387, 2014.

[196] G. Sellers. *Vulkan programming guide: The official guide to learning Vulkan*. Addison-Wesley, Boston, USA, 2017.

[197] S. Sharma, W. R. Leaitch, L. Huang, D. Veber, F. Kolonjari, W. Zhang, S. J. Hanna, A. K. Bertram, and J. A. Ogren. An evaluation of three methods for measuring black carbon in Alert, Canada. *Atmos. Chem. Phys.*, 17(24):15225–15243, 2017.

[198] P. Shirley. *Physically Based Lighting Calculations for Computer Graphics*. PhD thesis, University of Illinois at Urbana-Champaign, December 1985.

[199] K. Sims. Particle animation and rendering using data parallel computation. In *Proceedings of the 17th Annual Conference on Computer Graphics and Interactive Techniques*, page 405–413, New York, NY, USA, 1990. Association for Computing Machinery.

[200] M. D. Skogen, R. Ji, A. Akimova, U. Daewel, C. Hansen, S. S. Hjøllo, S. M. van Leeuwen, M. Maar, D. Macias, E. A. Mousing, E. Almroth-Rosell, S. F. Sailley, M. A. Spence, T. A. Troost, and K. van de Wolfshaar. Disclosing the truth: Are models better than observations? *Marine ecology. Progress series (Halstenbek)*, 680:7–13, 2021.

[201] B. Srinivas and M. M. Sarin. Brown carbon in atmospheric outflow from the Indo-Gangetic Plain: Mass absorption efficiency and temporal variability. *Atmos. Environ.*, 89:835–843, 2014.

[202] K. Stamnes, S.-C. Tsay, W. Wiscombe, and K. Jayaweera. Numerically stable algorithm for discrete-ordinate-method radiative transfer in multiple scattering and emitting layered media. *Appl. Optics*, 27(12):2502–2509, June 1988.

[203] C. Stethem, B. Jamieson, P. Schaerer, D. Liverman, D. Germain, and S. Walker. Snow avalanche hazard in Canada — A review. *Nat. Hazards*, 28(2):487–515, 2003.

[204] M. Stokes, M. D. Fairchild, and R. S. Berns. Precision requirements for digital color reproduction. *ACM T. Graph.*, 11(4):406–422, October 1992.

[205] A. Stomakhin, C. Schroeder, L. Chai, J. Teran, and A. Selle. A material point method for snow simulation. *ACM T. Graphic.*, 32(4):102:1–9, 2013.

[206] M. C. Stone. *A Field Guide to Digital Color*. A K Peters, Natick, MA, USA, 2003.

[207] R. Sumner, J. F. O'Brien, and J. K. Hodgins. Animating sand, mud, and snow. *Comput. Graph. Forum*, 18(1):17–26, March 1999.

[208] M. Tester and C. Morris. The penetration of light through soil. *Plant Cell Environ.*, 10:281–286, 1987.

[209] J. L. Thomas, C. M. Polashenski, A. J. Soja, L. Marelle, K. A. Casey, H. D. Choi, J.-C. Raut, C. Wiedinmyer, L. K. Emmons, J. D. Fast, J. Pelon, K. S. Law, M. G. Flanner, and J. E. Dibb. Quantifying black carbon deposition over the greenland ice sheet from forest fires in Canada. *Geophys. Res. Lett.*, 44(15):7965–7974, 2017.

[210] D. R. Thompson, B.-C. Gao, R. O. Green, D. A. Roberts, P. E. Dennison, and S. R. Lundeen. Atmospheric correction for global mapping spectroscopy: ATREM advances for the HyspIRI preparatory campaign. *Remote Sens. Environ.*, 167:64–77, 2015.

[211] J. Tian and W. D. Philpot. Spectral transmittance of a translucent sand sample with directional illumination. *IEEE T. Geosci. Remote*, 56(8):4307–4317, 2018.

[212] K. Tokoi. A shadow buffer technique for simulating snow-covered shapes. In *International Conference on Computer Graphics, Imaging and Visualisation (CGIV'06)*, pages 310–316. IEEE, 2006.

[213] K. E. Torrance and E. M. Sparrow. Theory for off-specular reflection from roughened surfaces. *J. Opt. Soc. Am.*, 57(9):1105–1114, 1967.

[214] N. v. Festenberg and S. Gumhold. A geometric algorithm for snow distribution in virtual scenes. In Eric Galin and Jens Schneider, editors, *Eurographics Workshop on Natural Phenomena*. The Eurographics Association, 2009.

[215] N. v. Festenberg and S. Gumhold. Diffusion-based snow cover generation. *Comput. Graph. Forum*, 30(6):1837–1849, 2011.

[216] P. M. Varsa and G. V. G. Baranoski. *In silico* assessment of light penetration into snow: Implications to the prediction of slab failures leading to avalanches. In K. Schulz, editor, *Proc. SPIE 11863*, pages 1186305:1–10, online only, September 2021. SPIE.

[217] P. M. Varsa and G. V. G. Baranoski. On the sensitivity of snow bidirectional reflectance to variations in grain characteristics. In C.M.U. Neale and A. Maltese, editors, *Proc. SPIE 11856*, pages 118560G:1–10, online only, September 2021. SPIE.

[218] P. M. Varsa and G. V. G. Baranoski. Rendering the bluish appearance of snow: When light transmission matters. *IEEE Comput. Graph.*, 44(1):50–61, January/February 2024.

[219] P. M. Varsa, G. V. G. Baranoski, and B. W. Kimmel. SPLITSnow: A spectral light transport model for snow. *Remote Sens. Environ.*, 255:112272:1–20, 2021.

[220] E. Veach. *Robust Monte Carlo Methods for Light Transport Simulation*. PhD thesis, Stanford University, California, USA, December 1997.

[221] M. J. Vepraskas and D. K. Cassel. Sphericity and roundness of sand in coastal plain soils and relationships with soil physical properties 1. *Soil Sci. Soc. Am. J.*, 51(5):1108–1112, 1987.

[222] B. Voight, B. R. Armstrong, R. L. Armstrong, D. Bachman, D. Bowles, R. L. Brown, R. D. Faisant, S. A. Ferguson, J. A. Fredston, J. L. Kennedy, J. Kiusalaas, E. R. LaChapelle, R. C. McFarlane, R. Newcomb, R. Penniman, and R. Perla. *Snow avalanche hazards and mitigation in the United States*. The National Academies Press, Washington, DC, USA, 1990.

[223] W. Wagner, J. R. Cooper, A. Dittmann, J. Kijima, H.-J. Kretzschmar, A. Kruse, R. Mareš, K. Oguchi, H. Sato, I. Stöcker, O. Šifner, Y. Takaishi, I. Tanishita, J. Trübenbach, and T. Willkommen. The IAPWS industrial formulation 1997 for the thermodynamic properties of water and steam. *J. Eng. Gas Turb. Power*, 122(1):150–184, 2000.

[224] D. A. Walker, W. D. Billings, and J. G. de Molenaar. *Snow Ecology: An Interdisciplinary Examination of Snow-Covered Ecosystems*, chapter Snow-vegetation interactions in tundra environments. Cambridge University Press, Cambridge, UK, 2001.

[225] B. Wang, H. Deng, and N. Holzschuch. Real-time glints rendering with pre-filtered discrete stochastic microfacets. *Comput. Graph. Forum*, 39(6):144–154, 2020.

[226] B. Wang, D. Su, and J. Liu. Analysis of snow covered radome with ray tracing method. In *APMC 2005*, volume 2, pages 1–3. IEEE, December 2005.

[227] C. Wang, Z. Wang, T. Xia, and Q. Peng. Real-time snowing simulation. *Visual Comput.*, 22(5):315–323, 2006.

[228] S. G. Warren. Can black carbon in snow be detected by remote sensing? *J. Geoph. Res.-Atmos.*, 118(2):779–786, 2013.

[229] S. G. Warren. Optical properties of ice and snow. *Philos. T. Roy. Soc. A*, 377(2146):20180161–20180161, 2019.

[230] S. G. Warren and R. E. Brandt. Optical constants of ice from the ultraviolet to the microwave: A revised compilation. *J. Geoph. Res.-Atmos.*, 113(D14):D14220:1–10, 2008.

[231] S. G. Warren, R. E. Brandt, and P. O'Rawe Hinton. Effect of surface roughness on bidirectional reflectance of Antarctic snow. *J. Geoph. Res.-Planet.*, 103(E11):25789–25807, 1998.

[232] S. G. Warren and W. J. Wiscombe. A model for the spectral albedo of snow. II: Snow containing atmospheric aerosols. *J. Atmos. Sci.*, 37(12):2734–2745, 1980.

[233] L. Wasserman. *All of Statistics: A Concise Course in Statistical Inference*. Springer, New York, NY, USA, 2004.

[234] J. G. Watson, Chow J. C., and L.-W. A Chen. Summary of organic and elemental carbon/black carbon analysis methods and intercomparisons. *Aerosol Air Qual. Res.*, 5(1):65–102, 2005.

[235] W. J. Wiscombe and S. G. Warren. A model for the spectral albedo of snow. I: Pure snow. *J. Atmos. Sci.*, 37(12):2712–2733, 1980.

[236] J. Wolper, Y. Chen, M. Li, Y. Fang, Z. Qu, J. Lu, M. Cheng, and C. Jiang. AnisoMPM: Animating anisotropic damage mechanics. *ACM T. Graphic.*, 39(4), aug 2020.

[237] S.-K. Wong and I-T. Fu. Hybrid-based snow simulation and snow rendering with shell textures. *Comput. Animat. Virt. Worlds*, 26(3–4):413–421, may 2015.

[238] J. T. Woolley and E. W. Stoller. Light penetration and light-induced seed germination in soil. *Plant Physiol.*, 61:597–600, 1978.

[239] C. Xiong and J. Shi. Simulating polarized light scattering in terrestrial snow based on bicontinuous random medium and Monte Carlo ray tracing. *J. Quant. Spectrosc. Ra.*, 133:177–189, 2014.

[240] C. Xiong and J. Shi. A new snow light scattering model and its application in snow parameter retrieval from satellite remote sensing. In *Geoscience and Remote Sensing Symposium (IGARSS)*, pages 1473–1476. IEEE, 2017.

[241] C. Xiong and J. Shi. Snow specific surface area remote sensing retrieval using a microstructure based reflectance model. *Remote Sens. Environ.*, 204:838–849, 2018.

[242] C. Xiong, J. Shi, D. Ji, T. Wang, Y. Xu, and T. Zhao. A new hybrid snow light scattering model based on geometric optics theory and vector radiative transfer theory. *IEEE T. Geosci. Remote*, 53(9):4862–4875, 2015.

[243] P. Yang and K. N. Liou. Geometric-optics-integral-equation method for light scattering by nonspherical ice crystals. *Appl. Optics*, 35(33):6568–6584, 1996.

[244] C. Yanyun, H. Sun, L. Hui, and E. Wu. Modelling and rendering of snowy natural scenery using multi-mapping techniques. *J. Visual. Comp. Animat.*, 14(1):21–30, 2003.

[245] X. Zhou, S. Li, and K. Stamnes. Effects of vertical inhomogeneity on snow spectral albedo and its implication for optical remote sensing of snow. *J. Geoph. Res.-Atmos.*, 108(D23):4738, 2003.

[246] T. Zirr and A. S. Kaplanyan. Real-time rendering of procedural multiscale materials. In *Proceedings of the 20th Annual Conference on Computer Graphics and Interactive Techniques (SIGGRAPH'16)*, I3D '16, page 139–148, New York, NY, USA, 2016. Association for Computing Machinery.

# APPENDICES

# Appendix A

# Optical Concepts and Terminology

This appendix describes the equations governing the transmission of EM radiation (light) from one medium into another that are particularly relevant for the work described in this thesis. In Section A.1, we provide the equations used to determine the fraction of EM radiation that is refracted vs. reflected at the interface boundary between two media. In Section A.2, we provide the equations to compute Snell's law. For many elementary purposes, the simplified version of Snell's law (Equation 2.3) may be employed. However, for the predictive simulation of light transport through various media, the equations that incorporate the complex index of refraction may be beneficial to use. More detailed descriptions of the equations provided in this appendix can be found in more comprehensive texts in this area such as the book by Pedrotti and Pedrotti [167].

We remark that both the real and complex parts of the indices of refraction are functions of the wavelength ($\lambda$) of light. For conciseness, this dependency is omitted in the equations presented in this chapter.

## A.1 Fresnel Equations

When light passes from one medium into a second medium, some fraction of the light will be *reflected* back into the first medium while the rest will be *refracted* into the second medium. The ratio of light reflected at a plane is given by the Fresnel equations [167]. These equations are dependent upon the indices of refraction of the materials, the angle of incidence and the polarization of the incident light.

The parallel (transverse magnetic) Fresnel coefficient ($\mathscr{F}_{r_\parallel}$) and perpendicular (transverse electric) Fresnel coefficient ($\mathscr{F}_{r_\perp}$) for reflection of polarized light are given by the following equations:

$$\mathscr{F}_{r_\parallel} = \frac{\cos\theta_i - \sqrt{\eta^2 - \sin^2\theta_i}}{\cos\theta_i + \sqrt{\eta^2 - \sin^2\theta_i}}, \tag{A.1}$$

and

$$\mathscr{F}_{r_\perp} = -\frac{\eta^2\cos\theta_i - \sqrt{\eta^2 - \sin^2\theta_i}}{\eta^2\cos\theta_i + \sqrt{\eta^2 - \sin^2\theta_i}}, \tag{A.2}$$

where $\theta_i$ is the angle of incidence for the incoming ray and $\eta = \eta_t/\eta_i$ is the relative index of refraction for complex indices of refraction $\eta_i$ and $\eta_t$. The respective reflectivities are given by $R_\parallel = \mathscr{F}_{r_\parallel}^2$ and $R_\perp = \mathscr{F}_{r_\perp}^2$. When one considers unpolarized light, which is the aim in most computer graphics applications [198], $R_\parallel$ and $R_\perp$ are averaged [167] to compute a single Fresnel coefficient.

## A.2 Snell's Law

Recall from Section 2.1.4 of Chapter 2, that the form of the complex index of refraction primarily used in this thesis is given by Equation 2.4. We repeat it here for convenience. Namely,

$$\eta = \boldsymbol{n} + ik. \tag{A.3}$$

Another representation of the complex index of refraction is:

$$\eta = \boldsymbol{n}(1 + i\mathscr{K}), \tag{A.4}$$

where $\eta$ and $\boldsymbol{n}$ are the same as in Equation 2.4, and $\mathscr{K}$ is related to $k$ as follows:

$$k = \boldsymbol{n}\mathscr{K}. \tag{A.5}$$

Various names have been given to $k$ and $\mathscr{K}$ in the literature. We continue to refer to $k$ as the complex part of the index of refraction and refer to $\mathscr{K}$ as the absorption index [167]. We note that the absorption index, $\mathscr{K}$, is employed in the remaining equations to be presented in this section.

Snell's law [167] is used to describe light refraction at a given interface between the two media, and the geometry employed in its formulation is schematically presented in Figure 2.5. This law is expressed as:

$$\frac{\sin\theta_i}{\sin\theta_t} = \frac{\boldsymbol{n}_t}{\boldsymbol{n}_i} \tag{A.6}$$

where $n_t$ represents the real part of the index of refraction for the transmitted material, $n_i$ represents the real part of the index of refraction for the incident material, $\theta_i$ represents the angle of incidence which is measured away from the normal to the surface, and $\theta_t$ represents the angle of refraction, which is measured away from the direction opposite to the normal of the surface.

It is worth noting that, when the complex index of refraction is employed at an interface boundary between one or more conductors, the angle of refraction, $\theta_t$, may be evaluated as follows [167]:

$$\cos\theta_t = \frac{n q(\cos\psi - \kappa \sin\psi)}{\sin^2\theta_i + n^2 q^2(\cos\psi - \kappa\sin\psi)^2}, \tag{A.7}$$

where $\eta = n(1 + i\kappa)$ is the representation of the index of refraction given in Equation A.4. and:

$$q = \left(\left(1 - \frac{1-\kappa^2}{n^2(1+\kappa^2)^2}\sin^2\theta_i\right)^2 + \left(\frac{2\kappa}{n^2(1+\kappa^2)^2}\sin^2\theta_i\right)^2\right)^{\frac{1}{4}}, \tag{A.8}$$

and

$$\psi = \frac{1}{2}\tan^{-1}\left(\frac{2\kappa\sin^2\theta_i}{n^2(1+\kappa^2)^2 - (1-\kappa^2)\sin^2\theta_i}\right). \tag{A.9}$$

# Appendix B

# Average Particle Distance Computation

In this appendix, we outline the main steps involved in the computation of the mean distance between grains, which is denoted by $\overline{d}$ and used in Equation (4.1). We remark that this quantity is dependent upon the density ($D$) of the snow sample. We begin with a treatment for homogeneous virtual snow samples in Section B.1, and then generalize this formulation to heterogeneous snow samples in Section B.2.

## B.1 Particle Distance Computation for Homogeneous Samples

We begin by converting density to porosity, which is denoted, $\mathscr{P}$. Porosity is a unitless value that represents the volume fraction of a snow sample not occupied by its constituent grains. Note that the porosity only excludes the grains, *i.e.*, it includes all interstitial media such as air and water. Computing porosity is accomplished using the method described by Kinar and Pomeroy [117] with the following expression:

$$\mathscr{P} = 1 - \frac{D}{D_{ice}}, \tag{B.1}$$

where $D$ is the density of snow and $D_{ice}$ is the density of ice. The density of ice varies with temperature. This necessitates adding snow temperature, $T$, as an input parameter to the SPLITSnow model. From this, the density of ice is linearly interpolated using the data available in the CRC Handbook of Chemistry and Physics [187].

The volume fraction of the snow grains within the snow sample is denoted $V_g$. This value is the complement of the porosity, $\mathscr{P}$, which can accordingly be expressed as:

$$V_g = 1 - \mathscr{P}. \tag{B.2}$$

Now, to compute the mean distance between snow grains, we employ the following equation [115]:

$$\overline{d} = \frac{1}{V_g K}, \tag{B.3}$$

where $K$ represents the cross-sectional area of snow grains per unit volume as seen in the direction of the ray. This quantity (which has units $[\mathrm{m}^{-1}]$) is defined as:

$$K = \int_{\mathrm{X}} \mathscr{N}(\chi) G(\chi)\, \mathrm{d}\chi, \tag{B.4}$$

where X represents the set of all grain geometries, $\chi$ is a member of that set, $\mathscr{N}(\chi)$ represents the number probability density of picking a grain with geometry $\chi$, and $G(\chi)$ is the cross-sectional area of $\chi$ projected onto the plane. The integral defining $K$ is separable [115] into:

$$K = K_1 K_2, \tag{B.5}$$

where $K_1$ models the grain size distribution and $K_2$ accounts for shape. For uniformly distributed grain sizes, an analytic solution for $K_1$ can be obtained by simplifying the following definite integral:

$$K_1 = \frac{\int_{\mu_{min}}^{\mu_{max}} \mu^{-2} \mathbb{P}(\mu)\, \mathrm{d}\mu}{\int_{\mu_{min}}^{\mu_{max}} \mu^{-1} \mathbb{P}(\mu)\, \mathrm{d}\mu}, \tag{B.6}$$

where $\mathbb{P}(\mu) = 1/\left(\mu_{max} - \mu_{min}\right)$ is the probability density function for a uniform distribution in the range of $[\mu_{min}, \mu_{max}]$. This simplifies to:

$$K_1 = \frac{\mu_{max} - \mu_{min}}{\mu_{min}\, \mu_{max} \left(\ln(\mu_{min}) - \ln(\mu_{max})\right)}. \tag{B.7}$$

For normally distributed sphericity, $K_2$ reduces to [115]:

$$K_2 = \frac{\int_{\Psi_{min}}^{\Psi_{max}} \aleph(\Psi) \varphi\left(\overline{\Psi}, \sigma_{\Psi}^2\right)(\Psi)\, \mathrm{d}\Psi}{4 \int_{\Psi_{min}}^{\Psi_{max}} \varphi(\Psi)\, \mathrm{d}\Psi}, \tag{B.8}$$

where $\varphi(\overline{\xi}, \sigma^2)(\xi)$ is the probability density function (PDF) for a normally distributed random variable with mean $\overline{\xi}$ and standard deviation of $\sigma$, $\aleph(\Psi)$ is the surface area to volume ratio of a prolate spheroid with $s = 2b = 1$ (where $b$ is the semi-major axis), and $\Psi$ represents inscribed circle sphericity [183]. The quantity $\aleph(\Psi)$ is given by [115]:

$$\aleph(\Psi) = 3\left(1 + \frac{\sin^{-1}\sqrt{1-\Psi^4}}{\Psi^2\sqrt{1-\Psi^4}}\right). \tag{B.9}$$

The limits of integration for Equation (B.8), $\Psi_{min}$ and $\Psi_{max}$, are used to restrict the numeric solution to the specified range of grain sphericities. Accordingly, there are four model parameters that categorize the sphericity, namely $\Psi_{min}$, $\Psi_{max}$, $\sigma_\Psi$, and $\overline{\Psi}$.

Note that even though it is numerically complex to calculate $\overline{d}$ given the density, this operation only needs to be performed once as a precomputation at the beginning of a simulation. It can then be used to compute the distance to the next grain in the ray's path using Equation (4.1).

## B.2 Particle Distance for Heterogeneous Samples

Accommodating heterogeneous samples requires only a small change to the mean distance computation [115]. Namely, that the computation of $\overline{d}$ must be performed for each grain type in the heterogeneous sample. More specifically, the value of $K$ in Equation B.3 must be scaled by the volume fraction of the specific grain. Thus, for the $m^{\text{th}}$ grain, Equation B.3 becomes:

$$\overline{d}_m = \frac{1}{V_{g_m} K_m}, \tag{B.10}$$

where $V_{g_m}$ is the concentration of the $m^{\text{th}}$ grain and $K_m$ is the value of $K$ computed for the $m^{\text{th}}$ grain. Note that $V_{g_m}$ is computed by multiplying the total concentration, $V_g$, by the fraction of snow grains that are of the $m^{\text{th}}$ type. The value of $\overline{d}_m$ is used only for grains of the $m^{\text{th}}$ type.

# Appendix C

# Parameter Input Conversion Methods

In this appendix, we examine how the representation of certain model parameters may be modified for consistency with the terminology employed in related field or laboratory studies. More specifically, in Section C.1, we provide a method to convert from (total) water content to water saturation. Then in Section C.2, we provide a method to convert the density of a wet sample to the density of a dry sample.

## C.1 Water Fraction to Water Saturation Conversion

In this section, we outline the derivation of Equation 4.9 discussed in Chapter 4. Recall from Section 4.3, that as light propagates through the interstitial (pore space) medium, it will pass either through water or air until it intersects the next grain of snow. For simulation purposes, whether the interstitial medium is water or air is stochastically determined by a Bernoulli trial. The saturation, $\mathscr{S}$, is the fraction of the pore space that is composed of liquid water. As pointed out in Section 4.3.5, sometimes the (free or liquid) water content in a sample is provided as a fraction of the entire volume of snow. Thus, we want to determine a relation to convert from (total) water content, $\mathscr{W}$, to saturation, $\mathscr{S}$.

Recall (Section 4.3.1) that we use the symbol $D$ to represent the density of a sample in the dry state, *i.e.*, without water present in the pore space. Accordingly, this quantity can be expressed as:

$$D = \frac{\overline{v}\, p\, D_{ice}}{\mathscr{V}}, \tag{C.1}$$

where $\mathscr{V}$ is an arbitrary volume of a virtual snow sample, $\overline{v}$ is the mean volume of a snow grain in the sample, $p$ is the number of grains in an arbitrary volume of snow and $D_{ice}$ is the density

of ice. Note that $\overline{v}\mathcal{p}$ is the volume occupied by ice in $\mathscr{V}$ in $[\mathrm{m}^3]$, and multiplying $\overline{v}\mathcal{p}$ by the density, $D_{ice}$, yields the mass of the volume. For convenience, we will use the symbol $\mathscr{V}_{ice}$ to represent the volume of the grains, *i.e.*:

$$\mathscr{V}_{ice} = \overline{v}\mathcal{p}. \tag{C.2}$$

Returning to Equation C.1, we solve for the number of grains, $\mathcal{p}$, which yields:

$$\mathcal{p} = \frac{D\mathscr{V}}{D_{ice}\overline{v}}. \tag{C.3}$$

Now let's consider the space in volume $\mathscr{V}$ that is not occupied by the ice grains (the pore space), which we denote by $\mathscr{V}_{ps}$. This volume is equal to the volume of $\mathscr{V}$ after removing the volume of ice grains, $\mathscr{V}_{ice}$:

$$\mathscr{V}_{ps} = \mathscr{V} - \mathscr{V}_{ice}. \tag{C.4}$$

We now have the terms required to define the saturation, $\mathcal{S}$, with respect to the total water content, $\mathscr{W}$:

$$\mathcal{S} = \frac{\mathscr{W}\mathscr{V}}{\mathscr{V}_{ps}}. \tag{C.5}$$

In Equation C.5, we scale the total water content by the total volume, $\mathscr{V}$, and divide it by the volume occupied by the pore space, $\mathscr{V}_{ps}$. Next, we simplify Equation C.5. First, we substitute the $\mathscr{V}_{ps}$ by Equation C.4:

$$\mathcal{S} = \frac{\mathscr{W}\mathscr{V}}{\mathscr{V} - \mathscr{V}_{ice}}. \tag{C.6}$$

We then substitute $\mathscr{V}_{ice}$ by Equation C.2 to obtain:

$$\mathcal{S} = \frac{\mathscr{W}\mathscr{V}}{\mathscr{V} - \overline{v}\mathcal{p}}. \tag{C.7}$$

Finally, we substitute $\mathscr{p}$ by Equation C.3 and simplify:

$$\begin{aligned}
\mathscr{S} &= \frac{\mathscr{W}\mathscr{V}}{\mathscr{V} - \overline{v}\frac{D\mathscr{V}}{D_{ice}\overline{v}}} \\
&= \frac{\mathscr{W}\cancel{\mathscr{V}}}{\cancel{\mathscr{V}}\left(1 - \frac{\cancel{v}D}{D_{ice}\cancel{v}}\right)} \\
&= \frac{\mathscr{W}}{1 - \left(\frac{D}{D_{ice}}\right)} \\
&= \frac{\mathscr{W}}{\frac{D_{ice} - D}{D_{ice}}} \\
&= \frac{D_{ice}\mathscr{W}}{D_{ice} - D},
\end{aligned} \tag{C.8}$$

which corresponds to Equation 4.9.

Note that $D_{ice}$ represents the density of solid ice, whereas $D$ represents the density of a snowpack consisting of solid ice grains dispersed in a less dense medium, with the space between the grains (pore space) occupied by air. Therefore, $D_{ice} > D$ for all snowpacks containing a non-zero amount of pore space.

## C.2 "Wet" to "Dry" Snow Density Conversion

In this section, we outline a formulation to convert between sample characterizations that include (liquid) water content in their density specification, namely "wet" snow samples, and those that do not. We begin with the work on Kinar and Pomeroy [117], who provide a method to compute the porosity, $\mathscr{P}$, of a snow sample:

$$\mathscr{P} = 1 - \frac{D}{D_{ice}}, \tag{C.9}$$

where $D$ is the density of snow and $D_{ice}$ is the density of ice. Let the volume fraction of the "wet" snow sample that is occupied by the ice grains be denoted $\mathscr{X}$. This is the complement of the pore space, and it is given by:

$$\mathscr{X} = 1 - \mathscr{P}. \tag{C.10}$$

Recall that the SPLITSnow model parameter for saturation represents the fraction of the pore space that is occupied by water and is denoted $\mathscr{S}$ (Chapter 4). Given the saturation and

the porosity, the volume fraction of the total volume that is occupied by water, denoted by $\mathscr{Y}$, is given by the expression:

$$\mathscr{Y} = \mathscr{P}\mathscr{S}. \tag{C.11}$$

The density of the "wet" sample has two components: the density of the water in the sample scaled by the fraction of the sample occupied by water, and the density of the ice grains in the sample scaled by the fraction of the sample that is composed of these grains. Accordingly, this quantity can be expressed as:

$$D_{wet} = D_{ice}\mathscr{X} + D_{water}\mathscr{Y}, \tag{C.12}$$

where $D_{ice}$ is the density of ice and $D_{water}$ is the density of water. Substituting $\mathscr{X}$ and $\mathscr{Y}$ from equations C.10 and C.11, respectively, yields:

$$D_{wet} = D_{ice}\left(1 - \mathscr{P}\right) + D_{water}\left(\mathscr{P}\mathscr{S}\right), \tag{C.13}$$

which simplifies to:

$$D_{wet} = D_{ice} - \mathscr{P}D_{ice} + D_{water}\mathscr{P}\mathscr{S}. \tag{C.14}$$

Substituting Equation C.9 into Equation C.14 yields:

$$D_{wet} = D_{ice} - \left(1 - \frac{D}{D_{ice}}\right) D_{ice} + D_{water}\left(1 - \frac{D}{D_{ice}}\right)\mathscr{S}. \tag{C.15}$$

Simplifying Equation C.15 yields an expression to convert a "dry" sample, where the density ($D$) is specified separately from the saturation ($\mathscr{S}$) into one whose density is specified as a combined total of both frozen ice grains and liquid water content. This yields:

$$D_{wet} = D + \left(1 - \frac{D}{D_{ice}}\right) D_{water}\mathscr{S}. \tag{C.16}$$

Reordering the terms in Equation C.16 provides an expression to determine $D$ from $D_{wet}$:

$$D = D_{wet} - \left(1 - \frac{D}{D_{ice}}\right) D_{water}\mathscr{S}. \tag{C.17}$$

# Appendix D

# Determining Virtual Snow Parameter Values from Recorded Characterization Data

In this appendix, we present a brief description of the sample characterization values provided along with the measured spectral datasets [54, 169, 190] and the parameter values used to specify the corresponding virtual snow samples (see Tables 7.1, 7.2, 7.4 and 7.5) that were used in our simulations. To select the latter, we first consulted the sample characterizations that were provided along with the measured spectral data. However, some amount of interpretation of the characterization data was required. For example, the sample thickness reported in the SISpec database [190] only reflects the top layer of snow. The same is true for the grain types reported in tabular format on the SISpec website[1]. Fortunately, for the selected SISpec snow samples examined in this thesis, a snow profile diagram (*e.g.*, see Figure 4.6) is provided alongside the measured reflectance datasets. Unfortunately, similar profile diagrams do not accompany the datasets provided by Dumont *et al.* [54] and Perovich [169]. Instead, we relied upon the description of the samples in their respective works. In all cases, when employing the SPLITSnow model to conduct our *in silico* experiments that make direct comparisons to these datasets [54, 169, 190], we incorporated the associated characterization data when selecting the simulation parameter values. In the remainder of this appendix, we outline the rationale behind the selection of parameter values for each virtual sample considered in the quantitative and qualitative evaluation of the predictive capabilities of the proposed framework.

We begin with Table 7.1, which provides the parameter values employed in the characteri-

[1] https://sispec.cnr.it/

zation of the virtual snow sample considered in our *in silico* experiment to generate reflectance curves that are compared with the measured Sample 3 that was provided by Dumont *et al.* [54]. We remark that a detailed characterization of the sample was not provided with the measured reflectance dataset. In fact, Dumont *et al.* state that their own "grain size measurements are too rough to be suitable as inputs" when they compared their measured results against values obtained from simulations using models provided by Mishchenko *et al.* [139] and Picard *et al.* [172]. However, in their comparisons to these models, they employed grain size inputs ranging from 100–1000 $\mu\mathrm{m}$. Furthermore, they state that the sample consisted of "rounded grains and mixed forms" that are "rounded and faceted." We therefore elected to consider mostly spherical snow grains with a moderately low facetness that are within the aforementioned size range in our simulations. Dumont *et al.* also remark that their Sample 3 consisted of "new wet snow." However, they also indicate that the extracted sample was placed in a cold room where it "refroze." Consequently, a small quantity of liquid water was included in the virtual snow characterization. Temperature and density were not measured by Dumont *et al.*. We, therefore, employed values that are within physically valid ranges for these characteristics [60]. Lastly, we remark that the sample extracted by Dumont *et al.* was 12 $\mathrm{cm}$ thick.

Next, we turn our attention to datasets obtained from the SISpec database [190]. Referring to Sample 195, Table 7.2 indicates that a thickness of 10 $\mathrm{cm}$ was used to conduct our *in silico* experiments with the SPLITSnow model. However, the SISpec database indicates that the sample thickness is only 2.8 $\mathrm{cm}$. Note that the value of 2.8 $\mathrm{cm}$ is indicative of the thickness of the top layer of snow, and *not* the entire sample. The examination of its associated snow profile diagram (available on the SISpec website) indicates that the top layer is 2.8 $\mathrm{cm}$ thick and that there are several additional layers of snow beneath this surface layer. Furthermore, this has been confirmed by the SISpec leading administrator [191]. Returning to Sample 195, we elected to use a sample thickness of 10 $\mathrm{cm}$, which includes the total thickness of all layers of the sample.

In addition to using the snow profile diagram to select a value for the thickness parameter, other parameter values were guided by the data provided in the snow profile diagram. These include density, grain size and temperature. Indeed, for Sample 195 [190], the top layer contained 80$\%$ rounded forms that were 0.5 $\mathrm{mm}$-sized crystals and 20$\%$ irregular crystals that were 0.8 $\mathrm{mm}$ in size. The second layer contained large rounded grains (0.8 $\mathrm{mm}$), while the third layer contained small rounded grains (0.5 $\mathrm{mm}$). The third layer has the greatest thickness ($\approx 5$ $\mathrm{cm}$). Consequently, we elected to use a larger range of grain sizes. The density was set to 340 $\mathrm{kg\,m^{-3}}$, which reflects the density of the thickest layer, and the temperature was set to -3$^{\circ}\mathrm{C}$. Note that -3$^{\circ}\mathrm{C}$ is within the range of temperatures reported for the snowpack, which is much warmer than the air temperature that was reported to be -15$^{\circ}\mathrm{C}$.

A similar process was followed for Sample 197 [190]. The parameter values employed in the characterization of this sample are presented in Table 7.4. Its profile diagram indicates that the

total thickness of all layers is 19 $\mathrm{cm}$. Consequently, we used this value as an input parameter to the SPLITSnow model. We elected to use a grain size parameter value range of 400–1000 $\mu\mathrm{m}$ since the bulk of the sample consists of 500–1000 $\mu\mathrm{m}$ grains, with only a thin layer consisting of smaller grains. Similarly, we used a relatively low number of faceted crystals, *i.e.*, a parameter value range of 0.2–0.4, since the sample's layers consisted of mostly rounded grains. The profile diagram only indicates a numeric density value for two of the four layers. More precisely, 180 $\mathrm{kg\,m^{-3}}$ for the second layer, and 320 $\mathrm{kg\,m^{-3}}$ for the third layer. However, three of the four layers (including the third layer) have a symbolic indication [60] that the density is in the range of 175–390 $\mathrm{kg\,m^{-3}}$. Therefore, we elected to use a density value of 300 $\mathrm{kg\,m^{-3}}$ as a parameter value for generating the corresponding simulated curve. Lastly, we used a temperature of -1$^{\circ}\mathrm{C}$, which corresponds to the temperature measured within the second layer.

Finally, for the virtual sample whose characterization is provided in Table 7.5, we used as reference the values provided by Perovich [169] in its description of the sample obtained on January 18, which for this discussion we will label P18. Sample P18 was composed of rounded grains. More precisely, for the thickness and grain size range of the sample, we assigned the values specified in Perovich's description, namely 11 $\mathrm{cm}$ and 400–1000 $\mu\mathrm{m}$, respectively. For its density, we selected a value, 300 $\mathrm{km\,m^{-3}}$, that corresponds to the value associated with the middle portion of sample P18 as also reported by Perovich [169]. As for the temperature of sample P18, although it was not measured by Perovich, based on his description of the metamorphic conditions of sample P18, we elected to set the temperature of virtual sample to -1$^{\circ}\mathrm{C}$, a value close to the snow freezing point.

# Appendix E

# Case Study: Avalanche Slab Failure

In this appendix, we discuss a case study involving the use of the proposed framework to advance the current knowledge about light penetration into snowpacks. It is expected that a better understanding of this phenomenon will be instrumental to improve the forecasting of the conditions that facilitate the formation of slab avalanches.

Avalanches are masses of snow that rapidly descend sloped terrain. In fact, they can be classified as a complex type of ground failure involving snow [222]. They are a hazard to human welfare. For instance, they have been known to cause more deaths annually in the USA than from other hazards such as earthquakes and landslides [222]. There are also economic consequences incurred by uncontrolled avalanches, notably to the forestry sector and to transportation corridors, which include highways and railways [203]. In addition to the destruction of property, there are great financial losses each year due to delays in transportation [100]. Avalanche detection [166] and prediction [222] can help to minimize these negative consequences. Studying the conditions that affect the release of a snow slab precipitating an avalanche can assist in the development of snow failure predictions.

Avalanches can be categorized as being either wet or dry, depending upon the quantity of moisture in the snowpack [3] and can be further subdivided into two distinct types of formations. The first type, commonly referred to as loose snow avalanches [25], are initiated by snow accumulations that lack cohesion. When the slope angle is steeper than the angle of repose, then an avalanche may occur after a localized area of snow exhibits failure and begins to progress downslope. The failure progresses in an inverted V-shape when loose snow encounters additional cohesionless snow in its path. This type of avalanche presents a lower degree of hazard since occurrences are comparatively easy to predict [222]. The second type of avalanche is known as a dry slab avalanche. For this type of avalanche, a cohesive slab of snow on the

scale of 10's of meters is released [193]. This cohesive slab rests on top of an extended plane of weakness called a weak layer, which is composed of poorly bonded snow crystals. The slab can be released due to a sudden, localized loading, such as from a skier, from gradual, precipitous loading or spontaneously, from changes in the snowpack properties such as warming [193]. The primary difference between the triggering methods is the rate of loading. Upon a triggering event, the stress on a snow slab exceeds the bonding strength of the weak layer that is holding it in place and a catastrophic failure occurs.

As mentioned above, the weak layer is composed of snow crystals with low bonding. The weak layer may form from various types of crystals including surface or depth hoar [193], graupel or new-fallen low-density stellars [25], or it may be comprised of near-surface faceted crystals [25, 193]. In particular, a significant fraction of slab avalanche accidents are formed with weak failure planes consisting of near-surface faceted crystals [25, 101]. After the formation of the weak layer, subsequent snowfalls bury the weak layer and form an upper cohesive slab.

In this case study [216], we focus upon the formation of near-surface faceted crystals, *i.e.*, the formation of a weak layer *before* it is buried by a cohesive surface layer. For near-surface faceted crystals to form, impinging light must penetrate to a depth below the surface of the snowpack. For snowpacks with a sufficient depth, this impinging light is scattered by the grains until it is either reflected or absorbed. The absorbed radiation is the energy source that creates temperature gradients and vapour pressure gradients within the snowpack. These vapour pressure gradients drive the process of snow crystal metamorphism, whereby matter from snow crystals is both vapourized and deposited between crystals as part of the radiation recrystallization process [25, 42]. This phenomenon occurs at high elevations where solar radiation is the strongest [42].

The penetration of solar radiation can be measured directly using a spectrophotometer [24, 52, 68, 169]. However, despite current efforts, there are few transmittance datasets available in the literature. Some of these were obtained at locations where impurities were known to affect the sample [169], which has a significant affect on the spectral characteristics of snowpack [232]. Other datasets were obtained using samples that were morphologically active due to temperature changes [68]. None of these datasets were obtained in high altitude locations where the conditions exist to form weak layers associated with slab avalanches. A lack of such studies may be attributed to the risk of triggering a snow failure event by human loading [193], difficulties to conduct transmittance measurements [70], including the placement of a measurement device that can alter the radiation EM profiles in the vicinity of the sample [55].

In order to overcome these limitations and contribute to the current knowledge about light penetration in snowpacks, we employed the SPLITSnow model, (Chapter 4) to conduct an *in silico* study of light penetration into snow. By using measured spectral data as a reference and

snow characterization values obtained from the literature, we performed experiments to investigate the light penetration depth for various snow samples. We remark that the SPLITSnow formulation takes into account various characteristics of the grains, including the grain size distribution, density and facetness, which are necessary for examining radiative transfer properties within snowpack.

The experiments in this case study assess the depth to which light penetrates into various snowpack samples with distinct characteristics. To our knowledge, no such investigation has been made available in the literature as of yet. By elucidating the light penetration depth for various snowpack samples, we hope to assist in the effort of avalanche prediction, thus improving the circumstances governing human safety. In addition to the application of near-surface faceted crystal formation *via* light propagation, the results of these experiments may also have an impact on other areas such as on the blooming of ice algae [45] and on the radiation budget of shallow lakes [170].

## E.1 Avalanche Formation

As mentioned earlier, there are two distinct types of dry avalanches. These are loose snow avalanches and dry slab avalanches. Loose snow avalanches occur when the slope angle is steeper than the angle of repose and a small amount of snow becomes unsettled and begins to progress downslope. This type of failure results in a characteristic inverted V-pattern, and it is less difficult to predict [222]. Dry slab avalanches are comparatively more difficult to predict. They are identified by the sudden release of a large slab of snow on the scale of 10's of meters across, and the released slab layer is usually less than one meter thick [193]. Given the gravity of this second type of avalanche, we will focus on dry avalanches in this study. Figure E.1 illustrates the process.

There are a number of terms commonly used in the literature regarding dry slab avalanches. The breakaway fracture point at the top of a dry slab avalanche is known as the crown, the downslope fracture surface, which is usually overridden, is known as the stauchwall, and the left and right edges are known as flanks [133]. As already described, the cohesive slab rests on top of a layer of weakly bonded grains such as faceted crystals. Beneath this layer, there is a basal layer of snow known as the substratum. This layer remains in place after a failure event.

Initiation typically begins with a loading event whereby a load is added to the surface of the snowpack. This load can be prompted by precipitated or wind-blown snow, snow fallen from a higher precipice or a human participating in a recreational activity such as skiing. The weak layer separates from the slab (and possibly from the substratum) as a localized failure

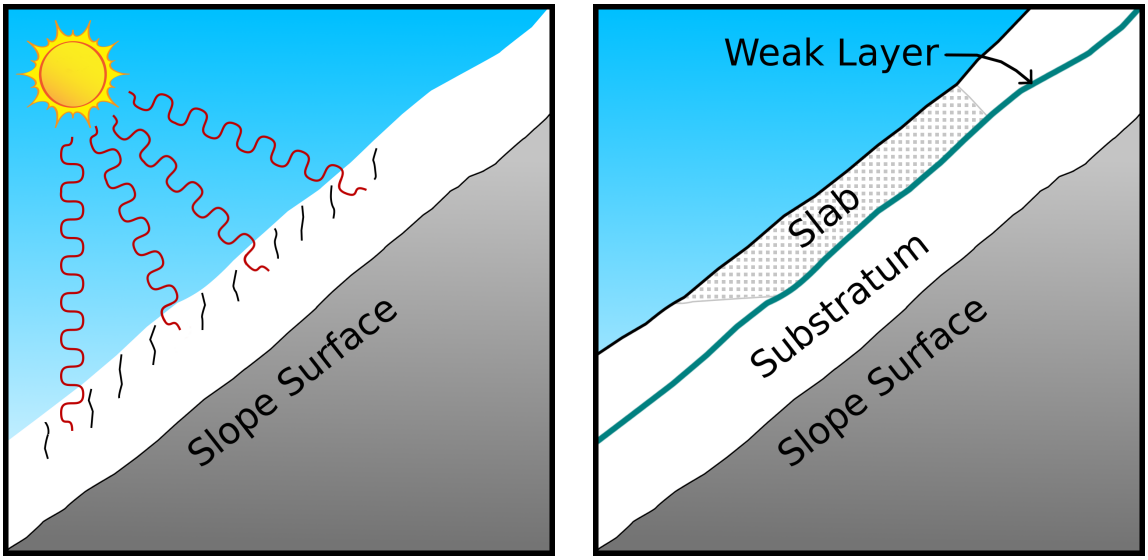


(a) (b)

Figure E.1: Illustration of the slab avalanche formation process. In (a), solar radiation permeates to a depth within a snow pack. In (b), a layer of weakly bonded faceted snow crystals has been formed at a depth within the snowpack. The absorption of the solar radiation and the ensuing morphological changes that affect the sintering[1] between the grains contribute to the formation of this layer.

at the point of loading. This localized failure propagates as a shear fracture below the slab in the plane of the weak layer. As a consequence of the shear stress, the large volume of snow contained in the cohesive slab is released as a single formation. The crown and flanks remain after the event and they can be observed after the mass of snow has progressed downslope.

We remark that the weak layer is initially formed either at the existing surface or at a depth just beneath the surface. The formation process may create hoar crystals, such as hollow cups or prisms [60], or solid faceted crystals. After formation, the weak layer is buried by further snow accumulation which forms a dangerous cohesive slab. Since a significant fraction of avalanche slabs have a bed surface consisting of faceted crystals [25, 101], we focus the attention of our experiments on the formation of subsurface faceted crystals. In particular, we investigate the light penetration depth of solar radiation since this radiation is the energy source which elicits the morphological processes underlying crystal growth [42].

[1]Sintering is the formation of bonds between the grains of snow [43].

## E.2 *In Silico* Experimental Setup

Our *in silico* experiments computed the light penetration depth through various natural snow samples. Each sample was selected with distinct characterization values that impact light penetration depth in snowpack. For each sample, a directional-hemispherical transmittance experiment was performed. Our experiments focused on the spectral domain of 400–1500 $\mathrm{nm}$ since the constituent components of snow are known to be absorptive in the near infrared domain [164, 230]. We remark that this domain includes the values commonly used in studies of light transmittance through snow [24, 52, 68, 169]. In our experiments, we considered a spectral resolution of 10 $\mathrm{nm}$.

Recall from Chapter 7 that we performed a baseline comparison between measured data provided by Dumont *et al.* [54] and simulated data whose parameter values are presented in Table 7.1. We deemed the resulting virtual snow sample as the *representative sample*, a convention that we also consider in this case study. Furthermore, we employed the same characterization values for our transmittance experiments, varying only the independent variable under test.

For our experiments, we selected two characterization traits to investigate, namely grain size and density, and varied the associated model parameter values. The transmittance curves were computed throughout the selected spectral domain for various thicknesses. For grain size, we selected two average sizes, 100 and 500 $\mu\mathrm{m}$, which we label *small* and *medium*-sized, respectively. The selected grain size under test is the mean of a uniform distribution of grain sizes, with a range of $\pm 50$ $\mu\mathrm{m}$. The two density values employed in our experiments are 100 and 400 $\mathrm{kg\,m^{-3}}$, which we label as *low* and *high*, respectively. Varying these two parameters yields four study samples. Our experiments were repeated four times for each sample using a selection of sample thicknesses. This approach produced a profile of the light penetration depth for each of the four samples.

## E.3 Experimental Findings

In this section, we present the results of our experiments and discuss their implications for remote sensing in the context of weak-layer formation and the prediction of slab avalanches. All transmittance graphs presented in this section were plotted using the same scale. This was done to illustrate the relative impact each independent variable has on the amount of solar energy transmitted through the snowpack.

Our first experiment investigates the effect of grain size on light penetration depth. We computed the transmittance values using two different grain sizes. All other parameter values

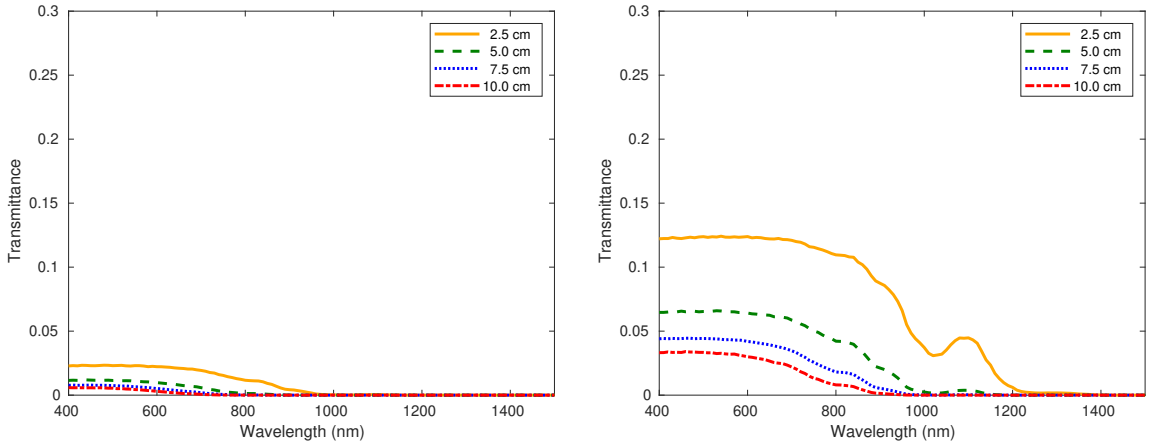


Figure E.2: Comparison of simulated transmittance curves computed for two different snow grain sizes for various sample depths (thicknesses). The curves depicted in (a) were computed using an average grain size of 100 μm, whereas the curves depicted in (b) were computed with an average grain size of 500 μm.

were kept the same as the representative sample. The data provided in the literature [194] suggest that weak layers contain grains that are 2 mm in size. However, these data were recorded after snow failure. For this investigation, we chose to study small and medium-sized grains, which have not completed the morphological processes induced by solar radiation penetrating the snowpack.

Figure E.2(a) presents graphs of light transmission through the snowpack with small grains (mean size 100 μm), whereas Figure E.2(b) presents similar graphs that were generated using medium-sized snow grains (mean size 500 μm). Observe that for small grain sizes, less than 3% of solar radiation (in the 400 to $\sim$ 800 nm range) is transmitted below 2.5 cm depth. However, for medium grain sizes over 10% of this radiation is transmitted to a depth of 2.5 cm, and nearly 5% is transmitted to a depth of 7.5 cm. This indicates that transmittance is directly proportional to grain size, which is consistent with observations reported in the literature for granular materials [5, 40, 208]. Thus, it provides evidence that sufficiently large snow grains will promote the formation of near-surface weak layers, which may lead to the precipitation of avalanches. Indeed, as stated above, large grain sizes have been observed in the residual weak layer after a failure event [194].

Our second *in silico* experiment investigates the effect of density on light penetration depth. We computed the transmittance values for the representative sample using two different densi-

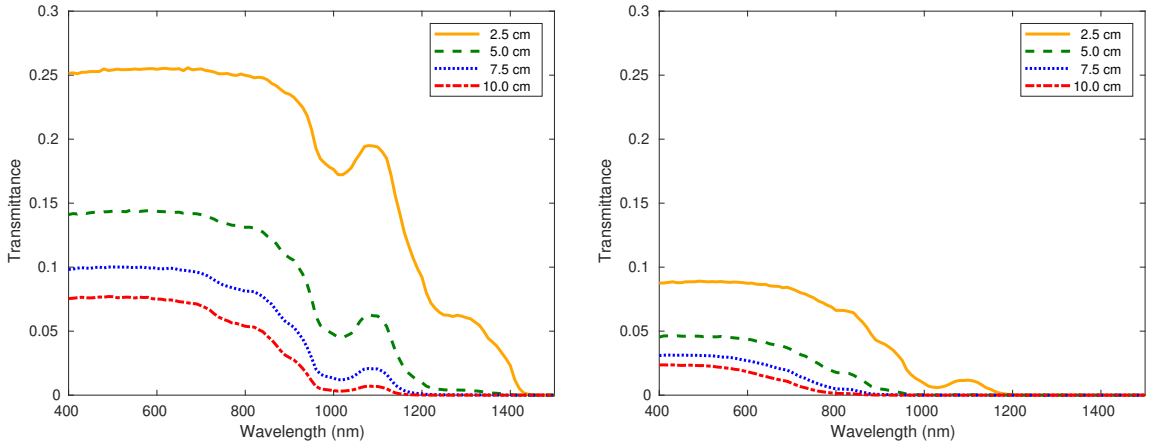


Figure E.3: Comparison of simulated transmittance curves computed for two different snow densities for various sample depths (thicknesses). The curves depicted in (a) were computed using a density of 100 $\mathrm{kg\,m^{-3}}$, whereas the curves depicted in (b) were computed with a density of 400 $\mathrm{kg\,m^{-3}}$.

ties. All other parameter values were kept constant with those of the representative sample. The low density (100 $\mathrm{kg\,m^{-3}}$) graphs are presented in Figure E.3(a) and the high density (400 $\mathrm{kg\,m^{-3}}$) graphs are presented in Figure E.3(b). The low density graphs show a greater transmittance, which is consistent with reports found in the literature [159, 238]. (See also Section 7.2.2.)

The curves in Figure E.3(a) indicate that a significant fraction of solar radiation penetrates low density snowpacks. At a depth of 2.5 $\mathrm{cm}$, approximately a quarter of the visible light is permeated. The quantity lessens in the infrared spectral domain, where absorption is more significant. However, a non-trivial amount of transmittance is still verified in the near-infrared domain, especially in the neighbourhood of 1100 $\mathrm{nm}$. Furthermore, less than 15$\%$ of solar radiation in the visible domain is transmitted below a depth of 2.5 $\mathrm{cm}$. Finally, approximately 7.5$\%$ of solar radiation in the visible domain is transmitted below 10 $\mathrm{cm}$.

The transmittance curves in Figure E.3(b) depict the fraction of solar radiation that penetrates through high density snow for various depths. With high density snow, less than 10$\%$ of the incident light penetrated below a 2.5 $\mathrm{cm}$ depth. At a 10 $\mathrm{cm}$ depth, less than 2.5$\%$ of the light is transmitted. These findings are consistent with radiation penetration theory predicting snow crystal growth [42], whereby faceted crystal growth is computed to be greatest below the surface at depths less than 15 $\mathrm{cm}$.

Our final experiment addresses the combination of the two independent variables already

examined in order to obtain insights into light penetration through four distinct study samples. Except for density and grain size, all other parameter values are kept consistent with the representative sample. The results are presented in Figure E.4. More specifically, the samples used to generate the graphs in the top row were computed using small grains, and the samples used to generate the graphs in the bottom row were computed using medium-sized grains. The samples on the left side were computed using low density snowpacks, and the samples on the right hand side were computed using high density snowpacks. It is interesting to observe that less than $2\%$ of the visible radiation was transmitted below $2.5\ \mathrm{cm}$ for the small grain, high density sample (Figure E.4(b)). In contrast, a significant fraction of visible and near infrared radiation was transmitted for the medium-sized grains with low density (Figure E.4(c)).

It is also interesting to make a direct comparison between Figures E.4(a) and (d). Observe that the transmittance values are approximately on the same order of magnitude. In Figure E.4(a), the transmittance of the solar radiation is affected by the low density of the snowpack, whereas in Figure E.4(d), the increase in grain size contributes to the quantity of light that is transmitted into the snowpack. A little more than $5\%$ of the visible solar radiation is transmitted to a depth of $2.5\ \mathrm{cm}$ as presented in Figure E.4(a), and a little less than $10\%$ of the visible solar radiation penetrates to the same depth as presented in Figure E.4(d). This indicates that both density and grain size are factors that affect the morphological processes that govern the formation of weak layers.

Given the relationship between the penetration of light into snow and the studied grain properties, we conclude that physically based estimations for both these snowpack properties would assist in the process of avalanche prediction. In particular, low density snowpacks with medium-sized crystals are susceptible to light penetration to a depth that is sufficient to foster the morphological processes that produce weak layers consisting of near-surface faceted crystals. Improved monitoring of snowpacks exhibiting these traits may eventually lead to improved prediction of snow slab failure events.

## E.4 Summary and Perspectives

Avalanches are natural events incurring significant costs in the form of transportation delays and property damage, while also posing risks to human life [100, 166, 203, 222]. We remark that dry slab avalanches are the most hazardous type of these events since they are more difficult to predict. The process of dry slab avalanche formation begins with light impingement on the surface of the snow and the induction of thermal and convective flows below the surface. These morphological processes may produce near-surface faceted crystals of which weak layers are formed. Once buried beneath a cohesive layer, these near-surface faceted crystals form the

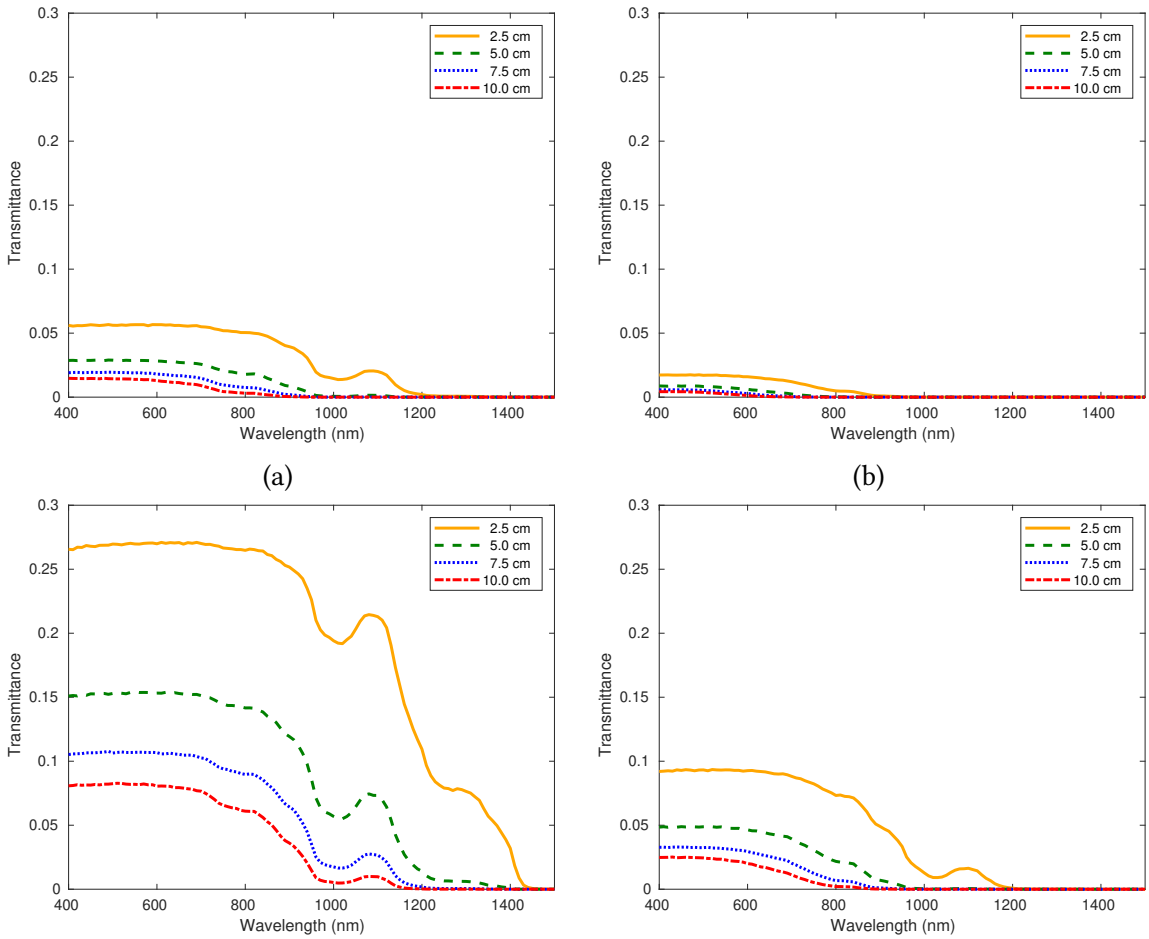


Figure E.4: Comparison of simulated transmittance curves computed for four different snow samples for various sample depths (thicknesses). The curves depicted in the top row were generated using small grains (100 $\mu$m), whereas the curves depicted in the bottom row were generated using medium-sized grains (500 $\mu$m). The curves depicted on the left were computed using a low snow density (100 $\mathrm{kg\,m^{-3}}$), whereas the curves depicted on the right were computed using a high snow density (400 $\mathrm{kg\,m^{-3}}$).

weak layer associated with slab failure. Although extensive studies have been conducted to investigate the cause of these failures, works addressing light transmission through snowpack are still scarce in the literature. This may be due to the challenging task of accounting for the morphological features at small scales. To address this concern, we performed experiments using an *in silico* investigation approach that is supported by actual measured data and allows for the configuration of the morphological features for various snow samples.

Our findings indicate that the transmittance of a snowpack is proportional to the size of its grains and inversely proportional to its density. Our calculations are also consistent with analytic approaches describing snow crystal growth [42]. More specifically, they demonstrate that particular combinations of grain size and density allow for light to penetrate to the depth required to facilitate near-surface faceted crystal growth in the snow pack. In addition, the results of our investigation strengthen the knowledge required for the predictive assessment of the factors leading to snow failure. In turn, such an assessment can be instrumental to the implementation of solutions that reduce the costs incurred from these hazardous events.

Our investigation focused on the effect that grain size and density have on light transmission through snowpacks in the formation of weak layers consisting of near-surface faceted crystals. In the future, we intend to expand upon this effort by increasing the quantity of samples that are examined for each trait, thus increasing the dimensionality of each independent variable. This will enable us to examine the relationship (*e.g.*, linear or quadratic) between the parameter values and their effect on transmittance. This may also add to the understanding of the effect of snow morphology on light penetration through snowpacks. For example, as morphological changes are induced by the impinging light, what is the effect on light penetration throughout the depth of the snowpack, and how is the process of weak layer formation bounded? We also note that other snow grain parameters may have an effect on light transmission through the material. We intend to incorporate other such parameters into our subsequent studies. In particular, we plan to investigate how snow grain facetness may also affect the transmission of light. We note that parameters such as facetness can be effectively studied using a first-principles approach such as the one employed in this work.

# Appendix F

# Case Study: The Effect of Grain Facetness on Directional Reflectance

Due to its reflective properties, snow plays a key part in the regulation of Earth's climate [22]. It is also relevant for agriculture, providing source water for irrigation purposes at mid-latitudes [21]. Quantifying this water resource is a challenge since significant volumes are deposited in remote regions that are often difficult or time consuming to access. Consequently, remote observations are often required in order to assess the properties of snow deposits with regularity.

Data acquisition by remote systems requires that the geometry of the observation be taken into account. This is due to the fact that the directional component of reflectance, *i.e.*, the BRDF, of snow is not directionally uniform. In addition to the angle of illumination and the angle of observation, other factors may affect the BRDF response of a material. For example, the wavelength of the incident light. Material characteristics also play an important role [30]. Since they vary with time [42] and with environmental factors associated with the snowfall [60], the BRDF values of fallen snow on the ground must take these variations into account. In order to properly assess the characteristics of the snowpack *via* remote observations, it is important to understand how BRDF responses are affected by these variations. For example, the grain size [54, 127, 231, 232] and facetness [54] of snow are known to have an effect on the directional responses.

To date, a number of studies have been conducted, whereby the bidirectional reflectance of snow has been measured [2, 54, 95, 126, 127, 163, 231]. Each study contributed a noteworthy dataset to the literature. Whereas some of these datasets do include measurements of multiple samples that exhibit varying grain characteristics [54, 127, 163], many datasets present measurements for just a single sample. As a consequence, it is difficult to isolate the effect that

varying the values of a particular snow grain characteristic imparts on the BRDF.

The case study described in this appendix aims to address these limitations and to add to the current knowledge about directional light reflectance from snowpacks. Accordingly, using the SPLITSnow model (Chapter 4), we carried out controlled experiments using measured spectral data references and snow characterization parameter values that are consistent with sample characterizations provided in the literature. Our findings expand upon the trends previously observed to exist between snow grain facetness and bidirectional reflectance. They also provide an original assessment of the effect of facetness on bidirectional reflectance, which had previously only been reported anecdotally in the literature.

Using this *in silico* approach, we investigated the bidirectional reflectance of a snow sample considering two markedly distinct degrees of facetness (Section F.1). The remainder of the characterization parameter values are provided in Table 7.1. We remark that snow grains with a large number of facets are commonly referred to as faceted crystals [60]. In this study, we use the terms *grain* and *crystal* interchangeably. In addition to varying the facetness, the sample was also irradiated using two different sources of illumination. The first illumination source (600 $\mathrm{nm}$) operates in the visible domain, in which snow is known to be highly reflective [228]. The second illumination source (1800 $\mathrm{nm}$) operates in the infrared domain in which light interacting with a snowpack undergoes a significant amount of absorption, while still exhibiting a complex pattern of bidirectional reflectance.

## F.1 *In Silico* Experimental Setup

Recall form Chapter 7 that we performed a baseline spectrometric comparison between measured data provided in the literature [54] and simulated data. The two corresponding reflectance curves are presented in Figure 7.1 and the simulation parameters are presented in Table 7.1. We deemed this virtual snow sample the *representative sample*, and we continue to refer to it as such in this case study.

The *in silico* experiments conducted for this case study consisted of the computation of the BRDF of the virtual snow sample using two distinct values for facetness, namely 0.1 and 0.9. The remainder of the parameter values were kept the same as those that were used to characterize the representative sample. Bidirectional reflectance experiments were performed for each value of facetness to obtain the modelled readings.

As mentioned above, our experiments examine the effect of facetness on the BRDF. Faceted crystals are identified by sharp edges and corners. This is in contrast to grains that exhibit

rounding at the edges and corners. Recall that, microfacets [44, 213] are employed in the formulation of the SPLITSnow model to account for faceted grains, and that facetness is a unitless parameter ranging from zero to one, where zero indicates a perfectly smooth grain. In practice, the facetness is specified as a distribution of values to be selected from stochastically.

We performed our experiments using two separate wavelengths of light. More specifically, we selected 600 $\mathrm{nm}$ for our first set of experiments since snow is highly reflective at this visible wavelength. The second wavelength that we chose for experimentation was 1800 $\mathrm{nm}$. This near infrared wavelength is much less reflective than 600 $\mathrm{nm}$. It was selected since it exhibits an appreciable amount of reflectance, and it is known to have reflectance features that differ widely in their directional component [95].

## F.2 Experimental Findings

In this section, we initially present the results of our experiments that make use of a virtual 600 $\mathrm{nm}$ light source to irradiate the virtual snow sample for both degrees of facetness. We then show the results of our experiments in which the sample is irradiated using an 1800 $\mathrm{nm}$ light source. Finally, we compare the outcomes of both experiments and discuss their implications for remote sensing applications.

Throughout this section, the parameter values for the sample were all kept the same as those used for the representative sample provided in Table 7.1. Only the independent variable under test was adjusted to suit the experimental conditions.

The plots in Figure F.1 present the results of our experiments using a 600 $\mathrm{nm}$ light source. Figure F.1(a) is a 3D plot of the directional response for an illumination source impinging upon the material at an angle of 60° away from the zenith. The surface plot represents the magnitude of the directional reflectance in the upper hemisphere over the sample. The sample in Figure F.1(a) has an average facetness of 0.1. Similarly, Figure F.1(b) represents the same sample and illumination source. However, in Figure F.1(b), the mean facetness has been set to 0.9. Figure F.1(c) presents slices of the 3D plots that have been taken through the principal plane, which is the plane that contains both the normal to the surface and the direction of incidence.

We remark that snow is highly reflective at 600 $\mathrm{nm}$ (see Figure 7.1). Yet even at this wavelength, the variation between the unfaceted and faceted responses is noticeable. The variation is not extensive, which is consistent with observations recorded in field studies [95]. Nevertheless, a forward-scattering peak can be observed for the unfaceted crystals, whereas the peak is reduced for faceted crystals. Although there have been observations reported in the literature whereby facets have been shown to affect bidirectional reflectance [54, 163], specific details of

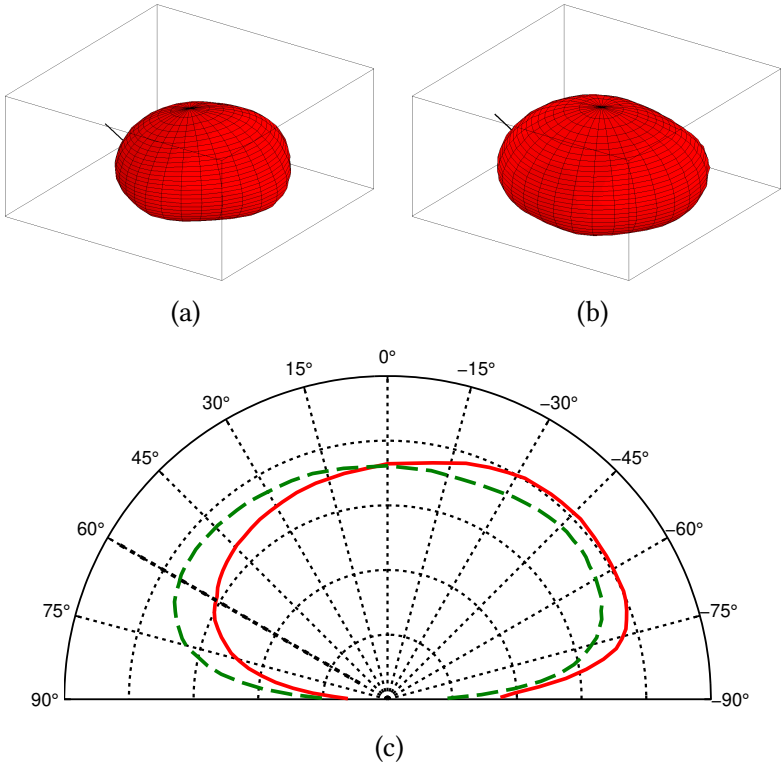


Figure F.1: BRDF plots computed for the representative sample considering a wavelength of 600 nm and two different quantities of facetness. The angle of incidence was set to 60°. A facetness of 0.1 was employed to produce (a) whereas (b) was computed using a facetness of 0.9. The solid black line in (a) and (b) indicates the direction of incidence. Slices (through the principal plane) of these two 3D plots are presented in (c). The red solid curve is a slice through (a) and the green dashed curve is a slice through (b). In (c), a black dotted line indicates the direction of incidence.

this effect are scarce. It is worth noting that, in field studies, it may be difficult to isolate the effect of facetness from the effect of grain size. This difficulty can be attributed to methodological constraints hindering the variation of only a single characterization trait of the measured samples.

The results of our second experiment are presented in Figure F.2. Similar to Figure F.1, Figure F.2(a) presents BRDF values for unfaceted crystals (mean facetness is 0.1), Figure F.2(b) presents BRDF values for highly faceted crystals (mean facetness is 0.9) and Figure F.2(c) presents a slice through the principal plane of the two 3D plots. Our results indicate a markedly different

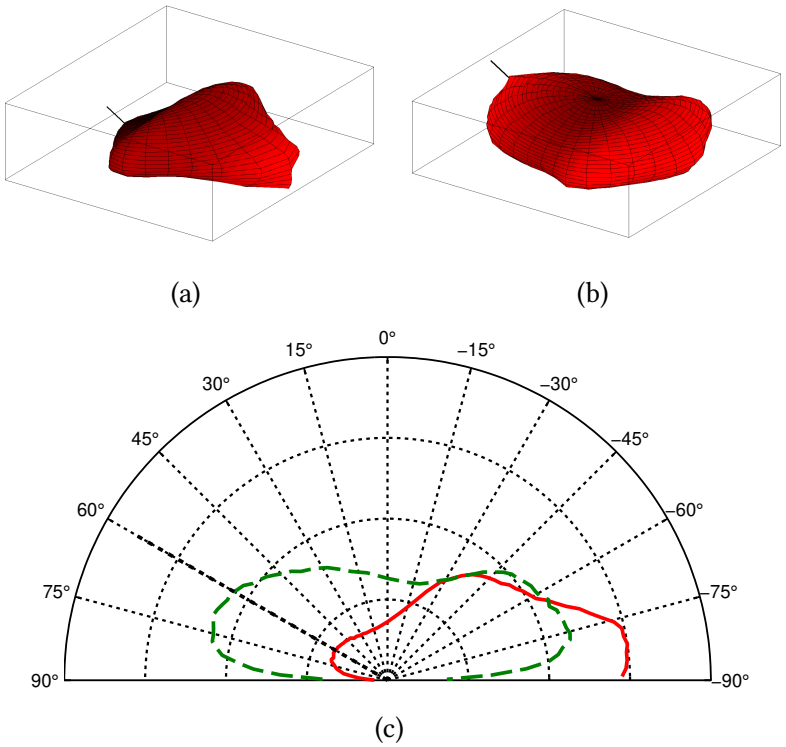


Figure F.2: BRDF plots computed for the representative sample considering a wavelength of 1800 nm and two different quantities of facetness. The angle of incidence was set to 60°. A facetness of 0.1 was employed to produce (a) whereas (b) was computed using a facetness of 0.9. The solid black line in (a) and (b) indicates the direction of incidence. Slices (through the principal plane) of these two 3D plots are presented in (c). The red solid curve is a slice through (a) and the green dashed curve is a slice through (b). In (c), a black dotted line indicates the direction of incidence.

response between unfaceted and faceted crystals. The sample, when characterized by smooth crystals, demonstrated a greater forward-scattering peak, whereas the sample, when consisting of faceted crystals, exhibited both forward- and backward-scattering peaks. These observations are consistent with the measured values presented by Painter and Dozier [163] where they observe a local backward-scattering peak in fine, faceted snow crystals. In addition to this, it has been observed by Aoki *et al.* [2] that bidirectional reflectance is known to have more directional variation in the near infrared. This phenomenon is also reproduced by our experiments, and it can be observed by comparing Figures F.1 and F.2.

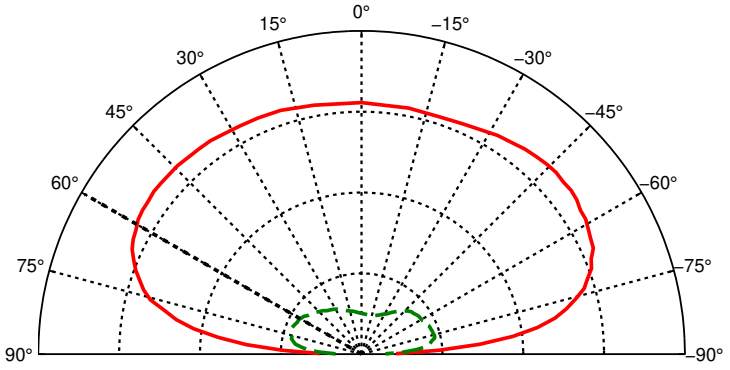


Figure F.3: BRDF plots (through the principal plane) computed for the representative sample considering two different wavelengths. The angle of incidence and facetness were set to 60° and 0.9, respectively. The two wavelengths employed were 600 nm (red solid line) and 1800 nm (green dashed line) to allow for a comparison to be made regarding relative brightness. A black dotted line indicates the direction of incidence.

As shown in Figure 7.1, spectral reflectance at 600 nm is significantly greater than at 1800 nm. To further illustrate this aspect, Figure F.3 presents a comparison of the directional profiles for faceted crystals (mean facetness is 0.9) for both 600 nm and 1800 nm depicted at the same scale. The red solid curve was reproduced using the same data that was used to obtain the green dashed curve in Figure F.1(c), and the green dashed curve was reproduced using the same data that was used to obtain the green dashed curve in Figure F.2(c). We remark that the same sample was used to produce the curves in Figures F.1 and F.2, and that only the wavelength of the illumination source was altered.

It has been demonstrated [2, 53, 95] that there is an increase in the variation of the directional reflectance when snow is illuminated with a wavelength of light that exhibits a smaller amount of total reflectance, *i.e.*, when a wavelength of light that is known exhibit a high total amount of reflective, the directional variation is reduced. This aspect has been attributed to an increase of the effect of single scattering [163]. The association between grain size and directional reflectance has also received attention in the literature [54, 95, 127, 163, 231, 232]. Although it has often been observed that an increase in grain size leads to an increase in the variation of directional reflectance [127, 163], it has also been noted that this is wavelength dependent [231].

The morphological changes observed throughout the metamorphic process of snow affect more than a single characterization trait, such as grain size, at a time [41]. Other characteristics, such as facetness, are also affected by morphological changes. This imposes limitations

on studies conducted in the field and complicates the analysis of their results [54]. By employing a first-principles *in silico* framework, we have been able to keep grain size constant and examine the effect of facetness on the BRDF of snow. Our experiments indicate that, at 1800 $\mathrm{nm}$, snow crystals with low facetness exhibit marked variation throughout their directional response curves. In particular, directional reflectance in the forward direction is greater. Although less pronounced, this phenomenon has also been reproduced in our experiments considering an incident light at 600 $\mathrm{nm}$.

In the case of natural snowpacks that have been precipitated as crystals, it is understood that morphological processes [41] alter the crystals so that they become less faceted over the course of several days. The same morphological processes also often contribute to the growth of the crystals, making the average crystal size increase with time. Due to the aforementioned limitations of field studies, it may be challenging to perform an *in situ* quantification of the effect of individual characterization value changes. In particular, as noted above, an increase in directional variation is often attributed to an increase in grain size. Our *in silico* experimental results indicate that grain size is not the only characteristic that affects the bidirectional reflectance.

Efforts have been made to estimate the grain size of snow using observations made in the near infrared domain [156, 157]. As smaller new-fallen faceted crystals morphologically change into larger less faceted crystals over time, the effect on the BRDF in the infrared domain is nontrivial, and it is affected by changes due to both characterization traits. The increased size of the crystals tends to increase the variations on directional reflectance [2, 53, 95]. However, our findings indicate that the decrease in facetness also augments the BRDF by increasing the amount of forward scattering. Therefore, attempts to assess snow grain size *via* remote observations could be improved by accounting for the faceted nature of the snow grains into these research initiatives.

## F.3 Summary and Perspectives

In this case study, we used SPLITSnow to conduct *in silico* experiments involving the bidirectional reflectance of snow. Given the abundance of snow and its relevance to climate and fresh water reserves, regular assessments of this natural resource are important to human welfare. Unfortunately, much of this natural material is precipitated at difficult or costly to access regions, thus requiring the use of remote observations for monitoring purposes. Viewed in this context, a comprehensive understanding about this material's scattering properties (quantified in terms of its BRDF) is essential for assessing snowpack properties on the ground.

Besides the material's macroscopic features and optical properties, their intrinsic characteristics, such as grain size, can also affect their directional reflectance. The effect of some of these characteristics has been examined in field and laboratory studies. Our investigation has shown that grain facetness is also particularly relevant for studies involving snow BRDF. Accordingly, it should be accounted for in related research initiatives in this area so that more insightful knowledge and reliable data about this complex natural material can be obtained.

In the future, we intend to extend this investigation by examining the BRDF associated with more wavelengths of interest. In particular, the 1030 $\mathrm{nm}$ band [157] as well as the 860 $\mathrm{nm}$ and 1640 $\mathrm{nm}$ bands [92] have been employed in snow grain size retrieval estimates. Examining a broader portion of the spectrum will aid in such studies. We also intend to investigate the effect that other snow sample characterization parameters have on the BRDF of snow. For example, snow grain shape (spherical vs. elongated), water content and density may all have an impact on the spatial distribution of light propagated by snow. For some characteristics, rather than altering the qualitative form of the BRDF, a scaling of the response values may be detected. For such cases, an *in silico* investigation would ideally suit the task of determining the relationship (*e.g.*, linear, quadratic, *etc.*) between the characterization trait and the effect on the response. Lastly, the transmission of radiation through thin layers of snow has an effect on the radiation budget of frozen lakes [170]. It might also be interesting to account for the thickness of the snowpack and its effect on the BTDF for such environments.

# Index